Satellite-enabled early warning system for geotechnical structures

Maral Bayaraa

Department of Engineering Science

University of Oxford, Wadham College

Supervisor: Dr. Brian Sheil

This dissertation is submitted for the degree of

Doctor of Philosophy

October 2024

Declaration

I declare that except where specific reference is made, the content of this thesis is my own original research and has not been submitted, in whole or in part, for any other degree at the University of Oxford or any other university. This work does not exceed the prescribed word limit.

Maral Bayaraa,

October 2024

Abstract

There is a critical need to protect communities, natural habitats and the ecosystems from toxic mine waste pollution that can result from the collapse of tailings storage facilities (TSFs). With increasing role of mining in the transition away from fossil fuels, the need to do mining safely and sustainably is of critical importance. Satellite Synthetic Aperture Radar Interferometry (InSAR) shows much promise towards this monitoring ambition on the global scale. In this work, the opportunities and challenges for developing a satellite based early warning system for TSFs are explored. This necessarily brings together three separate fields - geotechnical engineering, satellite remote sensing and deep learning.

Firstly, ground deformation measurements from InSAR and ground-based prism monitoring are compared to Finite Element (FE) simulation results for a recent tailings dam collapse. The study highlights the efficacy and complementarity of geotechnical and remote sensing techniques for the monitoring of TSFs. Moreover, extracting meaningful information and interpreting the deformation patterns from InSAR data can be a challenging task. One approach to address this challenge is through the use of data science techniques. The representation of InSAR metadata as Embedded Entities within a Deep Learning framework (EE-DL) is proposed for modelling the spatio-temporal deformation response. This study demonstrated that EE-DL can detect and predict the fine spatial movement patterns that eventually resulted in the TSF collapse. Overall, EE-DL is proposed as a promising approach for building early-warning systems for critical infrastructures that use InSAR to predict ground deformations. This research is designed to push the limits of what is possible from the globally available open source data from the Sentinel-1 satellite. Moreover, the value and improvement in the early warning framework offered by commercial, high resolution data from the satellite Radarsat-2 are also investigated.

Radarsat-2 [illegible] ᠃

[illegible] Sentinel-1 [illegible] ᠃ [illegible] ᠃

[illegible] ᠂ EE-DL [illegible] InSAR [illegible] (Embedded Entities within a Deep Learning framework - EE-DL) [illegible] (data science) [illegible] ᠃ [illegible] InSAR [illegible] ᠃ [illegible] InSAR [illegible] ᠃ [illegible] ᠃

[illegible] InSAR- [illegible] (Finite Element Modelling) [illegible] (deep learning) [illegible] ᠃ [illegible] ᠃ [illegible] (InSAR) [illegible] ᠃ [illegible] ᠃ [illegible] (᠑-᠑-᠓) [illegible]

Acknowledgements

First of all, I want to thank my mother and grand-mother, Dr. Bazarragchaa and Dr. Khand, who have achieved the unexpected, jumping above and beyond the boundaries of the societies into which they were born into. I also want to thank my father, Bayaraa, and the rest of my big beautiful Mongolian modern nomad family, relatives and ancestors. Thank you all for your unconditional love and support.

I want to thank Dr. Brian Sheil for the infinite patience, kind support and guidance through the PhD process and welcoming me into his research group.

I want to thank Dr. Cristian Rossi for his unending support, encouragement and inspiration to pursue my PhD dreams alongside our work at the Satellite Applications Catapult. I also want to thank Prof. Sinan Acikgoz for his kind support and welcoming me into his research group. I also want to thank Dan Wicks for helping me manage my work and study.

I want to thank Delia for the adventures in Peru and Machu Pichu, which have inspired the topic of my thesis. I want to thank my friends Christophe, Joel, Mina, Adrien and Tristan for their push to take the first steps of undertaking this PhD research. I want to thank Prof. Matthew Watson and Dr. Orolmaa Demberel for guiding my first steps into the world of research in 2014.

I want to thank the great friends I made in the department of engineering science and room 11. I want to thank the Wadham college for the Keeley Senior Scholarship. I also want to thank the Wadham college community, especially Julie Hage, Martin Bureau, Tamara Baker, Barnaby Norman and Martin Smith for their kind support through the four years, including hosting a visit from the deputy prime minister of Mongolia in 2023 and helping me articulate my research through public media.

I want to thank the Royal Commission for the Exhibition of 1851 for ultimately making my PhD dreams become reality through the Industrial Fellowship. I also want to thank the Prototypes for Humanity for awarding this research at COP28 in the category of Data Science and AI.

I hope the research themes presented in this thesis helps pave the road towards our much needed Net Zero future safer and more sustainable.

Contents

List of Figures

List of Tables

List of Abbreviations

BatchNorm	**Batch Norm**alisation
CSL	**C**ritical **S**tate **L**ine
CNN	**C**onvolutional **N**eural **N**etwork
DL	**D**eep **L**earning
EE-DL	**E**mbedded **E**ntities within **D**eep **L**earning
EPP	**E**lastic **P**erfectly **P**lastic
FE	**F**inite **E**lement
FRV	**F**orest **R**eef **Volcanics**
GPR	**G**aussian **P**rocess **R**egression
GAN	**G**enerative **A**dversarial **N**etworks
HH	**H**orizontal SAR signal polarisation for both transmitted and received
ID	**Id**entification
InSAR	**I**nterferometric **S**ynthetic **A**perture **R**adar
ISBAS	**I**ntermittent-**SBAS**
LOS	**L**ine-**O**f-**S**ight
MAXE	**Max**imum **E**rror
MCC	**M**odified **C**am **C**lay
MPM	**M**aterial **P**oint **M**ethod
N	**N**orth
PS	**P**ersistent **S**catterer
RBF	**R**adial **Basis Function**
ReLu	**Re**ctified **L**inear **U**nit
RF	**R**andom **F**orest
RMSE	**R**oot **M**ean **S**quared **E**rror
RS2	**R**adarsat-2
SAR	**S**ynthetic **A**perture **R**adar
SBAS	**S**hort-**BA**seline **S**ubsets
S1	**S**entinel-1
TSF	**T**ailings **S**torage **F**acility
N/STSF	**N**orth / **S**outh **T**ailings **S**torage **F**acility
TD	**T**ailings **D**am
VV	**V**ertical SAR signal polarisation for both transmitted and received
W	**W**est

List of Symbols

Δ	difference
π	pi, 3.14...
$\langle , \rangle$	dot product
$\lvert . \rvert$	magnitude or absolute value
α	angle of TSF section relative to satellite LOS
β	angle of TSF section relative to North
$\vec{b}$	vector of satellite baseline
$B \perp$	perpendicular baseline
c_v	Coefficient of consolidation
C_c	compression index
δ_T	horizontal motion in the transverse direction of TSF
δ_L	horizontal motion in the longitudinal direction of TSF
δx_{RS2}	horizontal motion of RS2-InSAR
δx_{FE}	horizontal motion of FE predictions
$\delta\theta$	difference in incidence angle
$\vec{D}$	vector of deformation
ϵ	embedding cardinality
γ_{InSAR}	InSAR coherence
γ_w	Unit weight of water
ϕ	radar phase
ϕ_{Atm}	phase component due to atmosphere
ϕ_{Displ}	phase component due to displacement
ϕ_{Noise}	phase component due to noise
ϕ_{Orbit}	phase component due to orbit
$\phi_{Scatter}$	phase component due to scattering properties
ϕ_{Topo}	phase component due to topography
h_{DEM}	height digital elevation model
h_{error}	height error
h_T	height of target
k_y	Vertical permeability
k_x	Horizontal permeability
k	swelling index
$\vec{l}_i$	vector between the satellite i to the ground
$\hat{l}_i$	unit vector between the satellite i to the ground
l_{Cadia}	distance from the centre of burst A to Cadia TSF
l_{burstA_burstB}	total distance between centres of burst A and B
$\tilde{M}$	Slope of critical state line
ρ_i	SAR signal range
R^2	coefficient of determination

σ	angle between satellite baseline and the horizontal
$\vec{T}$	vector of target
θ	incidence angle of satellite to the ground
θ	incidence angle of satellite to flat earth
θ_{burstA}	incidence angle for SAR signal burst A
θ_{burstB}	incidence angle for SAR signal burst B
$\theta_{heading\_N}$	satellite heading angle from the North
y_o	point on the Flat Earth surface
$Wrap\{.\}$	wrapping operator
x_lat	latitude
x_i	measured deformation for variable i
$\hat{x}_i$	predicted deformation for variable i
y_lon	longitude

Chapter 1

Introduction

To overcome the existential threats posed by climate change and limit global average temperatures to below 1.5°C, an estimated three billion tons of metals are required (Hund et al. (2020) and Rossi et al. (2022)). This crucial transition from fossil fuels to renewable energy technologies is driving the need for more minerals and metals worldwide. To put it in context of the challenge posed to the mining industry, this number is small compared to the amount of material that is actually taken out of the ground. For example, over 98% of the material in copper mining is waste, as illustrated in Figure 1.1 and 1.2. This is the forgotten consequence of our metal hungry future - the handling of the enormous amount of resulting mine waste.

Usually, mine waste is stored behind large 'earthen' dams (i.e. made out of earth, rather than concrete), known as 'Tailings Storage Facilities' (TSFs). Due to mining being one of the oldest industries, over 30,000 TSFs are estimated to exist worldwide, a quarter of which are abandoned and not monitored at all (WMTF (2020)). Even relatively well monitored TSFs can sometimes collapse, resulting in the release of toxic mine waste and socio-environmental tragedies, such as the Brumadinho failure of 2019, Brazil (Robertson et al. (2020)) and most recently, the Jagersfontein failure in 2022, South Africa (Torres-Cruz and O'Donovan (2023)). The cost of recent TSF failures in terms of their impact on stock price, social compensation and environmental remediation are in the range of USD 750M to USD 56B. These costs are significantly lower than the estimated costs of hypothetical, highest specification real-time monitoring technologies, which are estimated in the range of USD 400k to USD 500k (Clarkson

FIGURE 1.1: Visualisation of the volume of copper extracted from a typical open-pit mine. This example is the Palabora Mine in South Africa and the copper ball represents the 4.1 million tons of copper that was extracted. Modified from Marsh (2018).

FIGURE 1.2: Visualisation of the volume of metals extracted from Copperton mine, South Africa. The balls represent 462,500 tonnes of copper, 934,500 tonnes of zinc, and 1,000 tonnes of silver that was extracted. Modified from Marsh (2018).

et al. (2021)). Therefore, there is a critical need and a defend-able case for a global monitoring capability for TSFs to protect local communities, natural habitats and ecosystems.

Investors, governments and civil societies have been advocating for greater transparency on the global risks associated with TSFs (PRI (2020)). The largest TSF disclosure initiative was recently led by a group of ethical investors, yet accounted for only 30 % of global commodity production, with many companies seemingly reluctant to disclose their TSF risks (Franks et al. (2021)). Even those who were willing to disclose, many were unable to report complete engineering records, for 257 out of 1743 TSF facilities (15 %) surveyed in Franks et al. (2021). This is due to the complexities faced by mine operators, as TSFs are large, long term projects spanning decades, multiple mine ownership and political parties. The capability of remote sensing to 'go back in time', as illustrated in Figure 1.3, highlights the significant role Earth Observation (EO) technologies may play in bridging the gap in missing data and improving the understanding of historical operations. For instance, the first civilian EO satellite Landsat-1 was launched in 1972 (NASA (2024)). Even previously unavailable data from spy satellites going back to 1960 have recently been made publicly available (USGS (2022)).

The proposed research is based on real needs of the mining industry. The requirements of various stakeholders in the mining sector have been validated through interviews and workshops. These stakeholders include large mine operators, tailings engineers and Ministries of Mines and the Environment in countries such as Peru (e.g. Lumbroso et al. (2019, 2021) and UKSA (2018)), Chile (Bayaraa et al. (2018)), Brazil, Australia and Mongolia. These engagements have explored their monitoring needs within the context of the technology readiness level and suitability of different satellite technologies. The various requirements can be categorised based on the particular EO technology that can be used to tackle them. For instance, there is a need to determine whether tailings material is leaching into the surrounding environment, as illustrated in Figure 1.4, and to monitor the spatial extent of the decant pond and deposited tailings of TSFs. These needs are particularly suited to monitoring by optical multi-spectral EO technology (e.g. Navarro et al. (2019) and O'Donovan et al. (2022)). Another key requirement is monitoring the 'physical stability' of TSFs, which

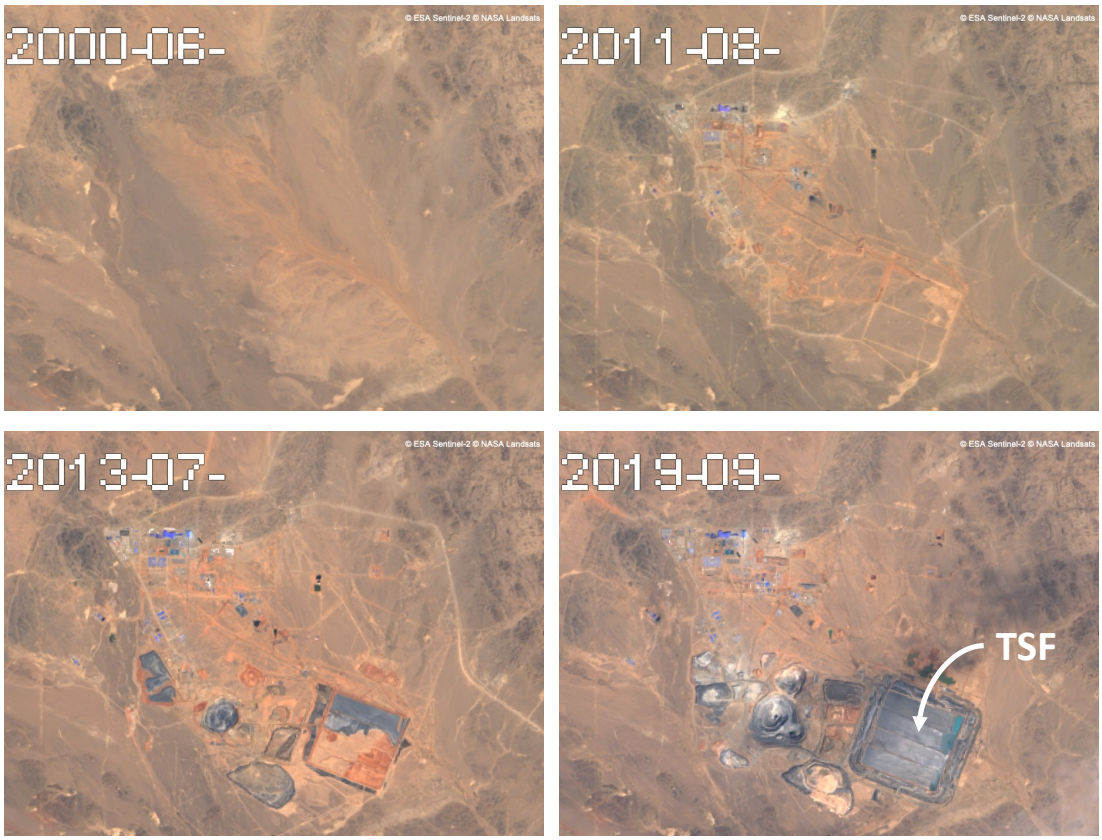

FIGURE 1.3: The power of satellites to 'go back in time'. The development of the Oyu Tolgoi Mine and TSF in the Mongolian Gobi desert can be seen from 2000 to 2019. In the year 2000, there is an empty desert followed by first signs of development in 2011. Then a rapid development can be seen, where most of the mine and the TSF is ready by 2013. The images are from a combination of © NASA Landsats and © ESA Sentinel-2.

may be possible through the monitoring of surface deformation of TSFs. The technology readiness level for applying optical multi-spectral satellite data to TSFs is deemed significantly higher than that for using radar satellites for the monitoring of surface deformation over TSFs. This is due to the large uncertainties regarding the extent to which satellite technologies can be trusted and how their measurements compare to current monitoring approaches. Consequently, this research focuses on parts of EO technology containing the greatest uncertainties, risks and the biggest gaps in research.

A technology offering much promise towards this ambition for global monitoring of the physical stability of TSFs is satellite Interferometric Synthetic-Aperture Radar (InSAR) (Bamler and Hartl (1998)). InSAR analysis enables the detection of millimetric-scale ground movements from satellite constellations hundreds of kilometres in space.

FIGURE 1.4: Tailings material leaching from a TSF in Chile. © DigitalGlobe © Satellite Applications Catapult

The prospect for global ground deformation monitoring with InSAR may be imminent, as exemplified by recent initiatives such as the European Ground Motion Service (Crosetto et al. (2020) and Siegmund et al. (2022)). The initiative aims to extend large scale InSAR monitoring capabilities to the continental scale. Realising the value of such initiatives hinges on the ability to demonstrate its reliability and benefits for specific applications, such as the monitoring of critical infrastructure. However, literature on detecting meaningful deformation behaviour over TSFs from InSAR is scarce. Therefore, there is a significant uncertainty surrounding the suitability of InSAR for the monitoring of TSFs.

While recent InSAR studies have hinted at the potential for detecting dangerous deformation signals before the failure of Brumadinho (e.g. Grebby et al. (2021)) and Cadia (e.g. Carlà et al. (2019)), these studies have taken a primarily ad-hoc InSAR approach. This is a common issue within the InSAR community, where the use of custom InSAR algorithms makes it challenging to reconcile differing interpretations.

For instance, some researchers report detecting precursory signals over an infrastructure, while others do not (further discussion in Section 2.1.4). Furthermore, there is no framework for defining what constitutes 'dangerous' deformation signals and how to effectively detect them. The complex spatial and temporal behaviour of InSAR measurements, combined with its large measurement distribution mean that data-driven approaches, such as deep learning (DL), hold much promise towards the task of early warning of failure (further discussion in Section 2.2). Finally, there is a lack of geotechnical context for interpreting the deformation signals and validating the reliability of InSAR measurements.

Current geotechnical approaches are typically based on visual inspections and ground based instrumentation, such as prisms for the monitoring of surface deformation. Relative to other critical infrastructure, TSFs are unusual in the sense that the construction and in-service phases run in parallel, with construction often occurring throughout the lifetime of the structure. This is particularly pertinent to TSFs, because ground based instrumentation have limitations on spatial coverage, are susceptible to damage, and occasionally need to be removed to facilitate construction activities. The removal of ground instrumentation can disrupt monitoring campaigns and limit the understanding of dam behavior during critical periods. For instance, at Cadia mine, the prisms in the failure area were dismantled to allow the construction of buttresses (Jefferies et al. (2019)). This meant that, post-failure processing of satellite- InSAR offered the only source of insight into the deformation behaviour immediately preceding the failure of the northern TSF (Thomas et al. (2019)). Addressing these challenges necessitates the bringing together of three previously siloed fields: satellite remote sensing, geotechnical engineering and DL.

Recognising the complexities related to availability, accessibility and capabilities of both geotechnical and satellite data, this research focuses on the importance of quantifying the value and benefit of having different tiers of data within an early warning system. On one end of the spectrum, government, community civil society, non-governmental-organisation, academic and investor stakeholders do not have access to geotechnical data over TSFs in the same way that TSF operators and mining companies do. However, the generation of a rigorous numerical model based on available ground-based geotechnical lab and monitoring data is resource intensive,

and contains uncertainties related to assumptions of the model parameters. Medium resolution SAR satellite data is available globally and open source from various space agencies. There are also commercial alternatives, which are often at higher spatial resolution but are not globally available and are expensive to access. The advantages and limitations of these monitoring and modelling technologies are like a puzzle that requires research on how to fit them together. This research seeks to push the limits of what is possible from global, open source satellite datasets whilst evaluating the value of investing in expensive data, both high resolution satellite data and resource intensive rigorous geotechnical modelling.

1.1 Research Questions and Objectives

The various research themes for the monitoring and early warning of TSF failure may be brought together within the umbrella concept of twin systems. Digital twin systems offer to overcome many of the inadequacies of current monitoring systems. For instance, simply prescribing the frequency of instrument measurements and thresholds, as outlined in currently rigid, prescriptive guidelines driven by regulation, is insufficient (Clarkson et al. (2021)).

Instead, TSF practitioners need a system that provide a deeper understanding of the response of each instrument and integration between them. Figure 1.5 illustrates the key differences between a true digital twin and any other digital model, which are in its ability to update itself automatically to the conditions of the physical twin, as the physical twin changes and vice versa (Sacks et al. (2020)). This research does not seek to develop a digital twin of TSFs, but recognises that the proposed research themes form some of the fundamental research components that are currently missing, before satellite-enabled digital twin systems may be achieved for the monitoring of TSFs.

To that end, monitoring data from InSAR and other sources are integrated together to generate the necessary insights for updating the state of the digital twin. The initial function of a digital twin system lies in data integration, which involves combining data from multiple sources and different formats. This encompasses **research question 1**: How effective is InSAR for TSF monitoring and can it serve as either complement to or replacement for current monitoring methods? The real value of digital

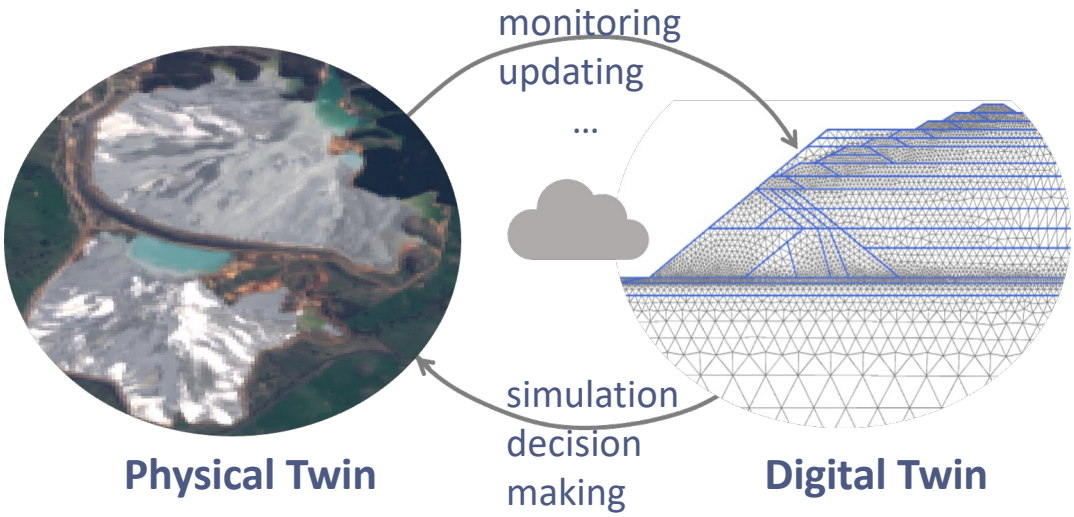

FIGURE 1.5: Digital and physical twins of TSFs.

twins is in its ability to forecast and simulate alternative future scenarios, so that the best actions are recommended for decision making. This is a significant task and may be feasible only with the promise of data-driven approaches, such as DL, at its core. It leads to **research question 2**: what is the feasibility of DL-based early warning? Can InSAR data within a DL system be used for an early warning of TSF failure? Ultimately, the real-world value of a monitoring system depends on the cost-benefit analysis of the different technological components. Therefore, **research question 3:** what are the minimum requirements of an early warning system? This involves establishing the minimum data requirements and anticipated levels of performance. The main objective of the research will be to investigate the value of investing in expensive commercial SAR data, resource intensive geotechnical modelling, and compute-intensive DL models for the monitoring of TSFs:

- Objective 1: assess the reliability of satellite InSAR for the monitoring of TSFs. This involves outlining the scenarios under which InSAR is most suitable for TSF monitoring and cases where it may not be. This objective includes comparing InSAR results against current monitoring technologies to quantify its performance.

- Objective 2: demonstrate the feasibility for a DL-based early warning system, by developing a framework for how to identify and detect dangerous deformation behaviour.

- Objective 3: to determine the minimum data requirements and performance levels for an effective early warning system for TSF failures. This involves analysing the trade-offs between using expensive commercial versus open source SAR data, and comparing the benefits of complex deep learning algorithms with more traditional shallow machine learning approaches.

The effectiveness of the early warning system is demonstrated through a detailed analysis of the Cadia TSF failure in Australia. A rigorous exploration of the proposed system's resilience and limitations on one case study was prioritised over conducting superficial evaluations of many examples of TSFs. For instance, if no anomalous behaviour is detected over a failed TSF, it is difficult to speculate as to the reasons without digging deeper. Although the Cadia TSF represents a specific case study, its failed sections represent the most risky of all construction methodologies - the upstream type (further discussion in Chapter 2). Upstream TSFs are twice that of downstream and six times more likely to report stability issues than de-watered 'dry-stack' facilities (Franks et al. (2021)). Although the construction of new upstream TSFs has now been banned in Chile and more recently in Brazil (BBC (2020)), this is not the case for many other countries, and many upstream TSFs are still in operation.

Finally, the intention of this research is not to villainise any one company or industry, but rather to use the failure case study as an opportunity to learn and gain a deeper understanding of the complexities involved in satellite-based management of TSFs. It aims to explore both the opportunities and limitations of the various technologies, contributing to the safe and sustainable mining practices that are desperately needed.

1.2 Thesis structure

An introduction to each of the technological streams and analogous studies is presented in the literature review in Chapter 2. It includes an in-depth exploration of the principles of SAR interferometry, InSAR-based ground deformation measurement and the application of InSAR to TSFs. Additionally, the engineering properties of tailings and the geotechnical modelling of TSFs are reviewed, forming the fundamental basis for interpreting the InSAR deformation signals.

Research directly combining InSAR, DL and geotechnical modelling technologies for TSFs does not yet exist. Therefore, a particular focus is directed towards previous studies that serve as analogues to the research aims. For instance, literature pertaining to other types of structure, such as hydro-dams and bridges have informed the developments in Chapter 3. In this chapter, a collapsed TSF case study is investigated from the perspectives of satellite InSAR-based ground deformation measurement, ground-based monitoring and geotechnical numerical modelling. Material from this chapter has previously been published in Géotechnique, in Bayaraa et al. (2024).

Despite the lack of studies applying ML based early warning to TSFs, there is a growing research interest combining InSAR and DL for e.g. volcanology. Additionally, the adoption of DL techniques in e.g. natural language processing with the aim of forecasting of taxi destinations, have served as a surprising and unexpected analogue for demonstrating the feasibility of early warning of TSF failure in Chapter 4. These results are published in Remote Sensing in Bayaraa et al. (2023).

The present research aims to leverage, as much as possible, globally available, open-source InSAR data. This ambition has driven the focus on InSAR measurements derived from the satellite Sentinel-1 (S1), as the main data source for Chapters 3 and 4. However, it is not possible to differentiate whether some of the limitations discussed in these chapters are inherent to InSAR, are perhaps due to the particular satellite characteristics or the particular InSAR processing methodology. Therefore, S1 is reprocessed using a different InSAR algorithm and compared to high resolution commercial Radarsat-2 (RS2) InSAR data in Chapter 5. By coincidence, the SAR data available over Cadia TSF during the critical timeframe leading up to the collapse were exclusively from C-band satellites, namely S1 and RS2. No X-band satellite data acquisition is available for the site within the required period. Finally, the improvement in the early warning capabilities from incorporating these additional InSAR datasets is explored in Chapter 6. It also demonstrates the flexibility of the algorithm, being able to integrate InSAR data of different types, both the line-of-sight and decomposed motions.

Finally, a summary of the thesis along with the multi-disciplinary software ecosystem employed in each chapter is presented in Figure 1.6. The primary programming

language used was Python, along with its associated libraries, complemented by specialist software required by each discipline (Anaconda, Inc. (2024) and Kluyver et al. (2016)). The PS-InSAR processing was conducted through the ENVI-SARscape remote sensing software (SARmap (2025)). The Sentinel-1 based ISBAS and commercial RS2-InSAR data were obtained from industry sources (European Space Agency (2024), MDA Space Missions (2024), and Sowter et al. (2013)). Finite element modelling was performed using Plaxis, a geotechnical numerical modelling software (Bentley Systems International Ltd (2019)). The early warning workflows were developed using various machine learning libraries in Python, with all computations executed in the cloud, leveraging GPUs on AWS and Google Cloud Platform (Amazon Web Services (2024) and Google Cloud (2024)). Additionally, the baseline Random Forest model was implemented in scikit-learn, Gaussian Process Regression in GPyTorch and deep learning workflows in PyTorch with the abstraction library FastAI (J. R. Gardner et al. (2018), Howard and Gugger (2020b), Paszke et al. (2019), and Pedregosa et al. (2011)). Data visualisation and management of both remote sensing and geotechnical data were handled through a combination of Python libraries and Geographic Information Systems (GIS) software (Esri (2024), Gillies and contributors to Rasterio (2024), Harris et al. (2020), Hunter (2007), Jordahl and contributors to GeoPandas (2024), McKinney (2010), QGIS Development Team (2024), and Virtanen et al. (2020)).

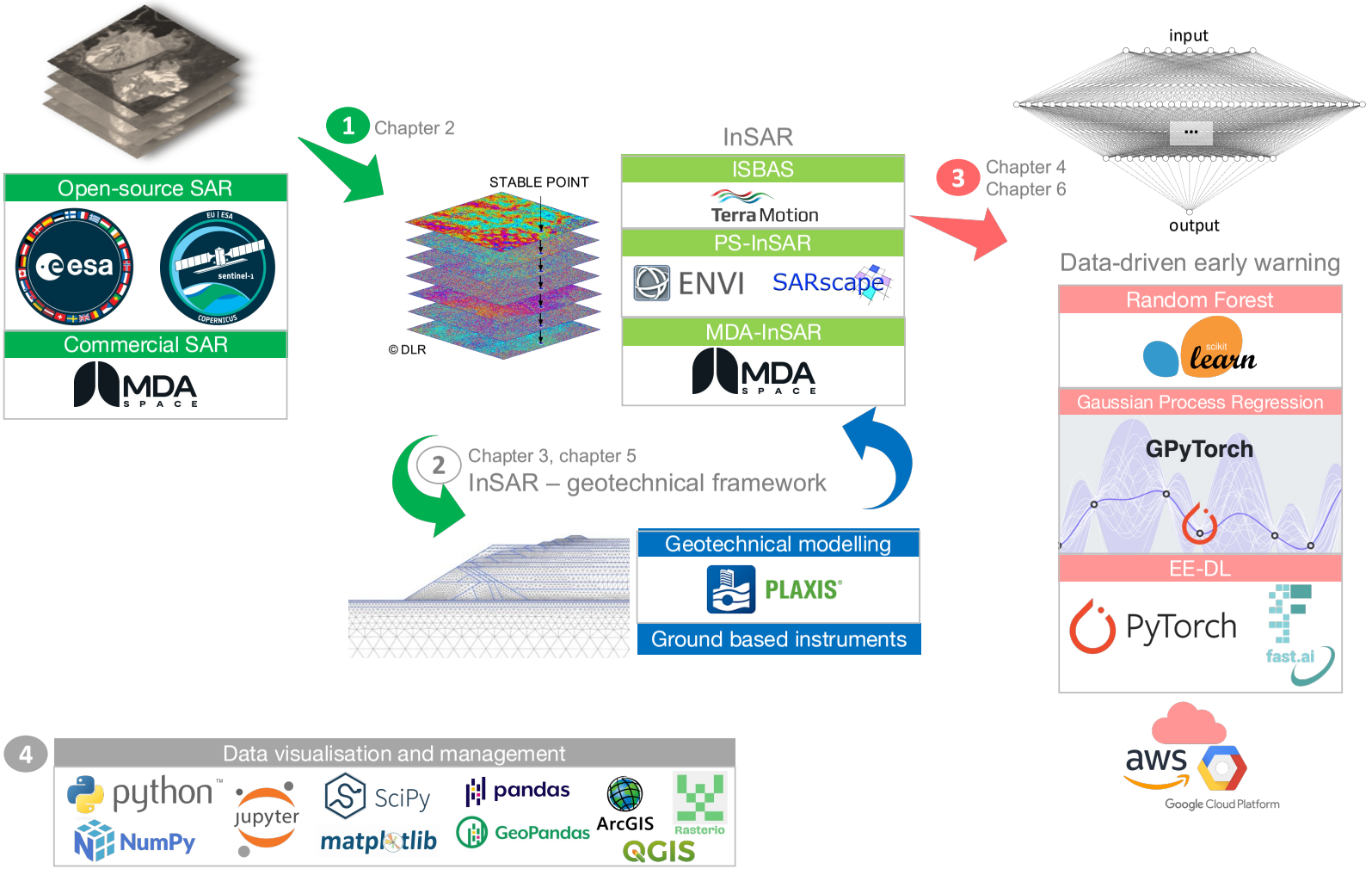

FIGURE 1.6: Thesis outline along with the multi-disciplinary software ecosystem that was required for each chapter.

Chapter 2

Literature Review

The research necessarily brings together several distinct disciplines, namely InSAR, deep learning and geotechnical numerical modelling. Together, these disciplines present an inspiring web of ideas and possibilities which inform the paths pursued in the technical chapters. A landscape of the core principles behind each technology and its application to TSFs are introduced in this chapter.

2.1 Satellite based InSAR

Whilst Synthetic Aperture Radar (SAR) data refers to the raw satellite data, InSAR refers to the processing chains of techniques used to estimate ground movement from different SAR acquisitions. Successive SAR data acquisitions in time are obtained by the same satellite or a constellation of satellites with similar instrumental and orbital characteristics scanning the area of interest. Thus, the frequency of measurements depends on the revisit frequency of the satellite.

A key characteristic of SAR is that it is an active sensor, where the signal is both emitted and then detected by the same satellite. SAR satellites operate at wavelengths within the microwave part of the electromagnetic spectrum. The data are complex, i.e. composed of measurements of both the amplitude and phase of the signal. Figure 2.1 plots two different reflected SAR signals (in time). When the reflector (i.e. the ground surface) moves, the distance between the satellite and the Earth's surface changes, resulting in a change in measurement before and after the movement. This difference in the phase ($\Delta\phi$) between satellite acquisitions is used to estimate ground surface movements in SAR interferometry (Bamler and Hartl (1998)). Because the difference

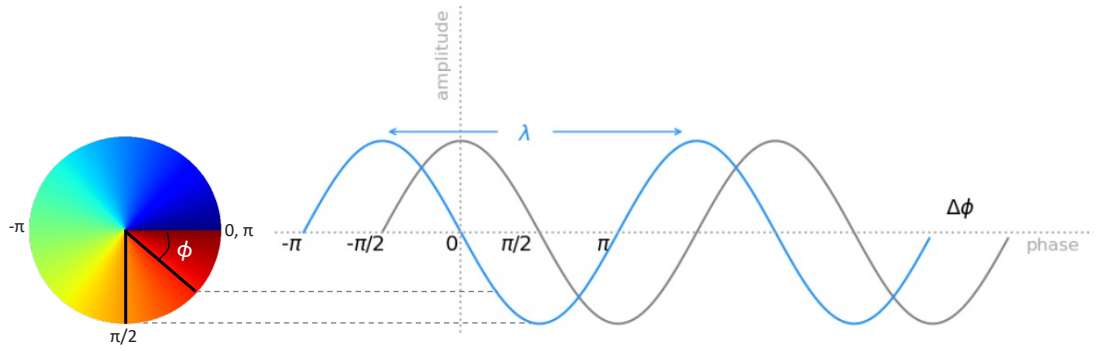

FIGURE 2.1: SAR signal characteristics. Two SAR waves with a phase difference of $\Delta\phi$, detected over the same location at different times. Due to the cyclic nature of waves, a change in cycles of 2 λ will result in the same wave.

in phase is used, the movement can be detected at high precision as a fraction of the wavelength of the signal.

Moreover, Figure 2.1 shows that the phase can be defined by $\frac{2\pi}{\lambda}$, where λ is the wavelength of the signal. In the case of SAR, the signal travels from the satellite to the ground and back to the satellite, travelling double the distance. Therefore, the phase of a SAR wave, ϕ, can be expressed as equation 2.1:

$$\phi = 2 * \frac{2\pi}{\lambda} = \frac{4\pi}{\lambda} \tag{2.1}$$

The phase of the blue wave in Figure 2.1 is measured in the interval of -π to π and the waves repeat in cycles of 2π. Due to the cyclical nature of waves, a change in cycles of 2π will give the same wave. Therefore, SAR interferometry can only measure the relative difference in the phase of the detected signals, without determining the exact number of complete cycles of 2π that passed. This phenomenon, known as phase ambiguity, is a fundamental aspect of InSAR and has several implications for TSF monitoring. For example, the measured deformation is not absolute, but is relative to the first SAR acquisition. Additionally, the specific methodology used to estimate the number of complete 2π cycles between acquisitions significantly affects the resulting deformation measurement, with deformation being either under or over estimated by integer(s) cycles of 2π. The impacts of phase ambiguity on TSFs are explored further in Chapter 5.

The measured phase differences may be due to a variety of changes on the Earth's

surface, including surface displacement and topographical differences. The main factors that contribute to the phase differences are described by equation 2.2 (Bamler (2000)). The aim of InSAR processing in this study is to extract the phase difference due to displacement of the target, ϕ_{Displ}, by separating it from the other contributions to the signal.

$$\Delta\phi = Wrap\{\phi_{Topo} + \phi_{Displ} + \phi_{Atm} + \phi_{Orb} + \phi_{Scatt} + \phi_{Noise}\} \tag{2.2}$$

where the measured phase difference, $\Delta\phi$, equals the 'wrapped' interferogram between two acquisition data-sets, where $Wrap\{.\}$ is the wrapping operator and refers to the fact that the phase is measured in cycles of 2π. The phase components due to atmospheric delay is ϕ_{Atm} in each data, the orbital error component is ϕ_{Orb} and the phase noise is ϕ_{Noise}. The phase related to variations in the scattering mechanisms ϕ_{Scatt} in a pixel and its effects can be separated into geometrical and temporal decorrelation. The topography-induced phase components are removed using open source digital elevation models. A digital elevation model at 20 m resolution is considered sufficient (Ferretti et al. (2001)) and even a horizontal plane can be used (Colestani et al 2003). The phase component ϕ_{Topo} is related to the difference between the elevation of the target with respect to a digital elevation model height. The displacement and topography terms can be modelled and their equations are derived in Sections 2.1.1 and 2.1.2, respectively. The other terms cannot be modelled, but are treated statistically and are discussed in Section 2.1.3.

2.1.1 Derivation of the Displacement Term From Phase Difference

Derivation of the displacement term, ϕ_{Displ}, from the measured phase difference can be obtained using either geometrical or statistical approaches, as proposed by Rosen et al. (2000) and Bamler and Hartl (1998), respectively. Figure 2.2 defines the SAR line-of-sight (LOS) geometry relative to the deformation vector $\vec{D}$ and the target $\vec{T}$; $\vec{b}$ is the vector between two satellite positions at $\vec{P}_1$ and $\vec{P}_2$, $\vec{l}_i$ describes the vector between the satellite i to the ground and ρ_i is the range. The basic vector relations can be described as:

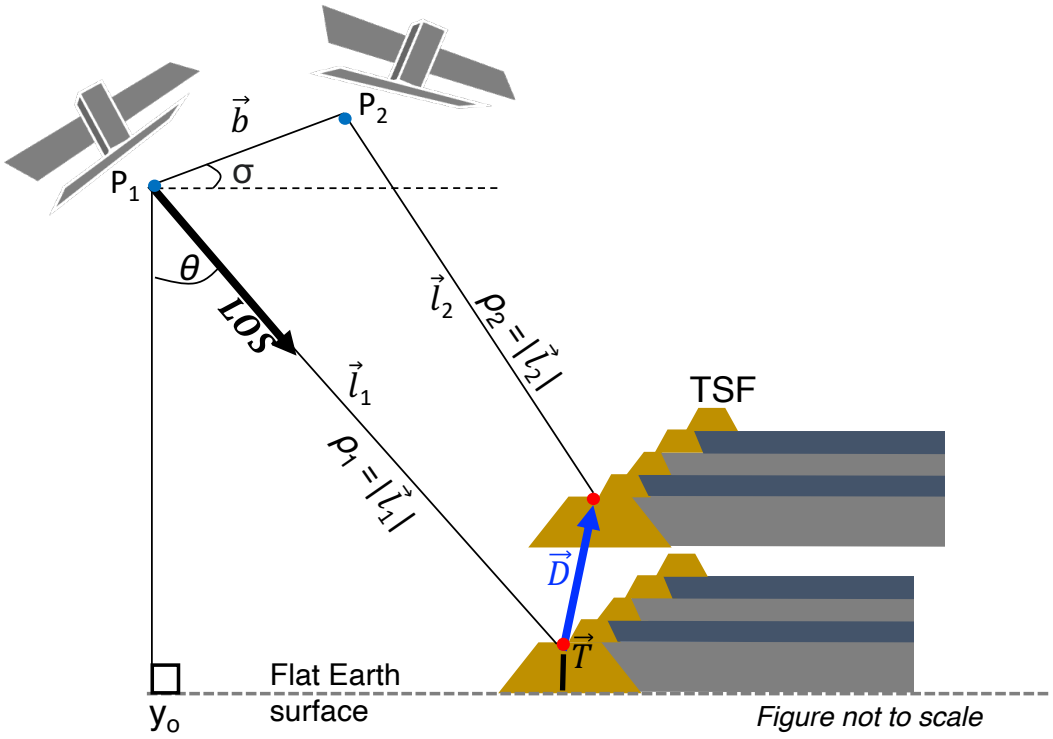

FIGURE 2.2: SAR geometry containing both deformation $\vec{D}$ and topographical $\vec{T}$ components.

$$\begin{aligned} \vec{b} &= \vec{P}_1 - \vec{P}_2 \quad = \vec{l}_1 - \vec{l}_2, \\ \vec{l}_2 &= \vec{D} + \vec{l}_1 - \vec{b} \end{aligned} \tag{2.3}$$

An interferogram can be formed by subtracting one SAR acquisition from another. The resulting phase difference between the two acquisitions, $\Delta\phi$ can be expressed in terms of vectors $\vec{D}$,$\vec{b}$, $\vec{l}_1$ and the dot product denoted by $\langle , \rangle$.

$$\begin{aligned} \Delta\phi &= \frac{4\pi}{\lambda}(\rho_2 - \rho_1) = \frac{4\pi}{\lambda}(|\vec{l}_2| - \rho_1) \quad \text{by } (|\vec{l}_2| = \langle \vec{l}_2, \vec{l}_2 \rangle^{\frac{1}{2}}) \\ &= \frac{4\pi}{\lambda}(\langle \vec{l}_2, \vec{l}_2 \rangle^{\frac{1}{2}} - \rho_1) \quad \text{by (2.3)}, \\ &= \frac{4\pi}{\lambda}[\langle \vec{D} + \vec{l}_1 - \vec{b}, \vec{D} + \vec{l}_1 - \vec{b} \rangle^{\frac{1}{2}} - \rho_1] \\ &= \frac{4\pi}{\lambda}[\langle \vec{D}^2 + 2\vec{D}\vec{l}_1 - 2\vec{D}\vec{b} - 2\vec{b}\vec{l}_1 + \vec{l}_1^{\,2} + \vec{b}^2 \rangle^{\frac{1}{2}} - \rho_1] \end{aligned} \tag{2.4}$$

The baseline $|\vec{b}|$ is the distance between the satellites and is on the order of 100 meters, whereas the ground movement $|\vec{D}|$ is on the order of 10s of millimeters. Thus, the range distance of the satellite from the ground ρ_1 is much larger, on the order of 10^5

meters in equation 2.4. Therefore $|\vec{D}|, |\vec{b}|$ and $|\vec{D}\vec{b}|$ are negligibly small compared to ρ_1, such that equation 2.4 becomes:

$$\Delta\phi = \frac{4\pi}{\lambda}[\langle 2\vec{D}\vec{l_1} - 2\vec{b}\vec{l_1} + \vec{l_1}^2\rangle^{\frac{1}{2}} - \rho_1] \tag{2.5}$$

Given $\rho_1 = |\vec{l_1}| = \langle \vec{l_1}^2 \rangle^{\frac{1}{2}}$, then $\vec{l_1}^2 = \rho_1^2$. Substituting $\vec{l_1}^2$ into equation 2.5 gives equation 2.6 and enables its simplification.

$$\begin{aligned} &= \frac{4\pi}{\lambda}\rho_1[\frac{\langle 2\vec{D}\vec{l_1} - 2\vec{b}\vec{l_1} + \rho_1^2\rangle^{\frac{1}{2}}}{\rho_1} - \frac{\rho_1}{\rho_1}] = \frac{4\pi}{\lambda}\rho_1[\langle \frac{2\vec{D}\vec{l_1} - 2\vec{b}\vec{l_1} + \rho_1^2}{\rho_1^2}\rangle^{\frac{1}{2}} - 1] \\ &= \frac{4\pi}{\lambda}\rho_1[\langle \frac{2\vec{D}\vec{l_1} - 2\vec{b}\vec{l_1}}{\rho_1^2} + 1\rangle^{\frac{1}{2}} - 1] \end{aligned} \tag{2.6}$$

Moreover, Equation 2.6 can be expanded through the first order Taylor series approximation, defined as: $(1+x)^n = 1 + nx + ...$, which corresponds to : $1 + \frac{1}{2}(\frac{2\vec{D}\vec{l_1} - 2\vec{b}\vec{l_1}}{\rho_1^2})$. Substituting the Taylor series expansion into Equation 2.6 simplifies to:

$$\begin{aligned} \Delta\phi &= \frac{4\pi}{\lambda}\rho_1[1 + \frac{1}{2}(\frac{2\vec{D}\vec{l_1} - 2\vec{b}\vec{l_1}}{\rho_1^2}) - 1] = \frac{4\pi}{\lambda}[\frac{\vec{D}\vec{l_1} - \vec{b}\vec{l_1}}{\rho_1}] = \frac{4\pi}{\lambda}[\frac{\vec{D}\vec{l_1}}{\rho_1} - \frac{\vec{b}\vec{l_1}}{\rho_1}] \\ &\quad \text{substitute by unit vector } \hat{l_1} = \frac{\vec{l_1}}{|\vec{l_1}|} = \frac{\vec{l_1}}{\rho_1} \\ &= \frac{4\pi}{\lambda}[\langle \vec{D}, \hat{l_1}\rangle - \langle \vec{b}, \hat{l_1}\rangle] \end{aligned} \tag{2.7}$$

Importantly, the fact that the measured deformation is a projection of the displacement vector $\vec{D}$ onto the satellite signal path $\hat{l_1}$ in equation 2.7, highlights the fact that InSAR does not measure 'true' deformation, but measures deformation in the line-of-sight of the satellite. Section 2.1.2 demonstrates that $\langle \vec{b}, \hat{l_1}\rangle$ corresponds to the topographical component ϕ_{Topo}, which means, it can be easily estimated and removed using external data such as digital elevation models, which are available globally. Finally, the deformation $\langle \vec{D}, \hat{l_1}\rangle$ (i.e. ϕ_{Displ} in equation 2.2) can be estimated from the phase difference $\Delta\phi$ by separating it from the topographical component.

2.1.2 Derivation of the Topographical Term From Phase Difference

To further isolate the deformation component from the phase difference, the topographical component must be estimated. This is achieved by considering a scenario where no deformation is present, which simplifies the SAR geometry to Figure 2.3. This figure shows the geometry used for calculating only the topographical term. Instead of equation 2.3, $\vec{l_2}$ can be defined with equation 2.8.

$$\vec{l_2} = \vec{l_1} - \vec{b} \tag{2.8}$$

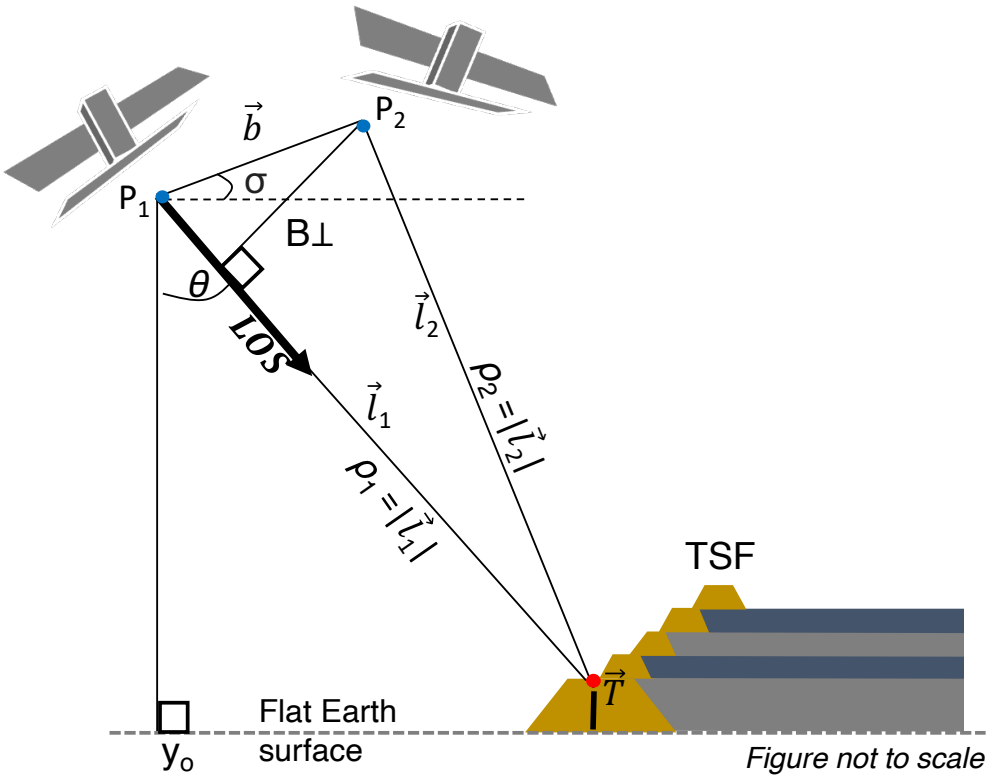

FIGURE 2.3: SAR geometry illustrating a scenario where there is no deformation, but a topographical component $\vec{T}$ only.

The phase difference, $\Delta\phi$, can be expressed in terms of $\vec{b}$ and $\vec{l}_1$ in equation 2.9.

$$\begin{aligned}
\Delta\phi &= \frac{4\pi}{\lambda}(\rho_2 - \rho_1) && = \frac{4\pi}{\lambda}(|\vec{l}_2| - \rho_1) = \frac{4\pi}{\lambda}(\langle\vec{l}_2, \vec{l}_2\rangle^{\frac{1}{2}} - \rho_1) \\
&= \frac{4\pi}{\lambda}(\langle\vec{l}_1 - \vec{b}, \vec{l}_1 - \vec{b}\rangle^{\frac{1}{2}} - \rho_1) && \text{by (2.8)} \\
&= \frac{4\pi}{\lambda}(\langle\vec{l}_1{}^2 - 2\vec{l}_1\vec{b} + \vec{b}^2\rangle^{\frac{1}{2}} - \rho_1) && \text{by } \rho_1 = |\vec{l}_1| = \langle\vec{l}_1{}^2\rangle^{\frac{1}{2}} \\
&= \frac{4\pi}{\lambda}[(\rho_1^2 - \langle 2\vec{l}_1\vec{b}\rangle + \vec{b}^2)^{\frac{1}{2}} - \rho_1] && = \frac{4\pi}{\lambda}\rho_1[\frac{(\rho_1^2 - \langle 2\vec{l}_1\vec{b}\rangle + \vec{b}^2)^{\frac{1}{2}}}{\rho_1} - \frac{\rho_1}{\rho_1}] \\
&= \frac{4\pi}{\lambda}\rho_1[\frac{(\rho_1^2 - \langle 2\vec{l}_1\vec{b}\rangle + \vec{b}^2)^{\frac{1}{2}}}{(\rho_1^2)^{\frac{1}{2}}} - 1] && = \frac{4\pi}{\lambda}\rho_1[(\frac{\rho_1^2}{\rho_1^2} - \frac{2\langle\vec{l}_1\vec{b}\rangle}{\rho_1^2} + \frac{\vec{b}^2}{\rho_1^2})^{\frac{1}{2}} - 1] \\
&= \frac{4\pi}{\lambda}\rho_1[(1 - \frac{2\langle\vec{l}_1\vec{b}\rangle}{\rho_1^2} + (\frac{\vec{b}}{\rho_1})^2)^{\frac{1}{2}} - 1] && && (2.9)
\end{aligned}$$

The component $(\frac{\vec{b}}{\rho_1})^2$ is negligibly small compared to ρ_1. Equation 2.9 then simplifies to equation 2.10.

$$\begin{aligned}
\Delta\phi &= \frac{4\pi}{\lambda}\rho_1[(1 - \frac{2\langle\vec{l}_1\vec{b}\rangle}{\rho_1^2})^{\frac{1}{2}} - 1] = \frac{4\pi}{\lambda}\rho_1[(1 - \frac{2\langle\vec{l}_1\rangle}{\rho_1}\frac{\langle\vec{b}\rangle}{\rho_1})^{\frac{1}{2}} - 1] \quad \text{by unit vector } \hat{l}_1 = \frac{\vec{l}_1}{|l_1|} = \frac{\vec{l}_1}{\rho_1} \\
&= \frac{4\pi}{\lambda}\rho_1[(1 - \frac{2\langle\hat{l}_1\vec{b}\rangle}{\rho_1})^{\frac{1}{2}} - 1] \qquad (2.10)
\end{aligned}$$

Equation 2.10 can be expanded through the first order Taylor series approximation as defined for $f(x) = (1-x)^{\frac{1}{2}} = 1 + \frac{1}{2}(1-x) + \frac{\frac{1}{2}(\frac{1}{2}-1)}{2!}(1-x^2) + ... = 1 - \frac{1}{2}x - \frac{1}{8}x^2 + ...$ and simplifies to equation 2.11.

$$\Delta\phi = \frac{4\pi}{\lambda}\rho_1[1 - \frac{1}{2}(\frac{2\langle\hat{l}_1\vec{b}\rangle}{\rho_1}) - 1] = -\frac{4\pi}{\lambda}\langle\hat{l}_1, \vec{b}\rangle \qquad (2.11)$$

Equation 2.11 demonstrates that it represents the topographical term in equation 2.7. Moreover, the topographical term can be further expressed in terms of the baseline between the satellite positions and the incidence angle by considering the following geometry:

Figure 2.4 illustrates the 'parallel ray approximation' theory, which is based on the fact that the distance between the two satellite positions is small compared to the distance to the ground, on the order of hundreds of meters compared to thousands, respectively. This justifies estimation through the projection of vector $\vec{b}$ onto the unit vector $\hat{l}_1$, which results in the dot product $\langle\hat{l}_1, \vec{b}\rangle$. Using this geometry, $\langle\hat{l}_1, \vec{b}\rangle$ can be

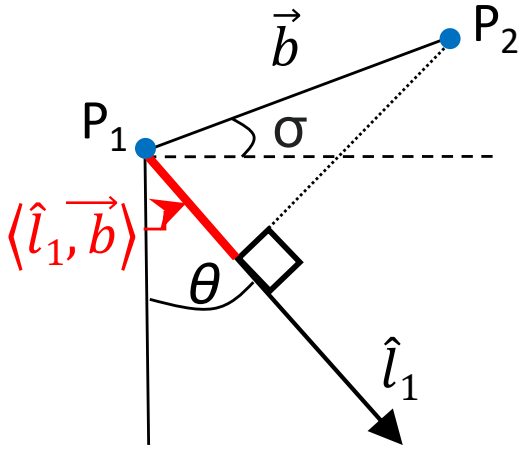

FIGURE 2.4: SAR geometry. Representation of the baseline vector $\vec{b}$ as a projection onto the unit vector.

related to the incidence angle of the satellite through trigonometry in equation 2.12.

$$\cos(\sigma + 90^\circ - \theta) = \frac{\langle \hat{l}_1, \vec{b} \rangle}{|\vec{b}|} \tag{2.12}$$

Equation 2.12 can be simplified and rearranged[1] to equation 2.13.

$$\langle \hat{l}_1, \vec{b} \rangle = b \sin(\theta - \sigma) \tag{2.13}$$

Substituting equation 2.13 into equation 2.11 relates the phase change due to topography as a function of physical constants, the distance between the satellites (i.e. the baseline, b) and the angles between them as defined in Figure 2.4:

$$\Delta\phi = -\frac{4\pi}{\lambda} \langle \hat{l}_1, \vec{b} \rangle = -\frac{4\pi}{\lambda} b \sin(\theta - \sigma) \tag{2.14}$$

Flattened Phase

Finally, phase changes are observed even when there is no topography nor deformation. This is called the phase contribution from the flat earth and needs to be removed, as illustrated in Figure 2.5. In this figure, $\hat{l}_1$ is a vector pointing from the sensor to a location on the ground and $\hat{l}_0$ is the corresponding vector to the reference flat Earth

[1] Equation 2.12 can be simplified using the trigonometrical identities $\cos(\tau_1 + \tau_2) = \cos(\tau_1)\cos(\tau_2) - \sin(\tau_1)\sin(\tau_2)$, where τ_1 and τ_2 are hypothetical angles, to simplify to $\cos\sigma\cos(90 - \theta) - \sin\sigma\sin(90 - \theta) = \cos\sigma\sin\theta - \sin\sigma\cos\theta$. Finally, given the identity $\sin(\tau_1 - \tau_2) = \sin(\tau_1)\cos(\tau_2) - \cos(\tau_1)\sin(\tau_2)$, equation 2.12 simplifies to equation 2.13.

surface at the same signal range. Moreover, θ is divided into θ_o which is the angle to the flat earth surface and $\delta\theta$ which is the difference between θ and θ_o. The resulting phase is called the 'flattened' phase and can be described with equation 2.15.

$$\Delta\phi_{flat} = -\frac{4\pi}{\lambda}(\langle\hat{l}_1, \vec{b}\rangle - \langle\hat{l}_0, \vec{b}\rangle) \tag{2.15}$$

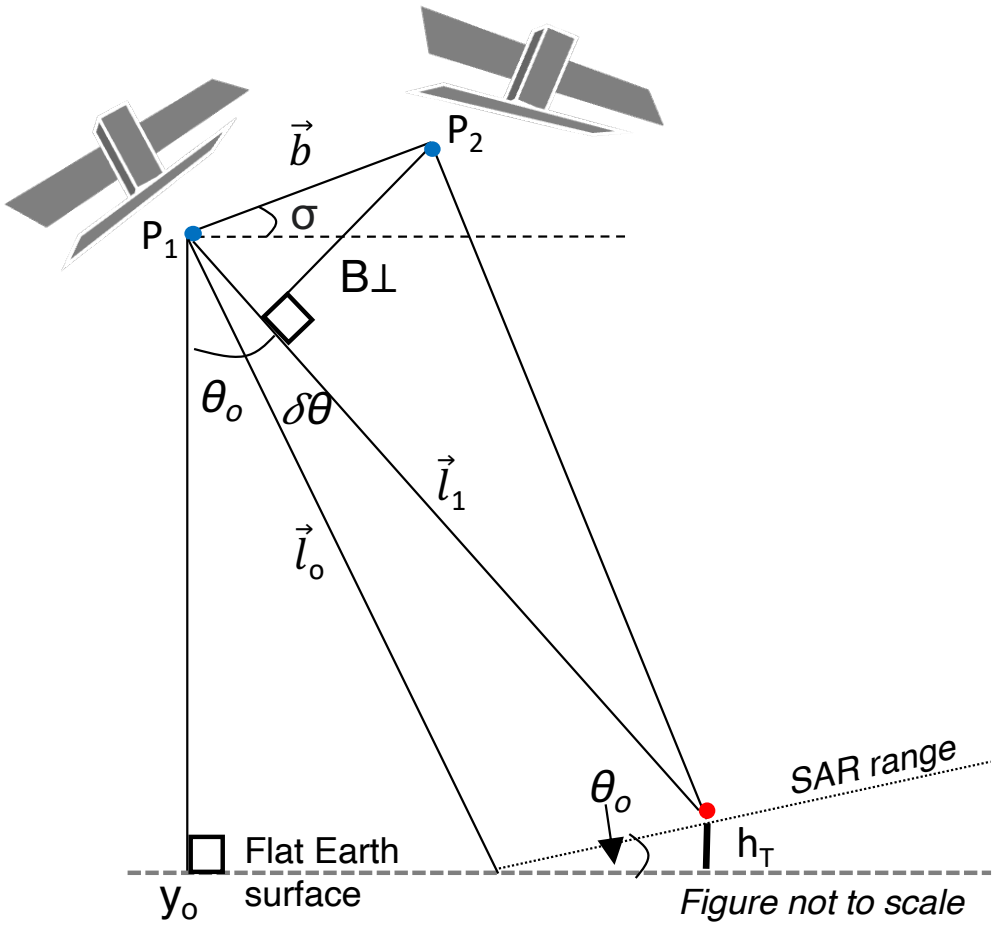

FIGURE 2.5: SAR geometry. Phase contribution from flat Earth.

Substituting equation 2.14 into equation 2.15:

$$\begin{aligned}\Delta\phi_{flat} &= \frac{4\pi}{\lambda}b(\sin(\theta-\sigma) - \sin(\theta_o-\sigma)) \\ &\approx \frac{4\pi}{\lambda}b\cos(\theta-\sigma)\delta\theta\end{aligned} \tag{2.16}$$

Moreover, several equations can be derived from Figure 2.5. The perpendicular baseline, $b_\perp$, can be defined as $b_\perp = cos(\theta - \sigma)$. Also the difference in the angle, $\delta\theta$,

can be expressed as $\delta\theta = \frac{h_T}{\rho sin(\theta_o)}$. And substituting both $b_\perp$ and $\delta\theta$ into equation 2.16 gives the topographic portion as a function of the length of the perpendicular baseline and distance to the target (ρ):

$$\begin{aligned}\Delta\phi_{flat} &= \frac{4\pi}{\lambda} b_\perp \delta\theta \\ &= \frac{4\pi}{\lambda} b_\perp \frac{h_T}{\rho \sin(\theta_o)}\end{aligned} \tag{2.17}$$

2.1.3 Multi-Temporal InSAR

The availability of more SAR constellations with greater temporal and spatial resolution has prompted an InSAR renaissance. A large SAR data archive presents opportunities for significantly improved estimation of the deformation component of the signal from phase difference. A host of multi-temporal InSAR techniques have been proposed, which differ in their assumptions and methods for estimating the various components of the phase difference (equation 2.2). These can be broadly categorized as follows: (a) Persistent Scatterer Interferometry (PS-InSAR), as originally developed by Ferretti et al. (2001), (b) Short-BAseline Subsets (SBAS) and its variants, initially proposed by Berardino et al. (2002), and (c) hybrid approaches combining both PS and SBAS elements, such as StaMPS (Hooper (2008)) and SqueeSAR (Ferretti et al. (2011)). A sample of the main multi-temporal techniques are summarised in Table 2.1, with their key differences highlighted. More detailed reviews of the various techniques are available in e.g. Crosetto et al. (2016), Lanari et al. (2007).

TABLE 2.1: Characteristics of the main multi-temporal InSAR approaches. Modified from Crosetto et al. (2016).

Reference	**Baseline**	**Pixel selection**	**Deformation estimation**
Ferretti et al. (2001)	Single master	Amplitude dispersion	Linear deformation in time
Berardino et al. (2002)	Small baselines	Coherence	Spatial smoothness
Hooper et al. (2004)	Single master	Amplitude and phase criterion	Spatial smoothness
Kampes (2006)	Single master	Amplitude dispersion; Signal to clutter ratio	Different types of deformation models
Ferretti et al. (2011)	Single master after triangulation	Statistical homogeneity test	Deformation model in time
Devanthéry et al. (2014)	Small baselines	Amplitude dispersion; Cousin PS	Spatial smoothness

The fundamental differences between the two main approaches, PS-InSAR and SBAS are summarised in Figure 2.6. A key difference between them is the type of signal (i.e. scattering mechanism) they aim to detect. PS-InSAR processing aims to detect strong, stable signals, typical of man-made, sharp objects and buildings which act as dominant reflectors of the radar signal. In contrast, SBAS detects the cumulative contribution from smaller, distributed scatterers of the radar signal typically present in non-urban areas. For instance, agricultural fields and mixed land covers may behave as distributed scatterers. The reference image chosen by each approach for interferogram formation is different depending on the category of the algorithm. In PS-InSAR, all the interferograms are calculated relative to one reference image known as the 'master' (single master). Typically an acquisition towards the middle of the temporal stack is chosen. In contrast, SBAS-type techniques use multiple 'master' interferograms which are paired with a 'replica', (also known in the literature by the controversial term, 'slave'). Master-replica pairs of interferograms within a user defined temporal and spatial baselines are generated. The PS-InSAR algorithm will be discussed in greater detail, as the underlying assumptions in its processing will be explored to further investigate the suitability of InSAR for TSFs in Chapter 5.

In the original multi-temporal approach, persistent scatterers are a subset of pixels that exhibit a stable phase behaviour. Although determining phase stability of a pixel is complex, measuring its amplitude through time is straightforward. Importantly, Ferretti et al. (2001) have shown that phase stability can be estimated with a simple ratio of the temporal standard deviation of the amplitude and the average temporal amplitude of a given pixel. Both experimental and simulation results have demonstrated that small values of this ratio, also called the amplitude dispersion index, estimate pixels with phase stability sufficiently accurately (Kampes (2006)). Other methods for finding persistent scatterers have been proposed, such as ones based on the signal to noise ratio and have shown to improve the reliability of finding pixels with stable phases (Gernhardt et al. (2010)).

The phase difference of a differential interferogram can be expanded with the displacement and topographical phases derived in equations 2.14 and 2.17:

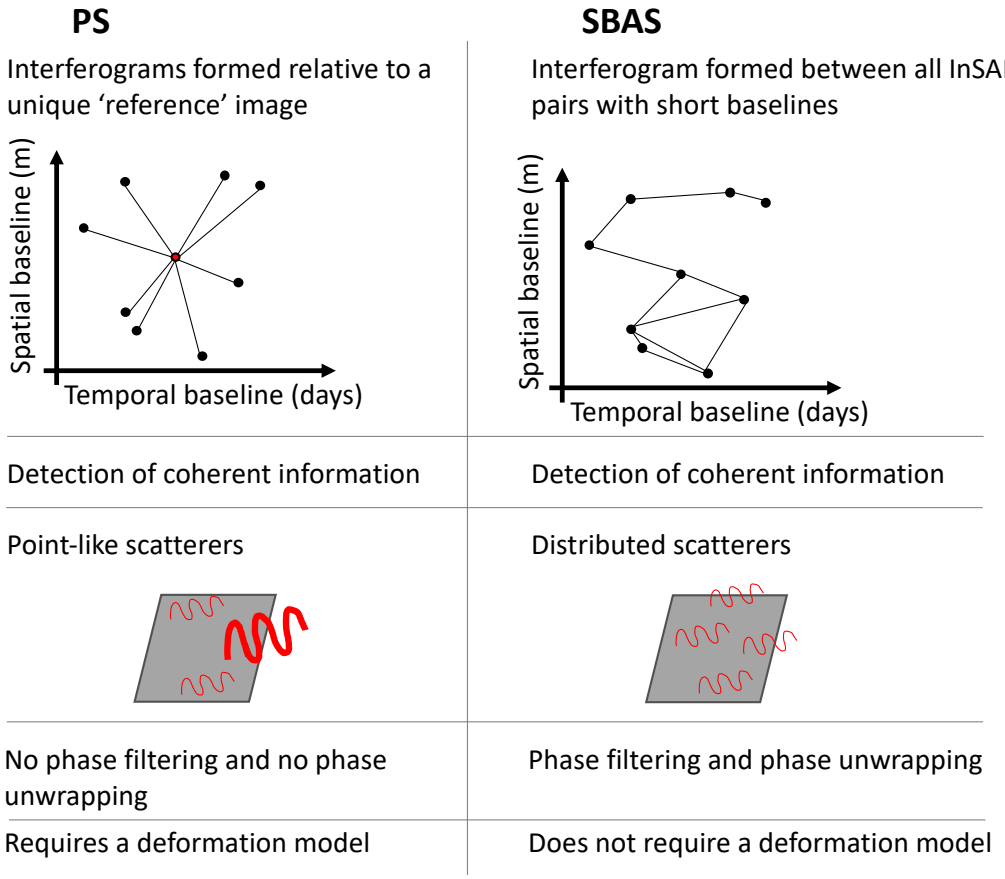

FIGURE 2.6: Comparison of the key differences between the main InSAR approaches: PS-InSAR and SBAS. Adapted from Meyer (2023).

$$\begin{aligned}\Delta\phi &= Wrap\{\phi_{Topo} + \phi_{Displ} + \phi_{Atm} + \phi_{Orb} + \phi_{Scatt} + \phi_{Noise}\} \\ &= Wrap\{\frac{4\pi}{\lambda}\frac{b_{\perp}}{\rho\sin(\theta_o)}h_{error} + \frac{4\pi}{\lambda}v\cdot\Delta t + \phi_{Atm} + \phi_{Orb} + \phi_{Scatt} + \phi_{Noise}\}\end{aligned} \tag{2.18}$$

where $h_{error} = h_{true} - h_{DEM}$, as it is assuming that the topographical phase is compensated by a digital elevation model. Therefore, the difference between the true height of a pixel and a digital elevation model is kept track of in h_{error}. Once the deformation components for SAR acquisitions are estimated, a deformation model is introduced to establish the relationship between these deformations. Typically, a linear model is assumed, where v is velocity and Δt is the time between acquisitions, but other non-linear models can also be used as shown in Table 2.1.

Atmospheric states are smooth in space but change rapidly on the scale of seconds, making the atmospheric phase delay not correlated between SAR acquisitions (i.e.

random in time). Therefore, the mean of the atmospheric contribution for a large SAR data stack is zero. It has been shown for PS-InSAR, at least 25 data stack are required, along with persistent scatterer measurement density of 5 - 10 PS/km^2 for a proper estimation of the atmospheric component (Colesanti et al. (2003)). The atmospheric contribution of every single data-set can be calculated by a simple subtraction of the master contribution from the estimated phase of each interferogram (Kampes (2006)). It is calculated for all acquisitions relative to the master on the sparse pixels exhibiting persistent scattererers. Then the estimations are interpolated for the whole area and represent the phase contribution from the atmosphere, ϕ_{Atm}. In comparison, the phase component due to noise (ϕ_{Noise}) are random in both time and space. The orbital error component (ϕ_{Orb}), can be removed almost completely using precise orbit information. Moreover, the quality of the interferogram between the two data-sets y_1 and y_2 can be estimated through calculating the complex correlation, known as the 'coherence' (γ_{InSAR}):

$$\gamma_{InSAR} = \frac{\sum_W y_1[m,n] * y_2[m,n]}{\sqrt{\sum_W |y_1[m,n]|^2 \sum_W |y_2[m,n]|^2}} \tag{2.19}$$

within a kernel window W of m rows and n columns in the interferogram. Coherence is measured in the range of 0 to 1, with 1 denoting best phase correlation between acquisitions. Low coherence is usually interpreted as the phase values being unstable and not containing valuable information. The topographical error and the velocity can be estimated through the ensemble phase coherence of the whole data stack in equation 2.19. Originally, the periodogram is used as a technique to maximise the ensemble phase coherence for the interferogram stack. Finally, the observed phase needs to be 'unwrapped', because the measured phase is in cycles of 2π. Whether a deformation model or the phase is unwrapped through other methods, the complexity of this process acts as a major source of uncertainty in the resulting deformation measurements (Rosen et al. (2000)). The impact of phase ambiguities in PS-InSAR within the context of TSFs will be further explored in Chapter 5.

Finally, the end-to-end PS-InSAR processing chain is summarised in Figure 2.7. All calculation steps have been discussed except for co-registration and geocoding,

as these are primarily data management steps. Co-registration ensures the spatial alignment of SAR data, allowing InSAR calculations to be performed on consistent pixel locations through time. Geocoding, on the other hand, assigns the processed PS-InSAR measurements to a geographic coordinate system, enabling their visualisation and analysis in maps - in relation to real-world locations on Earth. The InSAR measurements have been projected onto the World Geodetic System 1984 ensemble using the Universal Transverse Mercator projection, specifically zone 55S for the Southern hemisphere (WGS 84 / UTM zone 55S).

2.1.4 Application of InSAR to TSFs

There is a wealth of literature on the application of InSAR to the monitoring of natural hazards, including volcanology (e.g. Biggs and Pritchard (2017)), earthquakes (e.g. Simons et al. (2002)) and landslides (e.g. Cigna et al. (2013), Peduto et al. (2021)). Recently, multi-temporal InSAR techniques (Even and Schulz (2018)) have been adopted to monitor critical infrastructure such as bridges (e.g. Selvakumaran et al. (2018), Peduto et al. (2018)) and dams (e.g. Milillo, Bürgmann, et al. (2016),Corsetti et al. (2018)), underground construction activities (e.g. Macchiarulo et al. (2021)), and ground dewatering (e.g. Cigna and Tapete (2021)). Although relatively sparse, an increasing number of studies have explored the use of multi-temporal InSAR for the monitoring of TSFs. A common aim of these studies is to identify dam deformation signals which are precursory indications of structural failure, such as the Brumadinho (e.g. Grebby et al. (2021)) and the Cadia failure (Thomas et al. (2019), Carlà et al. (2019), Hudson et al. (2021)).

In the case of the Brumadinho failure, Grebby et al. (2021) reported monitored deformation trends preceding the collapse which were inconsistent with the expected consolidation settlement of the tailings dam only. Recent application of an 'inverse velocity method' to the InSAR data (Carlà et al. (2019)) revealed anomalous deformation behaviour $\sim$40 days prior to collapse (Grebby et al. (2021)). However, this contrasts with the previous findings of Holden et al. (2020) that the statistical significance of these anomalous trends was insufficient (due to low signal-to-noise ratio) to trigger an early warning alert. Additionally, none of these studies evaluate the InSAR measurement reliability within a geotechnical context, nor do they employ any

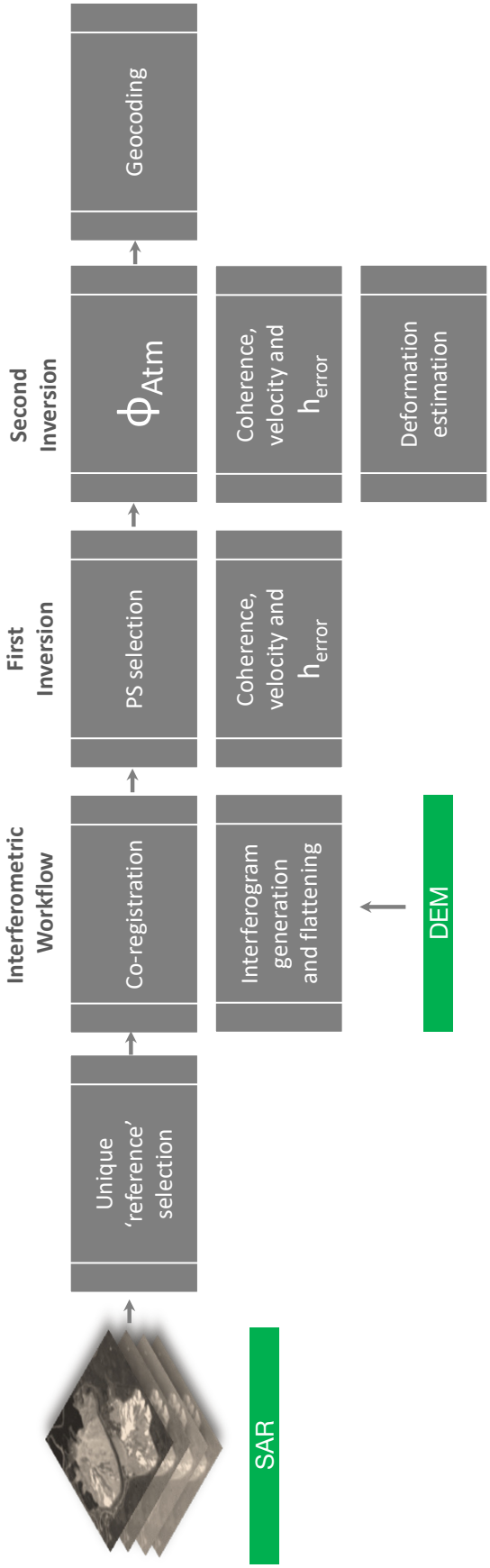

FIGURE 2.7: An end-to-end flowchart summarising the PS-InSAR processing chain.

data-driven methodologies for detecting anomalous deformation.

Most of these studies explore the application of InSAR from the perspective of analysing the robustness and limitations of particular custom post-processing of the raw SAR data into InSAR. Due to the variability in their approaches, it is difficult to conclusively resolve discrepancies in the interpretations. This is a common point of contention within the InSAR community and have led to interesting debates on the nature of the techniques. For example, new experimental InSAR approaches have identified subtle movements that were not previously detected, preceding the collapse of the Morandi bridge (Milillo et al. (2019), Milillo et al. (2020)). However, Lanari et al. (2020) debated the reliability of their novel processing techniques and questioned the possibilities of having detected 'false positives' instead.

2.2 Data-driven Approaches in Earth Observation

Most of the literature on data-driven approaches, including deep learning in satellite Earth Observation, primarily focuses on the use of optical multi-spectral data instead of SAR data. This is partly due to the more abundant availability of data from optical satellites. Advancements in camera technology has led to the trend of miniaturising satellites, making it much cheaper to launch into space. This enabled incredible achievements by companies such as Planet, who provide satellite images for everywhere on Earth daily. The same capability is not yet available for SAR satellites, due to the sensor being inherently more complex compared to optical instruments. Although the miniaturisation trend has started in SAR by start up companies such as Iceye and Capella Space, they do not yet offer interferometric capabilities. This is due to difficulties in miniaturising the precision of the instrumental characteristics necessary for SAR interferometry, such as being able to come back to the same location on Earth for each acquisition (i.e. precise orbital tube).

Moreover, optical data are more similar to the image data commonly used in the fields that lead developments in deep learning, such as computer vision. In contrast, complex pre-processing steps are required before any meaningful information can be extracted from the raw SAR data, as described in Section 2.1 for SAR interferometry. This section focuses the review to the limited, yet growing research available on the

application of data driven approaches for InSAR. The literature is divided into studies that focus on the use of deep learning within the interferometric process and those based on the derived InSAR products such as interferograms and ground deformation for monitoring.

2.2.1 Data-driven InSAR processing

Although still in its infancy, data driven approaches are showing much promise in SAR interferometric processing. For instance, the SAR signal delay due to atmospheric conditions (ϕ_{Atm}) is considered as one of the major sources of error in SAR interferometry. Chen et al. (2021) proposed estimating ϕ_{Atm} through training convolutional neural networks (CNN) based on synthetic interferograms, which are designed to replicate real interferograms. An example of this process is illustrated in Figures 2.8 (a) to (f), where phase components due to surface deformation, topography and noise from the atmosphere are simulated and then wrapped (Brengman and Barnhart (2021)).

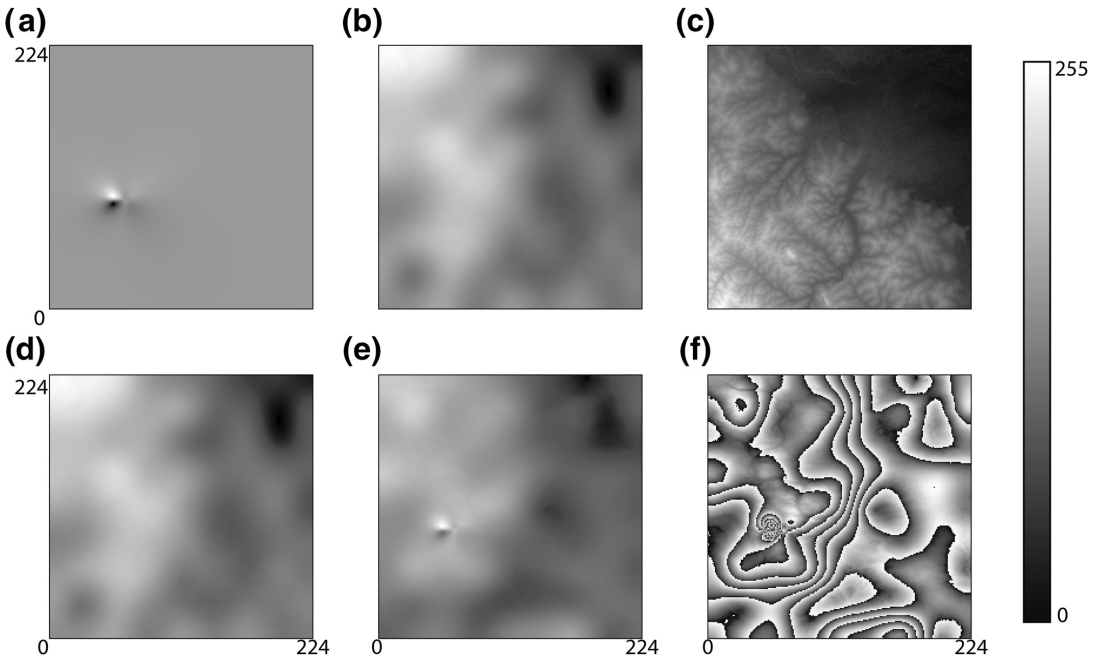

FIGURE 2.8: Example of synthetic interferogram generation workflow. (a) Modelled surface deformation of a geological fault slip. (b) Random spatially coherent noise, simulating atmospheric noise. (c) Random scaling applied to a digital elevation model to simulate topographically correlated noise. (d) Final atmospheric noise by combining (b) and (c). The synthetic interferogram is generated in (d) by combining the deformation in (a) with the atmospheric noise in (d). Finally, the synthetic interferogram is wrapped in (f). From Brengman and Barnhart (2021).

Essentially, the synthetic data were used to learn the non-linear relationship between clean and noisy interferograms for improving deformation data quality in Chen et al. (2021). Whilst Rouet-Leduc et al. (2021) have also trained their deep learning model on synthetic data, interestingly, Chen et al. (2021) have refined their synthetic data through the use of generative adversarial networks (GANs). GANs proposed by Goodfellow et al. (2014) have been revolutionary and have shown to improve training data quality and diversity of examples. In GANs, two networks are made to compete against each other. Whilst one of the CNNs are tasked with creating a fake (i.e. synthetic) map of ϕ_{Atmo}, the other is tasked with learning to distinguish between real and fake data created by the generator. As the generator gets better at creating more realistic fakes, the discriminator starts to struggle to tell the difference between the fake and the real data.

The CNN model in Chen et al. (2021) performed well in estimating the atmospheric component from interferograms, but struggled with interferograms that contained large deformation signals. These fast deformation signals were typically confused with ϕ_{Atm} and were removed as part of the atmospheric phase screening. This is because these purely CNN approaches do not account for the temporal behaviour. The fact that ϕ_{Atm} is uncorrelated in time is used by traditional, non data-driven InSAR approaches to estimate the atmospheric component.

Moreover, an ambitious attempt has been made to estimate the deformation, ϕ_{Displ} directly from a sequence of interferograms using deep auto-encoders in Rouet-Leduc et al. (2021). The data-driven approach in that study performed well, where the estimated location and deformation magnitude of geological faults largely agree with previous traditional estimates. As this technology matures, deep learning based interferometric processing may simplify the complex InSAR processing steps.

2.2.2 Early Warning of Anomalous InSAR Deformation

Recently, there has been a significant interest in the application of DL for InSAR-based ground deformation monitoring. DL models have been tasked with identifying the presence of deformation over volcanoes (Anantrasirichai et al. (2019)), tunnels or gas/water extraction (Anantrasirichai et al. (2020)), airports (Chen et al. (2021), Ma et al. (2020), and Zhao et al. (2021)) and geological faults (Brengman and Barnhart

(2021) and Rouet-Leduc et al. (2021)). Both sequential-data-based recurrent neural networks (RNN) and image-based CNN approaches have been considered in the literature. The InSAR deformation through time was treated as purely sequential data within RNNs in Zhao et al. (2021). Those authors treated each InSAR deformation measurement separately and based their predictions purely on the two dimensional deformation time history. However, their approach requires the generation of synthetic data and completely neglects the inherent spatial relationship between deformation measurements. In image-based models, synthetic data were also used to train CNNs in Anantrasirichai et al. (2020) and Chen et al. (2021).

In Anantrasirichai et al. (2020), the synthetic data were used for classifying deformation patterns related to underground gas/water extraction or tunnelling. The synthetic data generation workflow is similar to that in Figures 2.8 (a) to (f), but with different deformation models (step outlined in Figure 2.8 (a)). Instead of a geological fault, they simulated the expected deformation from point- and line-like geometries. It is important to highlight that underground construction methods like tunnelling typically exhibit well defined Gaussian settlement profiles on the surface. This assumption significantly simplifies the process of synthetic data generation. The discussions in Section 2.3 presents the complexities related to TSF construction and modelling, potentially making synthetic data generation of TSF deformations significantly more complex.

Moreover, various tweaks to traditional CNN approaches have explored combining the spatio-temporal components together. For example, a modified U-Net architecture was used to ingest a sequence of 12 temporal InSAR deformation maps to predict the following 12 time steps in Ma et al. (2020). Similarly, auto-encoders have been trained on synthetic data to extract deformation signals directly from a sequence of nine interferograms to predict the next nine in Rouet-Leduc et al. (2021). Ma et al. (2020) were able to predict both linear settlement and non-linear seasonal deformation from InSAR data over an airport. However, the potential issues with applying CNNs on InSAR data are that InSAR-based ground deformation measurements are not spatially continuous and measurement gaps are common. Multi-temporal InSAR

approaches depend on the presence of objects on the ground surface with particular scattering mechanisms, whether it is persistent or distributed scatterers. The absence of such scatterers or large changes on the ground result in measurement gaps. Therefore, interpolation techniques are applied on InSAR before its input into CNN-type approaches, as CNN-type approaches are known to struggle with data gaps (Anantrasirichai et al. (2018)). The type of spatial interpolation techniques and assumptions likely impact the performance of the CNN models and potentially contribute a level of uncertainty to the predictions.

In the case of TSFs, the DL task must be redefined and cannot merely focus on detecting the presence or absence of deformation. Some level of deformation is expected due to the consolidation processes inherent to the tailings. Therefore, the DL task will need to evaluate whether the observed deformation is as expected and 'normal' or deviates in a way that could indicate potential danger ('abnormal').

2.3 Geotechnical characteristics of TSFs

The extraction of valuable minerals and metals from the mined ore begins with crushing the rock to particles size of less than 0.5mm. Then, water along with other harsh chemical agents are added. This process results in a concentration of the valuable commodities (i.e. metals) at the top, or 'head', and the waste is called the 'the tail'. Consequently, the resulting mud-like mine waste slurry is referred to as 'tailings' (ICME and UNEP (1998)). The most common way of storing tailings are in tailings storage facilities, which are huge earthen dams, often constructed with the coarser rocks from the mine waste. There are three main types of TSF construction methods, as shown in Figure 2.9. In upstream and (to a lesser extent) centreline construction types, parts of the dam rest on the tailings itself. Therefore, consolidation of the underlying tailings has direct implications for TSF stability.

Relative to other critical geotechnical infrastructure, upstream and centreline tailings dams are unusual in the sense that the construction and in-service phases run in parallel, with construction often occurring throughout the lifetime of the structure. For dams founded on cohesive materials, each new construction stage results in a complex interplay between excess pore pressure generation and dissipation (Vick

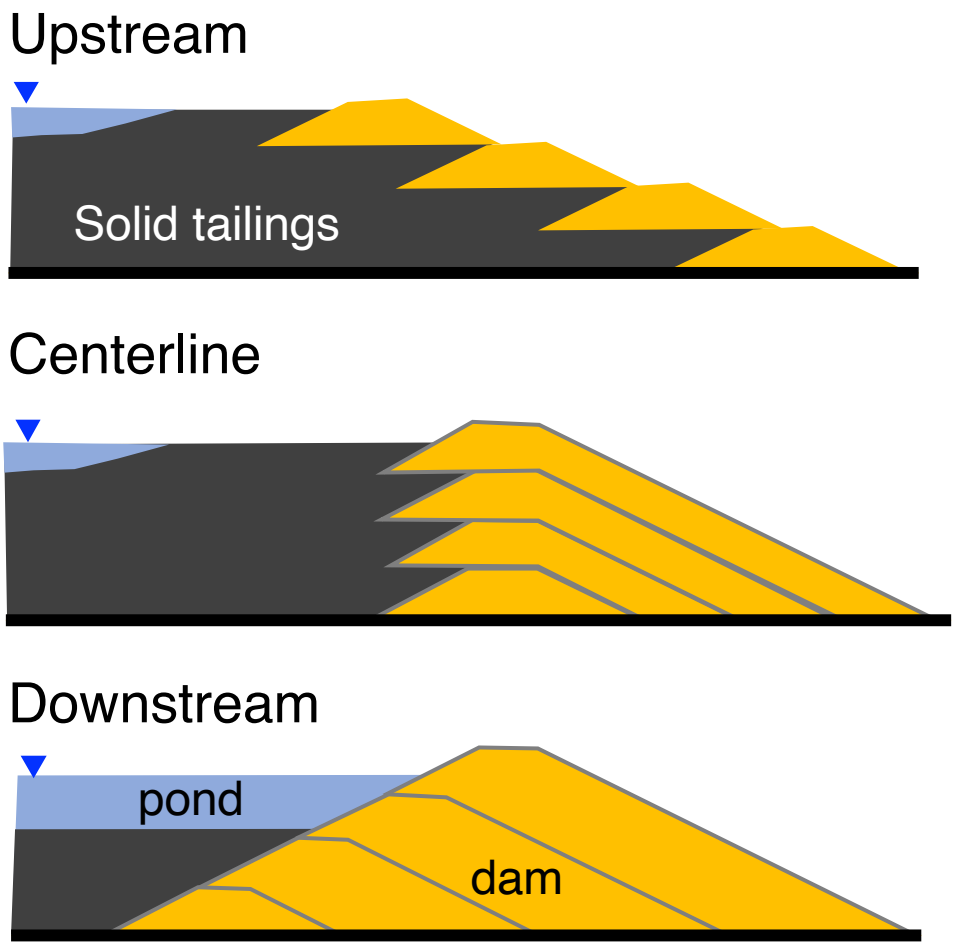

FIGURE 2.9: Main construction methods of TSFs including upstream (dam built on solidified tailings), centreline (dam partly build on solidified tailings) and downstream (dam does not rest on tailings). Note: in upstream and centreline types, the dam and tailings are constructed in parallel throughout the life of a TSF. Modified from Vick (1990).

(1990)). Using finite element (FE) analysis, Psarropoulos and Tsompanakis (2008) explored the mechanical behaviour of tailings dams, the likely mode of failure and the potential impacts of dam construction type (i.e. upstream, centreline, downstream) on geotechnical stability. The dissipation of pore pressure was shown to be dependent on a range of external operational factors including the rate at which the dam is raised/constructed. Recently, Do et al. (2021) investigated the role of the tailings deposition rate on pore pressure generation and dissipation. Those authors demonstrated that lower deposition rates (2.5 m/year - 5 m/year) are safer and more in line with safety standards compared to higher rates (5 m/yr - 10 m/yr). Laboratory experiments have also shown the tailings consolidation process to be a key factor governing dam stability. Insufficient consolidation periods create an unstable condition within the tailings

with a series of alternating layers of more competent tailings overlying very weak tailings (Garino Libardi et al. (2021)).

2.3.1 Geotechnical Properties of Tailings

The behaviour of tailings may be interpreted within classical theories of soil mechanics and compared to natural soil of equivalent gradation (i.e. natural analogue). However, there are unique characteristics of tailings that can add complexity. Tailings are initially much more compressible than their natural equivalents, because tailings particles are more angular and are deposited in a loose state (Blight et al. (2000), Bhanbhro et al. (2021)). The chemical make up of tailings varies hugely, depending on the ore, the host rock geology and the added processing chemicals. The gradation of tailings are commonly divided into coarser 'silty sand' or finer 'clayey silt' known as 'slimes' (Vick (1990)).

The behaviour of tailings is also controlled by the deposition mechanism. Commonly, tailings are deposited by 'spigotting', which means the slurry deposition happens along the perimeter of the TSF (e.g. Jefferies et al. (2019)). Dividing the deposition into smaller volumes and slower flows along the perimeter helps to achieve laminar flow rather than turbulent flow. The coarser particles of the tailings are deposited nearest to the discharge location, forming the tailings beach and finer slimes travel farthest away into the tailings pond, as annotated in Figure 2.10(a). The amount of fine particles increases and the grain size decreases towards the tailings pond (Witt et al. (2004)). Figure 2.10(b) shows a conceptual summary of the tailings properties in centreline and upstream TSFs. The coarser particles being deposited closest to the discharge zone means, the permeability is highest in this region and decreases as a function of the distance from the spigot. The tailings sands and slimes are often found in separate distinct zones, but sometimes they are highly inter-layered. However, studies of tailings deposits have shown that they do not always exhibit this systematic variation in permeability (Soderberg and Busch (1977)).

The tailings properties depend on the spigotting procedures and the nature of the tailings itself which are unique to mines and TSFs. Often mines end up with a very complex spigotting schedule. For example, for Cadia, the schedule divides the TSF

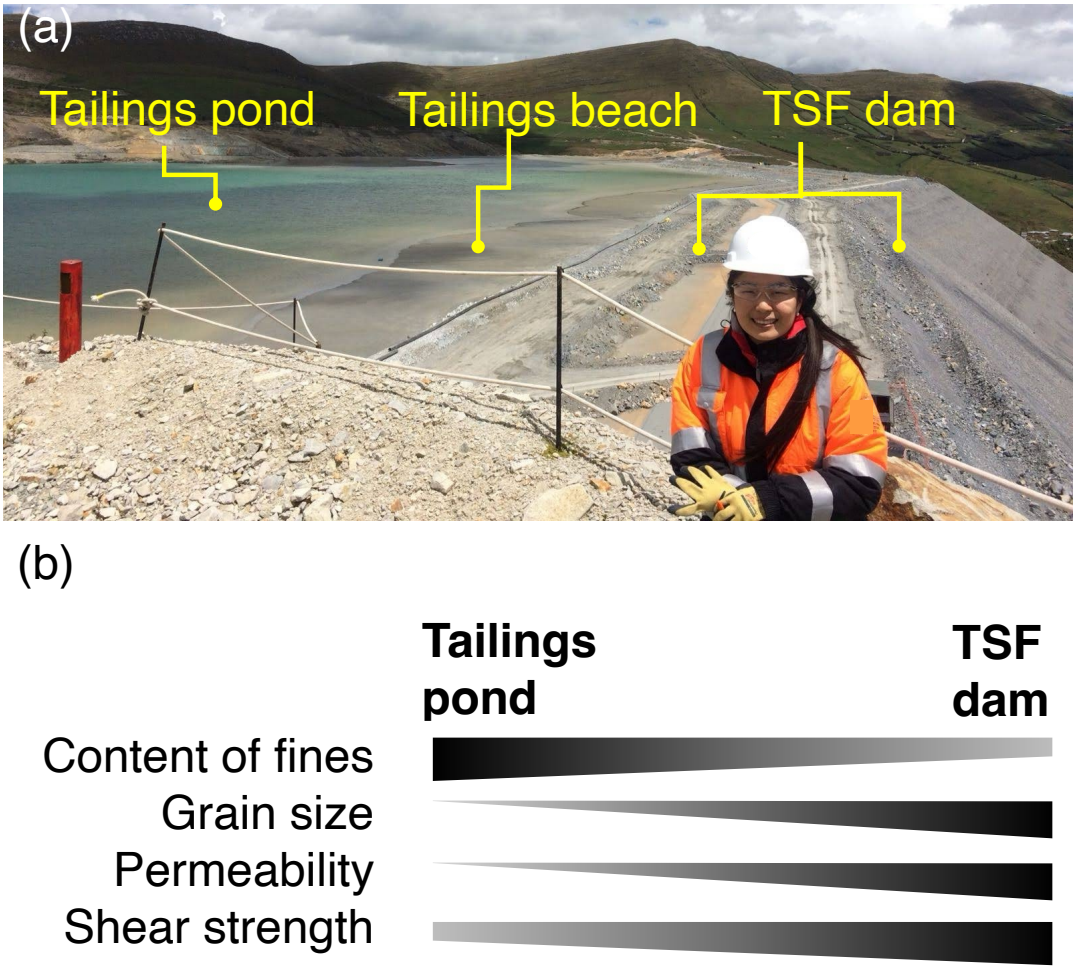

FIGURE 2.10: (a) Photograph from a field visit to a TSF, with the tailings pond, beach and the dam annotated. (b) Expected tailings characteristics relative to the discharge (spigot) location on TSF dam. Modified from Witt et al. (2004)

into zones, with rules preventing dam construction on tailings that have not been consolidating for at least 60 days (Jefferies et al. (2019)). The spigotting schedule seems to balance the deposition of fresh tailings with time required for drying and consolidation prior to construction of the next dam layer. Therefore, the permeability of the tailings are challenging to estimate. The average permeability varies from 10^{-2} cm/sec for coarse sand tailings to as low as 10^{-7} cm/sec for consolidated fines. Its layered nature give a large difference between the horizontal (k_h) and vertical (k_v) permeability of tailings. A ratio of $k_x = 10k_y$ is commonly assumed for modelling purposes e.g. Ormann et al. (2013), Do et al. (2021). This inherent variability in permeability introduces uncertainties into the estimation of expected settlement of the tailings and the

dam. The tailings deformation may be estimated through the coefficient of consolidation (c_v), which is related to permeability k as follows:

$$c_v = \frac{k}{\gamma_w m_v} \tag{2.20}$$

where γ_w is the unit weight of water and m_v is the coefficient of volume change. Slime tailings exhibit a consolidation behaviour much like natural clays, with the coefficient of consolidation c_v spanning 10^{-2} to 10^{-4} cm^2 / sec (Vick (1990)). After primary, secondary consolidation can occur which is a result of the soil internal fabric changing. For example, for sand tailings, the compression index C_c is 0.05 to 0.10 and for slime tailings, it is comparable to natural clays, with C_c of 0.20 to 0.30 (Lambe and Whitman, 1969).

Both drained and undrained conditions can prevail in TSFs. Tailings have a high particle angularity and so, the drained, effective-stress shear strength of sands and slimes is often higher than its natural analogues. Highly angular grains experience very high stress at grain contacts and particle crushing (Bhanbhro et al. (2021)). Particle crushing and dilatancy are pronounced at lower stresses and the friction angle varies less once these processes are stabilised at higher stresses (Reid et al. (2022)). Typical drained friction angles of tailings are in the range of 30° - 37° over a wide stress range and are cohesionless (Vick (1990)). Loose and dense tailings behave differently under both drained and undrained conditions (Reid et al. (2022), Mánica et al. (2021)). Recently, Reid et al. (2022) demonstrated that the undrained shear strength of tailings is sensitive to whether the tailings are compacted to a dense initial state or achieve the same consolidation stresses from samples in initially loose states.

The deposition characteristics of tailings also vary through time. This results in different parts of the TSF dam resting on tailings with variable material properties (Ormann et al. (2013)). Some parts of the dam may rest on loosely deposited layers and these are especially susceptible to becoming unstable under undrained conditions. Undrained conditions can prevail in TSFs due to increased excess pore pressure resulting from rapid construction activities (Mánica et al. (2021)). Figure 2.11 shows an FE-based pore pressure analysis for the Aitik TSF, Sweden (Ormann et al. (2013)), which is very high after construction in Figure 2.11 (a) and decreases after a period

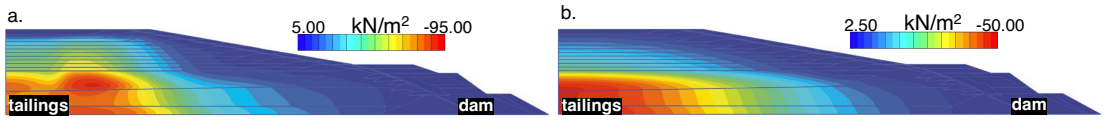

FIGURE 2.11: Example generation and dissipation of excess pore pressure in Aitik TSF, Sweden following (a) construction and (b) consolidation. Modified from Ormann et al. (2013).

of consolidation in Figure 2.11 (b). For the Aznocollar failure modelled in Gens and Alonso (2006), the magnitude of excess pore pressure was generated by the added weight of the overlying construction and demonstrated very limited dissipation. The rise in the excess pore pressure can transform the grain-supported soil matrix into a fluid-grain slurry. This phenomenon is static liquefaction and tailings are most susceptible if they are initially loose and remain saturated (Mánica et al. (2021)).

Other than construction activities, excess pore pressure can be generated by shearing and/ or the location of the phreatic surface. Changes in shear stress that are rapid relative to the tailings dissipation ability can generate excess pore pressure. This happens not only during loading but also during unloading (Vick (1990)). Removal of material at the dam toe can cause changes in shear stress that may lead to instabilities such as in Jefferies et al. (2019). Predicting the phreatic surface location for downstream TSFs is analogous to water dams, because it is largely controlled by the internal zoning of the dam itself, not the tailings properties. Prediction of the phreatic surface is much more complex for upstream TSFs, because the dam partly rests on consolidated tailings. Therefore, the location of the phreatic surface depends on factors such as the variation of permeability of the underlying tailings and the pond location.

2.3.2 Numerical Modelling of TSFs

The closest analogue structure to TSFs is a conventional water retention dam. Four types of calculations are typically employed to assess the stability of water dams: 1) end of construction, 2) staged construction, 3) long-term steady seepage and 4) rapid draw-down (Vick (1990)). Long-term steady-state seepage implies there will be no rapid change in external loading. The scenario of rapid drawdown is not applicable to TSFs, because the tailings solidify through sedimentation. Within the tailings and TSFs founded on cohesive materials, each new construction stage results in a complex interplay between excess pore pressure generation and dissipation. Therefore, staged

construction calculations are required to track the changes in excess and hydrostatic pore pressure with respect to time.

A plethora of approaches are available in modelling the behaviour of soils, from simple empirical to advanced numerical techniques. Advanced modelling methods such as Material Point Method (MPM) have recently been applied to slope stability applications and are reviewed in Soga et al. (2016). It does not suffer from mesh distortion problems and therefore, most suitable for large deformation problems. MPM has been used in modelling the runout of TSF failures, for the 2018 Cadia, Australia (Pierce (2021)) and the 2014 Mount Polley, Canada (Llano-Serna et al. (2017)) failures. In these analysis, MPM has been used for modelling the post-deformation kinematics of the runout and its consequences on the surroundings. MPM has rarely been used for TSF pre-failure modelling, except in the 1998 Aznacollar TSF failure in Zabala and Alonso (2011). However, MPM is computationally more expensive (Soga et al. (2016)) and suffers from numerical instabilities compared to the more established finite element (FE) modelling approach (Fern et al. (2019)). Therefore, MPM is rarely used in industry.

FE modelling is the most popular approach for the modelling of pre-failure behaviour of TSFs (e.g. Gens and Alonso (2006), Ormann et al. (2013), Mánica et al. (2021)). It calculates and keeps track of the complex accounting of the pore pressure and displacements. For example, in Psarropoulos and Tsompanakis (2008) the mechanical behaviour of tailings dams, the likely mode of failure and the potential impacts of dam construction type on stability are investigated using FE. A common technique to improve tailings dam stability is through the addition of buttresses at the toe of the dam to provide additional sliding resistance. For example, Ormann et al. (2013) used FE modelling to optimise the location and volume of rock fill required to increase the stability of the Aitik tailings dam in Sweden. Moreover, numerical analyses have been employed to investigate the slope stability (Whittle et al. (2022)) and identify the triggering mechanisms (Robertson et al. (2020), Arroyo and Gens (2021)) for the Brumadinho tailings dam failure.

To model the deformation behaviour of tailings dams, suitable constitutive soil models are required to represent the different components. There is a lack of consensus in the literature on the best modelling approach or constitutive model for the

various elements of a tailings dam as illustrated in Table 2.2. It shows that, whilst the dam has been commonly modelled using an elastic perfectly plastic (EPP) model, the tailings and the foundation have been modelled using a wide range of constitutive models. The tailings are sometimes modelled as a single material type in e.g. Gens and Alonso (2006) or sub-divided into zones with e.g. varying permeabilities in Whittle et al. (2022).

TABLE 2.2: Constitutive models employed for modelling tailings dams.

Reference	Dam	Tailings	Foundation
Whittle et al. (2022)	EPP	EPP	EPP
Mánica et al. (2021)	EPP	Clay And Sand Model (CASM)	-
Do et al. (2021)	EPP	UBCSAND	EPP
Robertson et al. (2020)	EPP	EPP with strain weakening	CHSoil
Jefferies et al. (2019)	EPP	Nor-Sand	CHSoil
Morgenstern et al. (2015)	EPP	Nor-Sand	-
Ormann et al. (2013)	EPP	EPP	EPP
Psarropoulos and Tsompanakis (2008)	EPP	EPP	EPP
Gens and Alonso (2006)	EPP	EPP	EPP
Priscu et al. (1999)	-	Modified Cam-Clay (MCC)	-

2.4 Summary and Gaps in Knowledge

The review of the literature on InSAR, geotechnical modelling and deep learning highlighted the significant potential for synergy between these domains. It also revealed a gap in research regarding the suitability of combining them within the context of TSFs. Fortunately, there are previous studies available that combine elements of these technologies for other applications and have served as analogues to the research aims. Unlike other critical infrastructure, TSFs represent an ambitious challenge due to their construction and operational phases often occurring throughout the lifetime of the structure. Therefore, this research will explore the extent to which these technologies can be effectively integrated to enhance the safety of TSFs.

Integration of InSAR with geotechnical modelling has been demonstrated as promising approach for interpreting the processes observed from various sensor measurements. For example, Corsetti et al. (2018) integrated InSAR with ground-based instrumentation (levelling) data and FE modelling for the monitoring of an embankment water dam. Moreover, Shamshiri et al. (2014) used data from a SAR sensor to calibrate an FE model of a causeway embankment, and data from a separate SAR sensor for validation. Similarly, Zhou et al. (2016) used monitored InSAR deformations to 'back-analyse' material properties of a rock fill water dam using an FE model. Other studies combined InSAR measurements with sub surface soil data from cone penetration tests and ground-based instruments (settlement plates) to calibrate the geotechnical model for railway- (Peduto et al. (2017)) and road- embankments (Peduto et al. (2020)). Moreover, the underlying failure mechanisms for deep seated landslides have been identified through comparing FE analysis and InSAR measurements in Frattini et al. (2018). In the context of concrete dams and bridges, the InSAR data has been interpreted within the expected seasonal movements by taking account of the underlying processes, hydrostatic loading (Milillo, Perissin, et al. (2016)) and thermal effects (Cusson et al. (2021)), respectively. Therefore, a thorough understanding of the mechanics of a likely TSF failure and its influence on InSAR measurements will be critical for rigorously identifying potentially dangerous or 'anomalous' movements. To the best of the authors' knowledge, no such framework currently exists for TSFs.

Recent studies have applied InSAR to failed TSFs, such as the Brumadinho (e.g., Grebby et al. (2021)) and Cadia failures (Bayaraa et al. (2024), Carlà et al. (2019), Hudson et al. (2021), and Thomas et al. (2019)). A key research question has been whether InSAR can detect precursory indications of structural failure preceding these failures. Carlà et al. (2019) proposed an 'inverse velocity method' for the estimation of the failure date using InSAR for a variety of slope instabilities, including the Cadia TSF failure. Their proposed technique has been adopted by a variety of InSAR-TSF-monitoring studies for both Cadia (Thomas et al. (2019)) and Brumadinho (Grebby et al. (2021)). In those studies, anomalous measurements were identified both qualitatively and visually, i.e., whether any obvious clusters of high subsidence measurements occurred near the failure area. However, the location of the failure surface is not known without the benefit of hindsight analysis. Therefore, there is a need for

a robust approach to identifying anomalous InSAR deformation behaviour as they develop over time.

Data-driven approaches, particularly deep learning, have shown promise for a variety of complex tasks such as anomaly detection and forecasting. Although there is currently no literature combining InSAR and deep learning for TSFs, analogous studies provide insights into the potential opportunities and challenges of different algorithms. Whilst typical image-based deep learning suffers from challenges around e.g. spatial data gaps commonly present in InSAR due to measurement coherence loss (Biggs and Pritchard (2017)), purely temporal approaches do not take into account of the inherent spatial relationship of the InSAR measurements (Zhao et al. (2021)). Therefore, for effective early warning of TSF failure, a data-driven approach must account for both spatial and temporal components of the InSAR data.

Moreover, the effectiveness of the early warning is likely influenced by uncertainties related to the characteristics of the particular InSAR data, such as its resolution. Although InSAR deformation signals were detectable regardless of the type and resolution of the raw SAR sensor, the quality of the signals varied over the Brumadinho (Holden et al. (2020)) and the Cadia TSFs (Hudson et al. (2021)). For example, in Hudson et al. (2021) the higher resolution Radarsat-2 InSAR (RS2-InSAR) detected more small spatial clusters of deformation, better outlined the location of the failure surface, and identified greater deformation magnitudes compared to Sentinel-1 InSAR. However, the limitations discussed in these studies raise the question of whether these differences in the deformation are due to the particular spatial and temporal resolution, assumptions made during the InSAR processing, or the satellite sensor characteristics (orbital geometry, signal incidence angle, and wavelength). Importantly, the extent to which these factors can then impact the early warning capability is currently unknown and needs further investigation.

Chapter 3

Comparison between InSAR and Geotechnical Approaches

This chapter explores the suitability of rigorous geotechnical modelling and satellite InSAR for the monitoring of TSFs. It involves a comparison of these results with ground-based prism deformation measurements, particularly focusing on a collapsed section of the Cadia TSF in Australia as a real world test case. This study constitutes the first systematic demonstration of the efficacy and complementarity of geotechnical and remote sensing techniques for the monitoring of TSFs.

3.1 Cadia Tailings Dam Case History

The Cadia failure occurred on the 9th of March 2018, in South-East Australia (Figure 3.1(a)). The Cadia mining complex contains two Tailings Storage Facilities to the North (NTSF) and South (STSF) of the site (see Figure 3.1(b)). The failure has been attributed to a brittle, low-density soil layer: 'Forest Reef Volcanics (FRV) Unit A'. The existence of this unit was not discovered until after the failure by an Independent Technical Review Board (ITRB) investigation (Jefferies et al. (2019)). Previous investigations of the Cadia failure are from a purely InSAR perspective and have demonstrated the presence of accelerating deformation signals immediately preceding the failure (Thomas et al. (2019), Carlà et al. (2019), Hudson et al. (2021)).

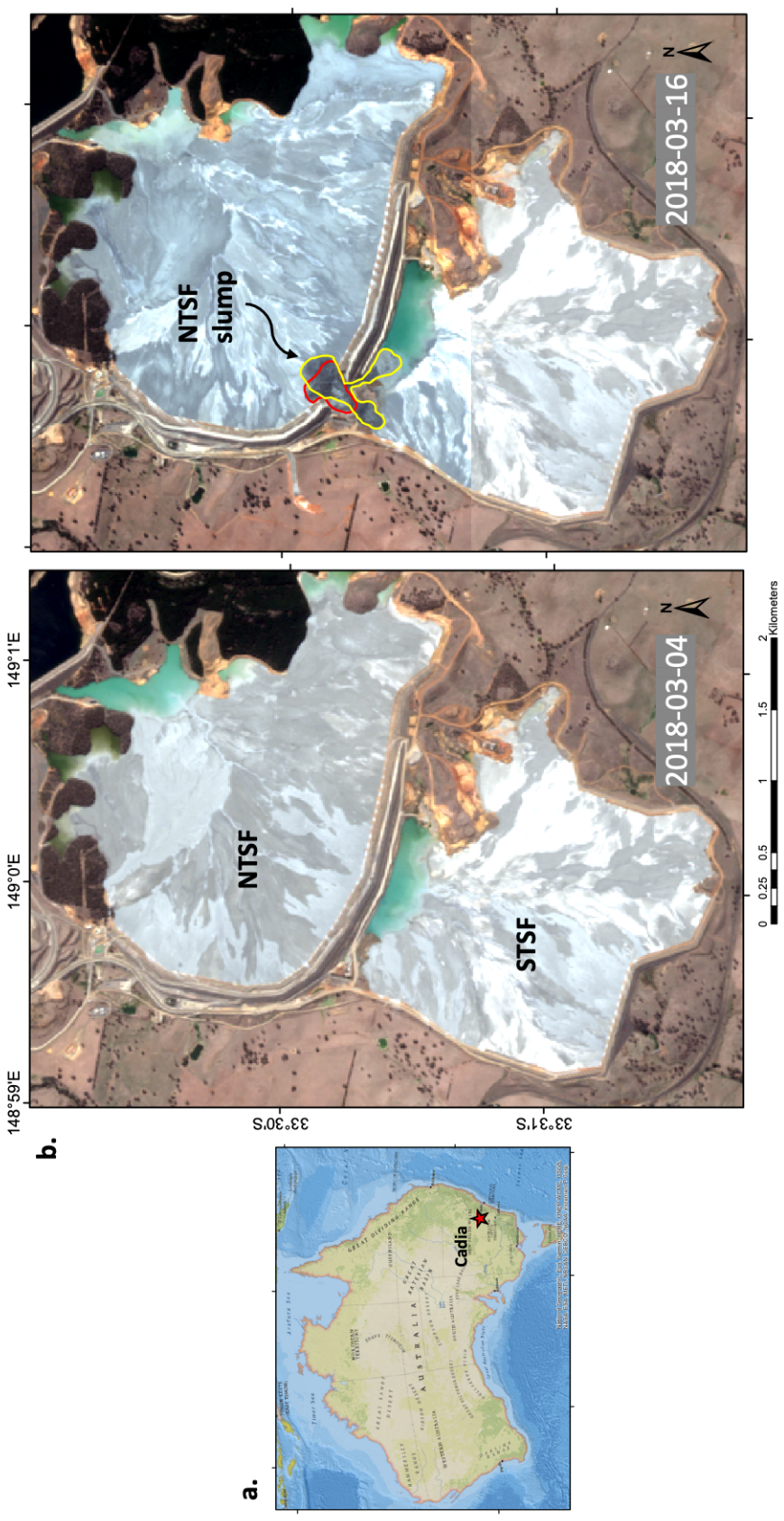

FIGURE 3.1: (a) Location of Cadia dam, Australia. Basemap images copyright © 1995–2020 Esri; (b) Cadia dam before and after failure. The failure occurred in two stages, as outlined in red and yellow (red predates yellow). © ESA Sentinel-2 data 2018.

There are many similarities between the Cadia slump and both the 1998 Aznalcollar failure in Spain (Gens and Alonso (2006)) and the 2014 Mount Polley failure in Canada (Cuervo et al. (2017)). The Aznalcollar failure was due to the development of progressive failure within the underlying brittle clay units whereas the Mount Polley failure was caused by dam construction which exceeded the capacity of the underlying weak glacio-lacustrine layers. Figure 3.2 shows the underlying geology and borehole locations in the Cadia slump zone. It illustrates the spatial extent of FRV relative to the surrounding geology and zone of failure.

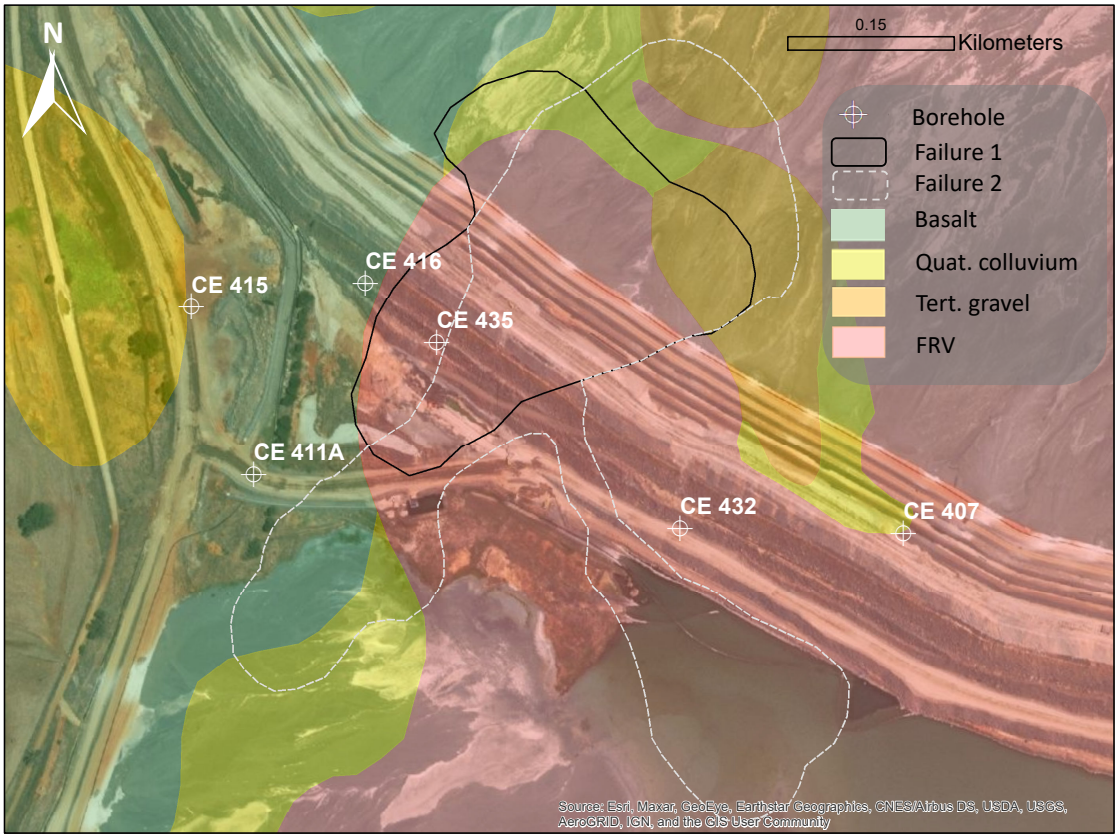

FIGURE 3.2: An overview of the geology and borehole data available over the slump zone. Failure 1 occurred on the 9th of March 2018. A secondary failure event ('failure 2') occurred on the 11th of March 2018. Distribution of lithologies are adapted and modified from Jefferies et al. (2019). Basemap images copyright © 1995–2020 Esri.

3.1.1 Geology and Stratigraphy

The soil stratigraphy in the vicinity of the slump comprises FRV, a sequence of mafic to intermediate volcanic-derived sedimentary breccias and sandstones intercalated with

basalts and andesites. The topmost zone of the FRV is the extremely weathered FRV Unit A which overlies a highly to moderately weathered FRV Unit B followed by a fresh igneous FRV bedrock (Jefferies et al. (2019)). Figure 3.2 shows the complex distribution of the underlying geological units under the NTSF. Outlines for the slump area correspond to two different dates post-failure: 9th and 11th of March 2018, denoted 'failure 1' and 'failure 2' respectively. Also shown are the locations of six nearby boreholes. Results from the three boreholes within the slump area (CE 416, CE 432 and CE435) are presented in Figure 3.3. The alluvial sediments discovered in borehole CE 416 had been eroded in boreholes CE 435 and CE 432. These paleosols are soil developed during past environmental settings, mainly composed of alluvium from lacustrine and fluvial deposits. The basalts overlying the paleosols are mainly olivine basalts beneath high to medium weathered basaltic clays. FRV Unit B depths are extracted from borehole CE 435 at the centre of the slump. The depth of weathering is most shallow at CE 435 compared to the two boreholes on either side (CE 416 and CE 432). The top section of FRV Unit A was significantly disturbed during the failure such that there remains considerable uncertainty in relation to the exact thickness of FRV Unit A within the failure zone.

3.2 Satellite SAR Interferometry

In this study, a variant of the SBAS algorithm (Chapter 2), called intermittent-SBAS (ISBAS) was used on 2.5 years of Sentinel-1 descending stack (Sowter et al. (2013)). 'Sentinel-1' is a SAR satellite from the European Space Agency's Copernicus program. Relative to high-resolution commercial satellites, Sentinel-1 data have an intermediate spatial resolution of 5 m x 20 m and temporal resolution of 6 or 12 day revisit depending on the location on Earth (Torres et al. (2012)). Over the Cadia TSFs, the temporal resolution of Sentinel-1 is 12 days. SAR satellites operate at wavelengths within the microwave part of the electromagnetic spectrum, with Sentinel-1 acquiring in the C-band, which has a wavelength of approximately 5.5 cm.

As demonstrated in Section 2.1.1, deformations are detected in the line-of-sight (LOS) of the satellite. The theoretical maximum LOS deformation which can be measured between two measurements is $\lambda/4$, where λ is the SAR signal wavelength

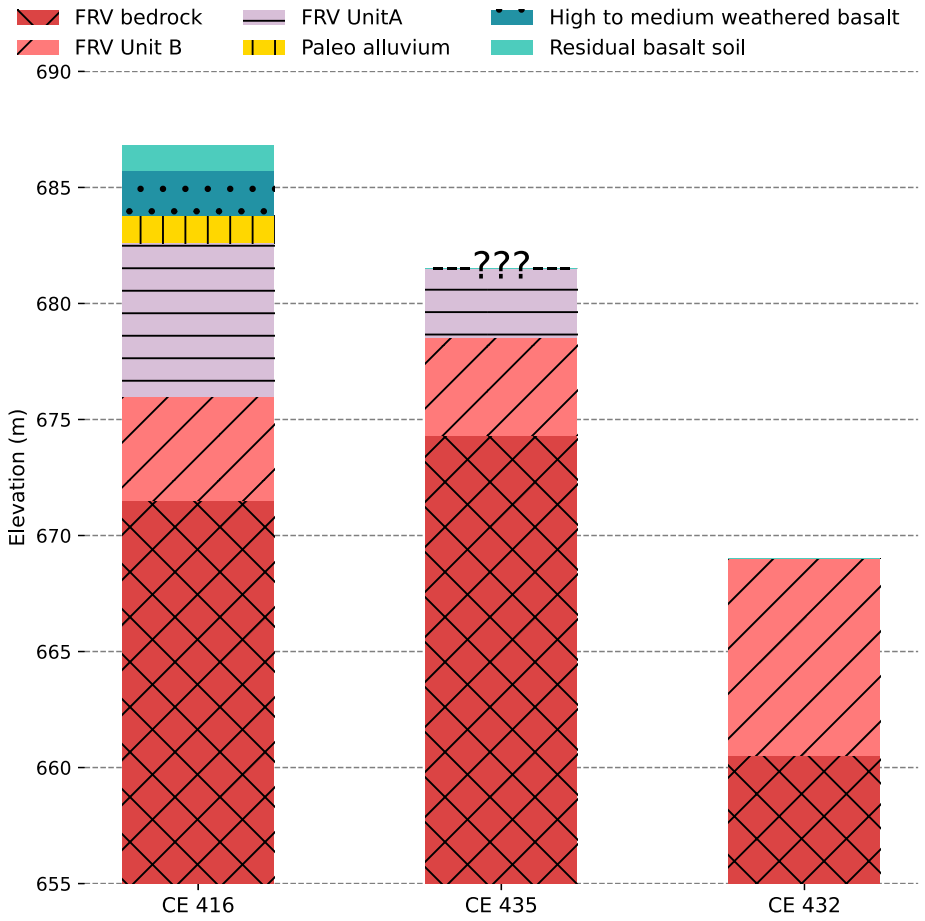

FIGURE 3.3: Soil stratigraphy derived from boreholes located near the slump zone. Note the thickness of FRV Unit A in the failure zone (borehole CE435) is unknown.

(Crosetto et al. (2016)). For Sentinel-1, the maximum detectable deformation equates to 426mm/yr. To allow comparisons with the present FE model and ground-based monitored data, the vertical and horizontal displacement components have been combined and transformed into LOS through Equation 3.1 following Selvakumaran et al. (2020):

$$\delta_{LOS} = \begin{pmatrix} \cos\theta \\ \sin\theta\cos\alpha \\ \sin\theta\sin\alpha \end{pmatrix} * \begin{pmatrix} \delta_v \\ \delta_L \\ \delta_T \end{pmatrix} \tag{3.1}$$

where θ is the satellite incidence angle, which is the angle between SAR signal LOS and the vertical (obtained from the raw SAR metadata and taken as 33°). The vertical, δ_v, and horizontal components of the displacement, with the latter being further resolved in the direction longitudinal δ_L and transverse δ_T to the dam. The geometrical relationship between the satellite LOS and the dam orientation is shown in Figure 3.4, where α depends on the orientation of the given dam segment.

FIGURE 3.4: Illustration of InSAR LOS deformations and the geometrical relationship between the dam orientation and the satellite flight path. Basemap image copyright © 1995–2020 Esri.

Equation 3.2 is used to calculate the value of α which is the angle of the TSF section relative to satellite LOS. β is the angle of the TSF section from the North as illustrated in Figure 3.4. The Sentinel-1 satellite heading angle is 167°, therefore, the heading angle clockwise from the North is $\theta_{heading\_N} = 180 - 167 = 13°$. The value of α for the slump area is taken as 22° for analysis of the Cadia slump area.

$$\alpha = 90 - \beta - \theta_{heading\_N} \tag{3.2}$$

Figure 3.5 shows the average LOS velocity measurements obtained from this stack over Cadia dam. The spatial distribution of the InSAR data is good over the dam, with approximately 27 measurement points per hectare, i.e. providing full spatial coverage with a measurement every 20 m. A significant amount of subsidence is visible in the failed NTSF, whilst the subsidence in the STSF is less pronounced.

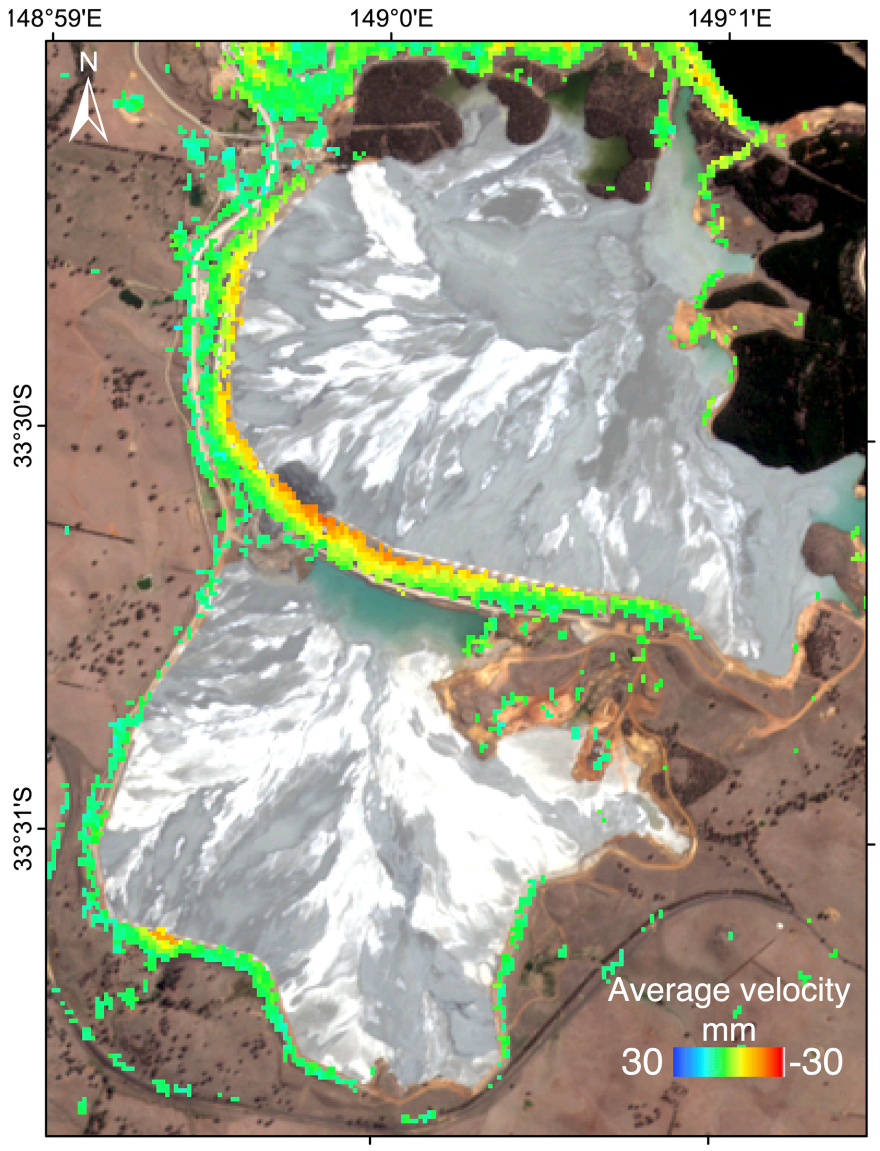

FIGURE 3.5: Illustration of InSAR velocity measurements over Cadia dam averaged over the whole SAR data stack (from 2015-12-02 to 2018-02-25). Basemap image copyright © ESA Sentinel-2 data 2018. © Terra Motion ISBAS data

To enable comparison with FE simulations, cross-sections of the InSAR displacement measurements have been constructed over the slump area, orthogonal to the construction stages. The locations of the cross sections are illustrated in Figure 3.6.

Also superimposed on the plot are the locations of three ground-based prism monitoring stations near the failure zone, namely prisms 4, 5 and 6.

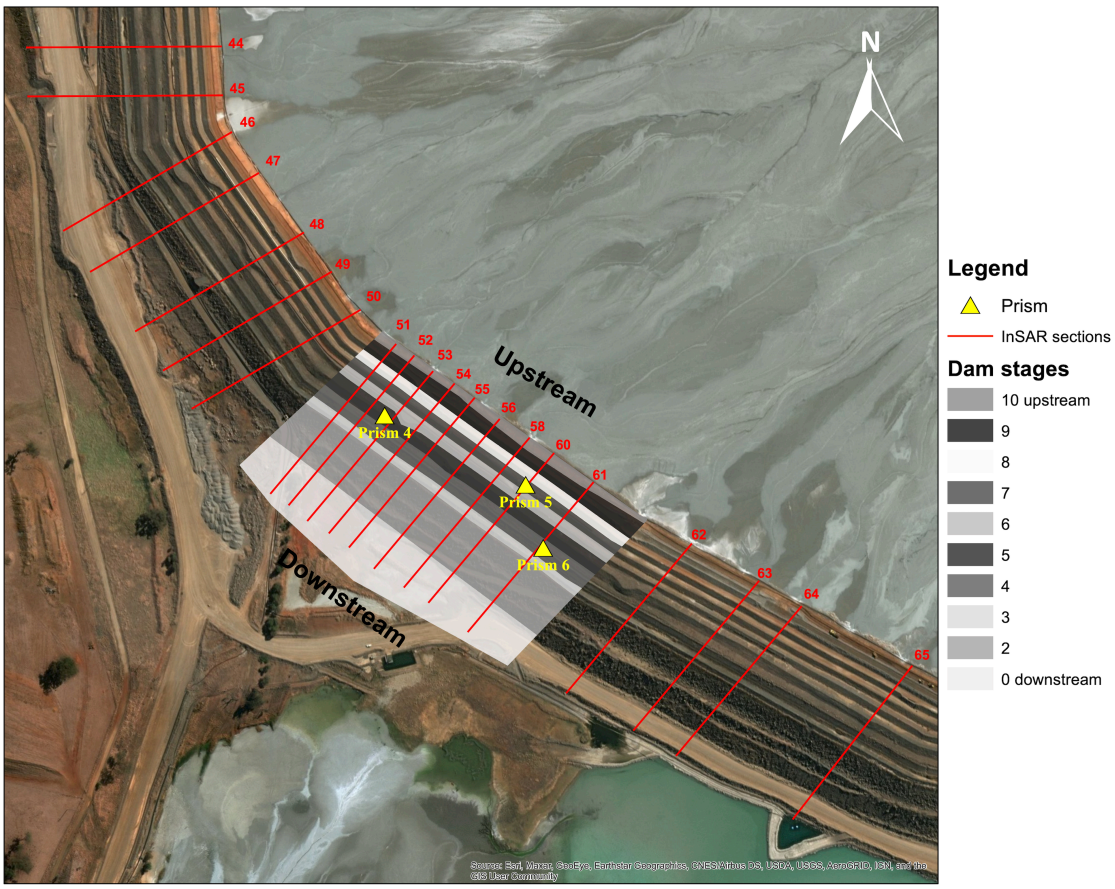

FIGURE 3.6: Location of InSAR sections and ground-based prisms relative to slump area. Basemap image copyright © 1995-2020 Esri.

3.3 Finite Element Model

3.3.1 Geometry and Material Parameters

In this study, the NTSF slump area is modelled using the FE package Plaxis 2D 2019. Given the scale of the dam, plane strain conditions have been assumed. Coupled-consolidation analyses have been used to faithfully replicate the timing of the various dam construction and filling stages, and the time-dependency of the dam/soil behaviour. The post-failure investigation reports by Jefferies et al. (2019) have provided an unprecedented level of public access to fundamental datasets on the TSF. This access has facilitated model development, with the underlying geological data,

dam geometry, construction sequences, raw laboratory data of the dam and foundation materials, and data from prisms being digitised and extracted from the reports. Such high-quality ground-truth data and insights are not publicly available for any other TSF failure.

Figure 3.7 provides a schematic illustration of the dam cross section within the failure area. The base of the computational domain is modelled at an elevation 682.5 m to minimise boundary effects. A stage 1 dam height of 17.5 m was adopted for the slump area. The thickness of stage 1 increases towards the East of the slump, due to underlying topographical variation, reaching a maximum thickness of 50 m. Dam stages 1, 2A and 2B are downstream-type construction comprising clay fill, transition fill and rock fill. Stage 3 is centreline-type construction whereas stages 4 through 10 are upstream-type construction; these stages have been modelled as rock-fill only. Following the construction of stage 10, a series of buttresses were planned with the aim of increasing the stability of the tailings dam. Buttress 1 was constructed on top of the upstream stages in three phases: 1A, 1B and 1C. Although buttress 2 had not started construction in the vicinity of the slump area at the time of failure, an excavation commenced at the toe of the NTSF in the slump area in preparation for the construction of buttress 2.

While FE modelling has provided valuable insights into tailings dam behaviour, there is little consensus in the literature on the best modelling approach or constitutive model for the various elements of the structure, as shown in Table 2.2. In keeping with previous literature, an EPP model with a Mohr Coulomb failure criterion was adopted for the dam structure whereas a linear elastic model was selected for the FRV bedrock; the corresponding material properties are summarised in Table 3.1. As recommended by the ITRB, the properties of the rockfill were taken from the Leps (1970) dataset (Jefferies et al. (2019)) which is an industry standard database of material properties for fine-grained igneous rocks similar to the rockfill materials used in the NTSF. A friction angle value of 40° was chosen, representing rock-fill properties under the average embankment height in the slump area corresponding to a normal stress of approximately 1 MPa. The elastic parameters for the dam structure are taken from Jefferies et al. (2019).

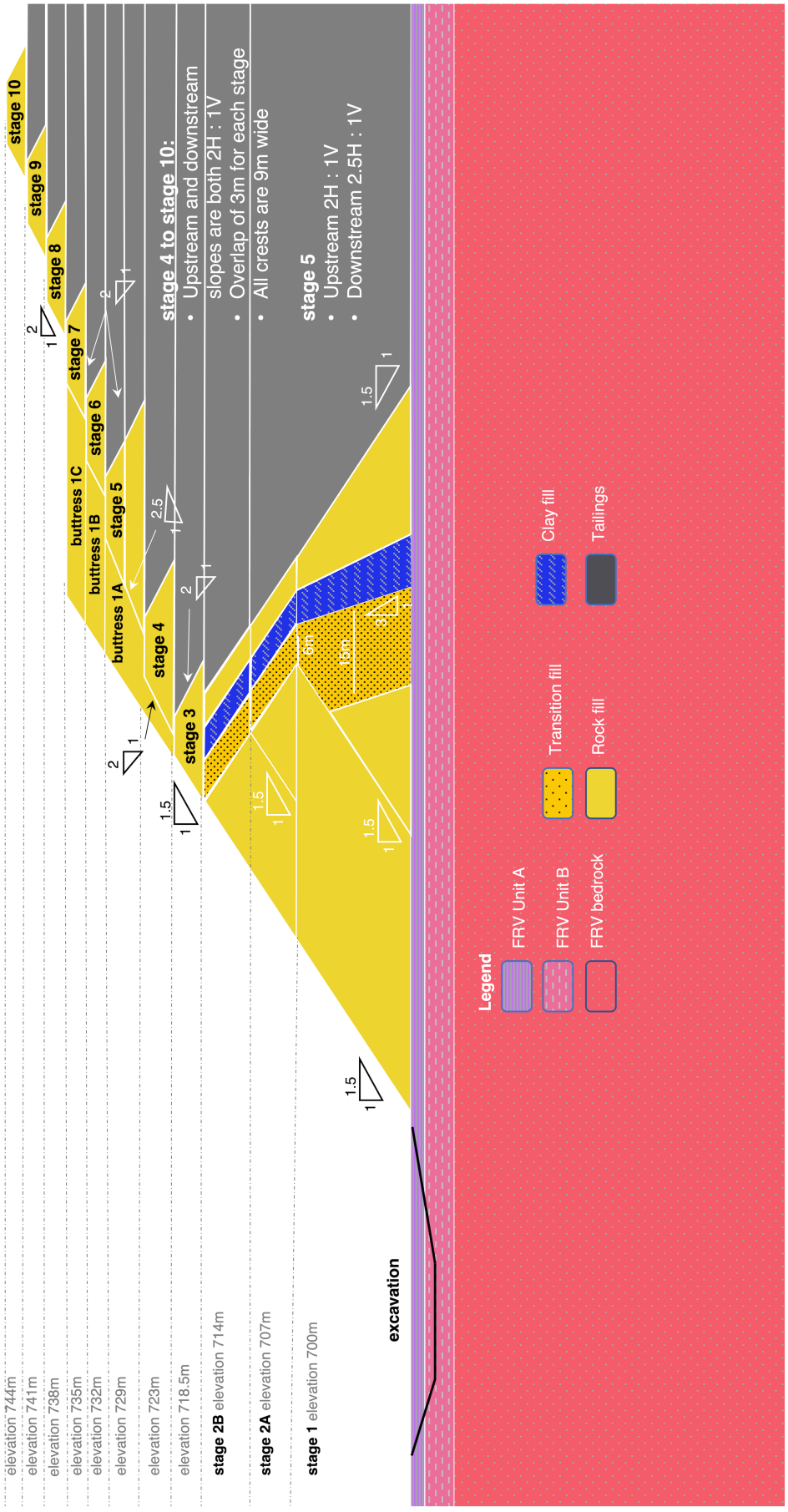

FIGURE 3.7: Geometrical arrangement of North Tailings Storage Facility in the slump area. The height for the base of the dam depends on the location of the cross section.

The Modified Cam Clay (MCC) constitutive model that is widely used in industry has been adopted to simulate the behaviour of the cohesive layers, namely FRV Unit A, FRV Unit B and the tailings. Strength and compressibility properties were determined from the raw undrained triaxial test (Figure 3.8) and oedometer test (Figure 3.9) data reported in Jefferies et al. (2019). Figure 3.8 plots the development of deviator stress as a function of mean effective stress for all undrained triaxial tests. A line of best fit was used to determine the slope of the critical state line (CSL).

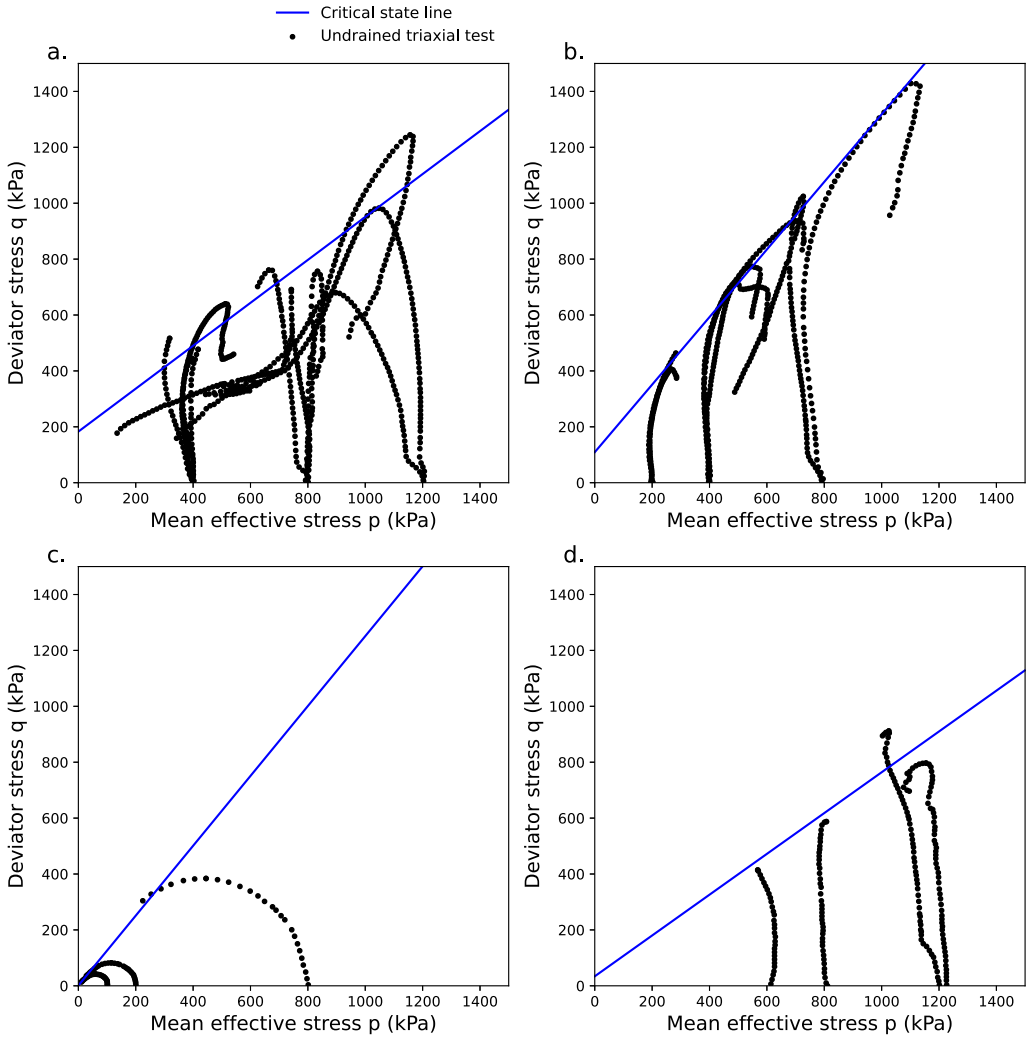

FIGURE 3.8: Undrained triaxial test results reported in Jefferies et al. (2019) showing present interpretation of the critical state line for (a) FRV Unit A, (b) FRV Unit B, (c) Tailings and (d) Clay core. The interpreted parameters are presented in Table 3.2

The soil compressibility characteristics were calculated from the oedometer results as shown in Figure 3.9 and Table 3.2. The oedometer tests were taken from boreholes CE415 and CE411A for FRV Unit A and FRV Unit B, respectively, which were located downstream of the dam and thus undisturbed by construction activities (see Fig. 3.2). Overconsolidation ratios were informed by the pre-consolidation pressures reported in Jefferies et al. (2019) and estimates of the current in-situ vertical effective soil stresses. Average overconsolidation ratio values of 2.34 and 1.36 were calculated for FRV Unit A and FRV Unit B, respectively. The vertical permeabilities, k_y, for FRV Unit A and Unit B have been determined from the oedometer tests corresponding to borehole CE 411A. In the absence of specific measurements, the corresponding horizontal permeabilities, k_x, are assumed equal to k_y (Jefferies et al. (2019)). The vertical permeability and compressibility parameters for the tailings have been determined based on the oedometer results corresponding to borehole CE 407. Due to the layered nature of the tailings, $k_x = 10k_y$ has been assumed; this is a common assumption for modelling tailings behaviour e.g. Ormann et al. (2013), Do et al. (2021). The coefficient of lateral earth pressure at rest is assumed to be 1 for all soil layers except for the tailings where a value of 0.7 has been adopted (Jefferies et al. (2019)).

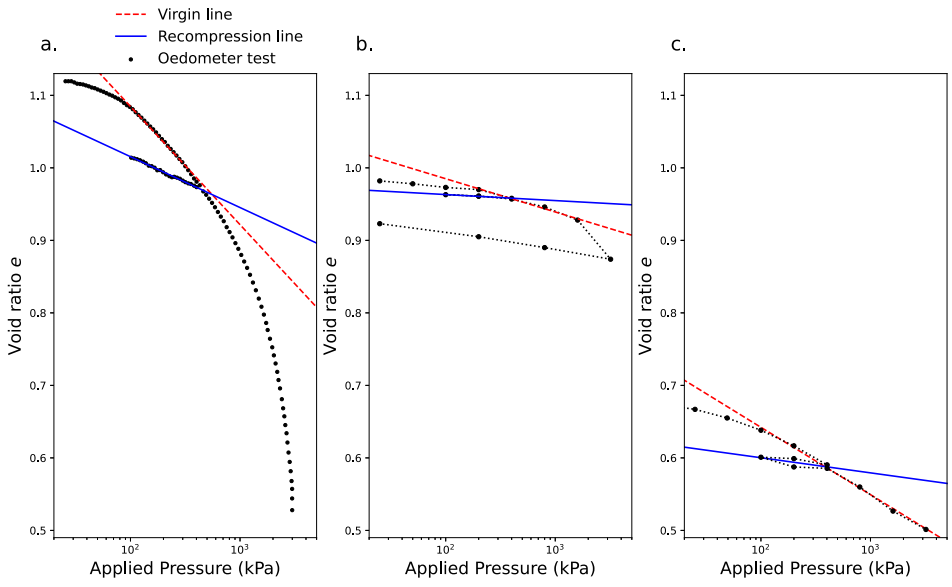

FIGURE 3.9: Oedometer test results reported in Jefferies et al. (2019) showing present interpretations of the virgin compression and recompression lines for (a) FRV Unit A, (b) FRV Unit B and (c) Tailings.

TABLE 3.1: Constitutive model parameters for FRV Bedrock and dam

Parameters	**FRV Bedrock**	**Rock fill**	**Clay fill**	**Transition fill**
Model	Linear-elastic		EPP	
Unit weight (kN / m^3)	22	19	19.5	20
Poisson's ratio	0.25	0.35	0.27	0.3
Shear modulus (MPa)	130	22	15	30
Cohesion (kPa)	–	0.1	16	0.1
Friction angle, (°)	–	40	19	42
Vertical permeability, k_y (m/day)	–	8.64E-02	8.64E-05	8.64E-02
Horizontal permeability, k_x (m/day)	–	8.64E-02	8.64E-05	8.64E-02

TABLE 3.2: Modified Cam Clay constitutive parameters for cohesive soil units FRV Unit A, FRV Unit B and tailings

Parameters	FRV Unit A	FRV Unit B	Tailings
Unit weight (kN/m^3)	17.8	18.5	24.8
MCC swelling index	0.0118	0.0016	0.0047
MCC compression index	0.0137	0.0044	0.0089
Slope of critical state line, Overconsolidation ratio	0.590 10.7	0.871 3.16	0.895 1.00
Vertical permeability, k_y (m/day)	5.36E-03	5.36E-03	6.31E-04
Horizontal permeability, k_x (m/day)	5.36E-03	5.36E-03	6.31E-03

The FRV bedrock, rock fill, and transition fill behaviour were assumed fully drained. The initial conditions for the clay core, FRV Unit A, FRV Unit B and the tailings were modelled as initially undrained such that pore pressure generation and subsequent dissipation within a coupled-consolidation analysis was allowed, if appropriate.

3.3.2 Finite Element Mesh

All soil and dam materials were modelled using fourth-order, 15-node triangular elements. The adopted FE mesh contains 13,254 elements and the refinement parameters for the foundation and TSF layers are summarised in Table 3.3. The mesh parameters were incrementally reduced to ensure a sufficiently dense mesh, achieving at least four layers of elements in the regions of interest. This includes the FRV Units A and B of the foundation, as well as the tailing sections located beneath the dam stages, as illustrated in Figures 3.10 (a) and 3.10 (b).

TABLE 3.3: The parameters of the adopted FE mesh. To achieve a balance between computational efficiency and mesh size, the mesh parameters were progressively refined until a sufficiently dense mesh was obtained.

Global	FRV Unit A	FRV Unit B	Stages 1/2A/2B	Stages 3 to 7	Stages 8 to 10	Buttress	Tailings
Medium	0.05	0.1	0.2	0.1	0.05	0.5	0.2

For instance, the dense layers of elements in Figure 3.10 (b) for FRV Unit A were achieved using a finer value of 0.05, while a coarser value of 0.1 was sufficient for FRV Unit B. To balance computational efficiency with mesh size, a coarser value of 0.2 was adopted for the tailings. Moreover, adopting finer mesh sizes for the upstream dam stages also has the effect of refining the elements of the tailings directly beneath and near these stages. This approach enables localised refinement of the tailings rather than adjusting the entire tailings layer. The lateral boundaries were restricted from movement normal to the respective surface whereas the bottom boundary was restrained from movement in both directions. The top drainage boundary was prescribed as free-draining to allow dissipation of pore pressure, whereas all other drainage boundaries were 'closed'.

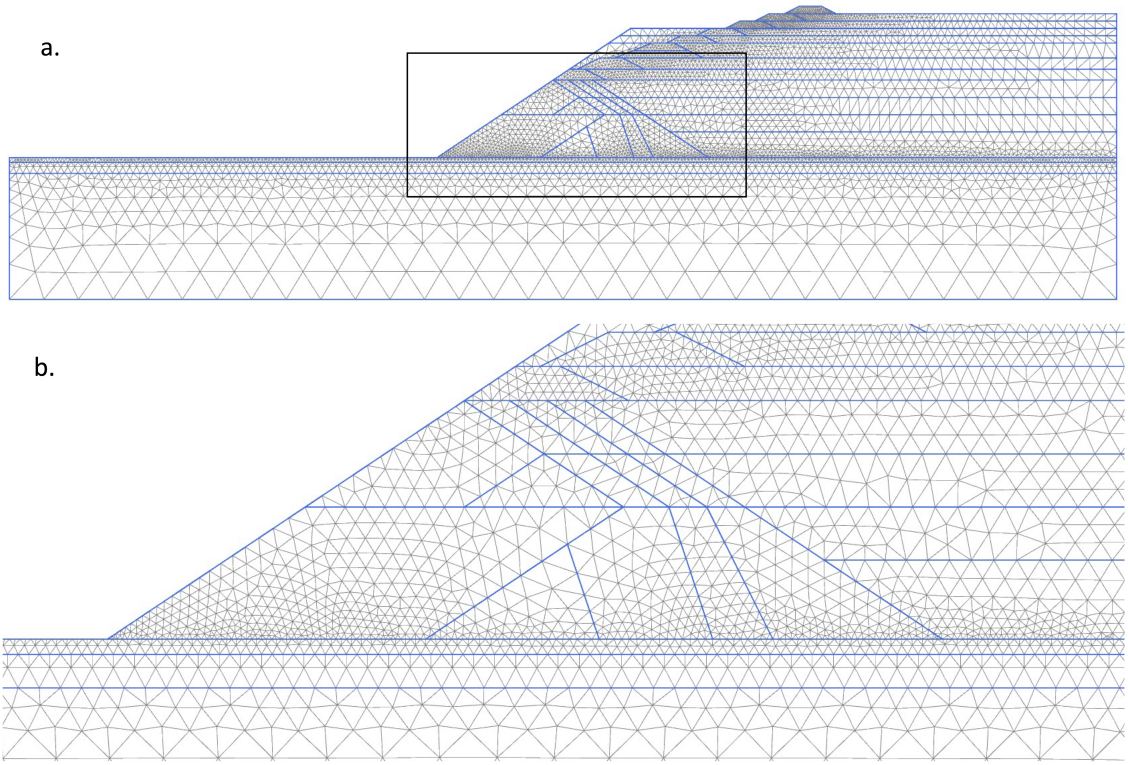

FIGURE 3.10: (a) Finite element mesh of Cadia dam, including (b) a zoomed-up image of the discretisation of FRV Unit A and FRV Unit B, and lower construction stages

3.3.3 Simulated Construction Stages

The modelled construction-consolidation cycles are summarised in Figure 3.11 and Table 3.4. While overall timelines for the individual dam stages are known, there are

uncertainties associated with the breakdown of the scheduling history into (i) dam construction, (ii) dam consolidation and (iii) tailings deposition. The number of days required for each activity typically depends on relevant design recommendations and considerations of the trade-off between dam stability and construction/deposition rates (Do et al. (2021)). Reported tailings deposition rates of ∼1.9 m/year pre-2010 and ∼2.4 m/year for post-2010, with a minimum number of 60 days for tailings consolidation before constructing the next stage (Jefferies et al. (2019)), were used to inform the modelled construction history. Water level data is not available for stages 1 to 3, so a freeboard height of 7 m was chosen based on heights in stages 4 to 10.

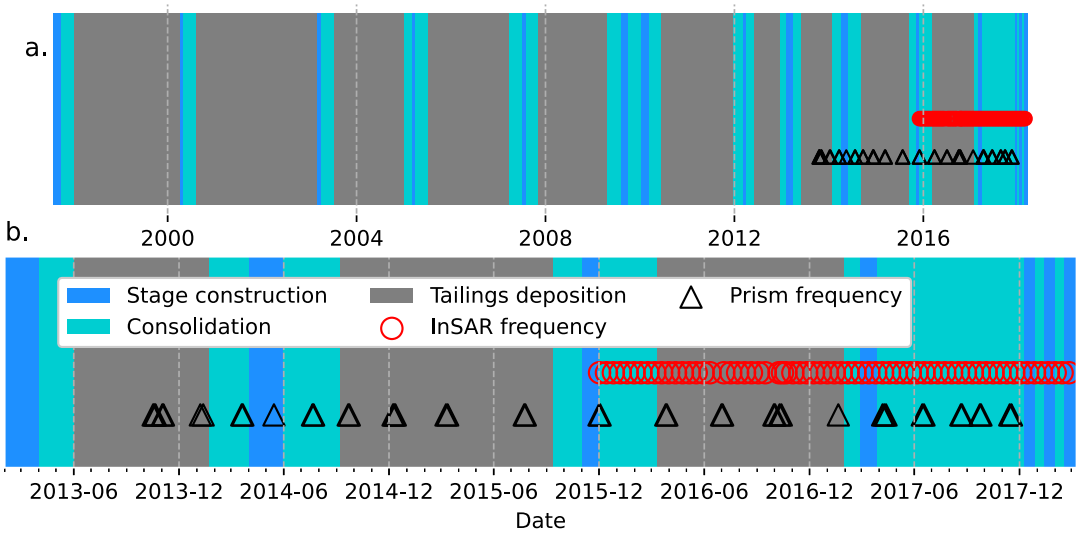

FIGURE 3.11: Schematic illustration of the modelled construction timeline including frequency of ground-based prism and InSAR monitoring: (a) Complete timeline covered by the FE modelling from 1997; (b) A more focused timeline covering recent prism and InSAR monitoring: the prisms are from 2013 and InSAR from 2015. The overlap in timelines from all data sources runs from December 2015 onwards.

This study uses a temporal approach to study the evolution of the failure. The timeline of the data is plotted in Figure 3.11. It shows that the FE modelling covers the entire period from the construction of stage 1 in 1997 through to dam failure in 2018 (in Table 3.4). The prisms were removed immediately prior to buttress construction, therefore, InSAR is the only source of measurements around the time of the failure.

TABLE 3.4: Cadia construction timeline adopted in the present FE modelling.

Stage	**Start date (YYYY-MM-DD)**	**Duration (Days)**
Stage 1 construction	1997-08-01	60
consolidation	1997-09-30	
tailings deposition	1998-01-08	
Stage 2A construction	2000-04-01	30
consolidation	2000-05-01	
tailings deposition	2000-08-09	
Stage 2B construction	2003-03-01	30
consolidation	2003-03-31	
tailings deposition	2003-07-09	
tailings deposition 2	2004-04-04	
consolidation	2004-12-31	
Stage 3 construction	2005-03-01	30
consolidation	2005-03-31	
tailings deposition	2005-07-09	
consolidation	2007-03-20	
Stage 4 construction	2007-07-01	30
consolidation	2007-07-31	
tailings deposition	2007-11-08	
consolidation	2009-04-21	
Stage 5 construction	2009-08-01	60
consolidation	2009-09-30	

Continued on next page

Table 3.4 – continued from previous page

Stage	Start date (YYYY-MM-DD)	Duration (Days)
Stage 5 construction 2	2010-01-08	60
consolidation 2	2010-03-09	
tailings deposition	2010-06-17	
consolidation	2011-12-21	
Stage 6 construction	2012-03-01	30
consolidation	2012-03-31	
tailings deposition	2012-05-30	
consolidation	2012-12-13	
Stage 7 construction	2013-02-01	60
consolidation	2013-04-02	
tailings deposition	2013-06-01	
consolidation	2014-01-21	
Stage 8 construction	2014-04-01	60
consolidation	2014-05-31	
tailings deposition	2014-09-08	
consolidation	2015-09-12	
Stage 9 construction	2015-11-01	30
consolidation	2015-12-01	
tailings deposition	2016-03-10	
consolidation	2017-01-28	
Stage 10 construction	2017-02-27	30
consolidation	2017-03-29	

Continued on next page

Table 3.4 – continued from previous page

Stage	Start date (YYYY-MM-DD)	Duration (Days)
Buttress 1A construction	2017-12-09	20
consolidation	2017-12-29	
excavation at toe	2018-01-07	
Buttress 1B construction	2018-01-12	20
consolidation	2018-02-01	
Buttress 1C construction	2018-02-15	22

3.4 Results and Discussion

3.4.1 InSAR Monitoring

The temporal development of the prism-monitored deformations within the failure zone is compared to those derived from the nearest InSAR monitoring point in Figure 3.12. The deformations are relative to the first SAR acquisition on 2015-12-02 and measurement dates are in yyyy-mm-dd format. These deformations correspond to the displacements measured on the top surface of construction stages 4, 5 and 7 (Figures 3.12(a) - 3.12(c) respectively). And the location of prisms relative to InSAR measurements over the slump area is presented in Figure 3.13. For the purpose of comparison, the InSAR measurements are plotted relative to the intercept of the prism best fit line in Figures 3.12(a) - 3.12(c). In all three cases, the InSAR monitored data show good agreement with the prism measurements thus giving confidence in the adopted post-processing of ϕ_{Displ} (equation 2.2). Further spatio-temporal comparisons are not possible given only three prism monitoring stations were located in the slump area.

A cross-section of the InSAR-monitored LOS surface deformations to the middle of the slump is presented in Figure 3.14; the cross-sectional distance corresponds to Figure 3.6. The plot reveals significant difference in the deformation behaviour across

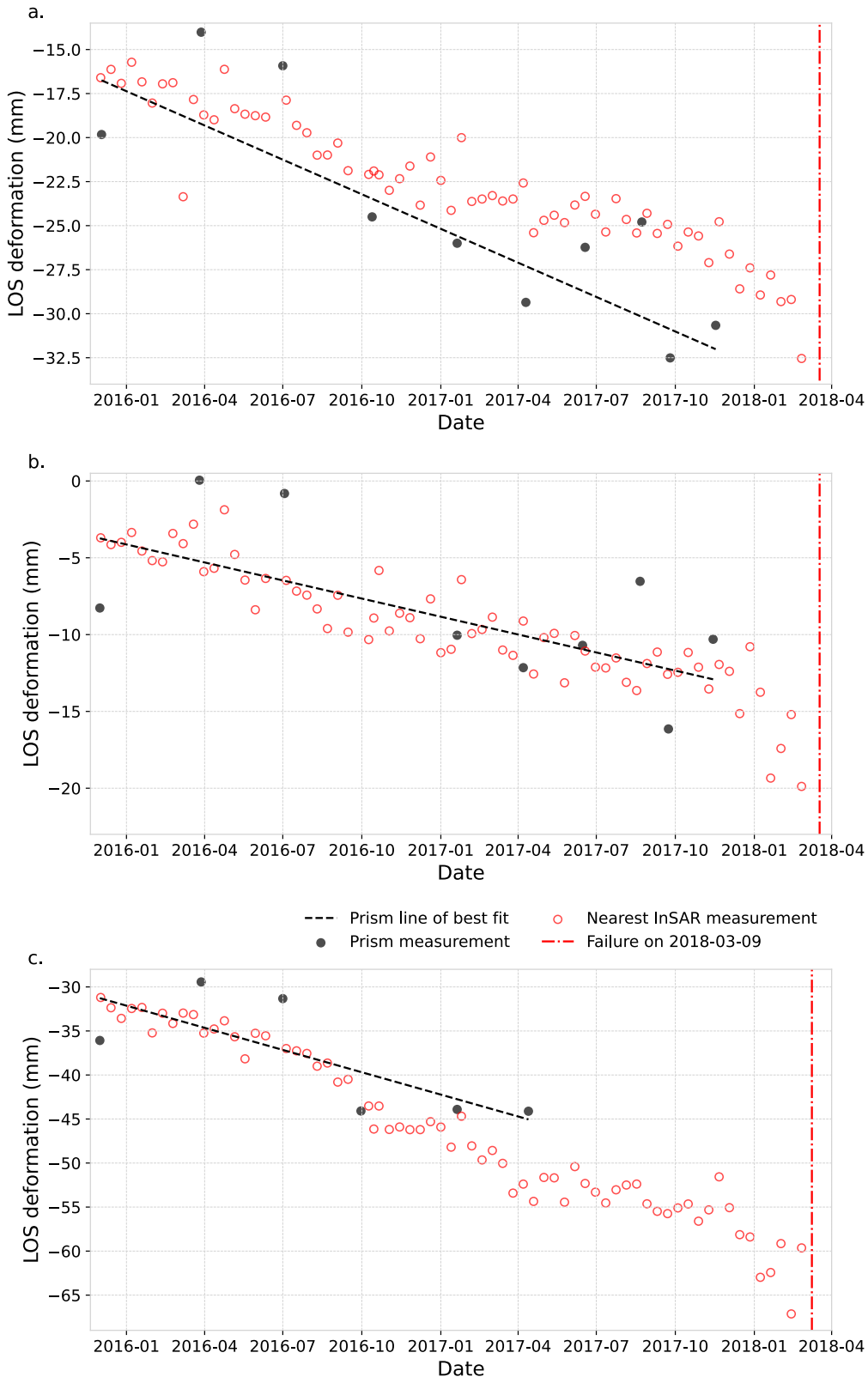

FIGURE 3.12: Comparison between InSAR-derived deformations averaged over the top surface of construction stages (a) 4, (b) 5 and (c) 7 within the failure zone compared to local ground-based prism measurements.

the dam cross-section where the upstream stages (4 - 10) experience notably greater deformations compared to the downstream stages (1-3).

The spatial and temporal variability of the dam deformation is summarised in Figure 3.15. In these plots, the deformations are spatially averaged into bins corresponding to the dam stages illustrated in Figure 3.6. For all three cross-sections, the deformation signals steadily increase with time. It can also be seen that deformations are concentrated towards the upstream side of the dam cross-section, most likely due to large parts of the dam resting directly on partially- or fully-consolidated tailings. Comparing Figures 3.15(a) - 3.15(c), there is an inherent spatial variability in the deformation detected along the failure zone; while the temporal evolution of displacements are similar, the magnitudes in the middle of the slump are notably larger.

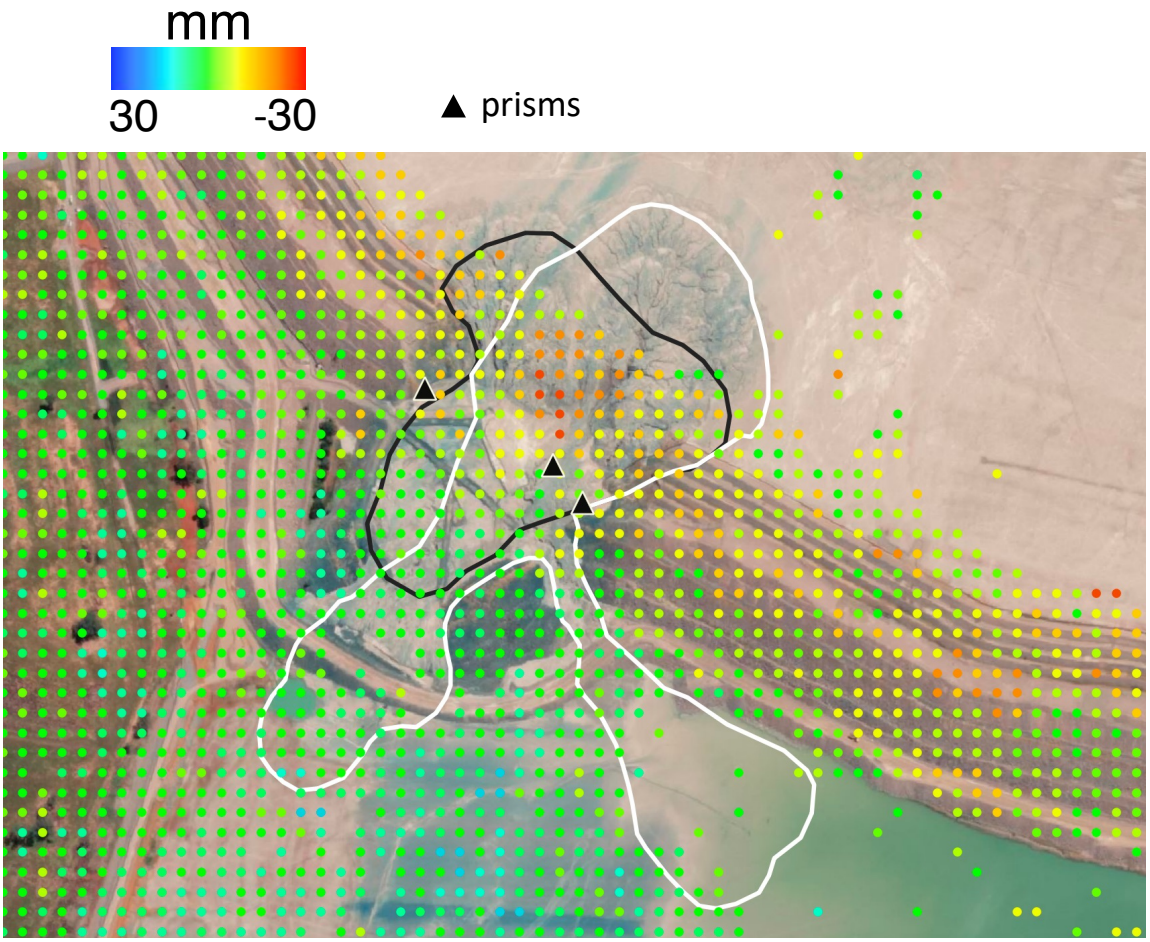

FIGURE 3.13: Location of ground-based prisms and InSAR measurements in the failure area. Spatial distribution of InSAR measurements from 2018-02-25 (YYYY-MM-DD) are plotted. The failure is outlined in black and white polygons (black predates white). Basemap image copyright ©1995-2020 Esri

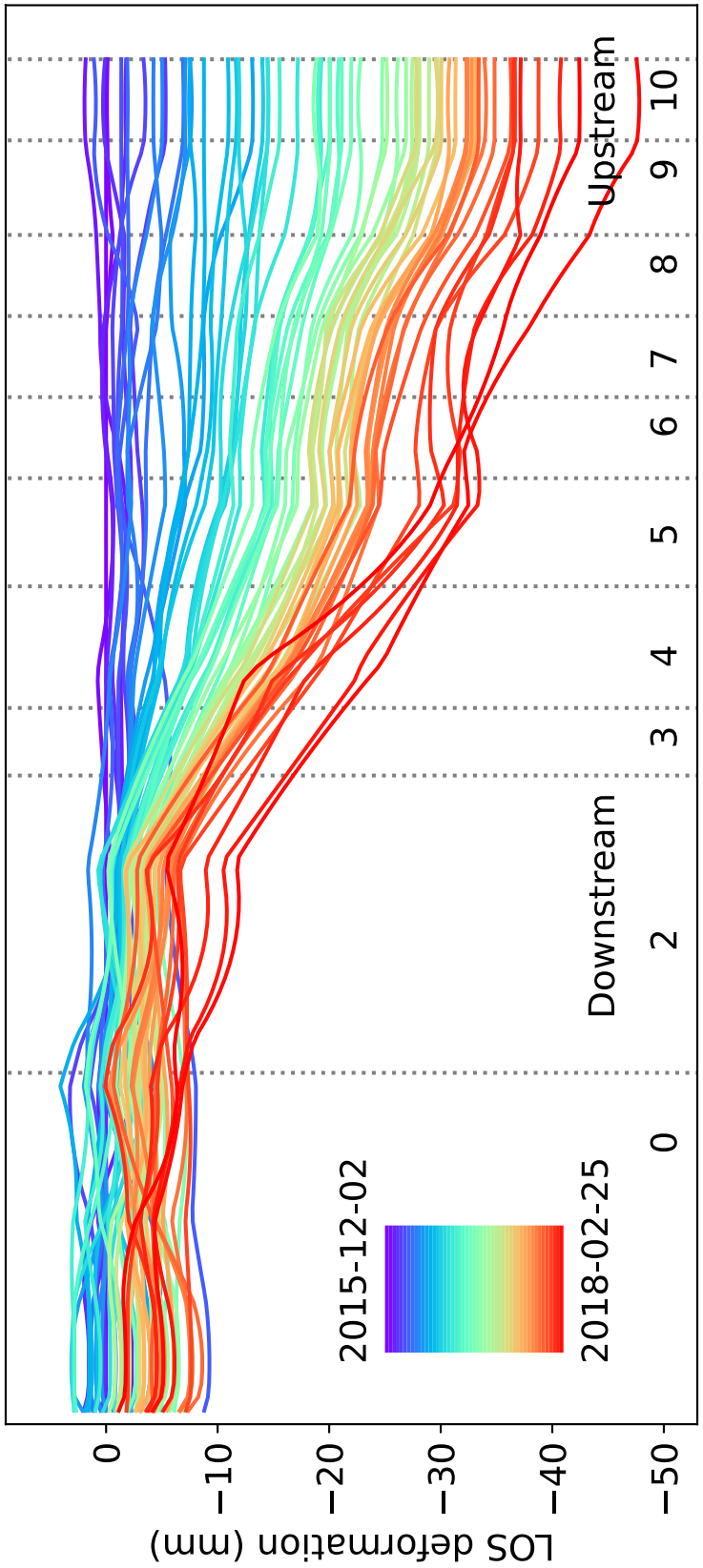

FIGURE 3.14: Cross-section of InSAR-monitored LOS surface deformations from first satellite acquisition in 2015-12-02 to 2018-02-25 located in the middle of the failure (ID 60).

To further explore the spatial variation in these displacements, InSAR deformations for the same three cross-sections have been extracted for comparison in Figure 3.16. The deformation magnitude is expected to increase towards the east (ID 63). This deformation behaviour is explained by the 'bowl-shaped' topography underneath the dam, where the initial dam (stage 1) gets thicker towards the east of the slump (Jefferies et al. (2019)). This expected deformation behaviour is observed at the downstream parts of all three cross sections. In contrast, the largest deformation magnitudes are observed in the middle of the area of eventual failure (ID 60) for the upstream parts, possibly representing early indications of collapse onset, as shown in Figures 3.16(b) and 3.16(c). Such significant and unexpected deformations were occurring one year prior to dam collapse, suggesting a strong early warning capability based on monitored ground movements.

Three-dimensional visualisations of the monitored LOS deformations are presented in Figure 3.17 corresponding to three dates: $\sim$2 years (2016-03-19; Figure 3.17(a)), $\sim$1 year (2017-04-07; Figure 3.17(b)) and $\sim$2 weeks (2018-02-25; Figure 3.17(c)) before failure. Two years prior to failure, no notable deformation signals are evident and the deformations appear consistent both longitudinally and transversely (see Figure 3.17(a)). In contrast, significant deformations are observed in Figure 3.17(b), suggesting a precursory signal of failure one year prior to failure. Differences in the upstream and downstream deformations also become more pronounced. Two weeks before failure, the slump zone can be distinguished clearly from the spatial distribution of the dam deformations (Figure 3.17(c)). Interestingly, the three-dimensional shape of the deformations immediately before failure are similar to those measured one year pre-failure except the magnitudes have been amplified. This lends further support to the hypothesis that onset of failure may be detected through monitored ground deformations.

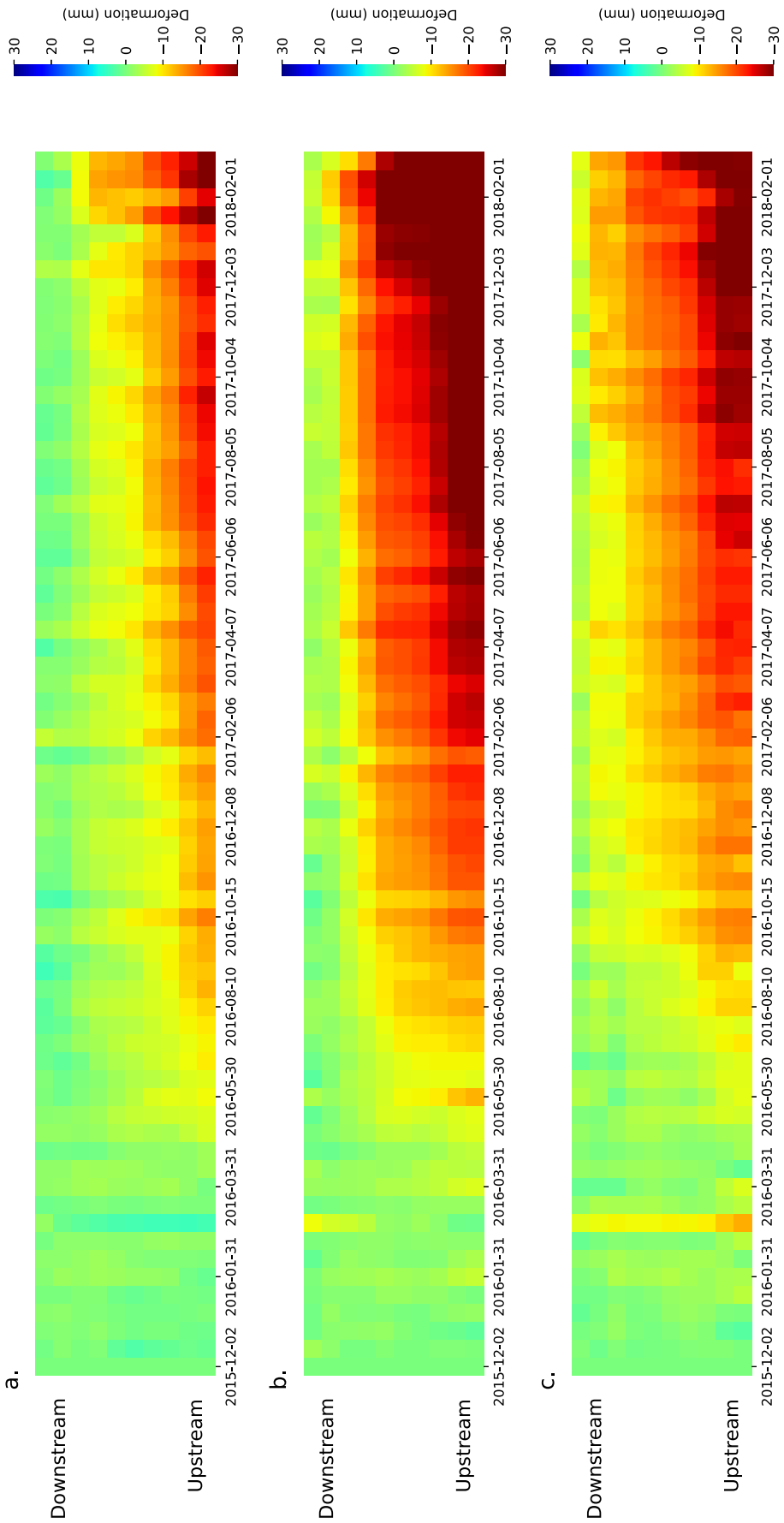

FIGURE 3.15: Visualisation of the spatial and temporal variability of the InSAR-derived LOS deformations for three different cross section chainage (IDs): (a) to the west of the slump (ID 51); (b) in the middle of the failure area (ID 60); (c) to the east of the slump (ID 63)

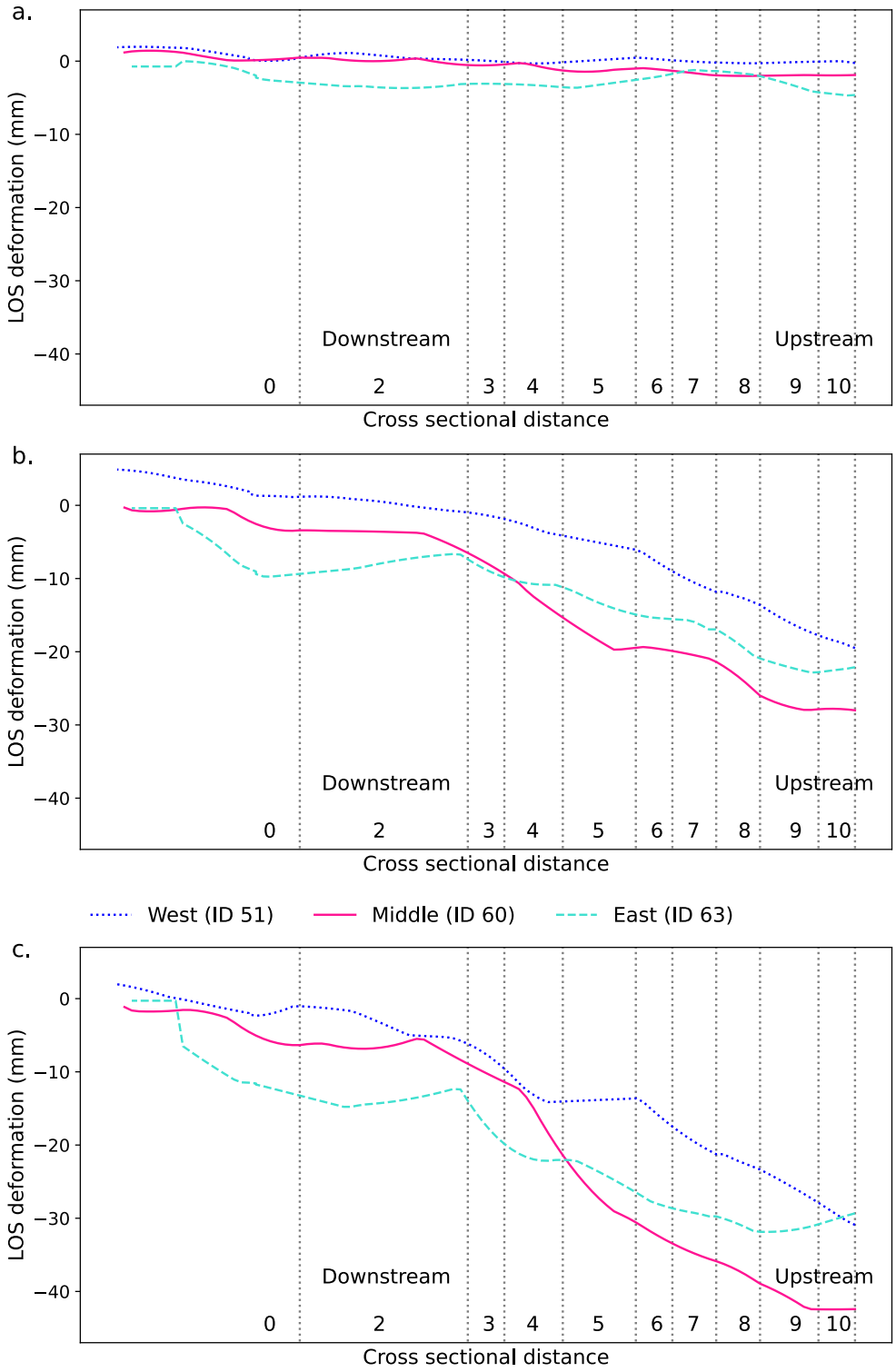

FIGURE 3.16: Comparison of InSAR cross sections at three different dates: (a) 2016-03-19 (∼2 years before failure); (b) 2017-04-07 (∼1 year before failure); (c) 2018-02-25 (∼2 weeks before failure). Cross sections are located to the West, middle and East of the failure, ID 51, ID 60 and ID 63, respectively.

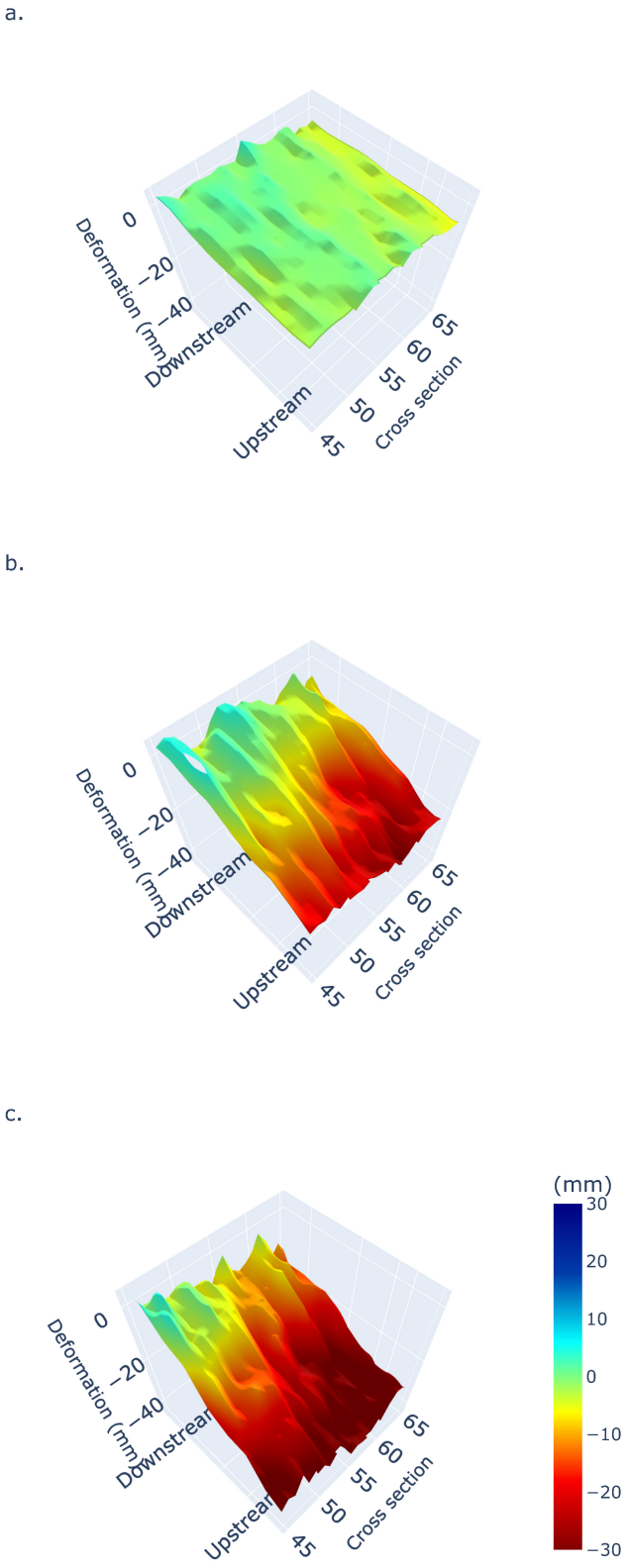

FIGURE 3.17: Three-dimensional view of the spatial distribution of InSAR-derived ground deformations for Cadia dam at three different dates: (a) 2016-03-19 (∼2 years before failure); (b) 2017-04-07 (∼1 year before failure); (c) 2018-02-25 (∼2 weeks before failure).

3.4.2 Comparison of FE predictions to Monitored Data

FE calculated LOS deformations are compared to the ground-based prism measurements as well as the nearest available InSAR measurements in Figure 3.18. FE calculations are in very good agreement with both InSAR and prism measurements until the beginning of the buttress constructions. These settlements are caused by dam stage construction and subsequent consolidation phases which appear to be well-captured by the present FE model. While the FE calculations show good agreement with the InSAR and prism data during buttress construction for stage 7, there are notable deviations between displacements for stages 4 and 5 (see Figures 3.18(a) and 3.18(b) respectively). The significant displacements predicted by the FE model for these two stages may be attributable to the buttresses being constructed on top of stages 4 and 5 but not on stage 7 (for dam configuration see Figure 3.7).

As prism measurements were only available for three points in the slump area of the dam (stages 4, 5 and 7), FE calculations of the deformations for the remaining stages are compared to the InSAR measurements only. Figure 3.19 plots the spatial variation of $\delta_{InSAR} - \delta_{FE}$ which have been binned according to both dam stage and cross-sectional chainage (see Figure 3.6) where δ_{InSAR} and δ_{FE} are the InSAR monitored and FE calculated deformation in mm. The InSAR monitored and FE calculated deformations (δ_{InSAR} and δ_{FE}, respectively) are geometrically transformed to the LOS direction. Figure 3.19 shows the difference in FE and InSAR results around the slump area. The results agree with up to 2mm difference for most of the dam stages for cross sectional chainage ID 55, with some deviation towards the edges of the slump. The difference increases to 4.8mm for the upstream stages 4 and 5 in the eastern parts of the slump - towards cross sectional chainage ID 61. Although this difference is negligible towards the western parts of the slump (towards ID 51), the deformation at stage 2 increases by $\sim$3mm. Most notably, there are significant differences between modelled and measured deformation in the upstream stages 9 and 10 for all cross sections.

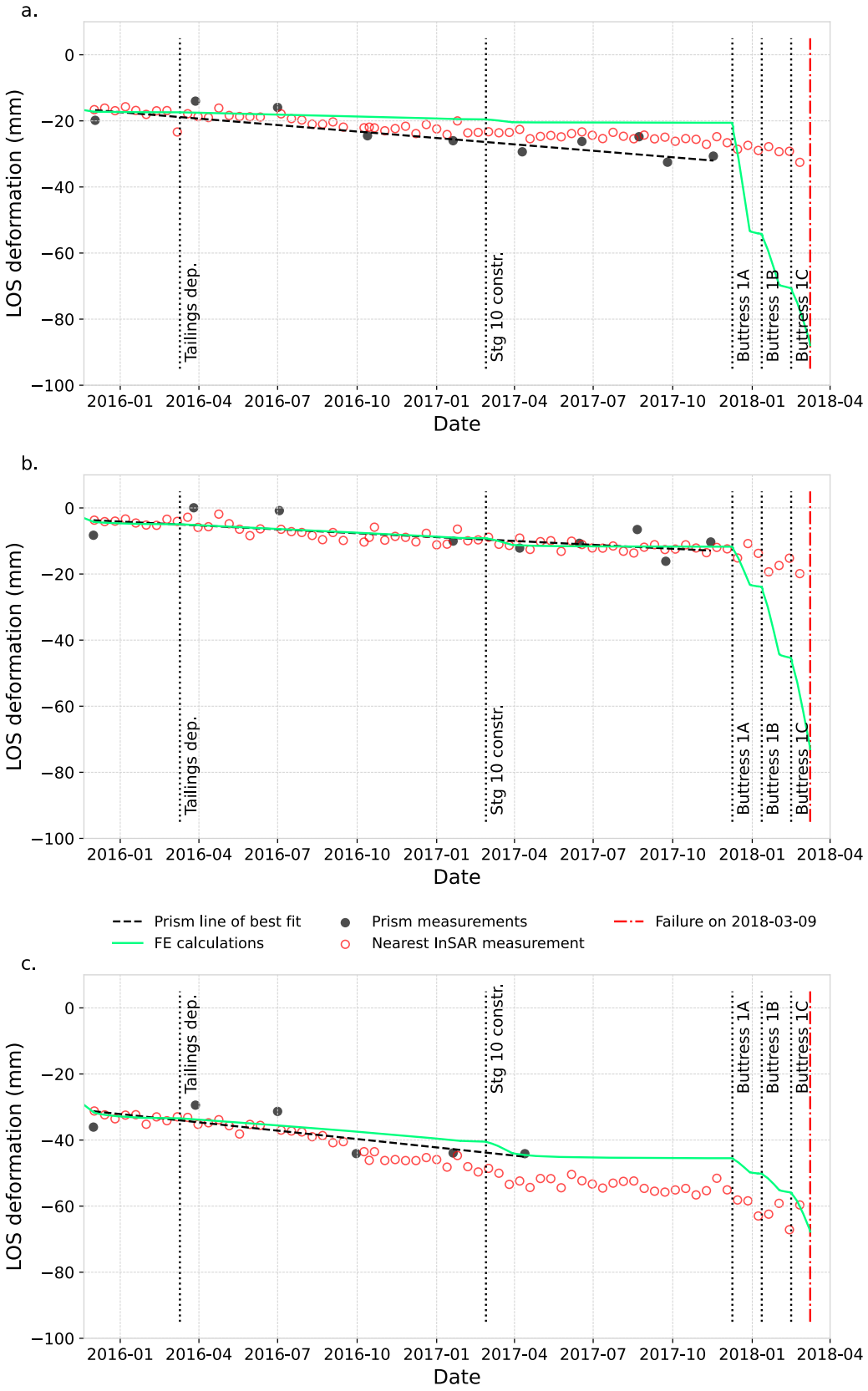

FIGURE 3.18: Time series comparison of FE calculations with nearby prism and InSAR measurements of construction stages (a) 4, (b) 5, and (c) 7. Cross-section location ID 60. Abbreviations: 'dep.' for deposition, 'Stg 10 constr.' refers to stage 10 construction.

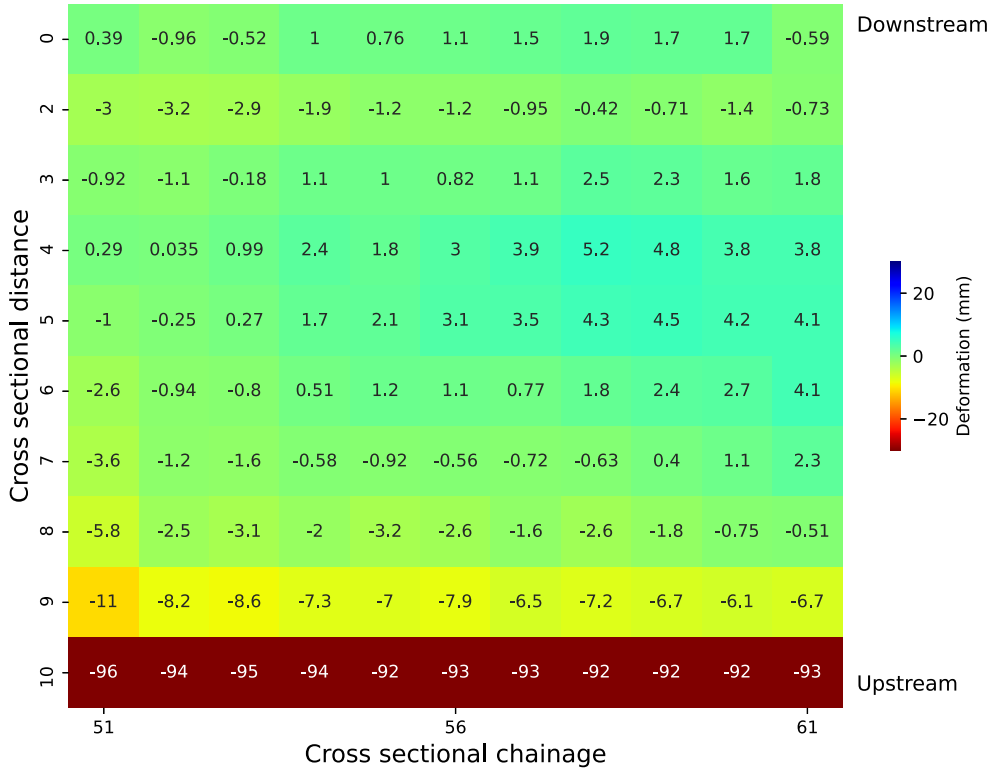

FIGURE 3.19: Averaged difference in deformation between FE calculations and InSAR measurements at stage 10 consolidation. Given the FE model is based on the slump area, the cross sectional chainage have been limited to ID 51 to 61. Positive values indicate FE over-prediction of the measured response.

The significant deviations between the InSAR measurements and the FE model are likely due to the inherent limitations of InSAR in detecting 'fast' movements. InSAR is more suitable for long term deformation detection, with its theoretical limitations corresponding to a quarter of its wavelength (Section 3.2). This means, for Sentinel-1 InSAR measurements, the maximum measurable deformation in the 12-day revisit time is 28mm. Stages 9 and 10 have been constructed within the same time frame as the InSAR data. It is therefore probable that the differences in deformation as illustrated in Figure 3.19, are due to the consolidation settlement following stage construction exceeding this limit. Similarly, the significant differences observed in Figures 3.18(a) and 3.18(b) are likely due to the large deformation experienced from the buttresses located on top of stages 4 and 5. The buttresses are not located on top of stage 7, therefore, the magnitude of the deformation is much less as shown in Figure 3.18(c). Differences between the measured and modelled deformation may also be partly attributable to the smoothing of measurements inherent in the adopted InSAR approach (Sowter et al.

(2013)). In particular, the ISBAS algorithm detects deformation from multiple smaller scatterers within a resolution cell and interpolates neighbouring cells to derive the deformation measurement.

FE calculated incremental displacements at the end of construction of the final dam section (stage 10) are presented in Figure 3.20. These results highlight the important influence of the tailings on the deformation behaviour of the dam: upstream construction stages experience significantly greater settlements owing to the fact that they rest primarily on the tailings. Given the typically significant uncertainty associated with the mechanical properties of dam tailings, and their development during consolidation, forecasting the behaviour of upstream tailings dams using numerical modelling techniques is challenging. This is evidenced by the incremental displacements before and after the consolidation period of stage 10 construction shown in Figures 3.20(a) and 3.20(b) respectively. Immediately after construction of stage 10, the resulting (undrained) soil displacements are concentrated directly beneath the stage. As consolidation progresses, soil settlements are focused towards the upstream of the dam due to continued consolidation of the last tailings deposition as well as the downstream toe of the dam, as shown in Figure 3.20(b).

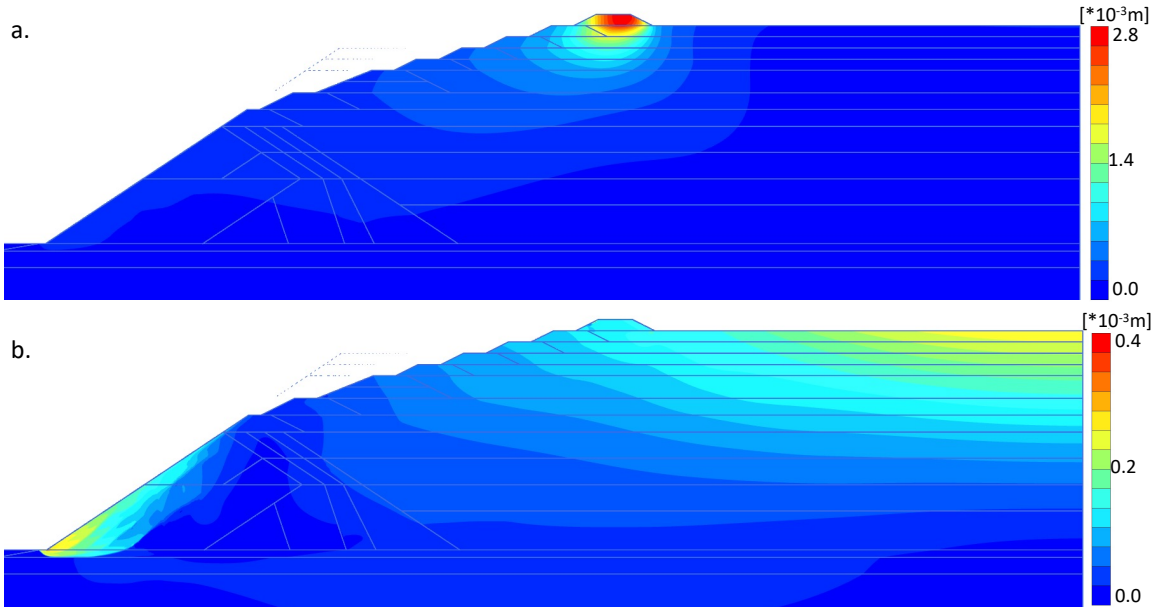

FIGURE 3.20: FE calculations of the deformation behaviour of Cadia dam. (a) Incremental displacement after stage 10 construction and (b) Incremental displacements after stage 10 consolidation.

The impact of later upstream dam stages on the downstream toe is most clear in

the incremental shear strain plotted in Figure 3.21 (a). This figure plots the development of incremental Cartesian strain within the FRV Unit A layer beneath the dam, which supports the conclusions of the ITRB analysis presented in Jefferies et al. (2019). The ITRB analysis attributes primary failure mechanism of Cadia TSF to the onset of strain weakening in FRV Unit A, as illustrated in Figure 3.21 (b). These conclusions are based on a series of 2D and 3D numerical analysis, which compare the likelihood of three potential scenarios: progressive foundation failure of FRV Unit A, rising ground water pressure, and external shock from earthquake related seismic triggering of liquefaction. The 3D numerical analysis of the ITRB are further discussed within the context of anomalous InSAR deformation in Chapter 6 (Figure 6.9).

In evaluating potential failure mechanisms, the ITRB also compare modelling results to observations, including InSAR measurements. However, they do not conduct a quantitative comparison between geotechnical and InSAR results. Instead, these datasets are plotted on separate axis, and the comparison is limited to a qualitative assessment of their trends. Therefore, the main contribution of this chapter to the findings of the ITRB lies in the demonstration of a framework for quantitatively comparing InSAR measurements with geotechnical modelling and prism measurements, as examined in Figures 3.18 (a) and 3.18 (b).

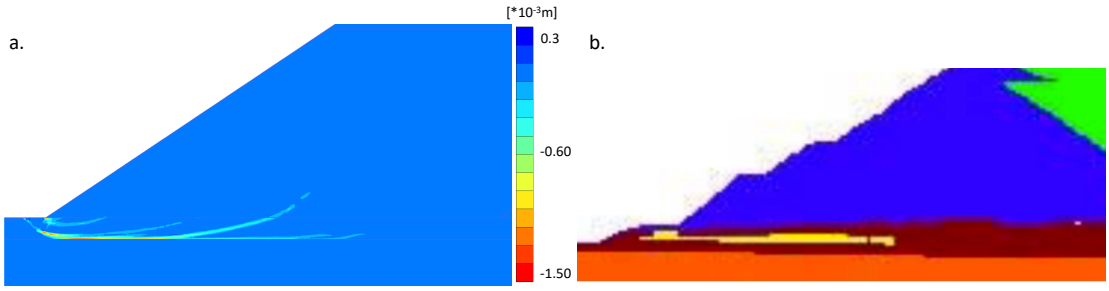

FIGURE 3.21: Development of strain weakening in FRV Unit A at the end of stage 10 consolidation. (a) Incremental Cartesian strain plotted from FE model developed in this thesis. (b) Screenshot of the strain weakening (shown as yellow zone) as reported in Jefferies et al. (2019).

3.4.3 Influence of FRV Unit A

The 'true' parameters of FRV Unit A, such as the thickness and consequently the back-calculated OCR, is uncertain as noted in Jefferies et al. (2019). In the preceding analyses, a best-estimate thickness of 2 m has been adopted. Figure 3.22 plot the total

surface deformations at the end of stage 10 consolidation resulting from varying the thickness of FRV Unit A. The vertical and horizontal components of the deformation are plotted in Figure 3.22(a) and (b), respectively. There is divergence in both the horizontal and vertical deformations in the downstream parts. However, the deformation of the upstream parts are largely similar in magnitude and are dominated by vertical deformation for all models.

To isolate the influence of stage 10 construction and subsequent consolidation on these results, the LOS deformation relative to the previous construction, stage 9 consolidation are presented in Figure 3.22(c). The deformation in both the downstream and upstream sections increase for thicker FRV Unit A. This supports the hypothesis that a change in the foundation properties in the slump area can result in the anomalous deformation signals measured from InSAR in Figures 3.15 - 3.17. Moreover, there is a heave or an uplift at the downstream toe and the deformations in the downstream sections are increased by up to ∼20mm, which is an order of magnitude greater than the change in the upstream sections (stage 4 onwards). This illustrates the significant influence the foundation properties have on the deformation behaviour of the downstream sections, compared to the smaller impact on the upstream sections. It also implies that the prisms, which were located on the upstream parts of the dam, are potentially less sensitive for detecting foundation issues. This provides a powerful recommendation for monitoring plans and requires further investigation of parameter sensitivity.

A rigorous geotechnical experimentation and soil parameter optimisation are beyond the scope of this thesis. Nevertheless, the effects of variations in the element mesh coarseness of the finite element model and tailings' compressibility are presented in Figures 3.23 and 3.24, respectively. The thicker FRV Unit A of 3m is used to demonstrate the influence of mesh coarseness on TSF deformation in Figure 3.23. The coarseness of the mesh size FRV Unit A is increased to 0.07 (blue), so that the density of the mesh in this layer is no longer made up of at least four layers of elements. The other mesh parameters are kept the same as those adopted in Table 3.3. As anticipated, a change in FRV Unit A mesh size has similar effect as the changes in the FRV Unit A thickness explored in Figure 3.22, with greater impact on the deformation of the downstream parts of the TSF than the upstream.

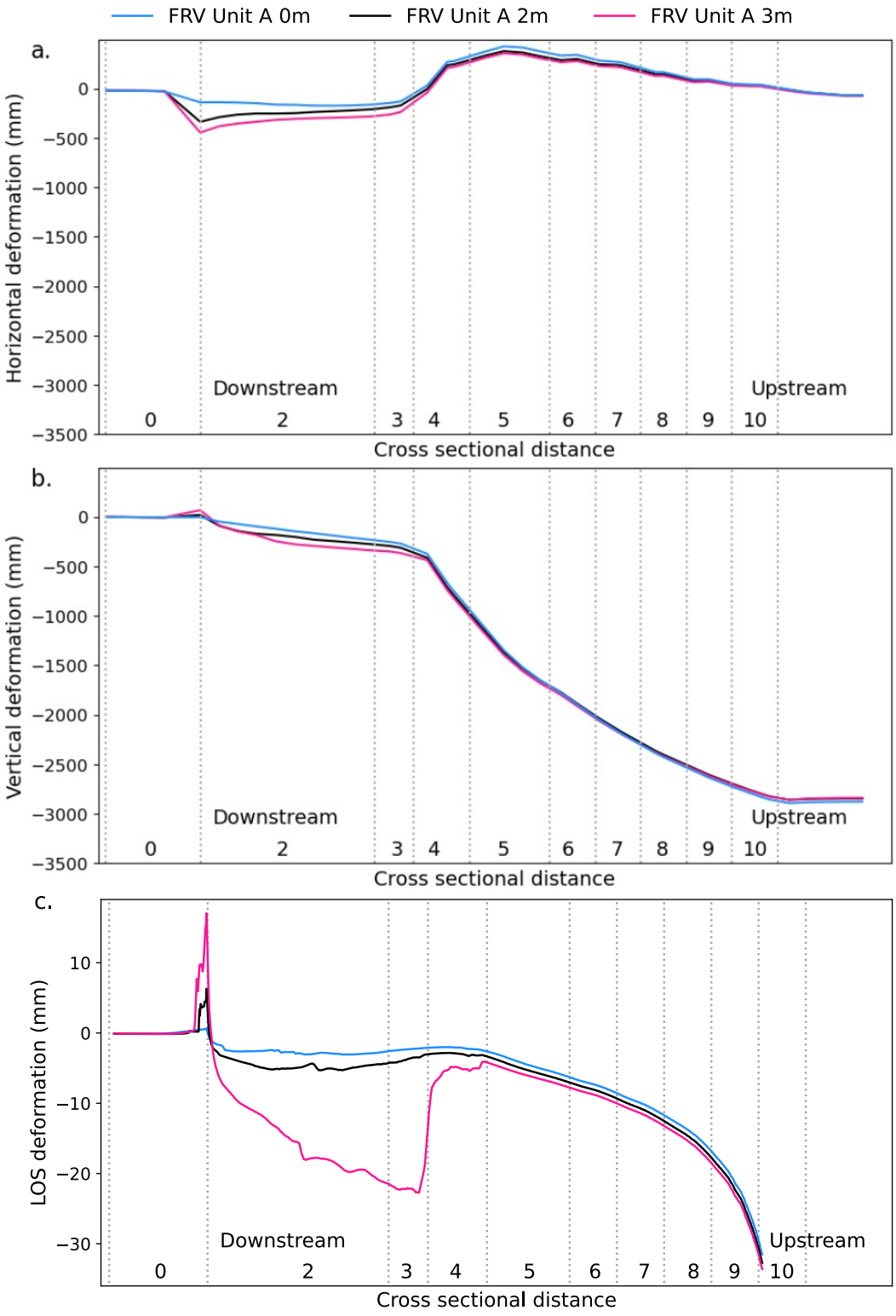

FIGURE 3.22: Influence of FRV Unit A parameters. (a) Total horizontal and (b) vertical deformation at the end of stage 10 consolidation for the entire duration of dam construction starting at stage 1. (c) The LOS deformation at the end of the stage 10 consolidation relative to stage 9 consolidation - within the same time scale as monitoring.

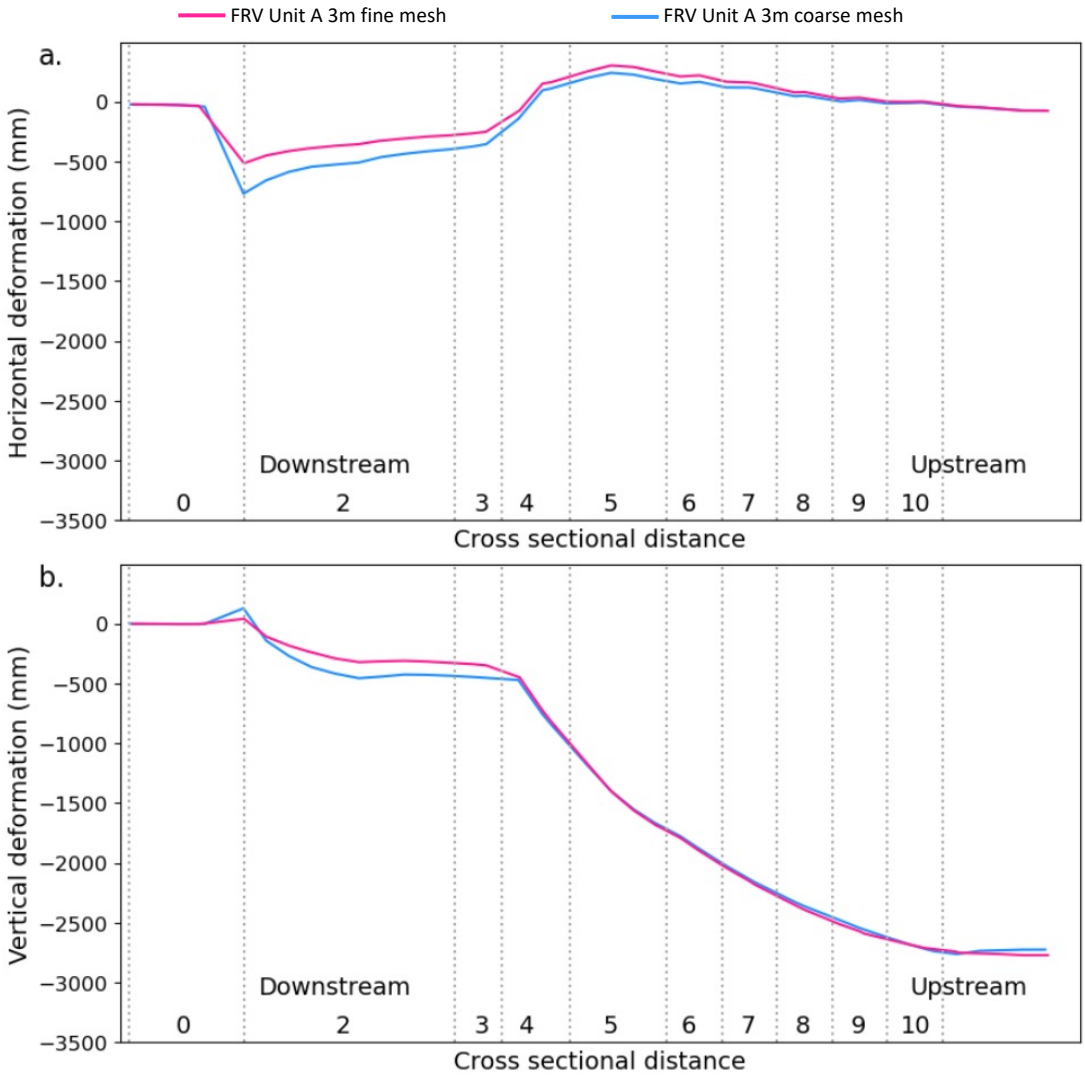

FIGURE 3.23: A thicker FRV Unit A of 3m is employed to demonstrate the influence of mesh size on resulting deformation.

Finally, to explore the impact of changing tailings properties on resulting deformation, the MCC compression index of the tailings parameters listed in Table 3.2 is adjusted by $\pm$ 0.002 and are illustrated in Figures 3.24 (a) and 3.24 (b). As expected, the compressibility of tailings has highest impact on the upstream parts of the TSF, as shown in Figure 3.24 (b). This is because more compressible tailings (pink) lead to greater deformation magnitudes in the upstream parts of the TSF, where thick layers of tailings are present compared to the downstream. Moreover, the effects of tailings compressibility on the horizontal deformation is considerably smaller for both downstream and upstream parts of the TSF, as shown in Figure 3.24 (a).

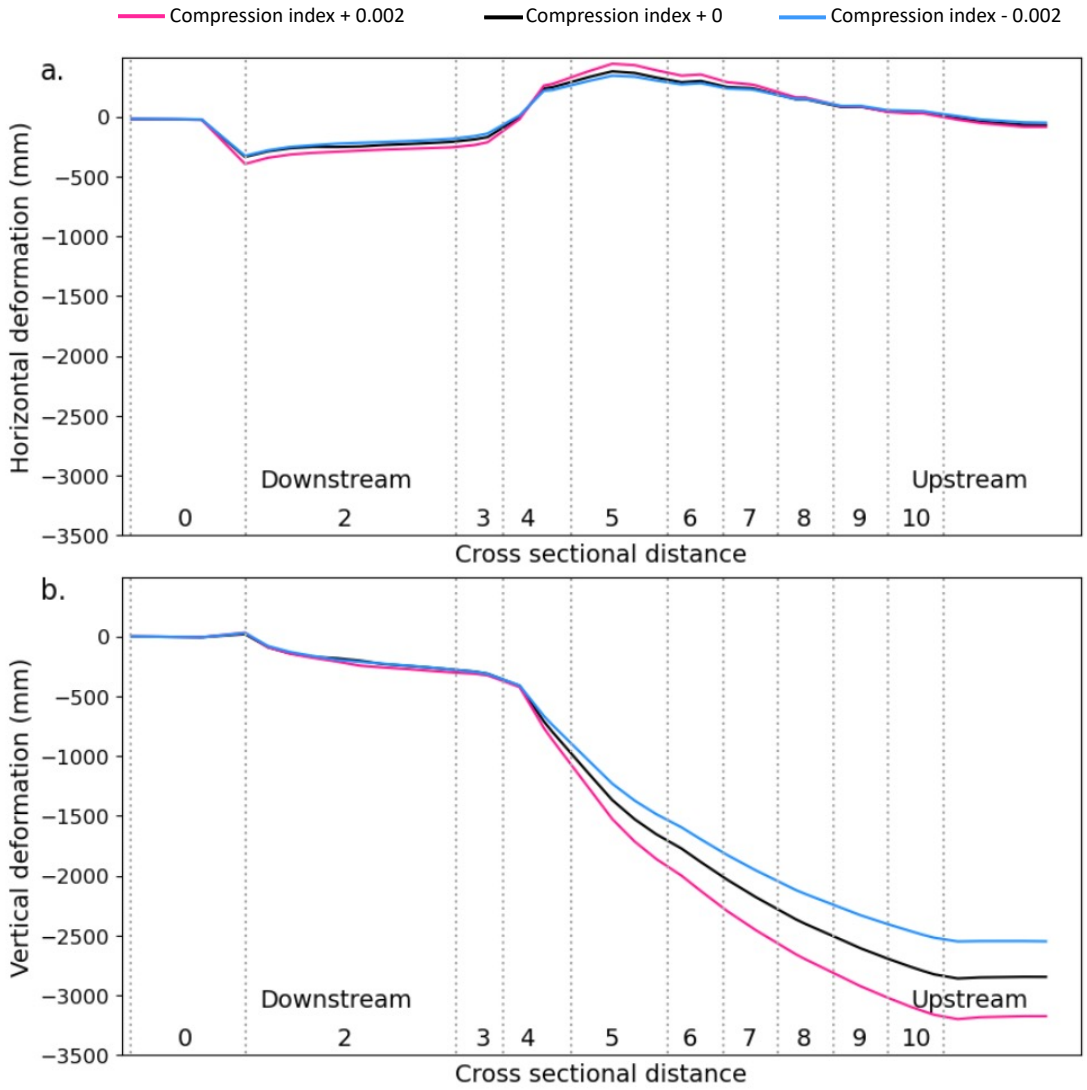

FIGURE 3.24: Influence of tailings' compressibility on TSF deformation. The MCC compression index adopted in Table 3.2 have been varied by $\pm$ 0.002 for the tailings.

3.5 Summary

This chapter has described an investigation of a failed tailings dam from a combined ground-based prism, satellite InSAR monitoring and numerical modelling approaches. Through comparisons to prism monitoring, InSAR was shown to provide reliable measurements of the temporal development of ground deformations for tailings dams. The InSAR monitoring also revealed the existence of important and complex spatial and temporal variability of the dam deformations which were not captured by the traditional point-based prism monitoring. These results revealed anomalous deformation trends up to one year preceding the dam failure which are inconsistent with

expected consolidation settlements of the dam. This suggests there is potentially ample time to trigger early warning alerts on the basis of InSAR monitored data for tailings dams.

Coupled-consolidation analyses and plane strain conditions were used to explore the behaviour of a 2D section of the dam during various construction stages. The widely adopted modified Cam clay constitutive model was employed to simulate the behaviour of key cohesive soil units. The FE calculations were shown to be in broad agreement with both the InSAR and prism monitored data, both in terms of deformation magnitudes and the trends preceding failure. Moreover, the FE model was shown to be sensitive to input uncertainties, particularly in relation to the thickness of the underlying FRV Unit A. A change in the FRV Unit A thickness has an influence on the deformation of both the downstream and upstream parts of the dam. However, its impact is significantly greater on the lower construction stages concentrated more downstream compared to the higher upstream stages. This is because the upstream stages rest primarily on tailings, and are therefore dominated by the behaviour of the dam tailings. The results support the possibility of detecting potential foundation-related stability issues in tailings dams from InSAR.

Chapter 4

Feasibility of Early Warning

A novel, data-driven approach for detecting 'dangerous' InSAR deformation signals is proposed in this chapter. The feasibility of using remote sensing derived data to provide early warning of TSF failure is explored. Due to time-dependent settlement processes (i.e. consolidation) inherent to the tailings, a certain level of deformation rate is expected and indeed 'normal'. The discussion in Chapter 3 reveals that deformation experienced in one part of the TSF might be very different depending on the location and time. Therefore, an early warning system is tasked with deciding whether a deformation at a particular location and date is as expected (i.e. 'normal') or anomalous.

In this chapter, a novel methodology for detecting anomalous InSAR deformation based on the use of Embedded Entities within a Deep Learning framework (EE-DL) is proposed. Embeddings are similar to the 'word vectors' used in natural language processing, providing a rich numerical representation of categorical variables. A variety of EE-DL applications have recently emerged, from predicting the final destinations using embeddings of taxi rides (De Brébisson et al. (2015)) to projecting sales using embeddings from stores (Guo and Berkhahn (2016) and Howard and Gugger (2020a)) and the fusing of data from different modalities based on shared embeddings (Girdhar et al. (2023)). In this study, embeddings were created to represent the categorical variables of the InSAR metadata. The use of embeddings captures both the spatial and temporal components of the InSAR measurements, without requiring the generation of image data. This makes the model more flexible and overcomes typical DL challenges around the handling of the inherent spatial data gaps present in InSAR. The advantages and limitations of other DL approaches are explored in Chapter 2.2.

Moreover, the EE-DL model is benchmarked using the results of a common probabilistic forecasting approach, namely Gaussian Process Regression (GPR) and a simple baseline Random Forest (RF) model. These models are chosen due to their highly interpretable nature and the fact that they represent a spectrum of model complexity. RF is a widely adopted benchmark and is a highly flexible shallow machine learning algorithm. Finally, the performance of the EE-DL algorithm for identifying anomalous deformation behaviour is illustrated using the failed Cadia TSF as a case study.

4.1 Data and Software

In this chapter, the ISBAS data described in Chapter 3 is employed. The across-dam temporal behaviour of the Cadia TSFs is illustrated in Figures 4.1(a) and 4.1(b) for the failed north TSF and stable south TSF, respectively, where "downstream" indicates towards the toe of the dam. In these figures, both failed and stable TSFs experience significantly higher deformations in the upstream compared to the downstream parts of the TSFs. These are due to the underlying thicker tailings towards the upstream, as demonstrated in Chapter 3. These figures also demonstrate the complexity of the deformation behaviour, with what is considered 'normal' for both TSFs changing based on their location in space and time.

Depending on the type of InSAR processing, a variety of attributes may describe the ground deformation measurements. The dependent variable, deformation, is predicted using the other attributes of the InSAR metadata: the date, the geographical coordinates (latitude and longitude), and the coherence of the measurements. Coherence serves as an indicator of the quality of InSAR data, where higher coherence corresponds to greater accuracy in the deformation signals. Moreover, it is possible to extract additional attributes such as the velocity or acceleration from InSAR data. However, it is essential to emphasise that, in the context of this study, which primarily focused on identifying anomalous deformations leading up to TSF failure, the importance should be placed on the actual deformation signal observed at each specific time instance (i.e., LOS deformation), rather than relying on the average deformation rate. While attributes such as the deformation rate might hold value in different scenarios,

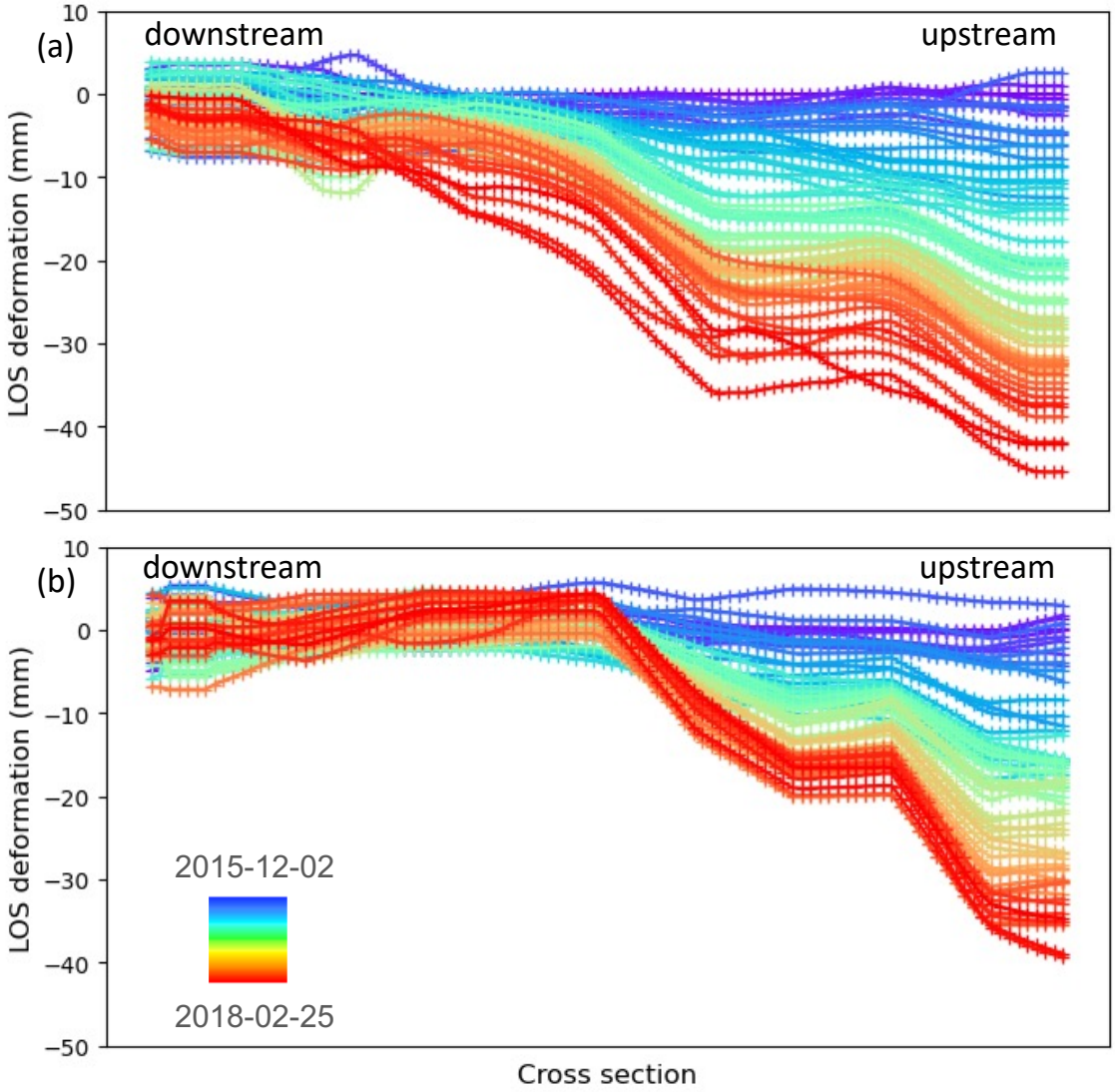

FIGURE 4.1: Indicative across-TSF temporal plot of InSAR Line-Of-Sight (LOS) deformation: (**a**) NTSF slump area and (**b**) stable south TSF. Downstream indicates the location of the dam toe, and upstream indicates the direction towards the deposited tailings.

considering the specific goal of this research, LOS deformation may serve as a more-direct and -sensitive metric. The deep learning training was implemented using the abstraction library FastAI (Howard and Gugger (2020b)) and the PyTorch framework (Paszke et al. (2019)). The Gaussian Process Regression was implemented in GPyTorch (J. Gardner et al. (2018)).

4.2 Methods

A common feature-engineering approach was applied to the date variable of the InSAR metadata before ingesting into the EE-DL and RF approaches (Howard and Gugger (2020b)). Instead of representing the date as a string such as "2023-05-22", it was expanded with other representative columns to enrich and assist the machine learning model. The date column was expanded into 13 other columns, such as the day, year, day of the week, and number of days elapsed since 1970. These were then calculated for each date of the InSAR measurement and were used as the input into the model.

The redundancy and importance of each of these InSAR metadata features were evaluated using a simple RF model. Figure 4.2 plots the relative importance of each of the features predicting deformation using all data points on the full temporal domain. For example, the top-three variables were the location of the measurement as described by the latitude ("x_lat"), longitude ("x_lon"), and the "elapsed" variable, which summarises each date as the number of days elapsed since 1970. The RF hyper-parameters are specified in Table 4.1. The most-important features were then used as guidance for choosing the variables to be taken forward into the EE-DL approach: latitude, longitude, elapsed, coherence, year, month, and day. The performance of the various approaches was evaluated using the Root-Mean-Squared Error (RMSE), which is described by Equation (4.1), where x_i and $\hat{x}_i$ are the measured and predicted deformations, respectively, for variable i, where N is the number of measurements.

$$RMSE = \sqrt{\Sigma_{i=1}^{N} \frac{(x_i - \hat{x}_i)^2}{N}} \tag{4.1}$$

TABLE 4.1: Random Forest hyper-parameter setup.

Random Forest	
n_estimators	40
max_samples	200,000
min_samples_leaf	5
max_features	0.5

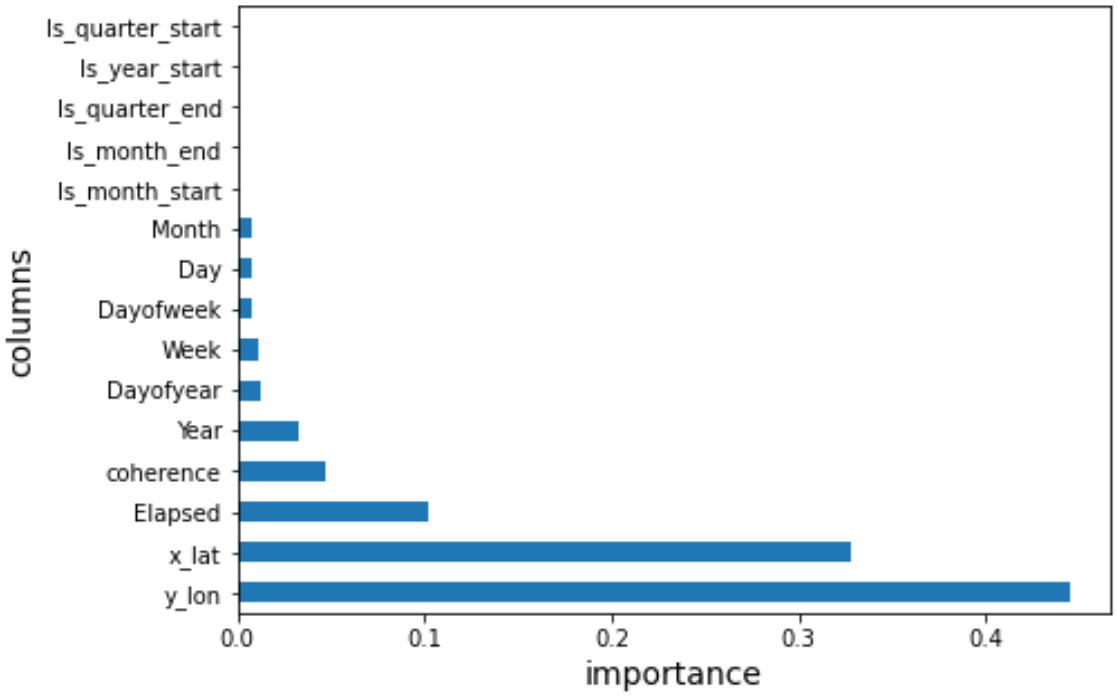

FIGURE 4.2: The importance of each InSAR metadata feature in predicting deformation, as determined by the Random Forest model.

4.2.1 Embeddings of InSAR Metadata

Embeddings capture both the spatial and temporal components of the InSAR measurements. A sequence of random numbers are assigned to each category of the InSAR metadata, also known as latent factors. The word "embedding" refers to the computational shortcut that links the particular entity in the InSAR metadata to its latent factors. These randomly initialised latent factors are then modified by the DL workflow for the prediction of deformation. Therefore, the latent factors capture the relationships between different categories.

Based on preliminary experiments, the best performance was obtained by treating all the InSAR metadata as categorical variables. The one variable that should not be treated as categorical is "elapsed". By definition, a categorical variable cannot extrapolate outside its defined range of values. Therefore, by setting "elapsed" as a continuous variable, the model is able to predict deformation values in the future. Therefore, embeddings will not be created for the continuous variable "elapsed". The entities chosen as categorical variables from the InSAR metadata are in Table 4.2. The cardinality is the number of unique categories representing each entity, for example the

cardinality of "Month" is 12. The embedding size is the number of values (i.e., vectors) representing each of the entities, so that entities with higher cardinality are captured by larger embeddings to help capture subtle non-linearities. The experiments on the embedding size have been conducted within various deep learning frameworks, which is based on some fraction of the cardinality. For example, Google/TensorFlow have adopted an embedding size of $\epsilon^{0.25}$, where ϵ is the cardinality (Blog (2017)). In this study, the embedding size proposed in FastAI/ Howard and Gugger (2020a) is adopted, where the embedding size equals $1.6\epsilon^{0.52}$.

TABLE 4.2: The embedding size is calculated based on the size of the cardinality of the entities. The cardinality is the number of unique categories representing each entity.

Entity	Cardinality	Embedding Size
Coherence	1016	77
Longitude	248	35
Latitude	205	32
Day	30	11
Month	12	6
Year	4	3

4.2.2 Fully Connected DL Architecture

A simple, fully connected neural network performed the best with embedded entities in the Kaggle-winning model (De Brébisson et al. (2015)). That model outperformed more-complex approaches, including recurrent neural networks and their variants. Therefore, for simplicity, fully connected architectures were adopted for training the InSAR embeddings. Figure 4.3 illustrates the fully connected architecture adopted for this study. This model has ten hidden layers, with each layer made up of *Linear–ReLU–Batch Norm–Dropout* layers. The first hidden layer starts with 1100 neurons, and in each subsequent hidden layer, the number of neurons reduces by 100. The hidden layer structure and the neuron size ratio are similar to the fully connected architecture adopted for training embeddings in Guo and Berkhahn (2016) and Howard and Gugger (2020a). The output layer is a linear layer with a sigmoid activation function.

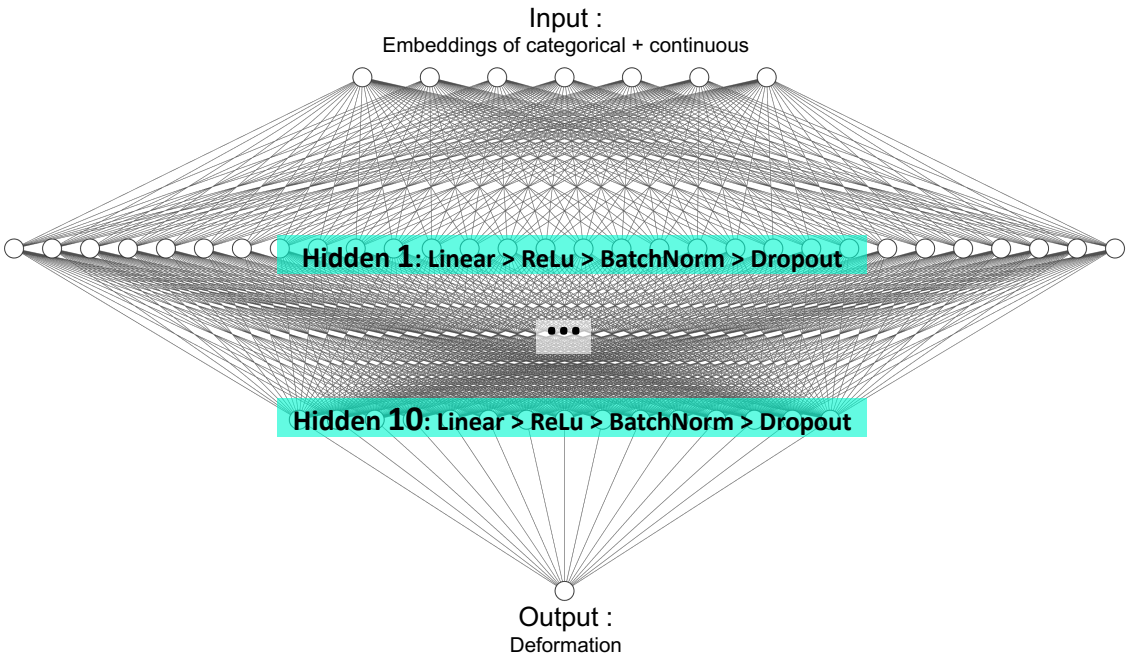

FIGURE 4.3: The fully connected architecture used in this study. The first hidden layer starts with 1100 neurons, and at each hidden layer, the number of neurons reduces by 100. The visualisation of the architecture is generated through the NN-SVG Lenail (2019).

Regularisation techniques such as batch normalisation (Batch Norm), weight decay, and dropout have been demonstrated to be vital in aiding deep learning model generalisation and improving training performance (He et al. (2019)). Batch Norm is made up of a multiplicative and an additive bias-like term (Ioffe and Szegedy (2015)). Santurkar et al. (2018) demonstrated the substantial regularising effect of Batch Norm. Therefore, a Batch Norm layer handles the continuous variables and is included in the hidden layers, as illustrated in Figure 4.3. The embedding dropout was set to 0.04, the dropout in the first hidden layer was 0.001, then 0.01 for the rest of the hidden layers, similar to the dropout sizes adopted in Howard and Gugger (2020a). Finally, stochastic gradient descent with momentum was adopted for minimising the loss function between predictions and measurements. A simple loss function, namely the mean-squared error, was adopted for training. A one-cycle policy learning rate with cosine annealing was adopted with a maximum learning rate of 0.01.

4.2.3 Gaussian Process Regression

A collection of random variables that have a joint Gaussian distribution can be completely described by their mean and co-variance (i.e., kernel) functions (Williams and Rasmussen (2006)). Gaussian Process Regression estimates the distribution of functions, x, that are most likely given the training data. The mean of those likely functions $m(x)$ estimates the most-likely prediction. The spread of the functions is described by the covariance $k(x_i, x_j)$ of the i-th and j-th random variable. Therefore, the covariance function provides the uncertainty envelope: a measure of the confidence interval for $m(x)$. Therefore, GPR is able to provide not only the prediction of InSAR deformation for a particular location, but also the uncertainty associated with its predictions.

The GPR noise is handled by introducing an extra variable for representing the noise variance in the modelling (McHutchon and Rasmussen (2011)). The exact mathematical treatment of the Gaussian noise within GPR carries a high computational load and has been shown to compare well with computational shortcuts. In short, the noise variance is inferred from the data and is represented as extra hyper-parameters, which are trained alongside the other hyper-parameters.

A critical advantage of GPR is the ability to encode prior knowledge of expected deformation behaviour through the choice of kernels. The commonly used Radial Basis Function (RBF) kernel was adopted here and is described by Equation (4.2). It has a length scale parameter l^2, which describes the smoothness of the function. This parameter controls whether the model captures the data similarity of measurements very close or far away from each other. Therefore, a large l^2 results in a smoother function:

$$K_{RBF}(x, x') = exp(-\frac{1}{2l^2}(x - x')) \tag{4.2}$$

The ability of the RBF kernel in capturing the InSAR deformation is shown in Figure 4.4. It is clear from Figure 4.4 (a) that the RBF kernel on its own tends to return towards zero and, therefore, does not adequately capture the expected behaviour of the InSAR deformation. This behaviour was corrected by combining the RBF kernel with a linear kernel, as presented in Figure 4.4 (b). This combination reflects the expectation that InSAR measurements showing subsidence will continue to exhibit

a subsiding trend. Although an uplift cannot be completely overruled, as there can be geotechnical mechanisms that may result in such a trend, the future is expected to reflect the historical behaviour of the measurement. GPR models are described by hyper-parameters, which influence the predictive performance. Therefore, these hyper-parameters were optimised using gradient descent methods and the likelihood function.

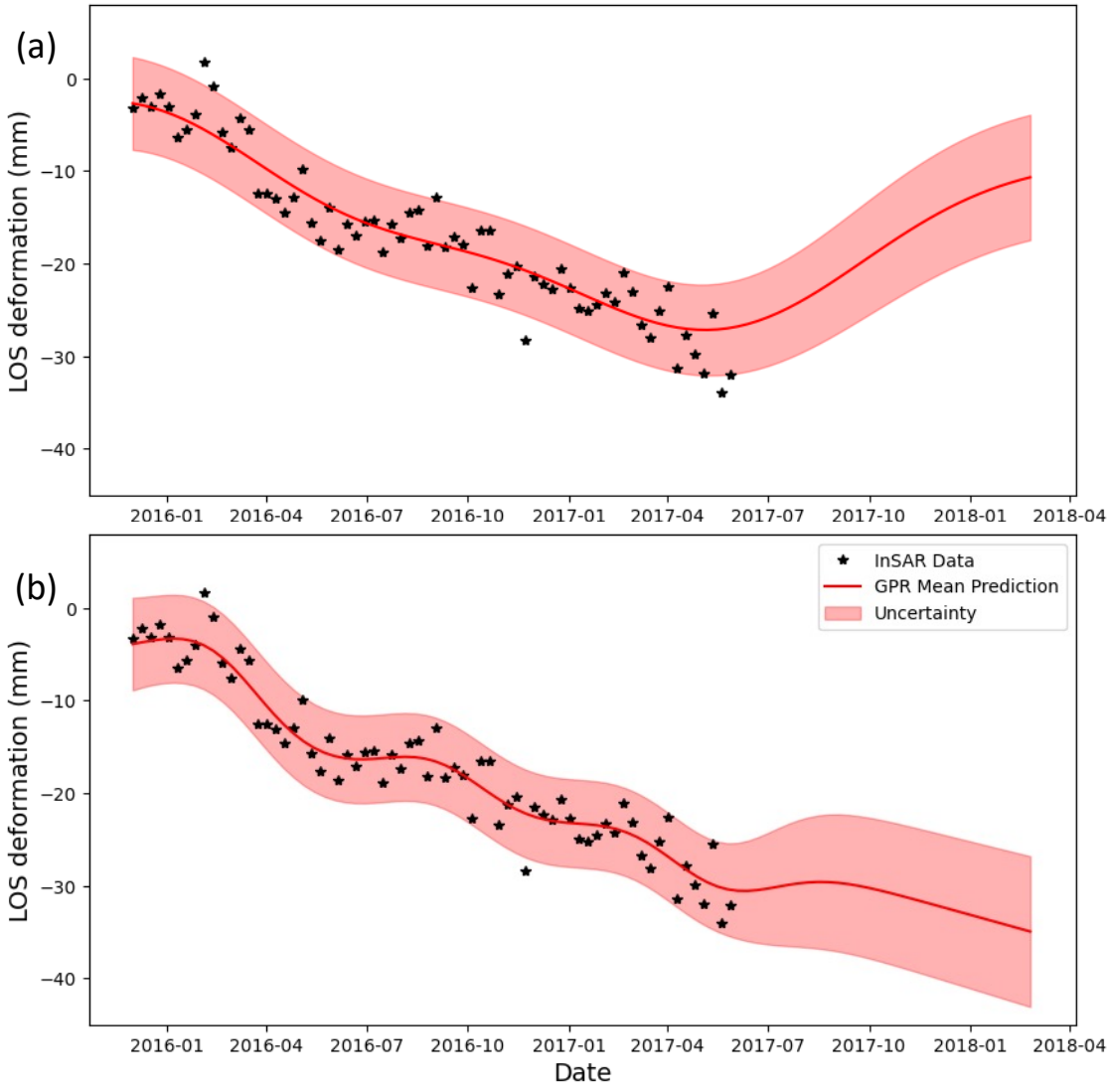

FIGURE 4.4: Comparison of GPR kernels in capturing the InSAR deformation behaviour: (**a**) Radial Basis Function kernel (RBF) and (**b**) combined RBF and linear kernels. The addition of a linear kernel gets rid of the tendency of the RBF to return towards zero.

4.2.4 Defining Anomalous Deformation Behaviour

A deformation behaviour may be described as anomalous if a measurement falls outside the "normal" variation of the data. In the case of GPR, the bounds between normal and anomalous behaviour are defined by the 95% confidence interval. Prediction uncertainty is not obtained using the EE-DL and RF approaches. Therefore, if a measurement is beyond the background noise level of the data, it will be outlined as an anomaly for the purposes of comparing the performance of the various models at detecting anomalous behaviour. The background noise level will be estimated using the RMSE between the measurements and predictions of the EE-DL approach.

Moreover, the anomalies are then clustered spatially so that anomalies next to other anomalies are given higher importance than those occurring on their own. Here, four neighbouring points was chosen as the minimum number of anomalies required for an anomalous cluster. For simplicity, anomalous clusters inside the failure area were classed as true positives, and any outside the immediate failure area were treated as false positives. A simple definition of anomalous behaviour was adopted, intentionally, to showcase the potential of the algorithms in a direct and concise manner.

4.3 Results and Discussion

4.3.1 Prediction Performance of EE-DL Model

Deep learning experiments were successfully undertaken on the embeddings of the InSAR deformation metadata. The temporal behaviour of the EE-DL predictions is given in Figure 4.5. It presents the error between InSAR measurements and the predicted deformations from a variety of experiments. The input timescale and prediction horizon (i.e., forecast steps into the future) of the experiments are detailed in Table 4.3. In these experiments, the steps correspond to the number of dates at which prediction was performed, and each step equals the temporal resolution of the SAR data, which is every 12 days over Cadia. In the case of one-step-ahead prediction, the inference starts from $n + 1$, where n represents the last date used in training. Similarly, in the context of four-step-ahead prediction (as seen in Run-C), following the completion of the four-step-ahead prediction, the data at $n + 4$ were inserted back into the training

dataset, and the model was re-trained. Therefore, it is important to note that training occurred after the introduction of each new set of predictions.

TABLE 4.3: EE-DL input training data with different lengths of temporal data points as described by the start and end dates. The total number of dates used in the training and the prediction horizon, i.e., forecast steps into the future, are also specified. There is a 12-day interval between each date.

	Start	End	Total Dates	Steps
Run-A	2015-12-02	2016-08-10	21	1
Run-B	2015-12-02	2017-01-25	35	1
Run-C	2015-12-02	2017-01-25	35	4
Run-D	2015-12-02	2017-10-04	56	1

For a typical stable location not experiencing deformation in Figure 4.5 (a), the absolute difference between predictions and measurements was within 6mm for all experiments, independent of the time frame and prediction horizons. However, the variation in the absolute error was significantly different for a typical measurement from the failure area, as plotted in Figure 4.5 (b). The absolute difference was within 8mm, which is $\pm$4mm, before almost doubling in the last three dates (2018-01-20 onwards) immediately before failure (2018-02-25). This is likely a sign of anomalous deformation behaviour arising from the TSF foundation issues attributed to the failure in Chapter 3.

The minimum number of temporal data points required as training data for an acceptable EE-DL model performance was also explored. Figure 4.6 plots the global RMSE for InSAR measurements and the predictions for each inference date. The shortest number of input dates used for training was in Run-A, which had an input of 21 dates (2015-12-02 to 2016-08-10). The RMSE for Run-A was noisy for the first 13 predictions until 2017-02-06, after which the RMSE variability was significantly less in time, plateauing at approximately 3mm. This implies that a minimum of 35 dates, from 2015-12-02 to 2017-01-25, is required to obtain a stable deformation prediction. The data up to 2017-02-06 were used for training Run-B and Run-C. The longest input of 56 dates from 2015-12-02 to 2017-10-04 was for Run-D.

As expected, the RMSE of all models gradually increased away from the 3mm plateau near the failure date in March 2018, as illustrated in Figure 4.6. This supports the hypothesis that an increasingly anomalous behaviour occurred before failure. There was also a sudden jump in the RMSE on 2017-10-16 for all models; this was

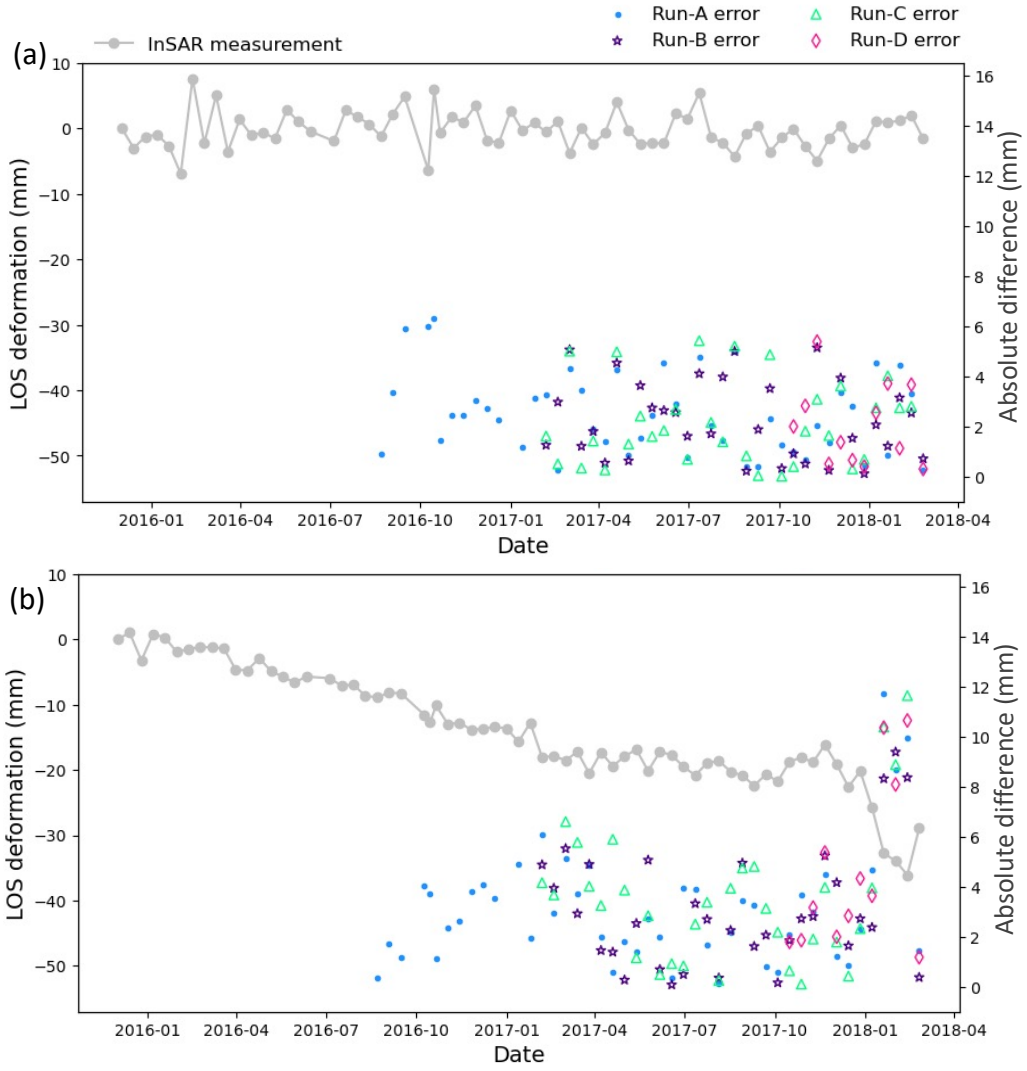

FIGURE 4.5: The absolute difference between the EE-DL prediction and the InSAR deformation measurements (grey) is plotted. (**a**) An example of an InSAR measurement not experiencing deformation. (**b**) A measurement displaying a deformation of 40mm and a clear anomalous deformation behaviour immediately preceding failure. Note the sudden jump in the absolute error for the last four dates.

likely due to inaccuracies in the InSAR processing, such as in the separation of the atmospheric phase component. Although the task of differentiating InSAR processing errors from anomalous deformation is beyond the scope of this study, the fact that these errors can be detected through the temporal behaviour of global RMSE in Figure 4.6 implies that the model is robust to the occasional occurrence of such inaccuracies.

Moreover, Run-B operated at a one-step-ahead ($n+1$) and Run-C at a four-step-ahead ($n+4$) prediction horizon. The variability in the RMSE of the four-step-ahead prediction horizon was larger at the 3mm plateau, but this difference disappeared as

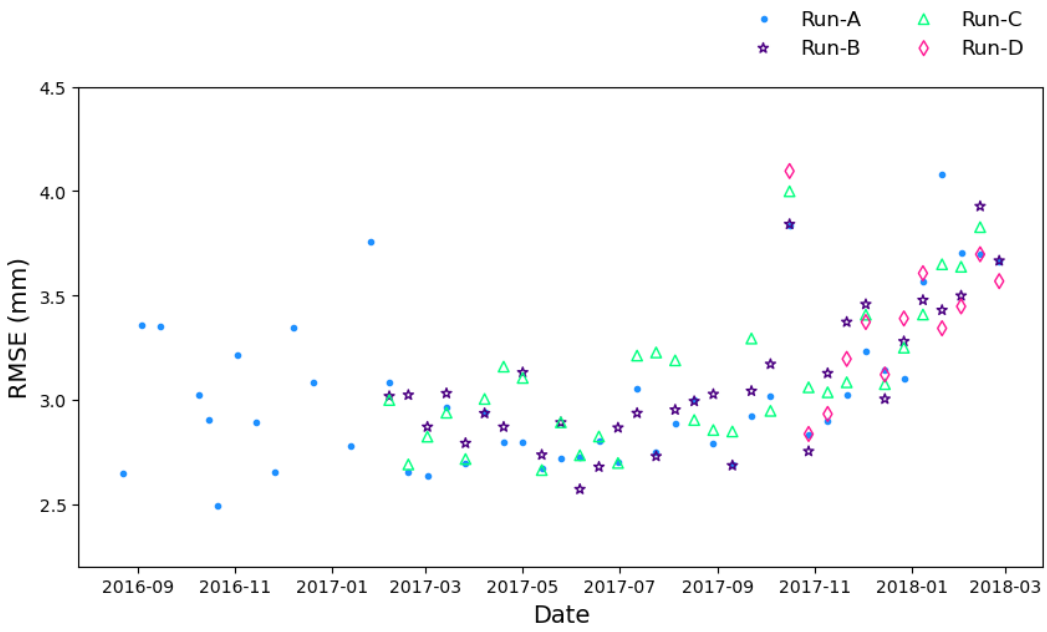

FIGURE 4.6: The global Root-Mean-Squared Error (RMSE) for different input timescales and prediction horizons. All experiments, except Run-C, predicted at one-step-ahead, and Run-C was at a four-step-ahead prediction horizon. The RMSE of all models increase away from the 3mm plateau near the failure date in March 2018.

the RMSE gradually increased for all experiments from 2017-10-28 to 2018-02-25. Finally, these results showed that the EE-DL model performed well at both one-step and four-step-ahead predictions. Therefore, the four-step-ahead prediction horizon, corresponding to 48 days of notice, was adopted for the purposes of comparing the performance of EE-DL with the GPR and RF models. The predictions of the last four temporal data points were used for comparing the performance of the models in detecting anomalous deformation behaviour.

4.3.2 Prediction Performance of GPR

The temporal history of some example InSAR measurements and GPR predictions is plotted in Figure 4.7. In these plots, the InSAR measurements from the last four dates were not included in the training of the model and were used as testing data. Figure 4.7 (a) displays a linear, relatively simple deformation behaviour. The test measurements may be described as displaying a "normal" behaviour, because they (blue) were captured within the uncertainty envelope. A more-complex, non-linear deformation

behaviour is captured in Figure 4.7 (b). In this plot, all test measurements fall significantly outside the uncertainty envelope—displaying an anomalous deformation behaviour.

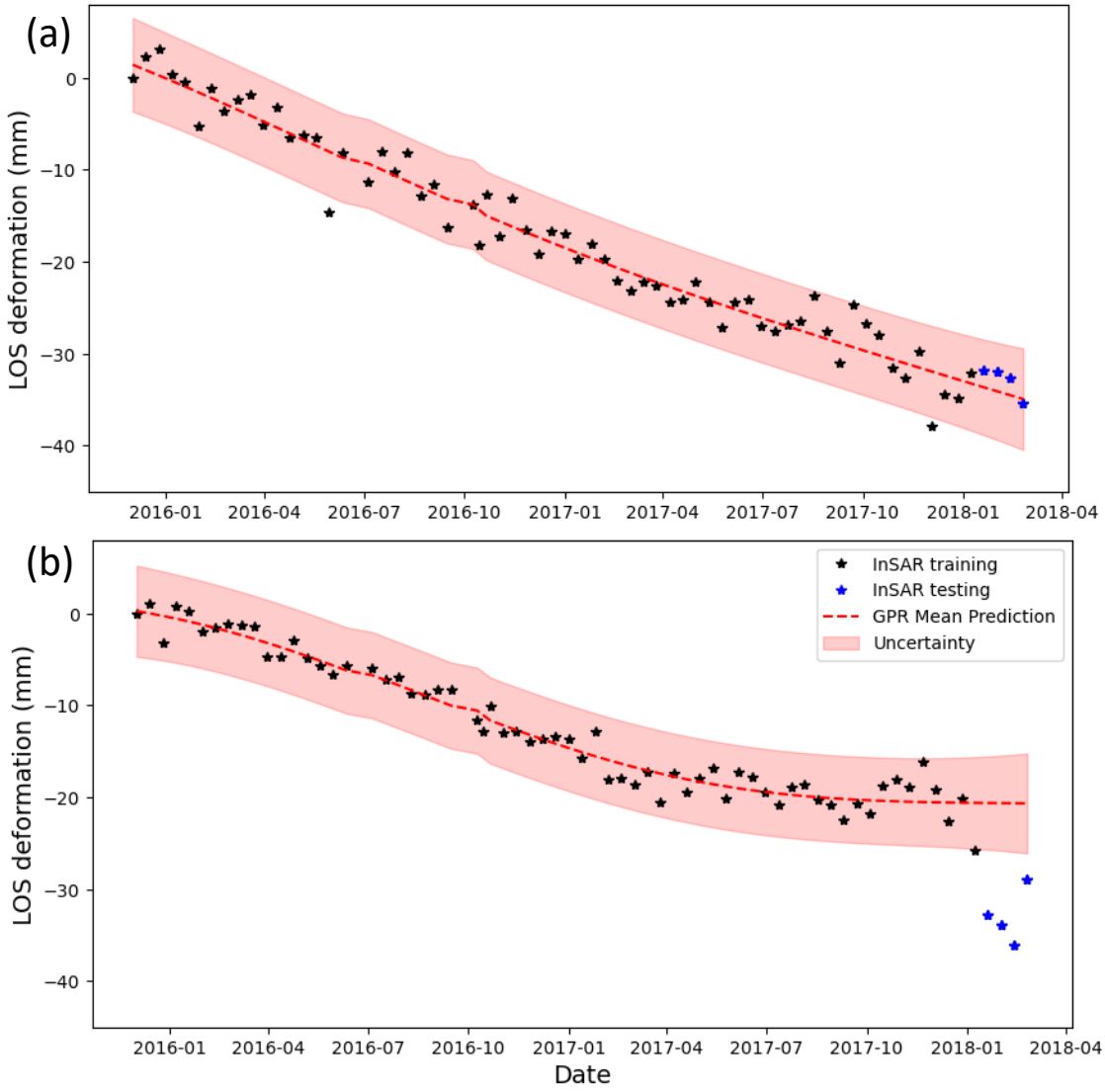

FIGURE 4.7: Temporal plots of example InSAR measurements and the GPR predictions. (a) A typical linear deformation with all test measurements within the uncertainty envelope, therefore displaying a "normal" behaviour. (b) An example of anomalous deformation behaviour with the test measurements falling significantly outside the uncertainty envelope.

Any measurements displaying such anomalous deformation behaviour in the last four temporal points were then clustered. The number of anomalous clusters detected at each date were counted and are summarised in Figure 4.8. As expected, there was a significant number of anomalous clusters detected in the failure area of the TSF for all dates, also referred to as true positives in the "T" column. However, this was at the

expense of a much larger number of false positives ("F" column). This large number of false positives limited the ability of using the GPR uncertainty envelope for localising the problematic parts of the TSF—the failure area.

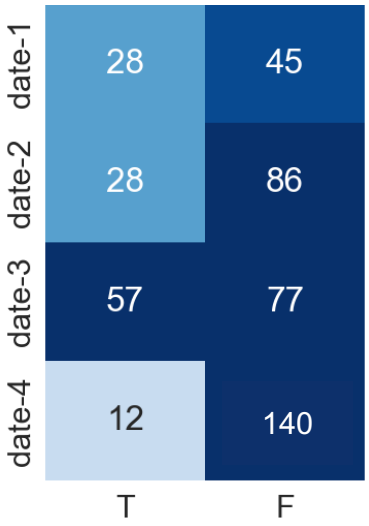

FIGURE 4.8: Measurements falling outside the GPR confidence interval are clustered and counted. A minimum of four or more anomalous measurements forms a cluster. If these anomalous clusters occur inside the failure area, they are counted as a true positive, "T", otherwise as a false positive, "F".

4.3.3 Comparison of EE-DL, GPR, and RF

The results of the EE-DL and GPR approaches were compared to the RF baseline model. The global error between the measured and predicted deformation is plotted in Figure 4.9. As expected, the simplest approach, RF, performs the poorest. It has a consistently high RMSE for all test dates compared to the other models in Figure 4.9 (a). The best-performing model is GPR, which had the lowest RMSE for all the time steps. The EE-DL performance is intermediate between RF and GPR for all dates. The RMSEs, varied between $\pm$4mm and were similar to the absolute error related to the background prediction noise level in Figure 4.5. A value of $\pm$4mm is consistent with the background noise level of InSAR measurements reported in previous studies, e.g. Boni et al. (2015), Cigna et al. (2012).

Therefore, an error envelope of 8mm is adopted as a threshold for separating normal from anomalous deformation behaviour. Similar to the RMSE results, the Maximum Error (MAXE) is also highest for RF. In Figure 4.9 (b), RF consistently has the highest MAXE for all dates. Interestingly, the trend of the MAXE is consistent for the

last three dates for all the models, which gave the highest MAXE for 2018-02-13 and the lowest immediately preceding the failure in 2018-02-25.

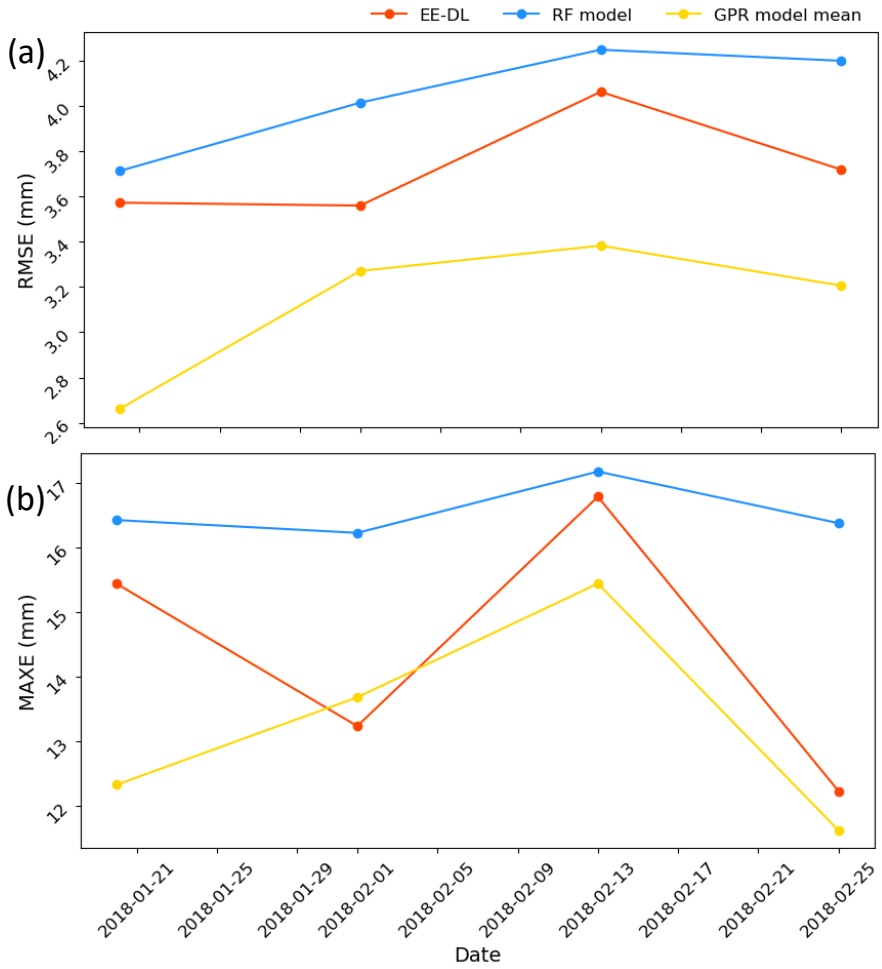

FIGURE 4.9: Global error metrics for the various models. (**a**) RMSE and (**b**) Maximum Error (MAXE).

A spatial visualisation of the anomalous clusters captured by the various models is given in Figure 4.10(a)–4.10(c). These maps show that all models successfully captured anomalous clusters in the failure area of the northern TSF. It is clear that the anomalous clusters in Figure 4.10 for (a) EE-DL and (b) GPR are much more focused around the slump area compared to (c) RF. Figure 4.10(c) RF contains many anomalous clusters outside the immediate slump area, spreading to all parts of the northern TSF. This large spread of anomalous clusters does not assist in narrowing down the area of potential problems. The RF model also detected a small number of anomalous clusters in the stable, south TSF. The anomalous cluster #1 in Figure 4.10(c) was only detected by RF and not the other two approaches, potentially limiting its reliability, whereas cluster #2 was detected by all models, giving more confidence to its

anomalous nature.

All the algorithms detected some false positives. Thus, it is important to note that not all the instances flagged as false positives in Figures 4.10 and 4.11 are necessarily incorrect in identifying anomalous behaviour. Even though these measurements were outside the slump area, they may still exhibit true anomalous behaviour that is unrelated to failure, for instance anomalous behaviour stemming from other construction processes. Interpreting the location and temporal occurrence of anomalies outside the slump area is beyond the scope of this study. Further clarification may be gained from combining InSAR with other data sources. The definition of true and false positives was intentionally simplified to enable a clear and concise comparison of the wide spectrum of algorithms employed in this study.

The number of true and false anomalies detected by the various models was counted and is summarised in Figure 4.11. It shows that EE-DL detected the most true anomalous clusters, with a total of 69 compared to 59 by RF and 26 by GPR. It can also be seen that the RF model consistently detected the most false positives, a total of 177 compared to 59 for EE-DL and 30 for GPR. Moreover, the RF model had a higher number of false positives than true positives for all dates, potentially limiting its ability to locate the failure area. Although the GPR detected the least amount of false positives, this was at the expense of the total number of anomalies. Therefore, the EE-DL approach detected the most true positives compared to the other approaches, but its true positives were not at the expense of false positives, like the RF model. This study therefore recommends employing EE-DL as the primary method for the early warning of TSF failure.

4.4 Summary

A new methodology for detecting anomalous InSAR deformation based on embedded entities within a deep learning (EE-DL) framework was proposed. Embeddings of InSAR metadata were used for training a fully connected neural network. The use of embeddings captured both the spatial and temporal components of the InSAR measurements, without the typical DL challenges related to InSAR data. The feasibility of the EE-DL approach was demonstrated by a failed TSF case study to detect anomalous

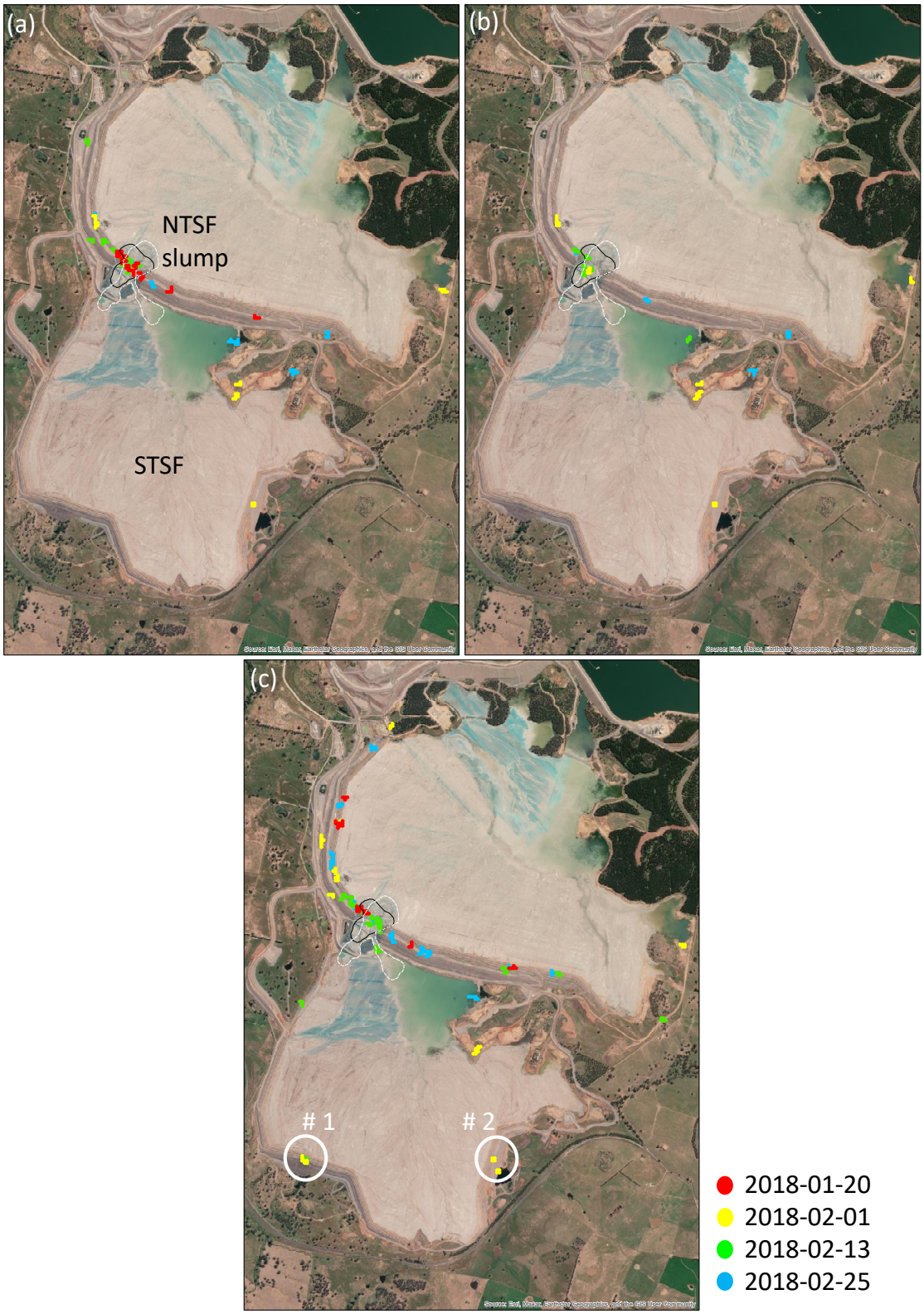

FIGURE 4.10: Spatial distribution of anomalous clusters detected on the last four test dates for (**a**) EE-DL, (**b**) Gaussian Process Regression mean, and (**c**) Random Forest baseline model. The failure area of the northern TSF is outlined. Slumping occurred in two stages; the black outline precedes white. Basemap image copyright © 1995–2020 Esri.

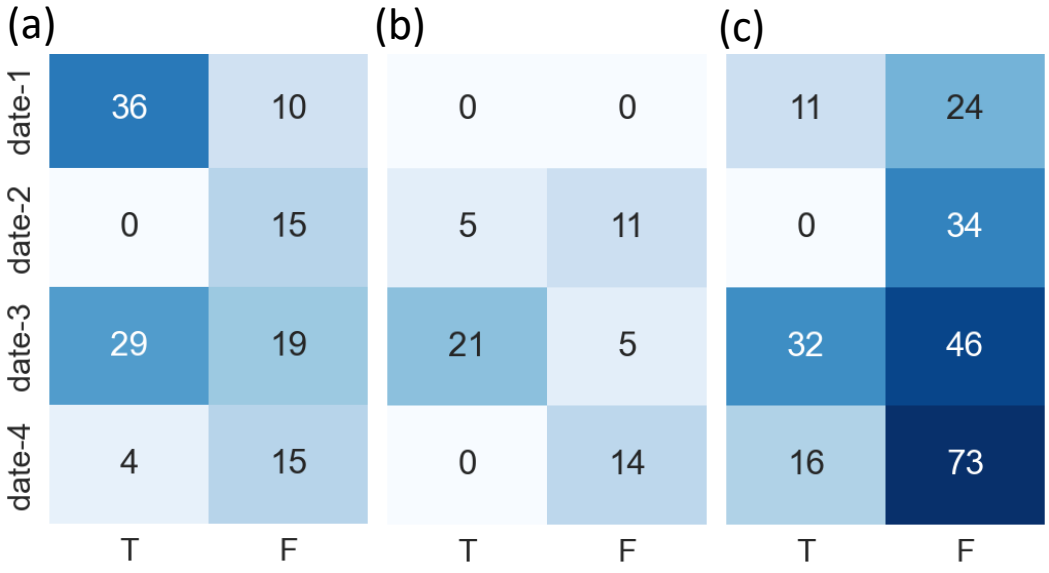

FIGURE 4.11: Summary count of the number of anomalous clusters detected by (**a**) EE-DL, (**b**) GPR mean, and (**c**) RF

deformation behaviour preceding failure. The performance of the EE-DL model was compared to a probabilistic approach, GPR, and a simple baseline model, RF.

The comparison outlined that the EE-DL approach performed better than both GPR and RF for predicting ground deformation from interferometric time series. The novel use of EE-DL provided an accurate geolocation of anomalous areas that could be subject to failure. The most true anomalous clusters were detected using the GPR uncertainty envelope. However, these anomalies were at the expense of the false positives, limiting its ability to geolocate the failure area. The EE-DL and RF approaches did not have an associated probabilistic uncertainty envelope; therefore, the background noise level of the predictions, an RMSE of $\pm$4mm, was used for defining an anomaly threshold. When this definition of anomaly was applied to the GPR mean predictions, GPR performance improved compared to the performance of its uncertainty envelope. The EE-DL approach still performed better than the GPR, because the improved GPR performance was at the expense of a significantly lowered detection of total anomalies, both true and false positives. The EE-DL also performed better than the RF, as the RF consistently detected more false positives than true positives.

The conclusions from this study set a promising direction for the establishment of early-warning systems for infrastructure failure with remote-sensing-derived data. These systems, alongside ground-based instrumentation, geotechnical simulations,

and inspection, can create a monitoring ecosystem aimed at mitigating and, ideally, preventing the catastrophic consequences of TSF failures.

Chapter 5

Impact of Satellite Sensor Characteristics and Processing

This research seeks to push the limits of what is possible from global, open source satellite data. This ambition has driven the emphasis on making the most out of Sentinel-1 InSAR (S1-InSAR) in the previous chapters. The comparison between S1-InSAR and geotechnical approaches explored in Chapter 3, reveals several limitations of InSAR. For instance, S1-InSAR is not able to capture the fast deformation following the construction of buttresses, where the deformation predicted by geotechnical modelling significantly differs from InSAR measurements. It remains unclear to what extent these limitations are: (1) inherent to the InSAR method, (2) due to the specific processing approach applied to Sentinel-1 (S1), or (3) related to the satellites' sensor characteristics, such as signal incidence angle, polarisation, resolution and orbit type. This chapter explores the potentials for overcoming these limitations by re-processing the S-1 data using a different multi-temporal InSAR approach and incorporating data from another satellite sensor, namely Radarsat-2 (RS2). By comparing S1-InSAR with commercial, high resolution Radarsat-2 InSAR stacks (RS2-InSAR), the chapter also evaluates the value of investing in commercial InSAR data.

The impact of the InSAR processing algorithm is investigated by re-processing the S-1 data using Persistent Scatterer Interferometry (PS-InSAR). The key characteristics and differences between PS-InSAR and the ISBAS are outlined in Chapter 2. Since Sentinel-1 data over Cadia are available only from a descending stack, it is not possible to decompose the line-of-sight deformation into its vertical and horizontal components (Chapter 2). Therefore, S1-InSAR is compared to the equivalent RS2-InSAR

data from descending orbit only. Additionally, these measurements are compared to available geotechnical simulations and ground based prisms. The spatial and temporal comparison of descending S1-InSAR (ISBAS and PS-InSAR) and RS2-InSAR are presented in Section 5.3.1. The expected impact of sensor characteristics, such as the signal incidence- and the orbital heading angles, on resulting deformation measurements are quantified in Section 5.3.2. Moreover, the impact of InSAR phase ambiguity and potential phase unwrapping errors are explored in Section 5.3.3.

RS2-InSAR data are acquired from both ascending and descending orbits, enabling the decomposition of the InSAR ground movements into its vertical and horizontal (East - West) components. Section 5.3.4 presents a comparison of these decomposed measurements to the equivalent motion components of geotechnical model results and prisms. The potential impact of phase unwrapping on the decomposed deformation is also examined.

Furthermore, due to licensing agreements between satellite operators and various governments, direct access to raw RS2 data over Cadia is restricted. This limitation applies to very high resolution data over Australia, to maintain confidentiality over specific countries. However, this research is able to access derived InSAR deformation products, courtesy of MDA Space Ltd., but not the raw RS2 data. Consequently, this limits the ability to test the impact of processing approaches on RS2 data.

Finally, commercial high resolution InSAR data coverage is often patchy and is not available globally. In the case of the Cadia failure, RS2 data is the only commercial InSAR data available for the time period preceding the failure. However, it is important to note that both cost and data availability factors are changing rapidly. With the current trend of increasingly cheaper launch capabilities and instrument developments, the cost of data is likely to keep reducing and therefore, the availability of high resolution data is likely to keep increasing (Curnick et al. (2022)).

5.1 InSAR Data Sources

The InSAR data sources are described in Tables 5.1 and 5.2 for RS2 and S1, respectively. The RS2-InSAR datasets are composed of data from both the line-of-sight (LOS) ascending and descending orbits, as well as the decomposed motions. Table 5.1 shows

that the frequency for descending data are stable at 24 days. However, the frequency for the ascending stack is mostly 24 days, with two acquisition gaps that result in 48 days. In comparison, the decomposed vertical and horizontal components are at a frequency of 12 days, with one data gap resulting in 24 days.

TABLE 5.1: Radarsat-2 InSAR data description. Descending LOS data frequency is stable, whilst ascending LOS data frequency is mostly 24 days with two acquisition gaps that result in 48 days. The vertical and horizontal components are at mostly 12 day frequency, with one data gap resulting in 24 days.

InSAR deformation	Date (YYYY-MM-DD) from	to	Frequency (days)
Descending LOS	2017-06-08	2018-02-27	24
Ascending LOS	2017-07-14	2017-10-18	24
	2017-10-18	2017-12-05	48
	2017-12-05	2017-12-29	24
	2017-12-29	2018-02-15	48
Vertical and horizontal	2017-06-08	2017-07-02	24
	2017-07-02	2018-02-27	12

TABLE 5.2: Sentinel-1 InSAR data processed with ISBAS and PS-InSAR algorithms. Sentinel-1 data over Cadia TSF is available from the descending orbit only.

InSAR algorithm	from	to	Frequency (days)
ISBAS	2015-12-02	2018-02-25	12
PS-InSAR	2016-12-08	2018-02-25	12

Table 5.2 shows that the ISBAS processing includes a SAR data stack spanning over 2 years, while PS-InSAR processing has been applied to a shorter stack, covering a total of just over 1 year. PS-InSAR requires re-processing of S1 data with a shorter temporal stack, to increase the likelihood of obtaining measurements. This is due to the scattering behaviour that may change over time, reducing the probability of finding persistent scatterers with consistent behaviour over extended periods. PS-InSAR may help resolve the discrepancies observed between FE model and ISBAS immediately preceding failure (Chapter 3). ISBAS is suited for distributed scatterers, where the deformation signal is uniform within a larger area, as the resolution cells are 'multi-looked', e.g. interpolated to a lower resolution. In contrast, PS detects

TABLE 5.3: Properties of descending S1 and RS2 SAR satellites.

	S1	**RS2**
Signal Wavelength	C-band (5.6 cm)	C-band (5.6 cm)
Revisit time	12 days	24 days
Azimuth Resolution	5m	1.3m
Range Resolution	20m	3.9m
Polarization	VV	HH
Incidence Angle	33.3°- 38.7°	38.5°
Heading angle	-167°	-163°

strong scatterers in each pixel and therefore, the deformation signal is dominated by the movements of the strong scatterers, and no multi-looking might be performed. A theoretical discussion and comparison of PS-InSAR, ISBAS and other types of InSAR processing approaches are available in Chapter 2.1.3.

In terms of the descending S1 and RS2 data, although both are C-band SAR satellites, there are several differences, including their spatio-temporal resolution, polarization, heading and incidence angles, as summarised in Table 5.3. RS2 is acquired at the highest possible spatial resolution, approximately five times that of S1. Moreover, RS2 data are available from both ascending and descending orbits, which enables rigorous decomposition of the LOS motions. Figure 5.1 illustrates the way the deformation is observed from the ascending and descending geometries and that they can be combined to estimate the true deformation. For instance, in Figure 5.1 (a), vertical subsidence is detected as negative in both geometries (moving away from the satellite). In contrast, a horizontal motion in Figure 5.1 (b) is detected as negative in ascending and positive (i.e. moving towards the satellite) in the descending geometry.

5.2 Methodology

5.2.1 Descending S1 vs RS2 comparison

The S-1 and RS2-InSAR data are acquired at different spatial and temporal resolutions, therefore require pre-processing steps before they can be compared, such as the approaches described in Sadeghi et al. (2021). To enable a spatial comparison of S1 and RS2-InSAR measurements, firstly, a common grid of pixels is defined with a size of 20m by 20m. The common grid (yellow) is illustrated in Figure 5.2 relative

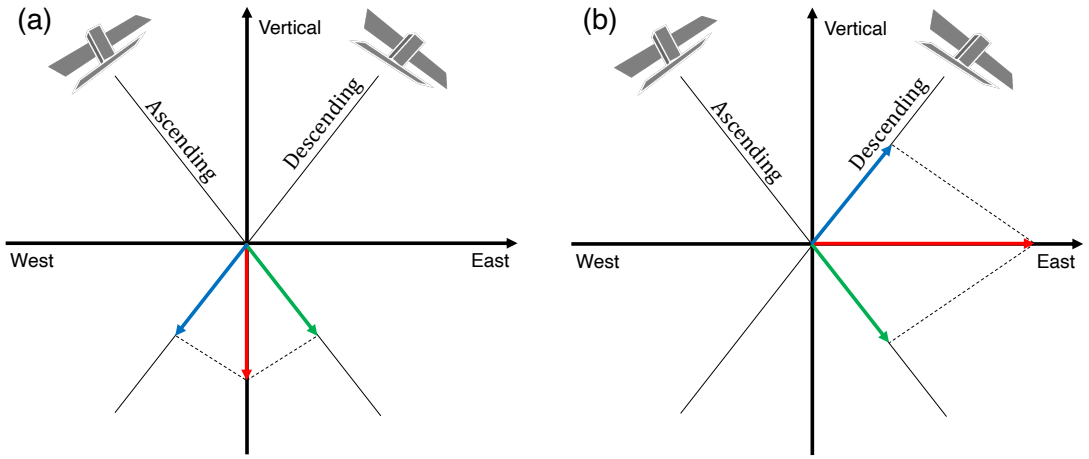

FIGURE 5.1: Obtaining true deformation by combining ascending and descending geometries. (a) Vertical ground deformation is negative in both ascending and descending directions (moving away from the sensor) and (b) only one vector is positive (moving towards the sensor) in the horizontal motion. Modified from Bateson et al. (2010).

to S1-ISBAS deformations (grey). To highlight the differences in spatial resolution and distribution of InSAR measurements, S1-based ISBAS and PS-InSAR are plotted alongside the common grid and the RS2-InSAR measurements in Figure 5.3.

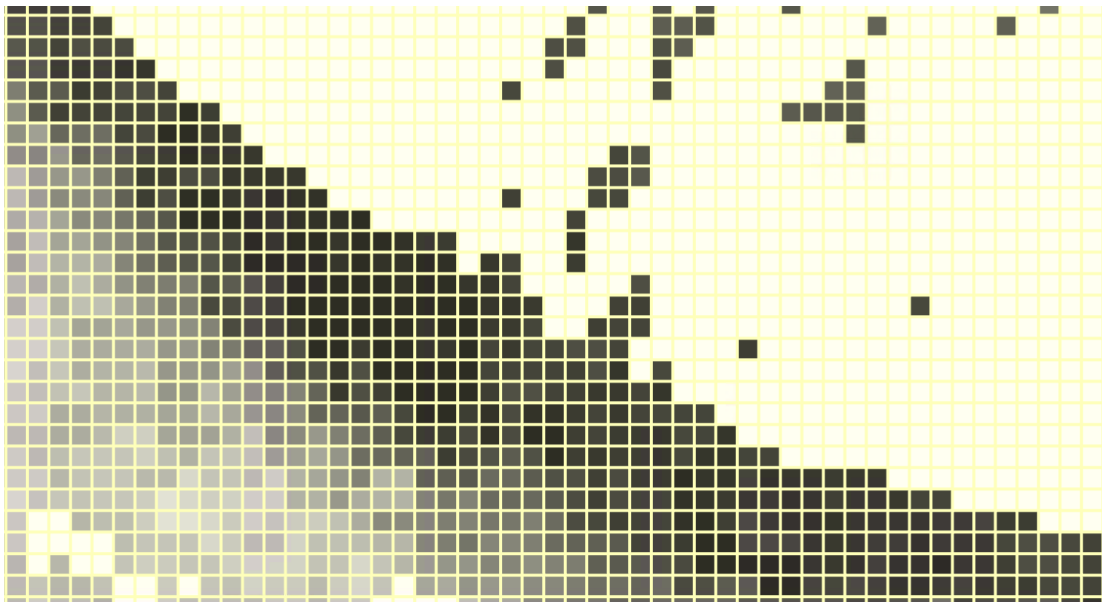

FIGURE 5.2: Common grid (yellow) of 20m x 20m for comparing InSAR products. The common grid pixel locations match S1-ISBAS (greys).

Moreover, the S1-InSAR (ISBAS and PS) and RS2-InSAR need to be aligned to the same temporal scale. Figure 5.4 compares the temporal resolution of the descending S1 and RS2 acquisitions, where S1 data is acquired at twice the temporal resolution at 12 days, compared to 24 days of RS2. To align the datasets, the S1-InSAR deformations

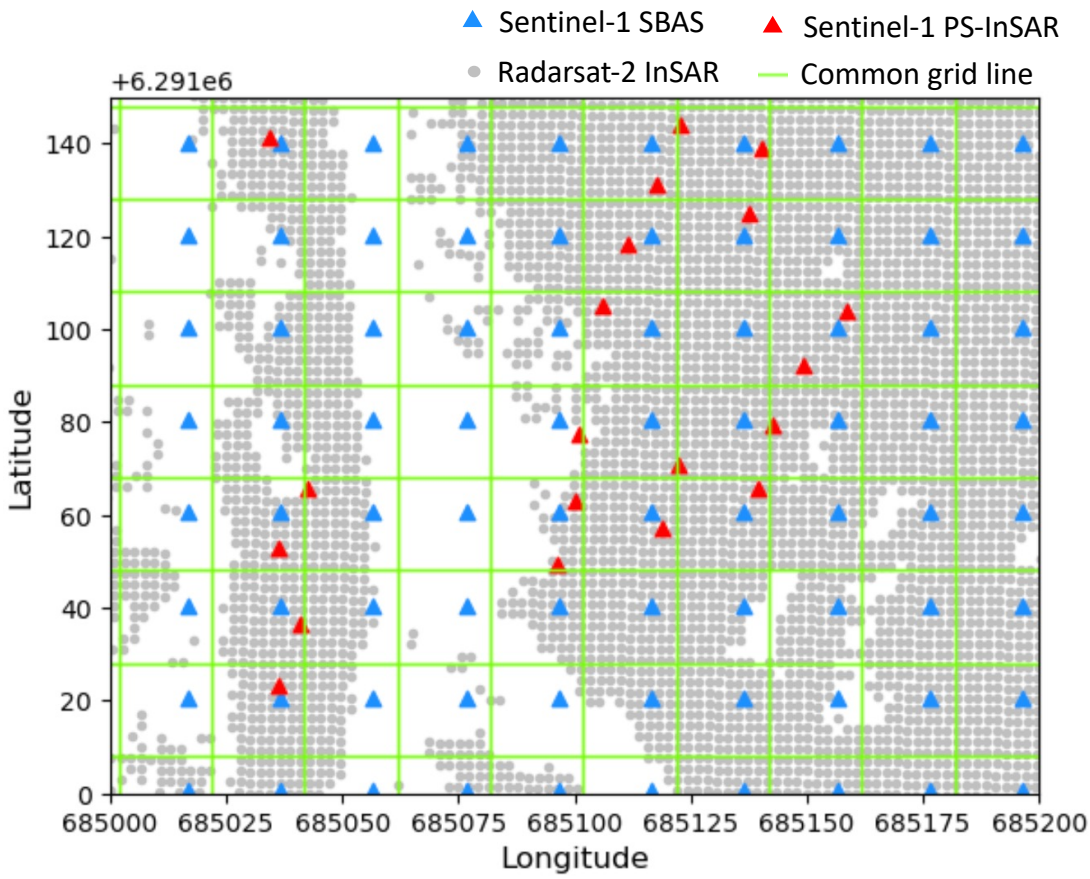

FIGURE 5.3: Visualisation of Sentinel-1 SBAS, PS-InSAR and Radarsat-2 InSAR data resolution, overlaid with the common grid of pixels defined with a size of 20m by 20m.

are set to zero on the start date of the first RS2 acquisition, which begins on 2017-06-08 (YYYY-MM-DD), with the nearest S1 acquisition at 2017-06-06. Therefore, the deformation measured on 2017-06-06 is subtracted from all subsequent S1 measurements.

Following the spatio-temporal pre-processing steps, various statistical parameters are calculated for the InSAR measurements intersecting the common grid. Firstly, the velocity ($mm/year$) between each acquisition is calculated. Then, the mean, standard deviation, maximum, and minimum of these velocities are determined for each common grid cell to enable comparison of the data sources.

5.2.2 Phase Unwrapping Correction

The basic principles of phase unwrapping are used to demonstrate the extent to which phase ambiguity and uwrapping errors may explain the large differences observed

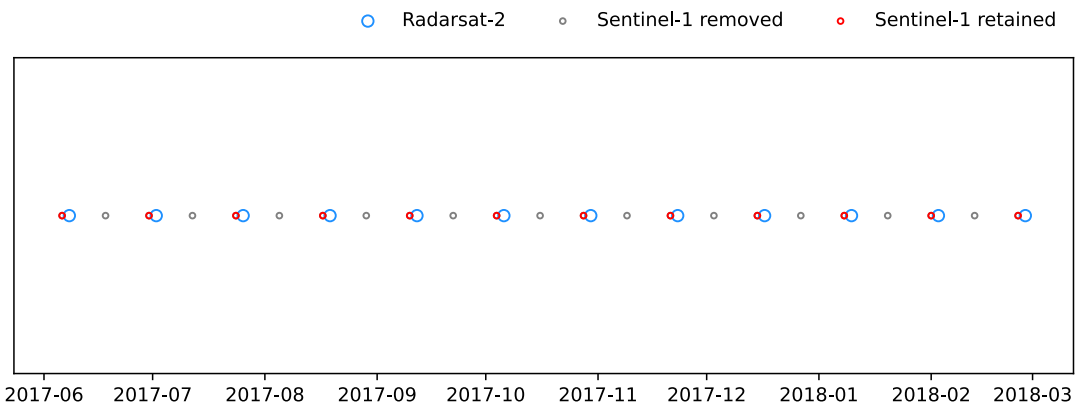

FIGURE 5.4: Common dates used for comparing RS2 and S1. The available S1 imagery are just two days before the RS2 acquisitions (YYYY-MM).

between ISBAS and FE predictions following buttress construction (Chapter 3, Figure 3.18). Once interferograms are generated as part of InSAR processing, the deformation components of the phase are separated from unwanted components such as noise. Because SAR Interferometry measures the relative phases between acquisitions, these steps result in phase measurements observed in cycles of 2π for each SAR acquisition, also referred to as 'wrapped phases', as illustrated in Figure 5.5. The figure demonstrates the basics of wrapped phase measurements being 'unwrapped' through a linear deformation model. According to Itoh's condition, the difference in phases between two adjacent samples cannot exceed π, ensuring that the phase values lie within the range of $-\pi < phase < \pi$ (Itoh (1982)). This means, firstly, the difference in phase between two adjacent samples must be calculated. If the difference is more than π, then a cycle (2 π) is subtracted. In contrast, if it is less than $-\pi$, then a cycle is added. The number of cycles of 2 π that needs to be added or subtracted is unknown and depends on the particular phase unwrapping methodology and assumptions.

Phase unwrapping is a critical research area, containing a variety of approaches to the problem (Yu et al. (2019)). Figure 5.5 illustrates a one-dimensional phase unwrapping example, which is based on the signal's behaviour through time. Other methods involve phase unwrapping in two spatial dimensions. However, as the number of dimensions increase, additional challenges emerge, such as path dependency. The specific starting location, the direction and the path followed during the phase unwrapping process can lead to different solutions. This is also called the 'residue

theory', where the location of the residues then inform the 'jump' in the phases. The details and the complications of advanced phase unwrapping techniques are beyond the scope of this thesis.

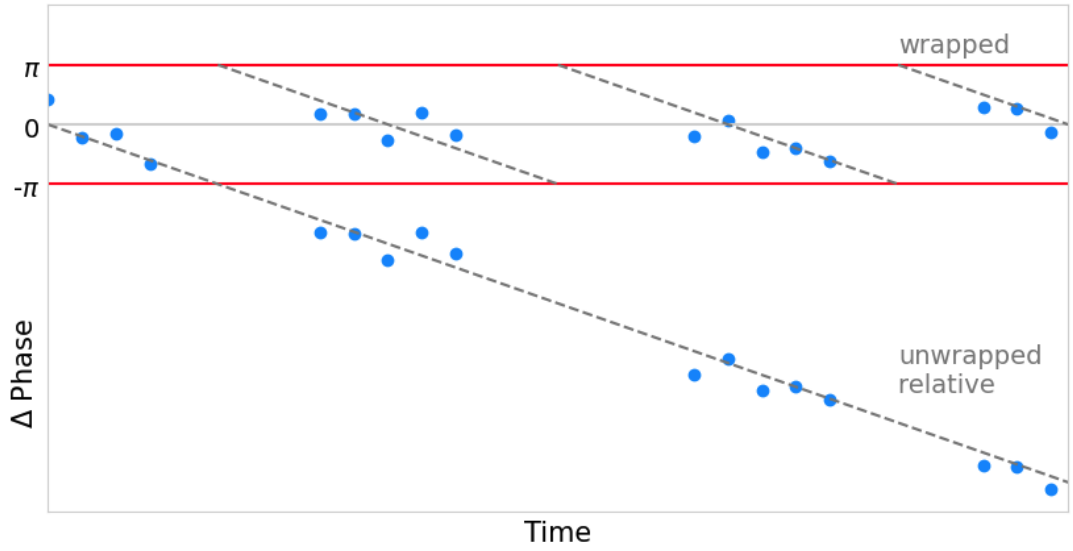

FIGURE 5.5: A simple example of wrapped and unwrapped phases. The wrapped signal is modulo 2π (1 cycle) of the relative unwrapped signal. Modified from Massonnet and Feigl (1998), Hooper (2016).

5.3 Results and Discussion

5.3.1 Spatio-temporal comparison

The distribution of descending InSAR data through time are visualised in Figures 5.6 (a) RS2 and (b) S1-InSAR. The violin plots indicate the density and median of the data, with most of the data lying within $\pm$ 20mm for both. The main differences between RS2 and S1-InSAR data are that RS2-InSAR data exhibit a greater range of outliers with subsidence exceeding -100mm immediately before failure, in contrast to ISBAS and PS-InSAR, where outliers generally do not surpass -40mm. Additionally, RS2-InSAR outliers display a clear trend of increasing magnitude with time, a pattern not observed for ISBAS and PS-InSAR. As expected, the measurement ranges for PS and ISBAS are very similar, since they are both derived from S1. An obvious explanation of the variation in RS2 and S1-InSAR outliers may be attributed to the SAR data spatial resolution. The RS2 pixel size is at a much higher resolution than S1, therefore the signals are potentially less tempered by signals from nearby. Another explanation

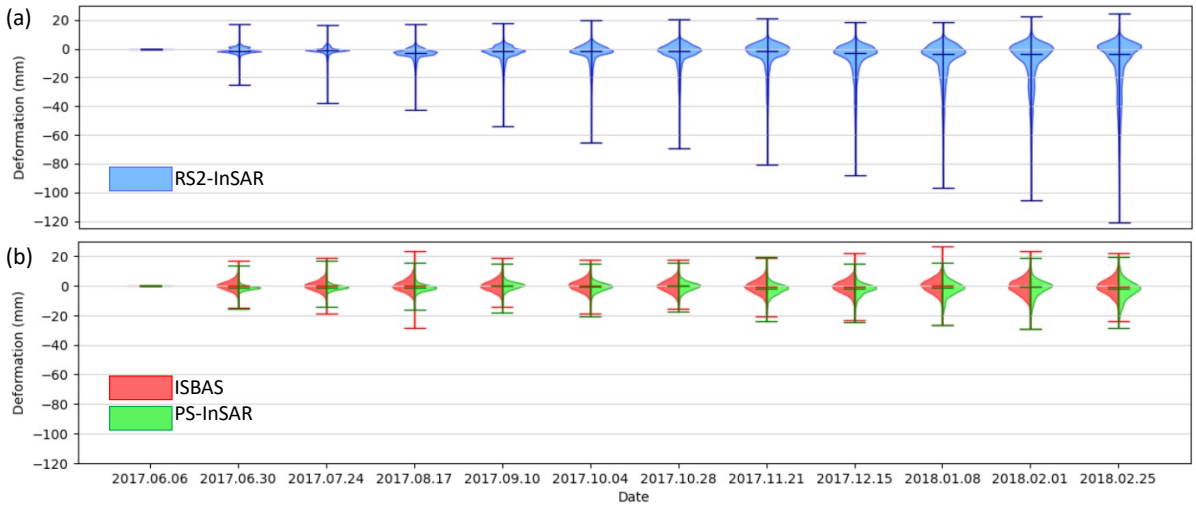

FIGURE 5.6: The distribution and density of (a) RS2-InSAR and (b) S1 based ISBAS and PS-InSAR visualised with a violin plot.

for these differences may be due to potential phase unwrapping issues and this is explored in Section 5.3.3.

The spatially common grid is aligned with the resolution of S1. The variation (i.e. standard deviation) of RS2 measurements within each grid cell are depicted in Figure 5.7 (a) from 2017-06-08 (YYYY-MM-DD) to 2018-02-03. Figure 5.7 (b) is a zoom-in to the last RS2-acquisition immediately before structural failure in 2018-02-27. Notably, it reveals two prominent layers of high standard deviation (dark red) areas running parallel to dam rim in the NTSF. These dark red regions represent common grid pixels where the deformation measurements are not uniform but highly variable, suggesting the presence of complex movements. The origin and development of these high standard deviation regions can be traced from the Western-most part of the TSF, extending past the slump area in Figure 5.7 (a) and (b). The alignment of these high variability areas along the dam rim may imply dynamic stress in these zones, potentially mirroring the construction of the buttresses through time. Therefore, the higher resolution data may reveal finer details of deformation behaviour, potentially leading to better insights before the occurrence of failure.

The spatio-temporal evolution of the deformation behaviour of various datasets is further examined by calculating the velocity differences between RS2 and S1-InSAR data across the common grids in Figures 5.8 - 5.10. In these figures, part (a) displays the evolution of velocity through time, while part (b) provides a close-up view of the

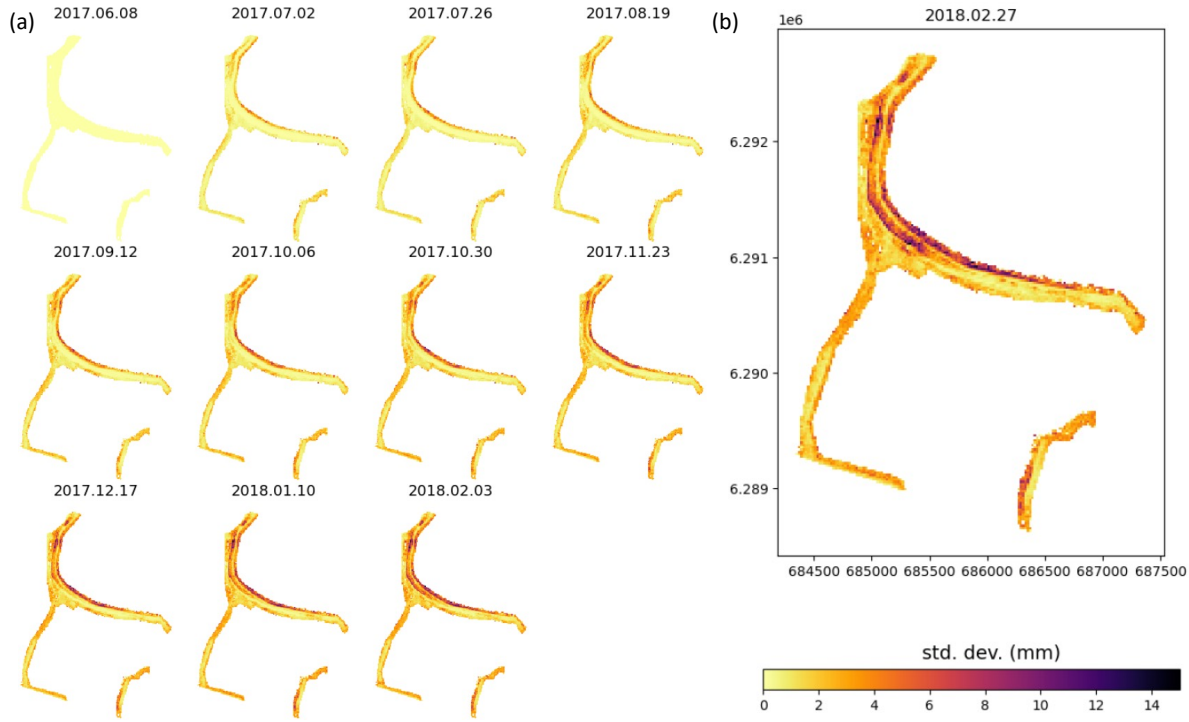

FIGURE 5.7: Standard deviation of RS2 InSAR measurements within the common grid.

velocity just before failure. A significant difference in velocity between RS2-InSAR and the S1-derived measurements is particularly noticeable in the slump area during the later dates immediately before failure. For the RS2-ISBAS pair in Figure 5.8, these velocity differences become visually obvious from 2017-12-15 (YYYY-MM-DD) onwards. A similar pattern is observed for the RS2-PS InSAR pair, although the spatial patterns are less distinct. The lower spatial distribution of PS-InSAR measurements result in a less defined outline of the slump and more diffuse boundaries for the PS-RS2-InSAR pair in Figure 5.9 (b). In contrast, the higher spatial distribution of ISBAS measurements compared to PS-InSAR allows for clearer tracking of the development of the velocity differences over time in the ISBAS- RS2 InSAR pair in Figure 5.8 (b).

As expected, the velocity differences are less pronounced for the PS-ISBAS pair in Figures 5.10 (a) and (b), suggesting that they provide similar results. The evolution of these high variability velocities can be tracked to 2017-11-21 in Figure 5.10 (a), where most of the TSFs show small velocity differences (green), followed by clusters of large velocity differences (blues and reds) spreading from the Western parts of NTSF. A closer inspection of Figure 5.10 (b) reveals small clusters of both high (blues) and low (reds) velocity differences in the PS-ISBAS pair. This indicates that PS-InSAR exhibits

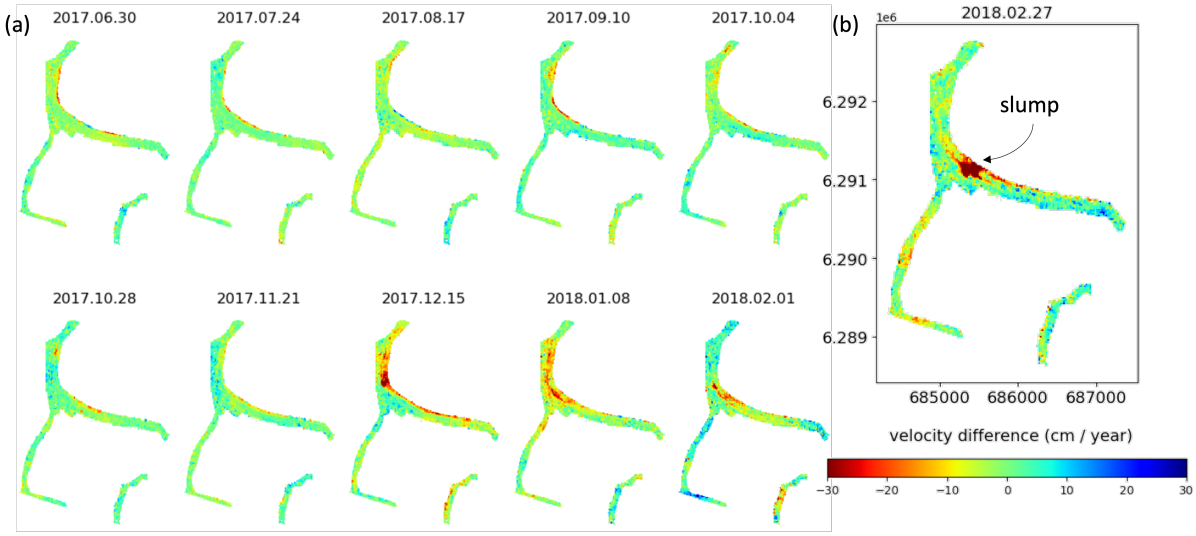

FIGURE 5.8: Spatial distribution of velocity difference between RS2-InSAR and S1-ISBAS. The temporal evolution of the velocity is in (a) and a zoom-in to the last date immediately before failure is in (b).

higher velocities in some locations and lower velocities in immediately adjacent areas. The underlying causes for this seemingly random distribution of low and high velocities in the PS-ISBAS pair are explained through investigation of the temporal time-series of the measurements.

Furthermore, Figures 5.11 (a) - (c) compare the geotechnical data with S1-ISBAS, PS-InSAR and RS2 InSAR data. There is a strong agreement between all measurements until the construction of buttresses. However, in the months before failure, large deviations are observed, especially between ISBAS and FE results. Interestingly, this deviation is not observed for RS2-InSAR, where it compares very well with the FE measurements for stages 4 and 5, as plotted in Figure 5.11 (a) and (b), respectively. However, for stage 7, RS2-InSAR measurement over-estimates the FE deformation in Figure 5.11 (c).

Moreover, the PS-InSAR measurements plotted in Figures 5.11 (a) to (c) exhibit strong correlation with ISBAS, RS2-InSAR, FE model and prisms until the construction of buttresses. Interestingly, following buttress construction the PS-InSAR signals demonstrate highly irregular behaviour. Notably, these signals do not subside like the FE model, but instead exhibit pronounced fluctuations compared to their previous behaviour (i.e. pre-buttresses). The causes of this phenomenon in PS-InSAR is further investigated in Section 5.3.3.

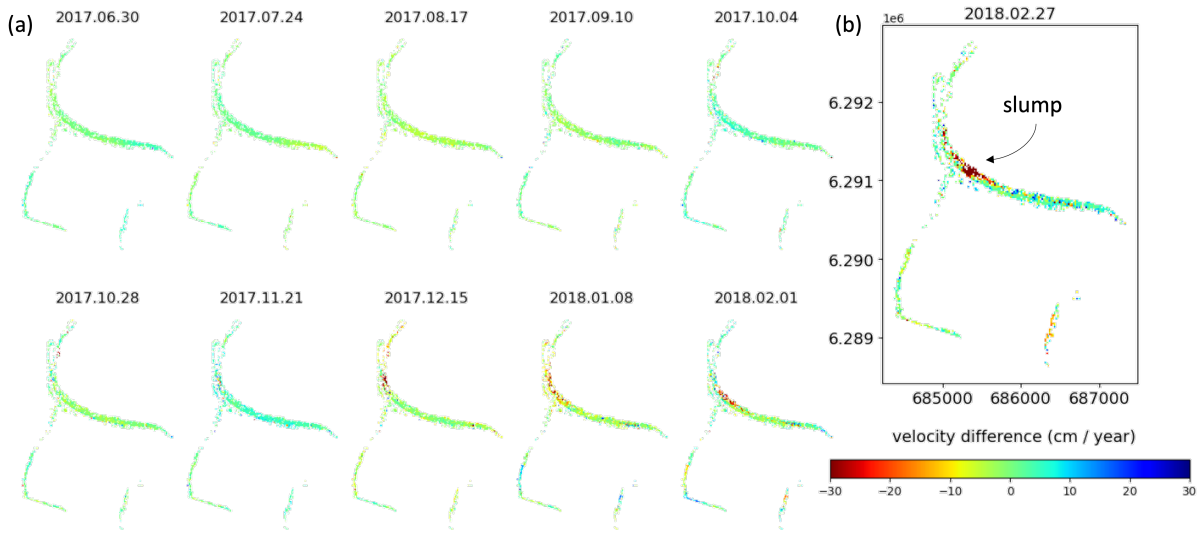

FIGURE 5.9: Spatial distribution of velocity difference between RS2-InSAR and PS-InSAR. The temporal evolution of the velocity is in (a) and a zoom-in to the last date immediately before failure is in (b).

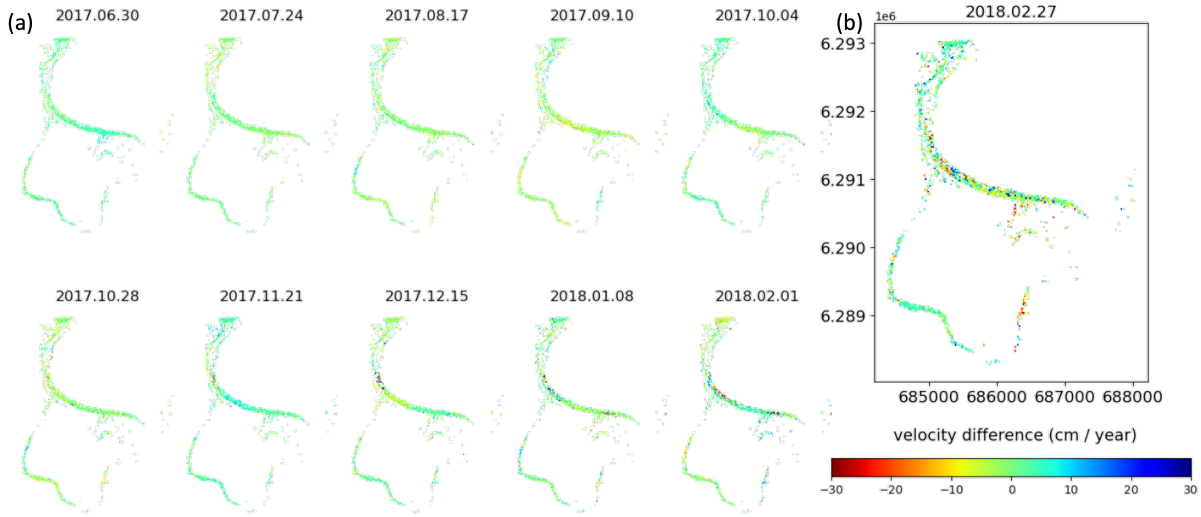

FIGURE 5.10: Spatial distribution of velocity difference between PS-InSAR and ISBAS. The temporal evolution of the velocity is in (a) and a zoom-in to the last date immediately before failure is in (b).

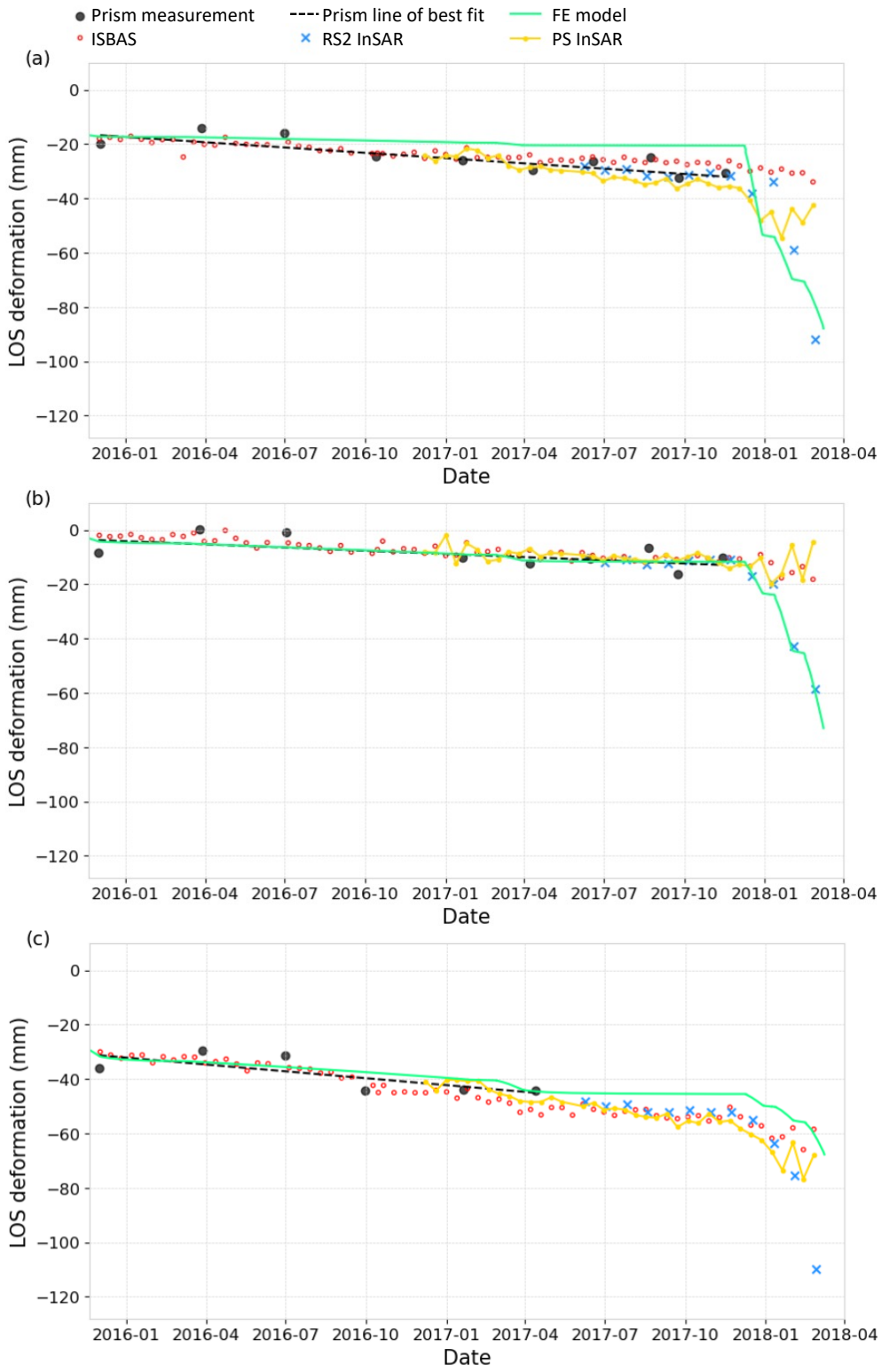

FIGURE 5.11: Temporal comparison of FE model, ground based prism measurements with ISBAS, PS InSAR and RS2 InSAR for construction stages (a) 4, (b) 5 and (c) 7.

5.3.2 Impact of Satellite Characteristics

Surprisingly large deformation differences are depicted in Figure 5.11 between open and commercial InSAR following the construction of the buttresses. The extent to which different sensor configurations of S1 and RS2 contribute to these differences are explored in this section. The potential impacts of changing incidence angles of the satellite beam and orbital heading angles on deformation measurements are quantified.

S1 incidence angle

While the incidence angle of RS2 is 38.5°, the incidence angle of S1 is within a range of 33.3°- 38.7°as outlined in Table 5.3. This is because, the spatial footprint of S1 data is very large, and therefore the incidence angle varies depending on the position of the site relative to the footprint, as illustrated in Figure 5.12. In the case of Cadia TSFs, there are two 'bursts' covering the test site. Bursts are sequences of radar pulses and are the fundamental imaging unit of radar data collected by S1. Figure 5.13 plots the location of Cadia TSFs relative to the ground footprint of S1 bursts. The incidence angles of the signal is reported in the S1 metadata and correspond to the centre of each burst. Therefore, given the incidence angles and the spatial footprint of each burst, the exact incidence angle corresponding to the location of Cadia, θ_{Cadia}, can be calculated using equations 5.1 and 5.2:

$$\delta\theta = (\theta_{burstA} - \theta_{burstB}) * \frac{l_{Cadia}}{l_{burstA\_burstB}} \tag{5.1}$$

$$\theta_{Cadia} = \theta_{burstA} - \delta\theta \tag{5.2}$$

The incidence angles for the centres of burst A, θ_{burstA}, and burst B, θ_{burstB}, are reported as 38.7° and 33.3°, respectively, where l_{Cadia} is the distance from the centre of burst A to the centre of Cadia TSFs and $l_{burstAburstB}$ is the total distance between centres of burst A and burst B. The burst distances are determined programmatically from the geo-coded vector files of the burst footprints. Equation 5.1 gives the difference in

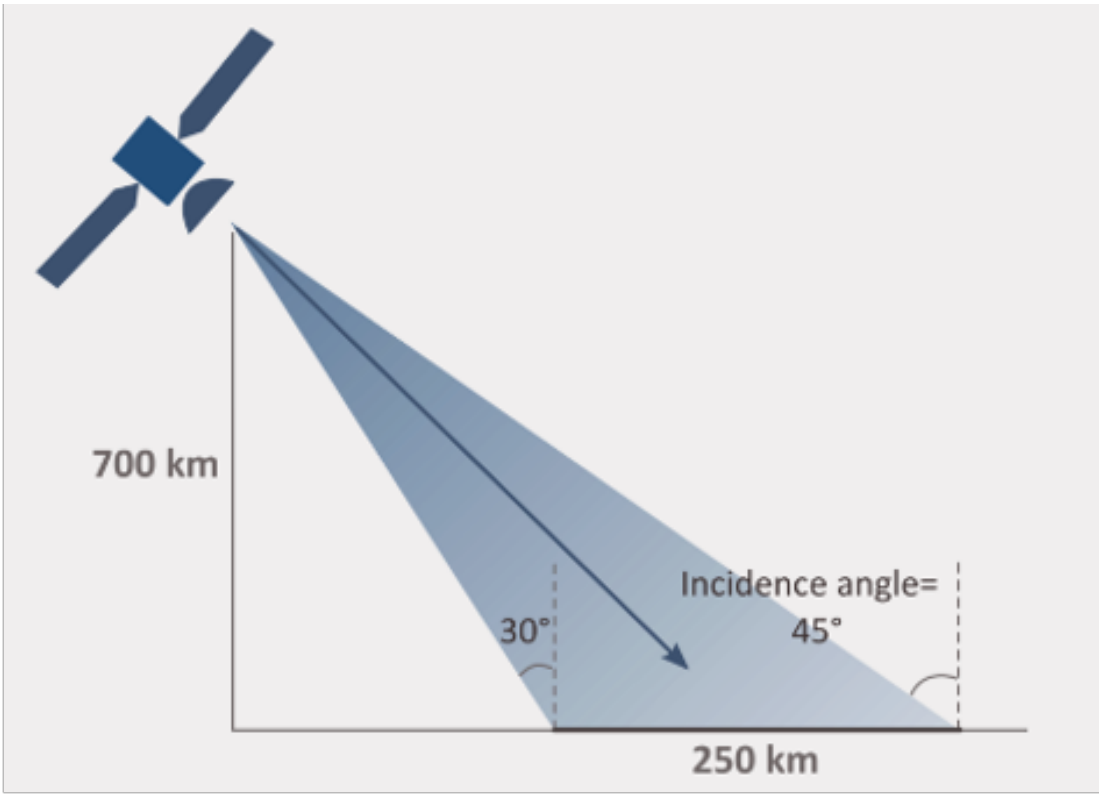

FIGURE 5.12: Sentinel-1 incidence angle values across the spatial footprint. The incidence angles over Cadia range from 33.3° to 38.7°. From ©Geological Survey of Norway.

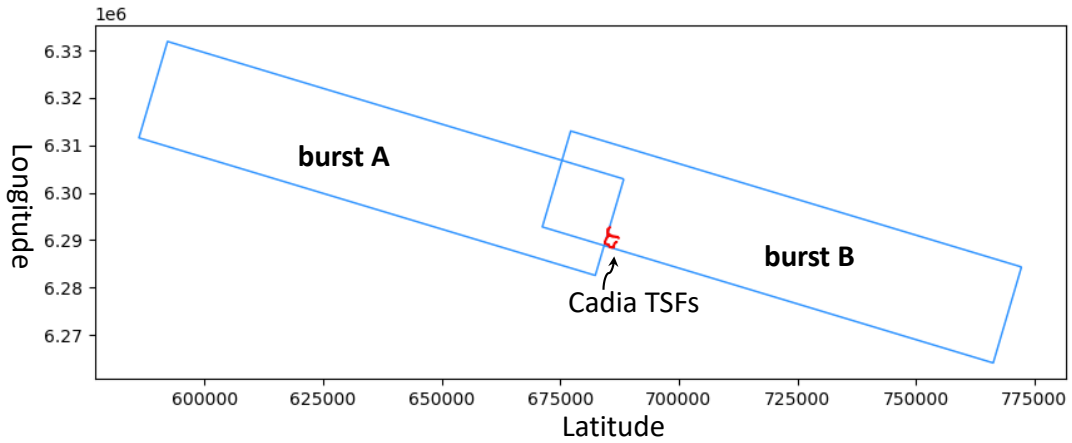

FIGURE 5.13: Location of Sentinel-1 bursts over Cadia TSFs.

angles between the centre of burst A to Cadia as 3.2°. Finally, Equation 5.2 results in an incidence angle for θ_{Cadia} of 35.5° for Cadia TSFs.

Finally, the combined impact of different satellite incidence and heading angles on InSAR-derived deformation measurements are quantified. The methodology described in Section 3.2 following Selvakumaran et al. (2020) is employed to simulate the LOS deformations measured from S1 and RS2 for different parts of the TSF. As the positions of the satellites change, it is expected that deformation measurements located in some parts of the TSF will be more sensitive to these changes than other parts.

Geometry of Sensor and TSF location

Figure 5.14 illustrates the geometrical relationship between dam orientation and the satellite flight path. For S1, the satellite heading angle is 167°; therefore, the heading angle measured from the North, $\theta_{heading\_N} = 180 - 167 = 13°$. For RS2, the satellite heading angle is 163°; therefore, $\theta_{heading\_N} = 180 - 163 = 17°$. As defined in Equation 3.1, the LOS deformation depends on θ and α, the signal beam incidence angle and angle of LOS relative to dam orientation. The beam incidence angles, θ, are 35.5°and 38.5°for S1 and RS2, respectively (derived in Section 5.3.2 and Table 5.3).

Figure 5.14 also plots the changing geometry corresponding to different orientations of the TSF sections. The angle of the TSF section from the North is indicated by β and the relationship between the TSF section relative to LOS is indicated by α. Using Equation 3.2, the resulting values of α for the slump area are 22° and 18° for descending S1 and RS2, respectively. A range of β values, varying from zero to 90°, are used to simulate the positions in various parts of the TSF section, as summarized in Table 5.4.

TABLE 5.4: Values of α relative to different parts of the TSF sections (β)

S1 Descending	RS2 Descending	TSF location
42°	38°	West of slump (β = 35°)
22°	18°	slump (β = 55°)
16°	12°	East of slump (β = 61°)
-1°	-5°	East of slump (β = 78°)

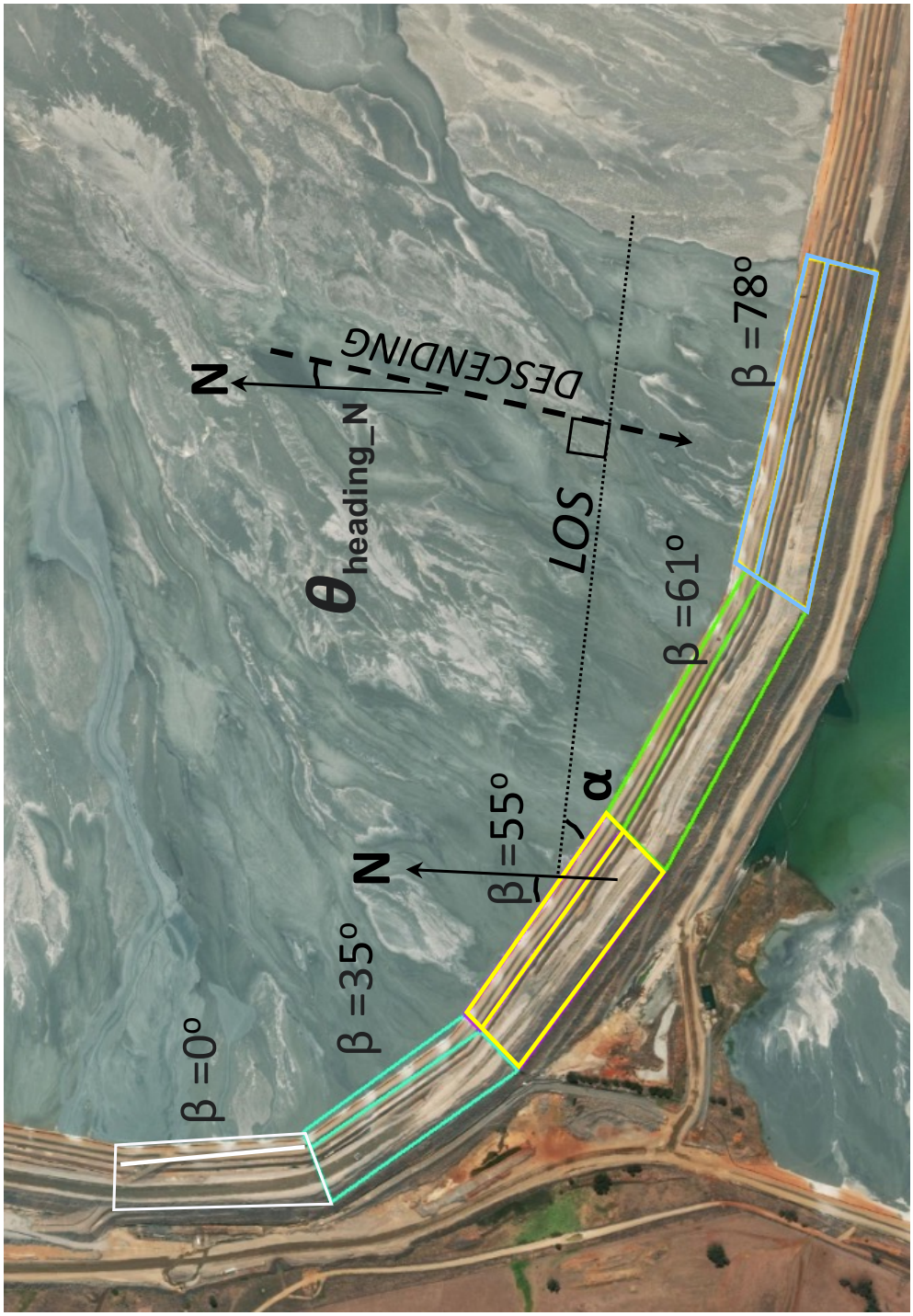

FIGURE 5.14: The geometrical relationship between the TSF orientation and the descending S1 satellite. Basemap image copyright ©1995–2020 Esri.

The simulated results of the relationship between the angle of the TSF sections relative to LOS are plotted in Figure 5.15. It quantifies the difference between LOS deformation measured by S1 compared to RS2, highlighting the difference between the two measurements for different TSF sections as indicated by β relative to different deformation magnitudes. It is clear that high magnitude deformations in the western-most parts of the TSF (towards $\beta = 0$) suffer from the highest error. The western parts are more impacted than the eastern sections. While some differences are expected in LOS deformation due to changing satellite position and the incidence angle of the signal beam, these differences are small, with maximum values are within $\pm$8mm. In the slump area, at $\beta = 55^{\circ}$ in Figure 5.15, the errors for S1 and RS2 are insignificant (green), even for high deformation magnitudes. Therefore, satellite position and beam differences do not account for the extreme differences observed between S1 and RS2 following buttress construction in Figure 5.11.

Finally, a source of further uncertainties arise from signal polarisation, which refers to the orientation of the signal's plane of oscillation (Cloude (2009), Flores-Anderson et al. (2019)). This affects the types of objects the SAR signals interacts with, as illustrated in Figure 5.16. It shows that both the transmitted and received signal polarisation can be controlled, each having different effects on signal interaction. Typically, the first letter represents the transmitting polarisation and the second the receiving polarisation. For instance, VV polarisation may interact more with the slopes of the TSF, while HH is likely to interact with horizontally aligned features, such as the TSF crest. Satellite signal polarisation cannot be corrected during post-processing and is therefore, beyond the scope of this research.

5.3.3 Impact and correction of phase unwrapping errors

From the basic SAR wave characteristics, it can be seen that $\pi = \lambda/4$ and the maximum movement that can be detected is 2π. Given Itoh's condition (Itoh (1982)), a wrapping threshold can be defined (Reinders et al. (2021)). In the case of C-band SAR sensors used in this study, Sentinel-1 and Radarsat-2, the wrapping threshold equals $\frac{\lambda}{4} = 14$mm. This means, if a measurement is close to the $\pm\frac{\lambda}{4}$ threshold, between any two dates of acquisitions, then there is a likelihood of phase ambiguity inherent to the

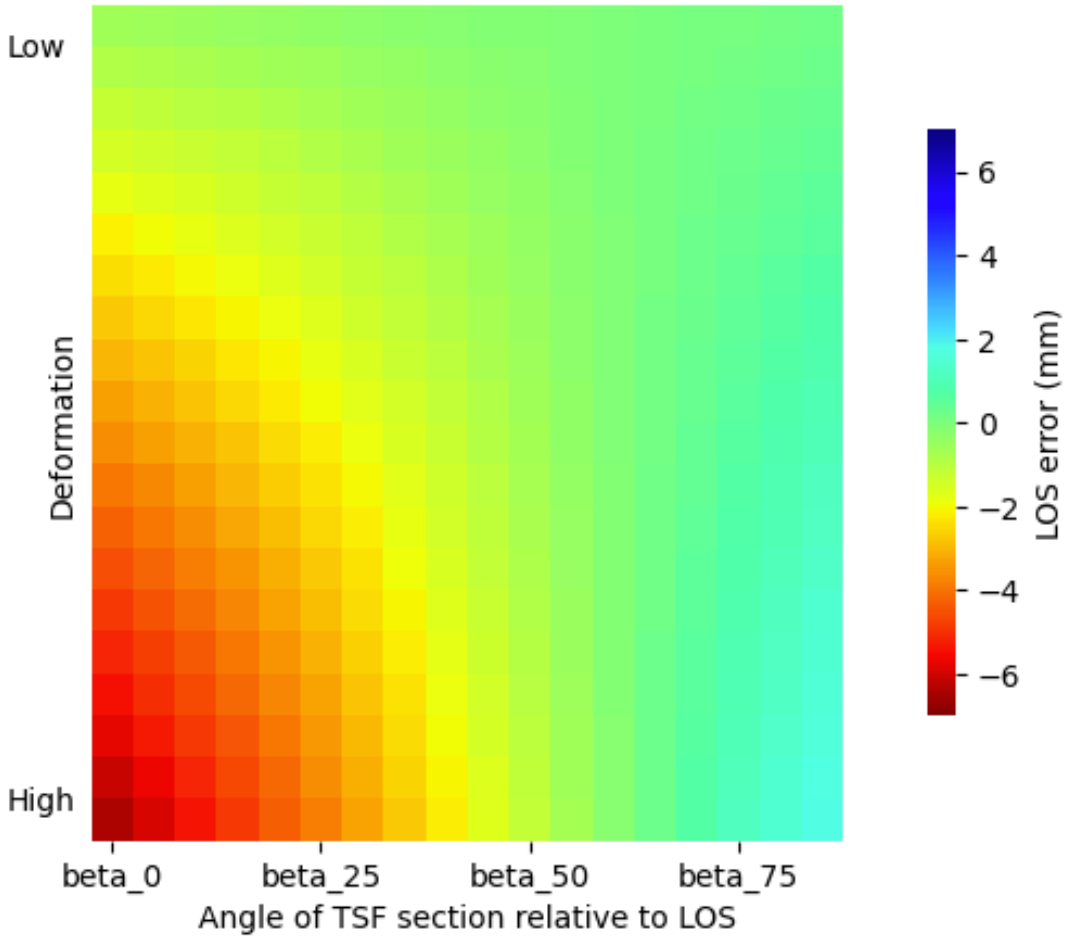

FIGURE 5.15: Relationship between the angle of TSF sections relative to LOS. The LOS error is defined as the difference in LOS deformation calculated for S1 and RS2 sensors relative to changing angle of TSF sections. Simulated vertical and horizontal deformation data are used to determine the resulting LOS deformation of the sensors. The TSF slump area is located at an angle of $\beta = 55°$.

InSAR measurements. In Reinders et al. (2021), the likelihood of phase ambiguity inherent to InSAR measurements close to the $\pm\pi$ are taken account of to consider other possible solutions at $\pm$28mm. Then, independent deformation measurements from levelling data are used to confirm the true InSAR solution possibilities.

In real world scenarios, the Itoh condition for phase unwrapping may not be fulfilled due to factors such as noise, fast deformation, or actual discontinuities between adjacent samples (Itoh (1982)). This can result in wrong multiples of 2π being added or subtracted in the phase unwrapping process. The geotechnical model results in Figures 5.11 (a) and (b) suggest that the deformation behaviour has changed due to a much faster deformation following the construction of buttresses, as discussed in

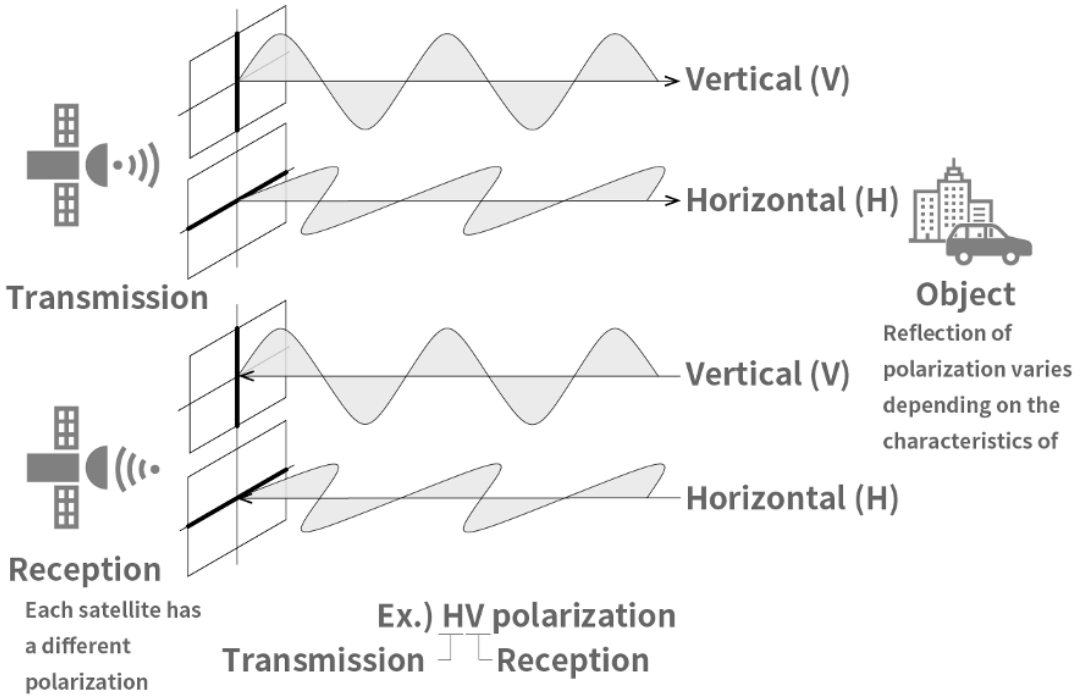

FIGURE 5.16: SAR signals polarisation describes the orientation of the plane of oscillation of the signal. The SAR signal can be both transmitted and received in different directions, depending on sensor characteristics. From Sorabatake (2020).

Chapter 3. The potential impacts of such a change of deformation to fast and non-linear behaviour on phase unwrapping is demonstrated graphically in Figures 5.17 (a) - (d). The true deformation is simulated in Figure 5.17 (a), where the trend changes over time from trend 1 to trend 2. For each measurement, multiples of 2π are added until the phases fall within the $\pm\pi$ range, as illustrated in Figure 5.17(b). The measurements in the $\pm\pi$ range represent the wrapped phases, which are what is actually measured through InSAR.

In the implemented PS-InSAR approach, an assumption of a linear deformation model is made, as represented by trend 1. The number of multiples of 2π that are required to be added to the true phases on trend 2 to obtain the wrapped phases is unknown. Given this uncertainty surrounding the exact solution, both plots in Figures 5.17(c) and (d) provide potentially viable but incorrect solutions to phase unwrapping. In this example, it is not possible to resolve the phase ambiguity and find the true solution from InSAR alone without external data.

In the case of Cadia TSF, the geotechnical modelling results, prism measurements

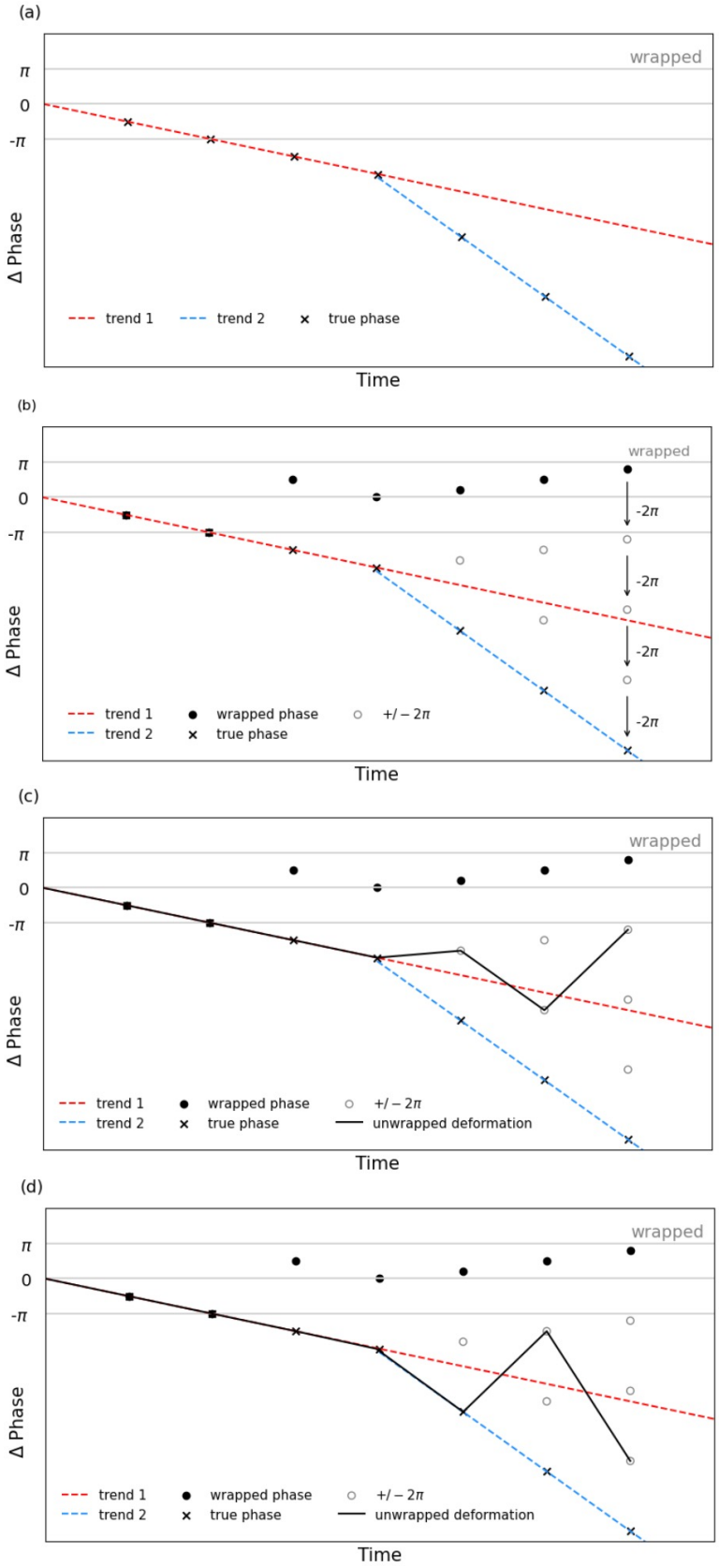

FIGURE 5.17: A demonstration of phase unwrapping using a linear deformation model. The true deformation trends are plotted in (a), where trend 1 changes to a steeper trend 2. The wrapped phases, confined within the $\pm\pi$ range represent what would be measured by InSAR, as shown in (b). To recover the true deformation trends from the wrapped phases, an unknown multiple of 2π needs to be subtracted. (c) and (d) illustrate potential unwrapping solutions, but these represent examples of incorrect phase unwrapping.

and RS2-InSAR data are available as external data for verifying S1 based ISBAS and PS-InSAR. Unfortunately, it is not possible to use the prisms, since they were removed as part of the construction of buttresses. Therefore, the FE model results and RS2-InSAR datasets may be used as reference for the number of multiples of 2π required for PS-InSAR phase ambiguity illustrated in Figures 5.18(a) - (c). In these plots, the InSAR data agree relatively well with geotechnical approaches up to the construction of buttresses. As discussed in Chapter 3, buttresses 1 and 2 were constructed in the slump area on 2017-12-09 and 2018-01-12 (YYYY-MM-DD), respectively. The phase ambiguity of PS-InSAR is addressed through subtraction of the following multiples of 2π from the last three measurements, 2018-02-01, 2018-02-13 and 2018-02-25: 1x2π, 1x2π, 2x2π, respectively. The phase ambiguity corrected PS-InSAR agrees well with both geotechnical FE predictions and high resolution RS2-InSAR measurements for dam stages 4 and 5 in Figures 5.18 (a) and (b).

However, in the case of dam stage 7 in Figure 5.18 (c), the phase ambiguity corrected PS-InSAR agrees well with RS2-InSAR but not the geotechnical model results. The post buttress construction behaviour of PS and RS2-InSAR data are similar to the behaviours observed for stages 4 and 5 in Figures 5.18 (a) and (b). Interestingly, for TSF stage 7, both S1 PS ambiguity-corrected data and RS2 InSAR exhibit a strong agreement with each other, but not with the FE model. The fact that deformation measurements from two independent InSAR processing methods using different types of SAR data agree is significant. However, given the uncertainties inherent in both InSAR and geotechnical modelling, it is challenging to resolve this discrepancy without external ground-truth data. If the FE model represents the truth, then the discrepancies may be attributed to factors such as distortions resulting from the interaction of the SAR signal relative to TSF geometry. For example, the steepness of the higher dam stages such as stage 7 may make it more susceptible to the impacts of known radar distortions such as shadow or layover. Other factors such as the size of the spatial footprint of the dam stages being relatively small compared to that of the buttresses may be resulting in the SAR signal to reflect in ways that result in mixed signals from stage 7 and the buttresses.

On the other hand, if the PS and RS2-InSAR data represent the truth, then it may indicate that the FE model is not able to accurately capture the deformation of higher

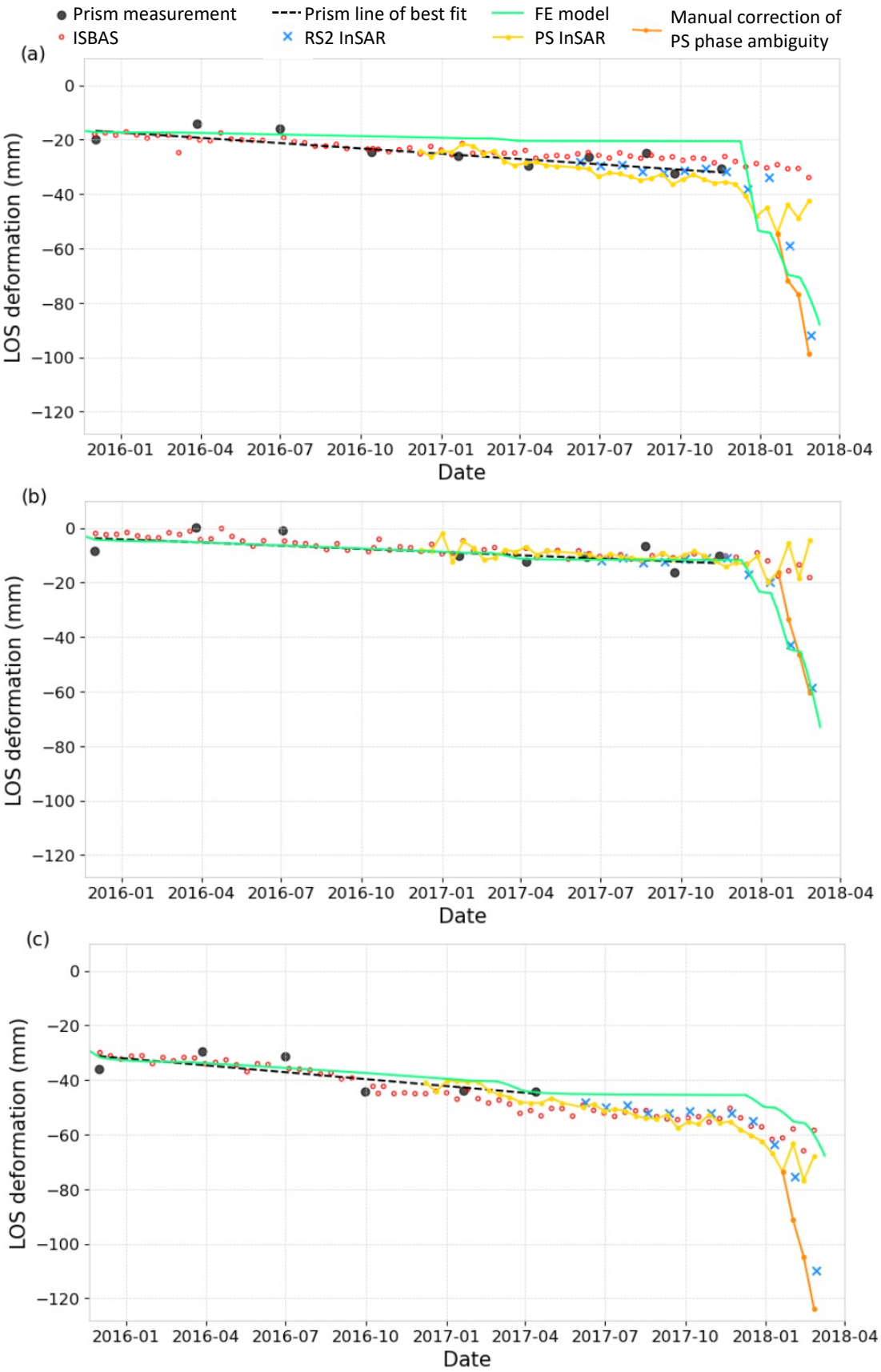

FIGURE 5.18: Potential solutions to PS phase ambiguity are proposed based on manual correction. Temporal comparison of FE model, ground based prism measurements with ISBAS, PS InSAR and RS2 InSAR for construction stages (a) 4, (b) 5 and (c) 7.

dam stages such as stage 7. This can result from the assumptions made in the modelling and parameter uncertainties. As demonstrated in Chapter 3, the deformation signals of higher dam stages are dominated by the deformation of the tailings, as they rest on thicker tailings. Therefore, this discrepancy may arise from uncertainties in the tailings parameters of the FE model. For instance, the tailings are represented as single units for each TSF stage, which does not capture the fact that tailings properties, such as particle coarseness, vary horizontally (Chapter 2).

Both differences in SAR data spatial resolution, along with phase unwrapping errors, have been proposed as possible explanations for the large discrepancies in the measurement distributions observed between PS-InSAR and RS2-InSAR in Figures 5.6 (a) and (b). The successful alignment of PS-InSAR deformation magnitudes with RS2-InSAR after phase ambiguity correction implies that pixel size differences have minimal impact. This indicates that the inability of Sentinel-1 InSAR to capture large magnitude deformations preceding TSF failure is not an inherent limitation of the sensor, but rather a challenge that can be addressed through adjustments in InSAR processing and phase ambiguity correction.

Moreover, Figure 5.17 illustrates a simplified scenario that does not take into account of other complexities such as noise in the data. The level of noise can disrupt the phase unwrapping process, as it may be confused with large deformation signals. The main sources of noise in SAR interferometry can be from sensor noise or from deficient atmospheric phase screening procedures. Therefore, phase unwrapping errors may occur in the InSAR data due to (1) a deformation approaching or exceeding the wrapping threshold, yielding an incorrect ambiguity number; (2) the assumptions made in the unwrapping methodology. In the case of PS-InSAR, if a linear deformation model is assumed and the deformation is non-linear, then this imposed linearity does not capture the deformation dynamics; (3) signal noise.

5.3.4 Vertical and horizontal RS2-InSAR motion

The distribution of the decomposed RS2 horizontal and vertical deformation over Cadia are plotted in Figure 5.19. Most of the data are within $\pm$25mm with large ranges of outliers. Before the decomposed motions of RS2-InSAR can be compared to results from FE model and prisms, the horizontal motions need to be aligned, because they

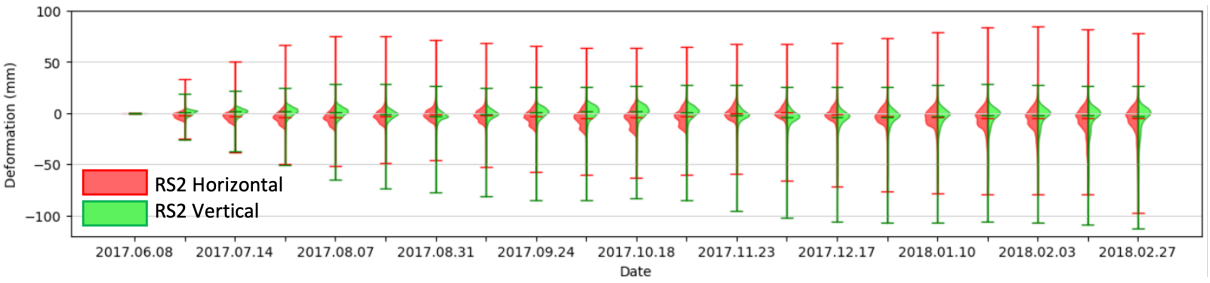

FIGURE 5.19: The distribution and density of decomposed RS2-InSAR data, (a) horizontal and (b) vertical components.

measure deformation in different directions. The horizontal motion modelled by FE is in the direction transverse to TSF, whereas the horizontal motion derived from InSAR is in the East to West direction. Figure 5.20 plots the geometry of the horizontal motion of RS2-InSAR relative to FE. The FE model gives horizontal motion results in the direction transverse, δ_T, to the TSF section as illustrated in Figure 5.20(a). The longitudinal deformation is assumed zero given the plane strain assumptions of the 2D model as discussed in chapter 3. The horizontal component of the motion derived from RS2 is plotted as δx_{RS2} in the Westward direction defined by 'W' and from FE is plotted as δx_{FE} in Figure 5.20(b). The FE model represents the slump area, which is located in a TSF section of $\beta = 55°$ from the North. The δx_{RS2} can be mapped onto δx_{FE} following:

$$\delta x_{FE} = \delta x_{RS2} cos(\beta) \tag{5.3}$$

The horizontal component of RS2-InSAR, δx_{RS2}, converted to the geometry of FE predictions, δx_{FE}, is shown in Figures 5.21 for the following stages: (a) and (b) correspond to stage 4; (c) and (d) stage 5; and, (e) and (f) stage 7. The horizontal deformation through time is plotted in Figures 5.21 (a), (c) and (e) (left column) and the improvements from the geometrical correction are quantified in Figures 5.21 (b), (d) and (f) (right column). The coefficient of determination, R^2, is calculated between FE predictions and the line of best fit for RS2-InSAR measurements, given their differing temporal sampling. Overall, the geometrical correction significantly improves the alignment, with R^2 increasing from 0.47 to 0.85 and from 0.15 to 0.8, for stages 4 and

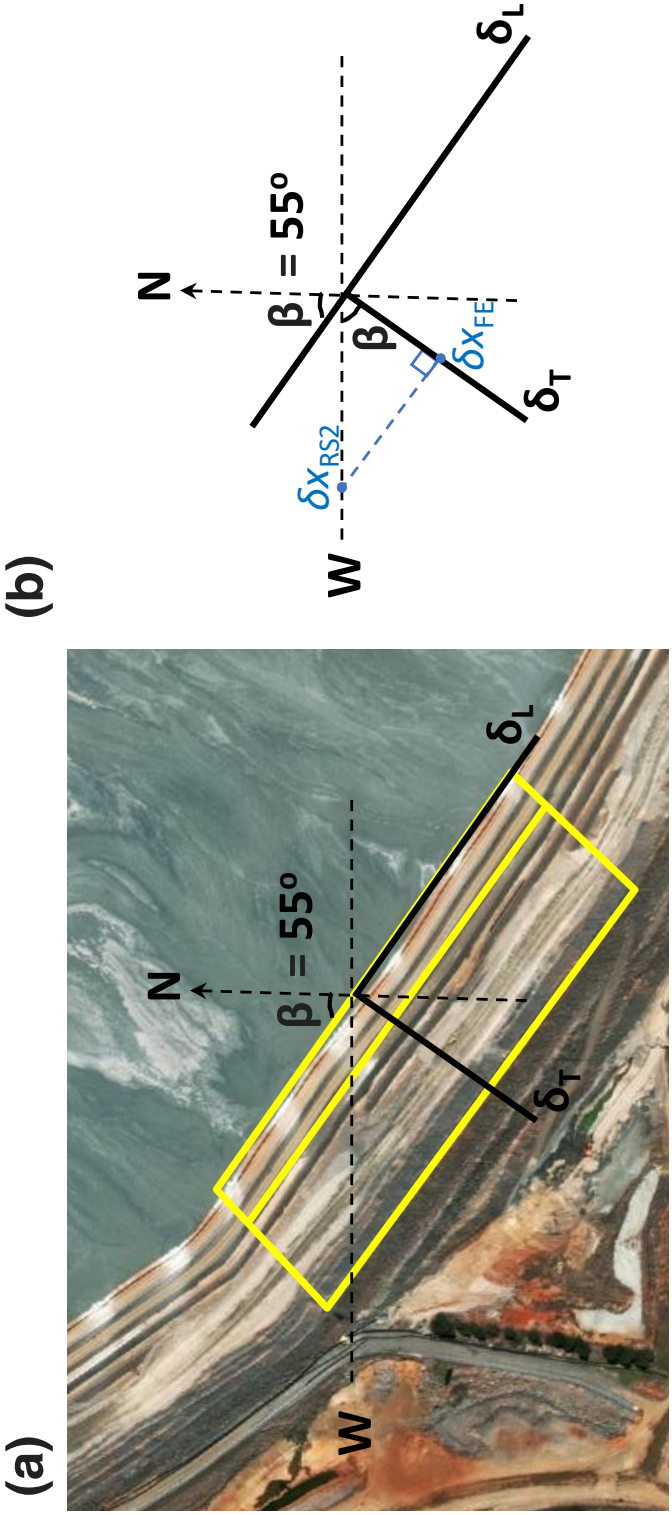

FIGURE 5.20: (a) Diagram for mapping RS2-InSAR horizontal motion (δx_{RS2}) onto FE horizontal deformation (δx_{FE}). FE horizontal motion is in the direction transverse to TSF, whereas the horizontal motion derived from InSAR is in the East to West direction. Basemap image copyright ©1995-2020 Esri. (b) Trigonometric transformation of δx_{FE} onto δx_{RS2}.

7, respectively. For stage 5, although the geometrically corrected measurements plot closer to the dotted line (where RS2 measurements equal FE predictions), the R^2 decreases slightly from 0.72 to 0.67. In these plots, the FE predictions suggest that the horizontal deformation is expected to be relatively slow and therefore, well suited to InSAR (i.e. below the wrapping threshold). Additionally, the fact that the horizontal components of FE and RS2-InSAR align well suggests that the limitations of InSAR in detecting North - South motion, due to the polar orbit of the SAR satellites, are negligible in the slump area of the TSF.

On the other hand, the FE predictions suggest that vertical deformation is expected to be rapid during buttress construction, making the InSAR measurements more susceptible to phase ambiguities. The large deviations between δy_{RS2} and δy_{FE} are illustrated in Figures 5.22 (a) to (f). The vertical components of RS2-InSAR, δy_{RS2}, are plotted for the following stages in Figures 5.22: (a) and (b) correspond to stage 4; (c) and (d) stage 5; and, (e) and (f) stage 7. The phase ambiguities are resolved manually following the discussion in Section 5.3.3. Specifically, a single cycle of 2π is subtracted from the deformation measurements in stages 4 and 5, and 2π is added in stage 7, as shown in Figures 5.22 (a), (b) and (c), respectively. The improvements are then quantified in Figures 5.22 (b), (d) and (f) (right column). In these figures, the R^2 values improved from negative for all stages to 0.6, 0.94 and 0.6, for stages 4, 5 and 7, respectively. Since R^2 is upper bounded by 1, values closer to 1 indicate a good fit, but it is not lower bounded, making negative values of R^2 possible, which suggest a worse fit than a horizontal line (Chicco et al. (2021)). Therefore, the phase ambiguity corrected deformations align well with the FE model and confirm that the main differences between FE predictions and InSAR measurements are due to rapid vertical subsidence resulting from buttress construction.

5.4 Summary

The limitations of InSAR, as identified in Chapter 3, have been further investigated to explore whether they are inherent to the InSAR method or due to sensor characteristics of S1. The extent to which the limitations can be overcome through re-processing with a different InSAR method or use of higher resolution SAR data have been presented.

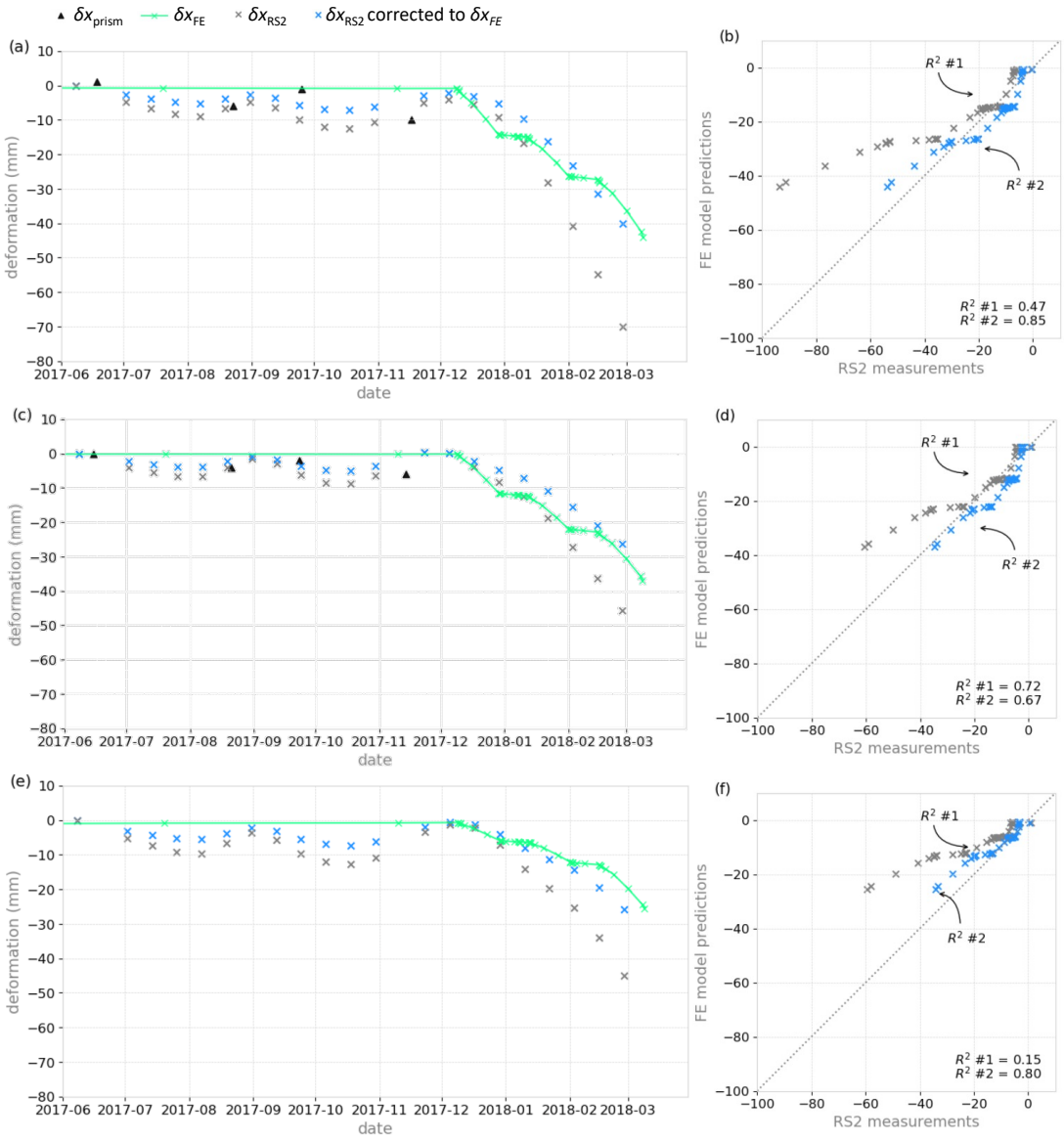

FIGURE 5.21: The horizontal deformation components (δx) for prisms, FE, RS2 are plotted. These plots represent the deformation measured at the following stages : (a) and (b) correspond to stage 4; (c) and (d) correspond to stage 5; and (e) and (f) correspond to stage 7. Since the horizontal measurements for RS2 and FE are in different directions, the RS2 has been adjusted to the same geometry as that of FE. The improvement resulting from the geometric correction is quantified in (b), (d) and (f) (right column); and the dotted line represents the line of perfect fit, where RS2 measurements equal FE model predictions.

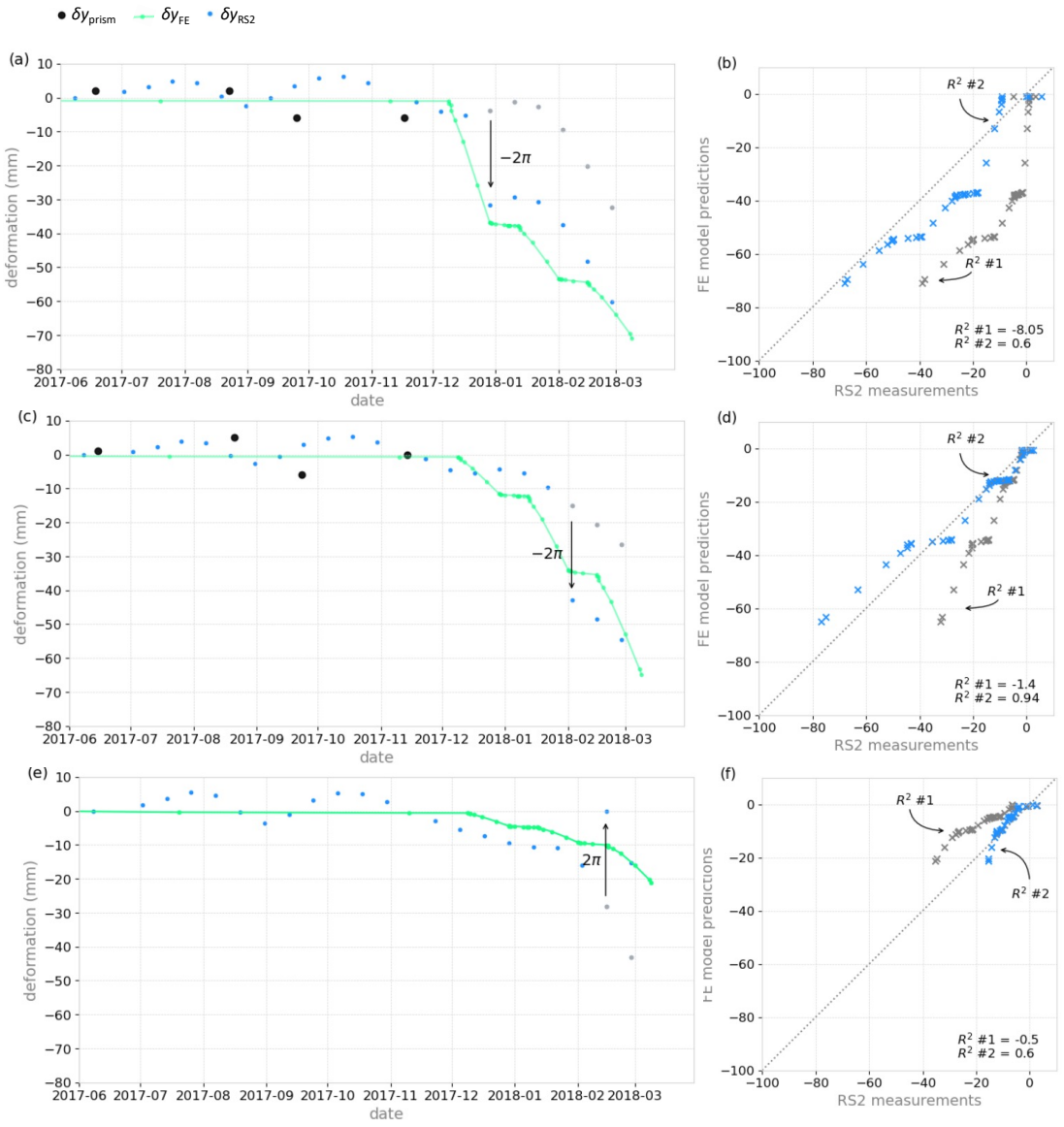

FIGURE 5.22: The vertical deformation components (δy) for prisms, FE, RS2 are plotted. These plots represent the deformation measured at the following stages : (a) and (b) correspond to stage 4; (c) and (d) correspond to stage 5; and (e) and (f) correspond to stage 7. The improvement of the manual phase ambiguity correction of RS2-InSAR is quantified in (b), (d) and (f) (right column); and the dotted line represents the line of perfect fit, where RS2 measurements equal FE model predictions.

The findings demonstrate the advantages and disadvantages of different InSAR processing approaches within the context of TSFs.

The main advantages of ISBAS are in its higher spatial density of measurements, which enables a better geo-location of the failure surface. In contrast, PS-InSAR provides spatially more sparse measurements, which lead to the boundaries of the failure surface being outlined less clearly and appearing more diffuse. On the other hand, the advantages of PS-InSAR over ISBAS are in its sensitivity to the occurrence of phase unwrapping errors. It is challenging to identify phase unwrapping issues from ISBAS time-series, making it difficult to correct for something that is not detected.

Resolving InSAR phase ambiguities is not possible without the guidance of external data. Initially, ground-based prisms were used as reference for comparing the InSAR and geotechnical FE predictions. However, the prisms were removed during the period when phase ambiguities are detected. Therefore, FE predictions and high resolution RS2-InSAR data have been used to correct for the phase ambiguities in PS-InSAR. The corrected PS-InSAR measurements show good agreement with the FE predictions for TSF stages 4 and 5, but not stage 7. Nevertheless, the corrected PS-InSAR measurements align well with RS2-InSAR across all three dam stages. Because both InSAR and geotechnical modelling are subject to inherent uncertainties, it is challenging to resolve the discrepancies present in stage 7, without an external ground truth data. Several potential explanations for this discrepancy are proposed, along with ways to test the hypothesis further. Finally, the workflows outlined in this chapter provide a framework for integrating these different technologies to help reduce the uncertainties present in each.

Chapter 6

Towards a More Robust Early Warning Framework for TSFs

An operational early warning system for TSFs would be made up of an interdisciplinary systems of governance, incorporating disaster management structures, addressing external and internal complexities related to risk and vulnerability assessments, emergency preparedness plans and the bureaucracy of the decision making process (Hudson-Edwards et al. (2024)). It represents a systems' architecture challenge, which falls outside the scope of this research. Therefore, the framework presented in this thesis is designed to serve as a component within this larger system, providing early warning insights.

This chapter explores the value and impact of different InSAR data sources on the performance of the early warning algorithm developed in Chapter 4, specifically the embedded entities within a deep learning (EE-DL) workflow. It evaluates the potential improvements in early warning capabilities that may be achieved with different types of InSAR datasets discussed in Chapter 5, including Sentinel-1 (S1) PS-InSAR and high-resolution commercial InSAR data from Radarsat-2 (RS2). Since the objective of this chapter is to evaluate the performance of EE-DL with different types of InSAR datasets, each dataset is analysed independently. Apart from the decomposed vertical and horizontal components of RS2-InSAR, no dataset merging has been performed.

The change from S1 to RS2 represents an increase of five times the spatial resolution and an order of magnitude in data volume. Such scaling provides an opportunity to demonstrate the kinds of modifications that are necessary for scaling up, which would be necessary in applying the EE-DL approach to large-scale projects like the

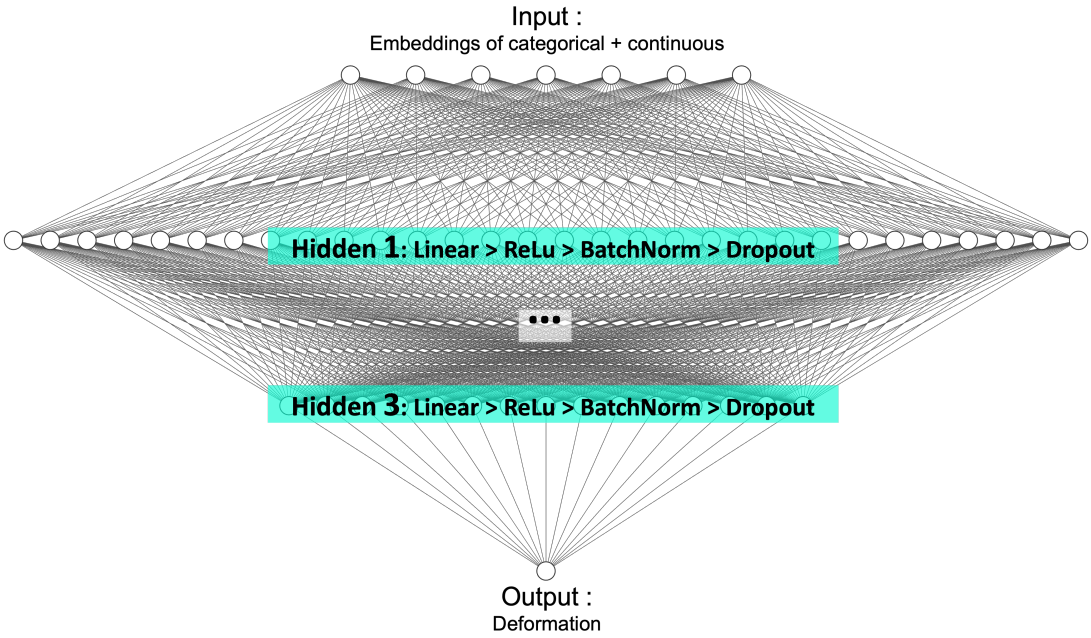

FIGURE 6.1: The three layer fully connected architecture used in this study. The first hidden layer starts with 1100 neurons, and at each hidden layer, the number of neurons reduces by 100. The visualisation of the architecture is generated through the NN-SVG tool (Lenail (2019)).

European Ground Motion Service (Crosetto et al. (2020) and Siegmund et al. (2022)). Moreover, the ease with which different data types can be integrated into the EE-DL framework is demonstrated using line-of-sight RS2 InSAR ascending, descending, as well as decomposed vertical and horizontal motion components.

6.1 Methodology

Given the significant increase in the size of the RS2-InSAR data compared to the S1-InSAR, a shallower neural network architecture is employed in this study with consideration to computational resource and efficiency. Figure 6.1 illustrates the adopted fully connected architecture, which is composed of three hidden layers. Each hidden layer consists of Linear–ReLU–Batch Norm–Dropout layers, with 1000, 500 and 250 neurons, respectively. The hidden layer structure and the neuron size ratio are similar to the architecture used for training embeddings in Guo and Berkhahn (2016), Howard and Gugger (2020a), Bayaraa et al. (2023). The output layer is a linear layer with a sigmoid activation function.

For all RS2-InSAR datasets, the same approach to embeddings as in Chapter 4 is

followed, where all InSAR metadata are treated as categorical, except for one continuous variable, "elapsed". Therefore, embeddings will not be created for this continuous variable. The entities selected as categorical variables are listed in Tables 6.1 and 6.2 for RS2-InSAR descending and 2D decomposed motions, respectively. The entities for RS2-InSAR descending are the same as the ones created for the S1 descending data in Chapter 4. Moreover, the embeddings and the model parameters from Chapter 4 are adopted without any changes for S1 based PS-InSAR data.

The decomposed vertical and horizontal components of RS2-InSAR are combined into a unified dataset, rather than being handled separately by different models. This integration approach potentially offers the model additional hidden insights and relationships within the dataset that are not captured if the data are handled separately. An additional entity for the direction of the motion component, termed *motion_comp* is introduced within the RS2-InSAR vertical and horizontal stack to distinguish between them. It is treated as a categorical variable, as summarised in Table 6.2. Following the approach in Chapter 4, this study adopts the embedding size proposed in FastAI/Howard and Gugger (2020a), where the embedding size equals $1.6\gamma^{0.52}$.

The EE-DL workflow described in Chapter 4 cannot be directly applied on RS2-InSAR. While the embedding size rule from Howard and Gugger (2020b) works well for Sentinel-1 InSAR, it does not work for RS2-InSAR. Specifically, when RS2-InSAR is directly applied in the EE-DL workflow described in Chapter 4, the model fails to train. The embedding size rule in Howard and Gugger (2020b) assigns a value of 600 to very high cardinality variables, which is potentially too large. Therefore, the embeddings for longitude and latitude are capped at 200. Other key variables that require adjustment include, an increase in the batch size from 1000 to 20,000 for ascending/descending, and 50,000 for the decomposed data. Moreover, the learning rate is adapted cyclically following Smith (2017).

Due to the differing temporal resolutions of RS2 and S1 acquisitions, RS2-descending experiments within the EE-DL workflow generate predictions for dates ranging from 2018-01-10 to 2018-02-27 ('YYYY-MM-DD'). These dates are the closest matches to the EE-DL S1 prediction dates in Chapter 4. Given the less frequent acquisitions of RS2-InSAR, predictions are made for three steps instead of four steps (i.e. dates before failure). In contrast, the decomposed RS2-InSAR data, derived from the combination

TABLE 6.1: Embeddings for RS2-InSAR descending. The embedding size is calculated based on the size of the cardinality of the entities. The cardinality is the number of unique categories representing each entity.

Entity	Cardinality	Embedding Size
Longitude	224161	200
Latitude	224161	200
Day	12	6
Month	10	6
Year	3	3

TABLE 6.2: Embeddings for RS2-InSAR vertical and horizontal stack. The embedding size is calculated based on the size of the cardinality of the entities. The cardinality is the number of unique categories representing each entity.

Entity	Cardinality	Embedding Size
Longitude	101813	200
Latitude	101813	200
Day	18	8
Month	9	5
Year	3	3
motion_comp	3	3

of ascending and descending acquisitions, offer a temporal resolution comparable to that of S1-InSAR. As a result, the last four dates closest to those in Chapter 4 are selected for prediction in these data sets.

6.2 Results and Discussion

A comparison between machine learning predictions and real measurements are presented in Figures 6.2 - 6.8. In these figures, green areas indicate good agreement between predictions and measurements, resulting in minimal or close to zero differences. In contrast, red and blue areas indicate locations of 'unexpected' or anomalous deformations. These figures will be referred to as 'difference maps' hereon.

In the S1 PS-InSAR difference maps shown in Figures 6.2 (a) - (d), the predictions and measurements agree relatively well on all dates. There are no visually obvious, large anomalous clusters present in any of the maps. As discussed in Chapter 5, the

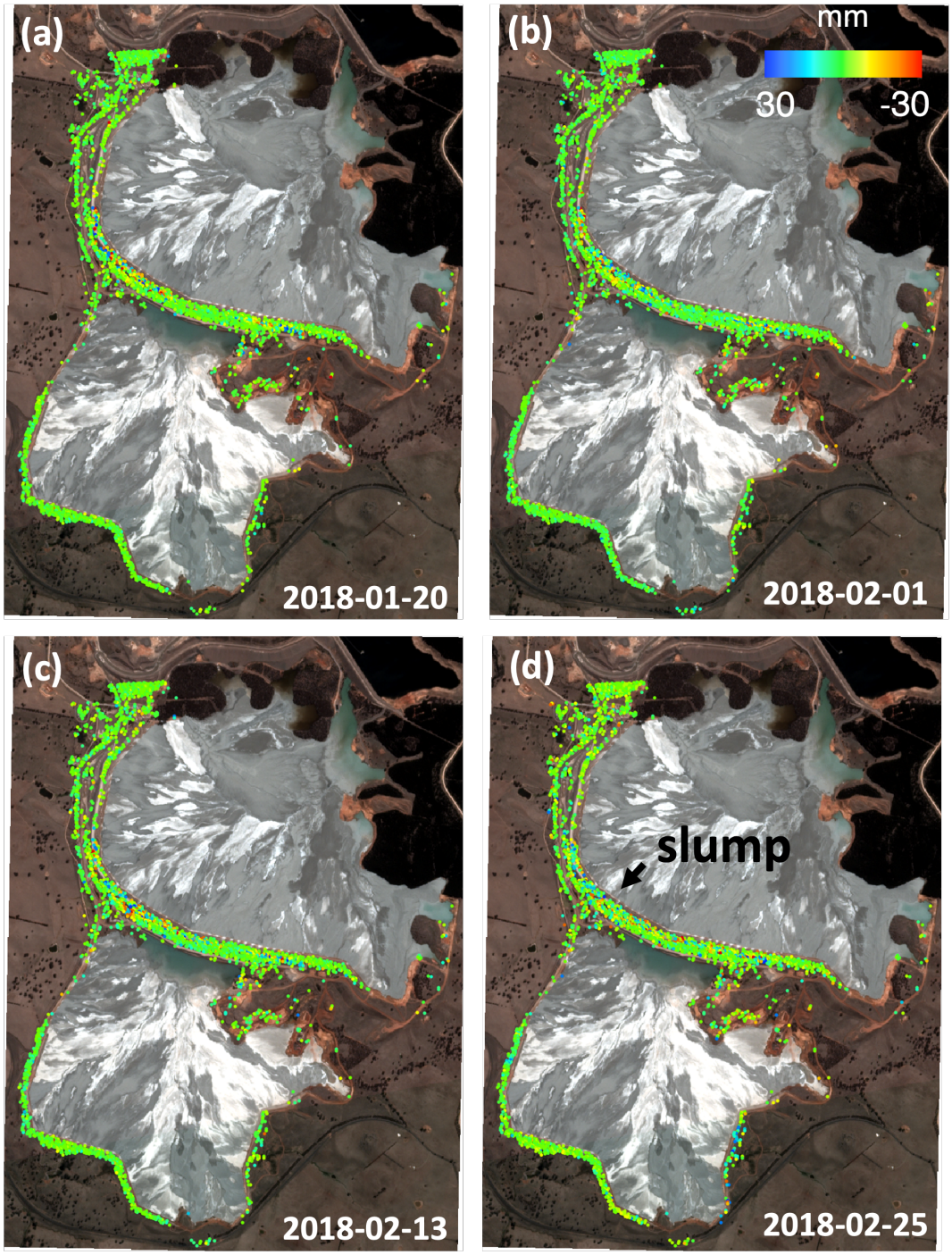

FIGURE 6.2: Difference between predicted and measured deformations on different dates using the PS-InSAR algorithm on S1 data. The dates are in the format of YYYY-MM-DD: (a) 2018-01-20, (b) 2018-02-01, (c) 2018-02-13 and (d) 2018-02-25. Basemap image copyright © 2020 Planet Labs PBC.

impacts of phase ambiguities are particularly pronounced in PS-InSAR, where temporal analysis of phase ambiguity (Figure 5.18) illustrates that the measurements are irregular and exhibit erratic patterns of both subsidence and uplift immediately before failure. This randomness in deformation is reflected spatially in the difference maps. The anomalous measurements are in small clusters scattered throughout the TSF and contain both low (red) and high (blue) measurements. Consequently, this may explain why the slump area is not clearly outlined in these PS-InSAR difference maps.

Moreover, the PS-InSAR difference maps have been clustered following the same methodology as the clustering of the ISBAS in Chapter 4. Figures 6.3 (a) and (b) compare the resulting clustered difference maps for ISBAS and PS-InSAR, respectively. The clustered ISBAS and PS results are spatially comparable, with most of the clusters being located in the slump area. There are noticeably more PS-InSAR clusters to the East of the slump and barely any clusters in the Southern TSF.

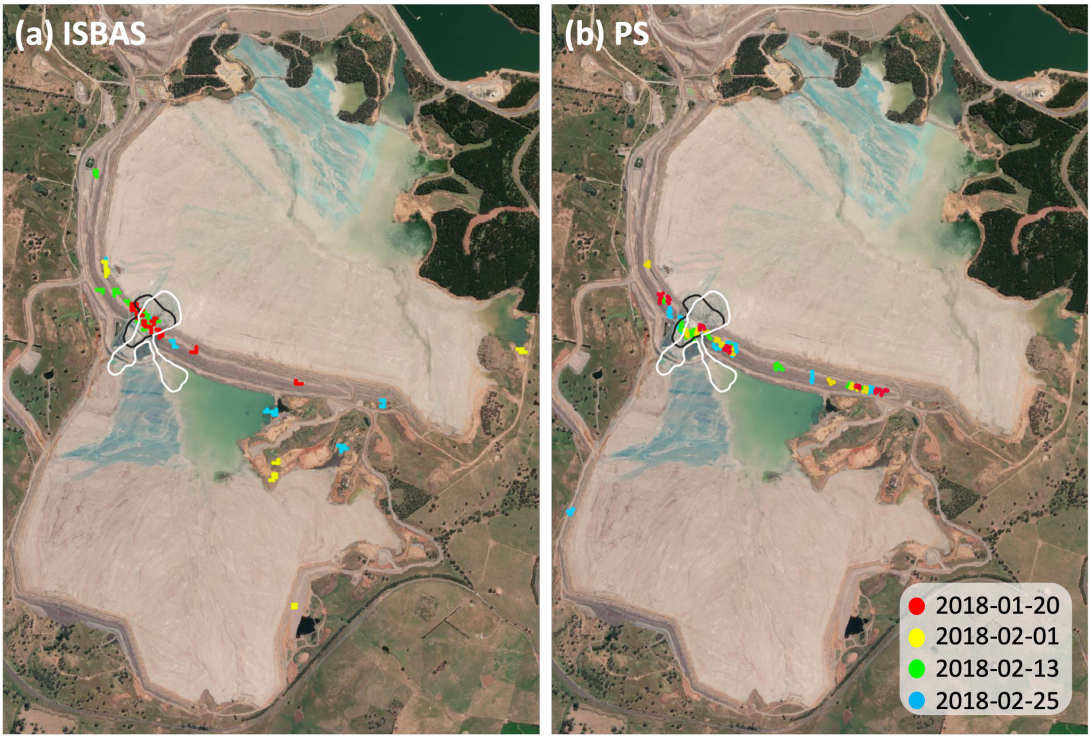

FIGURE 6.3: Spatial visualisation of clustered anomalies for (a) ISBAS and (b) PS-InSAR results. Basemap image copyright ©1995-2020 Esri

Additionally, the true and false anomalies detected by EE-DL were counted and are summarised in Figures 6.4 (a) and (b) for ISBAS and PS-InSAR, respectively. The results show that EE-DL consistently detects more true anomalies in PS-InSAR than in ISBAS across all dates. In PS-InSAR, the number of true anomalies consistently exceed

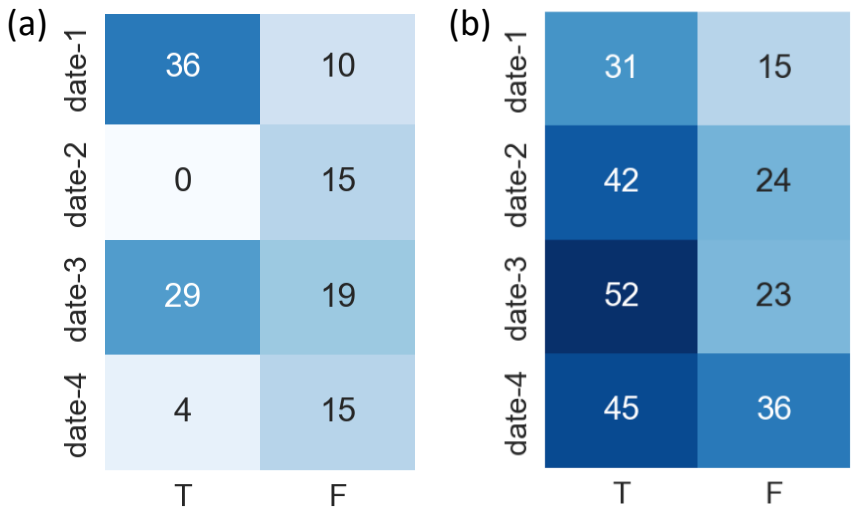

FIGURE 6.4: Summary count of the number of anomalous clusters detected by EE-DL for (a) ISBAS and (b) PS-InSAR.

the number of false anomalies, as shown in Figure 6.4 (b). In contrast, for ISBAS, the number of false anomalies exceed the true anomalies for dates 2 and 4 (Figure 6.4 (a)). This may be explained by the fact that phase unwrapping errors in PS-InSAR have an effect of exaggerating the signals of anomalous deformation behaviour, as discussed in Chapter 5, making the EE-DL task easier. This suggests that the occurrence of phase ambiguities potentially provide valuable insights, indicating changes in the deformation dynamics.

The RS2-InSAR ascending and descending difference maps are plotted in Figures 6.5 and 6.6, respectively. In the ascending data, the main rim of the NTSF is red for all the difference maps in Figures 6.5 (a) - (c). A noteworthy feature is the cluster of clear anomalous blue clusters visible in the slump area in Figure 6.5 (c) 2018-02-15. Unfortunately, it is not possible to track the development of this anomalous feature due to the large data gap of around 1.5 months that exists between the ascending dates in Figures 6.5 (b) and (c).

Interestingly, the descending RS2-InSAR difference maps in Figure 6.6 (a) and (b) reveal the evolution of two red parallel lines over time. These lines become more prominent and merge into a feature reminiscent of the slump morphology in Figure 6.6 (c). This observation raises the possibility that anomalous deformation patterns may be tracing the deformation associated with the buttresses. When the two parallel lines merge in Figure 6.6 (c), it potentially indicates the 'triggering' signature of the

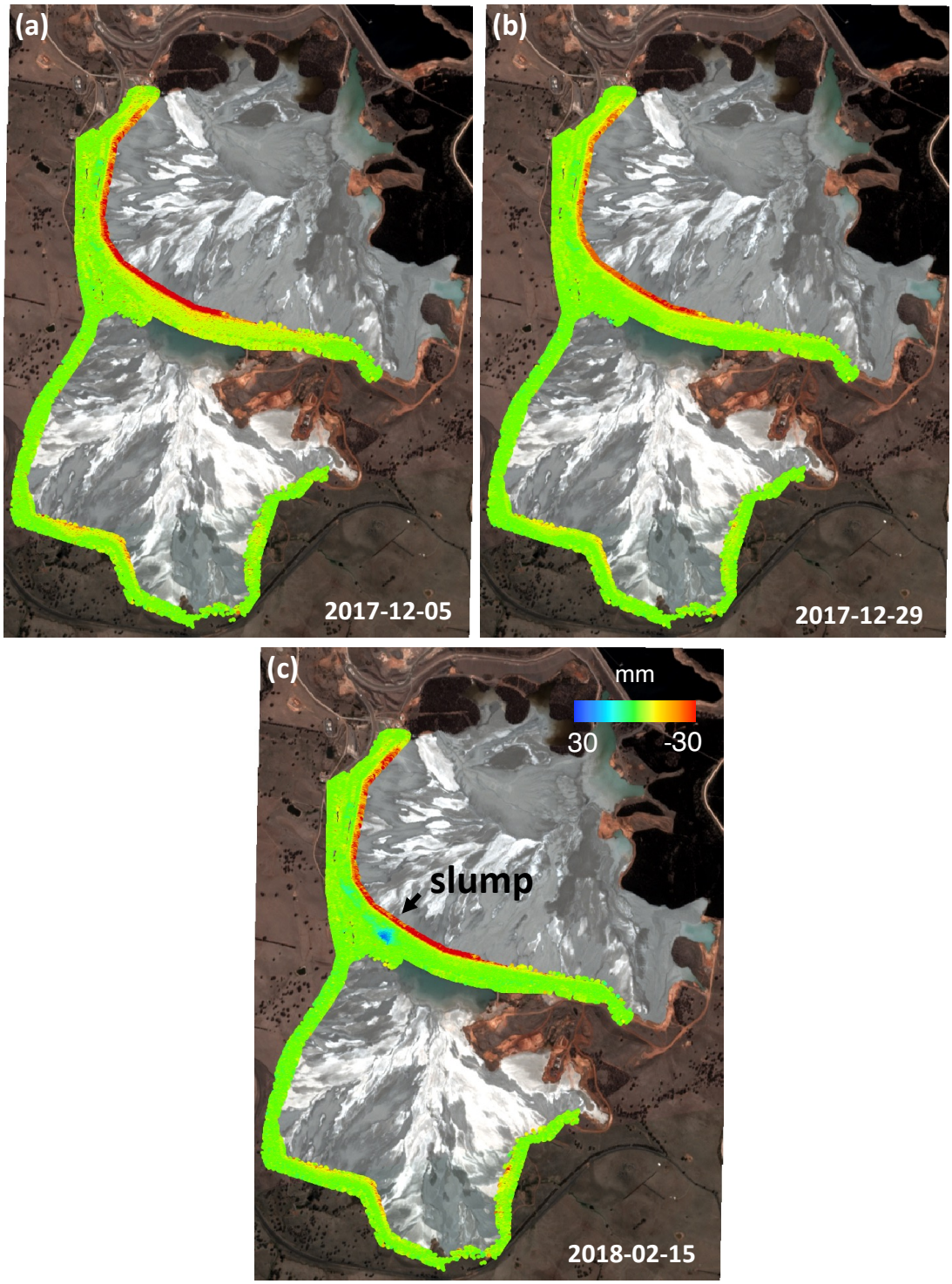

FIGURE 6.5: Difference between predicted and measured deformations on different dates on ascending RS-2 InSAR data: (a) 2017-12-05, (b) 2017-12-29 and (c) 2018-02-15. Basemap image copyright © 2020 Planet Labs PBC.

failure as distinct from buttress construction. Such a clear outline and development of different types of signals are detectable in these figures clearly due to the high spatial resolution of RS2 and is not visible in S1. This potentially implies that it may be possible to distinguish anomalous measurements due to the buttress construction and the triggering of failure. However, given that buttress construction itself contributed to the failure, it is challenging to highlight these signals as being distinctly separate.

Moreover, the lack of clear anomalous signature from the ascending data for Figures 6.5 (a) 2017-12-05 and (b) 2017-12-29 may be both due to the satellite orbit geometry or the temporal resolution of the ascending RS2-InSAR. In the descending difference maps, the anomalous deformation due to buttresses in the slump area reveal themselves in Figure 6.6 (b) 2018-02-03 which is around one month after Figure 6.5 (b) 2017-12-29. Therefore, the reasons for not detecting anomalous deformation in the slump area in Figures 6.5 (a) and (b) are probably due to the temporal resolution of the satellite rather than the ascending orbit geometry not being suitable. The fact that both ascending and descending geometries provide clear anomalous clusters in the last acquisition dates may indicate that both geometries are suitable for an early warning of failure for Cadia TSFs.

The decomposed RS2 vertical and horizontal difference maps are illustrated in Figures 6.7 and 6.8, respectively. The evolution of the vertical anomaly is made up of positive (blue) and negative (red) deformation clusters adjacent to each other, as seen in Figures 6.7 (b) to (d). This implies the presence of two different deformation mechanisms, resulting in the EE-DL model to either underestimate (red) or overestimate (blue) the measurements. A zoomed-in view of the failure area and a further interpretation of these clusters are available in Figure 6.9 (c). The anomalies in the slump area are most evident in the RS2 horizontal difference maps visualised in Figures 6.8 (a) to (d). The slump area is outlined as a distinct cluster adjacent to the anomalous deformations parallel to the dam. The slump area outline can be visually identified as early as 2018-01-22. This is the earliest point at which the anomaly can be observed compared to the other RS2 and S1 InSAR datasets. It makes sense that the horizontal motion components are best able to capture the failure signature, because horizontal motion is more directly related to failure than vertical motion.

Additionally, the anomalies observed in the the horizontal and vertical difference

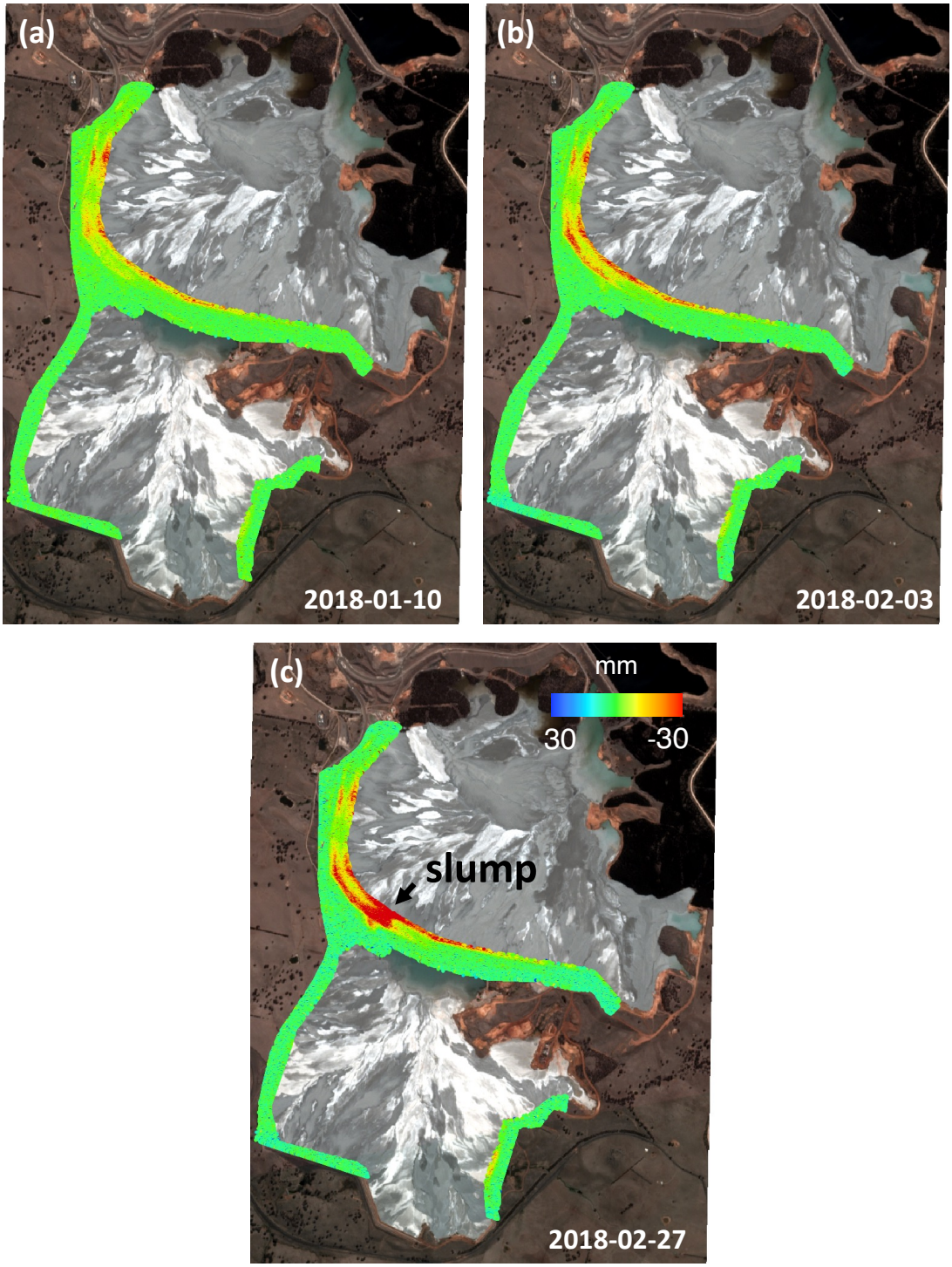

FIGURE 6.6: Difference between predicted and measured deformations on different dates on descending RS-2 InSAR data: (a) 2018-01-10, (b) 2018-02-03 and (c) 2018-02-27. Basemap image copyright © 2020 Planet Labs PBC.

maps are zoomed-in and discussed within the context of potential geotechnical interpretation in Figures 6.9 (a) to (d). The location and extent of the TSF failed area are depicted in Figure 6.9 (a). Figures 6.9 (b) and (d) provide a zoomed-in view of the

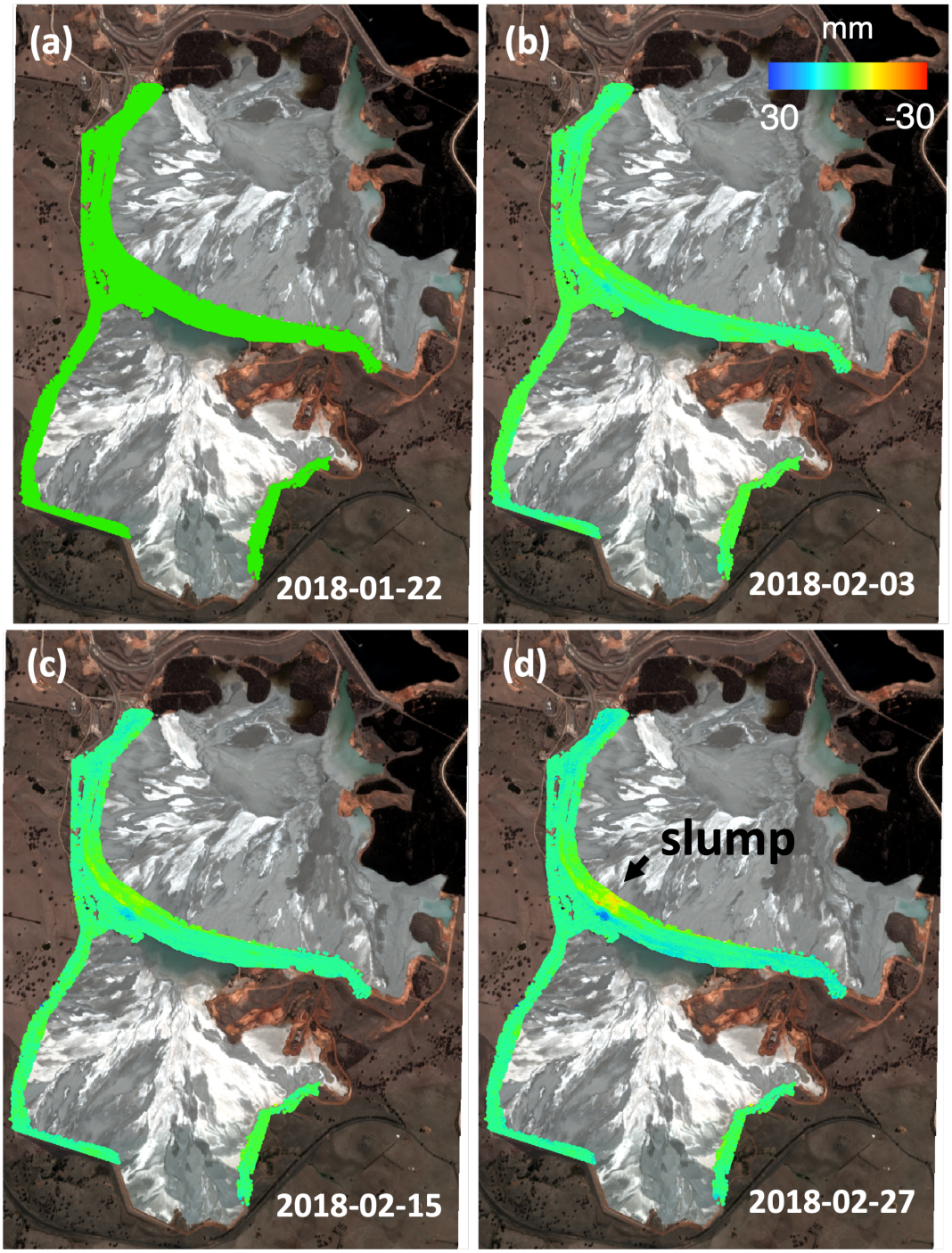

FIGURE 6.7: Difference between predicted and measured deformations on different dates for Vertical RS2 InSAR: (a) 2018-01-22, (b) 2018-02-03, (c) 2018-02-15 and (d) 2018-02-27. Basemap image copyright © 2020 Planet Labs PBC.

failure area within the horizontal and vertical difference maps presented in Figures 6.7 (d) and 6.8 (d). The highly anomalous regions (red) in the horizontal difference maps match with key observations, including the location of the failure area and the footprint of modelled horizontal deformations across the slump width in Figure 6.9

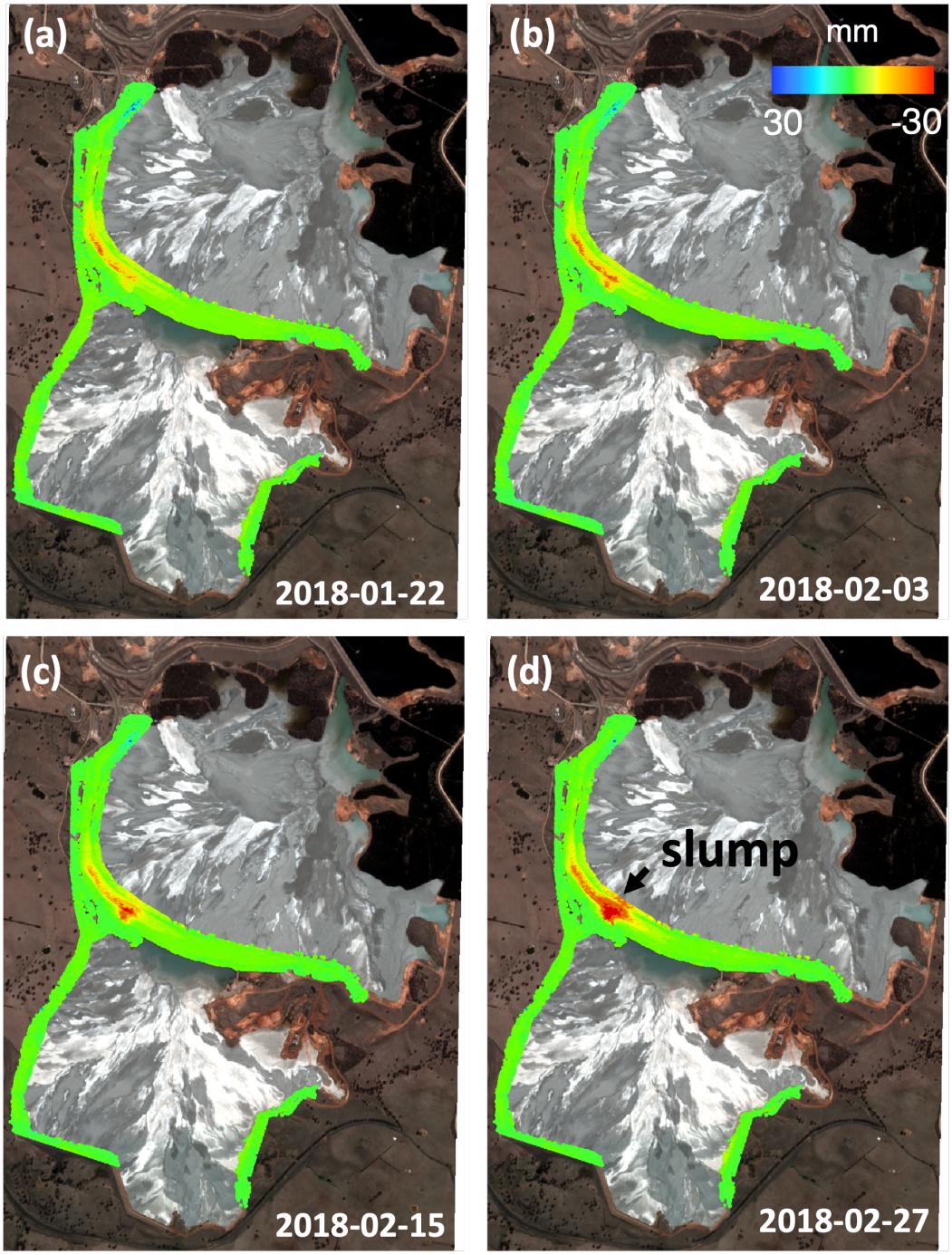

FIGURE 6.8: Difference between predicted and measured deformations on different dates for Horizontal RS2 InSAR: (a) 2018-01-22, (b) 2018-02-03, (c) 2018-02-15 and (d) 2018-02-27. Basemap image copyright © 2020 Planet Labs PBC.

(d), which are the horizontal deformations predicted by 3D numerical analysis from Jefferies et al. (2019). Interestingly, the anomalous clusters (red and blue) in Figure 6.9 (c) align with the FE modelled deformations described in Chapter 3. The FE model predicted that the upper stage dams would move in the opposite direction to the dam toe, with upper stages undergoing subsidence while the downstream toe of the TSF experienced an uplift or heave. These findings highlight the potential role of EE-DL in interpreting the vast number of measurements present in the InSAR data by outlining key signals to investigate, such as areas of unexpected deformation behaviour.

Finally, the anomalous measurements in the RS2-InSAR horizontal and vertical difference maps are clustered in Figures 6.10 and 6.11, respectively. Parts (a) of the figures are scatter plots of the predictions versus measurements at date 2018-01-22 (YYYY-MM-DD). The confidence interval captures 95% of the data and is plotted with a yellow ellipse in parts (a) of the figures. The ellipse is used for defining the upper and lower boundaries separating the two types of anomalies as plotted in blues and reds, respectively. Plotting these anomalies separately give very interesting results spatially. In Figures 6.10 and 6.11, the upper anomalies are in blue and are plotted in the top row (b) - (e), while the lower anomalies are in red and are in the bottom rows in (f) - (i). Interestingly, whilst the blues in Figures 6.10 and 6.11 capture the slump area, the reds seem to be capturing other movements, potentially related to the upstream tailings or the buttresses. This type of approach further demonstrates how anomalies that are identified in the early warning may be further classified based on their different behaviours.

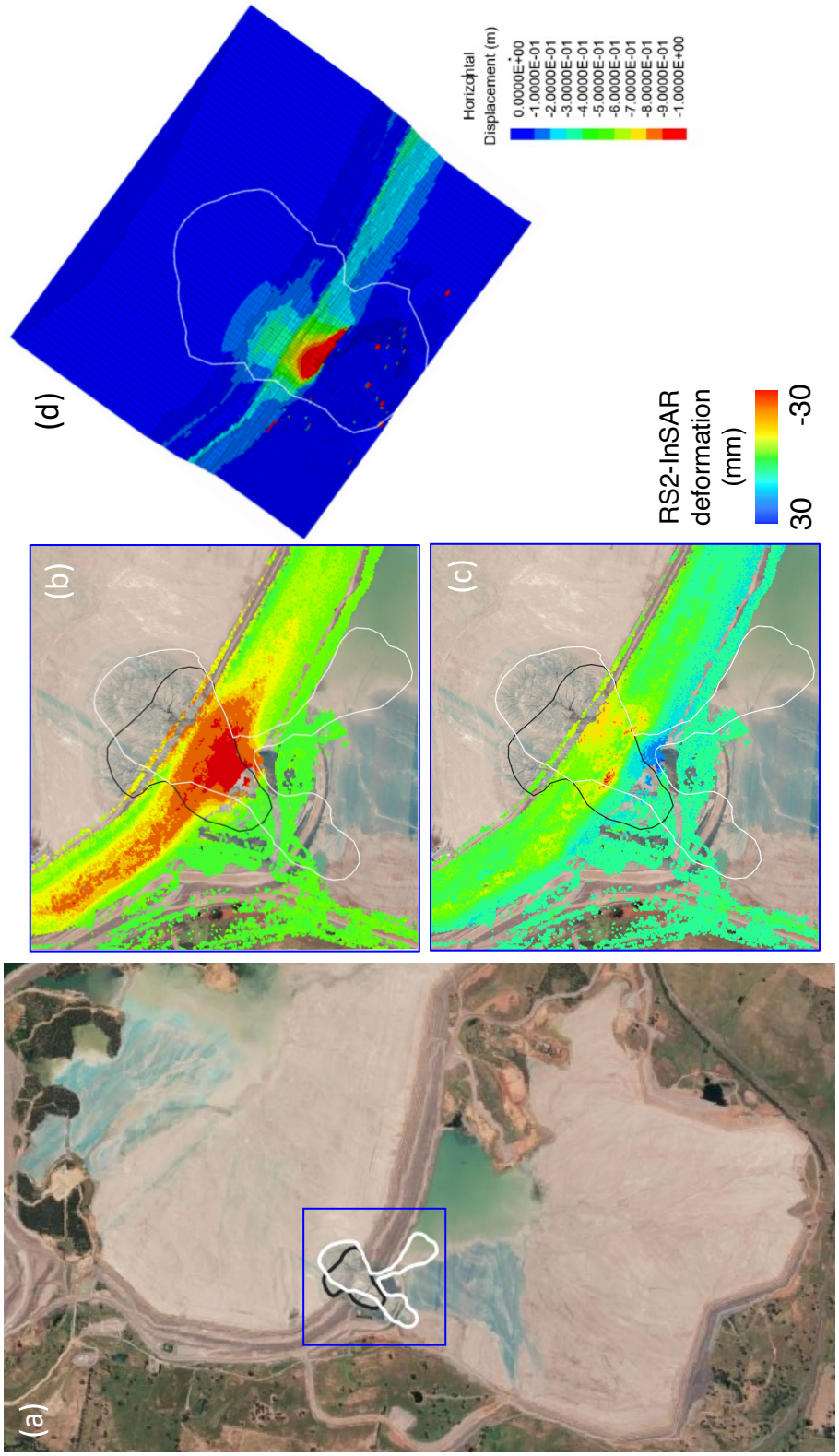

FIGURE 6.9: A zoomed in view of the failure area. (a) Location and extent of failure, which occurred in two stages, as outlined in white and black polygons (black predates white). The difference between predicted and measured deformations on 2018-02-27 RS2 InSAR (b) horizontal and (c) vertical. (d) The horizontal displacement contours from 3D numerical modelling results for 2018-03-08, from ITRB (Jefferies et al. (2019)). Basemap image copyright ©1995-2020 Esri

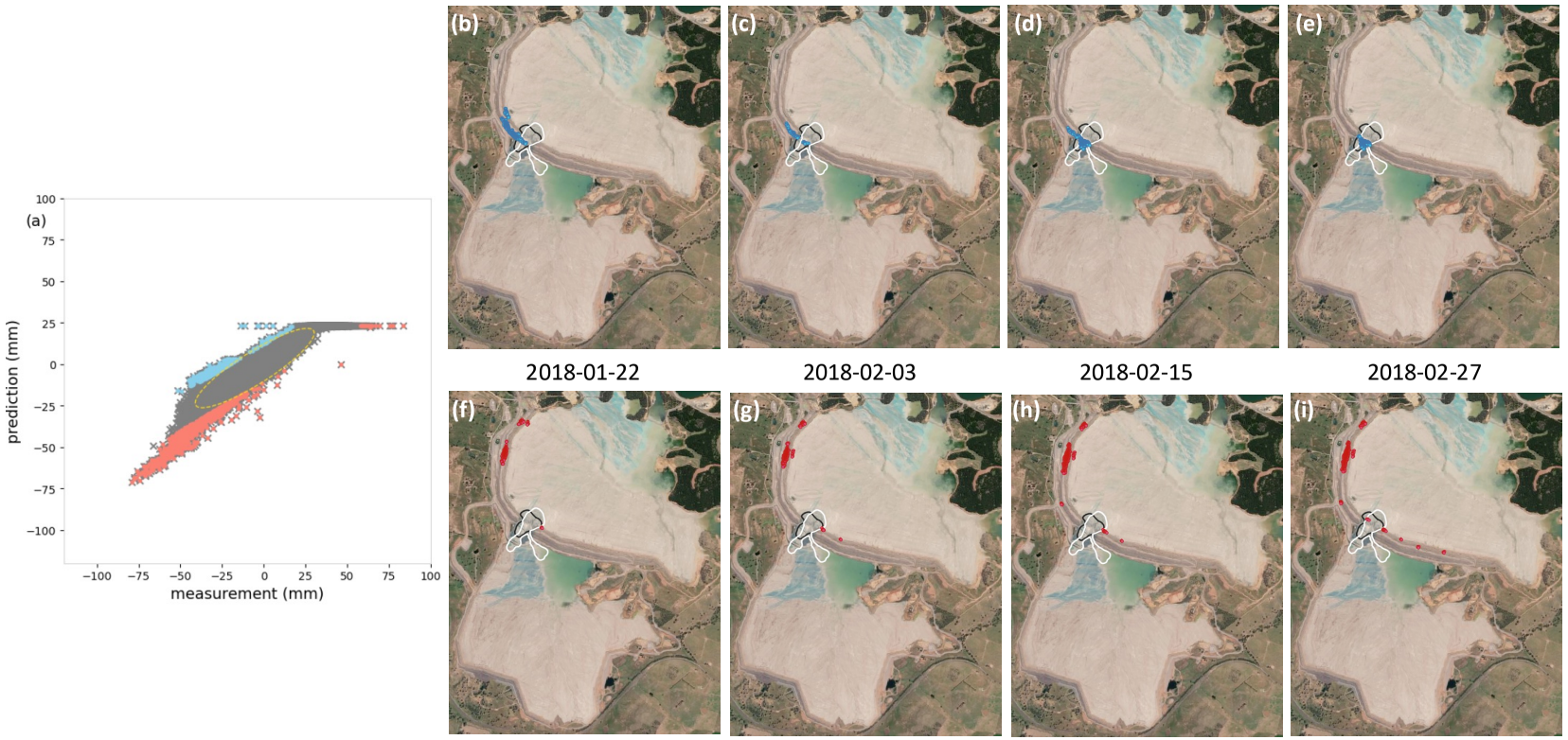

FIGURE 6.10: RS2 InSAR Horizontal anomalous measurements. (a) Scatter plot of predictions versus measurements for RS2-InSAR horizontal at 2018-01-22. The yellow ellipse captures the 95 % confidence interval of the data and is used for defining the upper and lower boundaries. Any points outside these boundaries are defined as anomalies and are spatially plotted in (b) to (i). The anomalies outside the upper bounds are in (b) to (e) and lower bounds are in (f) to (i) for the following dates: 2018-01-22, 2018-02-03, 2018-02-15 and 2018-02-27. Basemap image copyright ©1995-2020 Esri

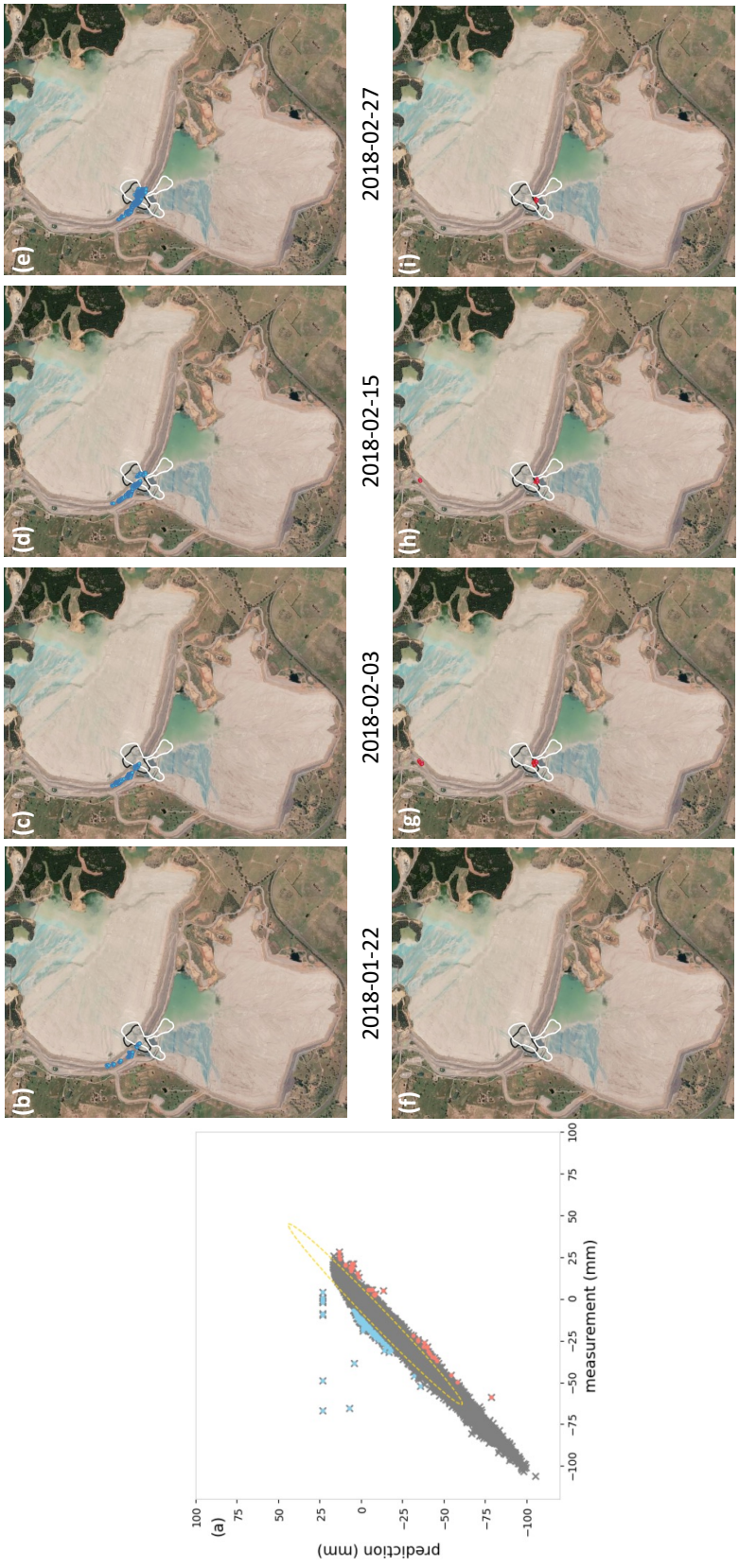

FIGURE 6.11: RS2 InSAR vertical anomalous measurements. (a) Scatter plot of predictions versus measurements for RS2-InSAR vertical at 2018-01-22. The yellow ellipse captures the 95 % confidence interval of the data and is used for defining the upper and lower boundaries. Any points outside these boundaries are defined as anomalies and are spatially plotted in (b) to (i). The anomalies outside the upper bounds are in (b) to (e) and lower bounds are in (f) to (i) for the following dates: 2018-01-22, 2018-02-03, 2018-02-15 and 2018-02-27. Basemap image copyright ©1995-2020 Esri

6.3 Summary

This chapter demonstrates the extent to which the early warning framework can be enhanced with the integration of S1 PS-InSAR and commercial high resolution RS2-InSAR data. The value and impact of different data sources for the detection of anomalous deformation have been evaluated. Using line-of-sight RS2 InSAR ascending / descending data, as well as decomposed vertical and horizontal motion component data, the chapter also demonstrates the ease with which different data types can be integrated into the EE-DL framework.

The performance of the early warning improved with PS-InSAR data compared to the ISBAS results discussed in Chapter 4. The EE-DL was consistently able to detect more number of true anomalies than false ones. This is likely due to the phase ambiguities present in PS-InSAR, which has an effect of amplifying the signals of anomalous deformation. Such exaggeration potentially makes it easier for EE-DL to identify anomalous behaviour. While phase unwrapping errors are typically considered a nuisance in most InSAR applications, the combination of InSAR with EE-DL suggests that these errors may act as a source of valuable insights for the early detection of changing deformation dynamics on the ground.

Moreover, the EE-DL performs well with both ascending and descending RS2-InSAR data. Ascending difference maps reveal clear anomalous clusters in the slump area only at the last prediction date, while descending maps display two red parallel lines that develop through time, possibly tracing buttress-related anomalous deformations. Based on this analysis, it is challenging to conclusively determine which satellite orbit is better for detecting anomalous deformation. This is because, the ascending and descending data are acquired at different acquisition dates and temporal resolution. The fact that both satellite geometries do detect clear anomalous clusters at least in the data immediately before failure implies that they are both potentially suitable for early warning of failures over Cadia TSFs.

Finally, the integration of decomposed RS2 vertical and horizontal difference maps exhibit the most distinct anomaly patterns. The vertical difference maps show positive and negative deformation clusters right next to each other in the slump area, which align with FE modelled predictions of the underlying deformation mechanisms.

And the horizontal difference maps are able to highlight the slump area as a distinct anomaly the earliest, as early as 2018-01-22. Based on the analysis in this chapter, the RS2 InSAR horizontal deformation offers greatest potential for early warning of failure over the Cadia TSF. A detailed discussion is available in Chapter 7.

Chapter 7

Conclusions

The ambition of this research is to protect communities, natural habitats and ecosystems from toxic mine waste pollution that can result from the collapse of tailings storage facilities (TSFs). A remote, satellite-based monitoring and an early warning framework has been proposed for this. The feasibility of data-driven approaches to early warning is presented. Regardless of how powerful the early warning algorithm is, it is ultimately redundant without reliable measurements. Therefore, the suitability of satellite-Interferometric Synthetic Aperture Radar (InSAR) has been rigorously investigated through remote sensing and geotechnical methods. This chapter summarises the main findings and outlines avenues for future work.

7.1 Complementary Monitoring Technologies

The investigation into the performance of open source Sentinel-1 (S1) and commercial Radarsat-2 (RS2) InSAR datasets indicate that satellite InSAR is a powerful tool, complementing traditional monitoring methods. The combination of InSAR with geotechnical Finite Element (FE) modeling results in Chapter 3 demonstrated the important role of FE modelling for validating and interpreting the underlying processes that led to the observed deformation behaviour. Moreover, the sensitivity of InSAR to changing foundation properties beneath the TSF has been simulated with FE modelling. And it showed that the downstream parts of the TSF are more sensitive to changes in foundation properties than the upstream, which has implications for planning and installation of effective monitoring campaigns.

Furthermore, the comparison highlighted the ability of InSAR to capture the complex spatial and temporal variability of TSF deformation behaviour, which traditional

monitoring methods with sparse measurements may miss. And its capabilities for long-term monitoring without the need to install ground instrumentation were particularly valuable for Cadia TSF, as ground-based prisms had to be removed to allow construction in the critical period leading up to the failure. However, the limitations of S1-ISBAS were also revealed, especially where S1-ISBAS measurements significantly underestimate the deformation compared to the expected deformation from FE predictions. This discrepancy is due to the changing deformation dynamics of the TSF, caused by the construction of buttresses before the failure. This raised questions on whether these limitations are inherent to the InSAR technique, specific to the S1 satellite characteristics or are due to the ISBAS processing method.

PS-InSAR and ISBAS are complementary InSAR techniques for TSF monitoring. To further explore the influence of the particular InSAR processing algorithm, the S1 data was re-processed using a PS-InSAR approach. As expected, the analysis demonstrated that both PS and ISBAS-InSAR are suitable for measuring deformations that are within the 2π ambiguity inherent to InSAR. Consequently, complications were shown to arise when deformation magnitudes exceeded the wrapping threshold of $\frac{\lambda}{4}$, where λ is SAR wavelength. Under such conditions, PS-InSAR measurements display clear signs of phase unwrapping issues. The temporal noise of the data remains low until the construction of buttresses, after which PS-InSAR exhibits an irregular behaviour with huge jumps in deformation measurements. It is not possible to correct for these phase ambiguities with InSAR alone.

An opportunity for novel cross-technology calibration strategy is demonstrated through the use of FE predictions to correct for phase ambiguities in PS-InSAR data. This calibration strategy suggests that PS-InSAR is not good enough on its own for rapid deformation behaviour. Unfortunately, it was challenging to apply the same calibration approach to ISBAS, because it does not display clear indications of phase unwrapping errors. This is likely due to the nature of SBAS-type methods, which includes 'smoothing' or multi-looking of the signals. Such averaging of the signals across pixels likely dampens these high magnitude irregularities. Therefore, it is challenging to correct for issues that cannot be detected in the first place.

On the other hand, the advantages of ISBAS over PS-InSAR are in its ability to

maintain a high spatial density of measurements even when processed over long periods of time. In contrast, applying PS-InSAR for extended periods is challenging due to the ease with which its measurement coherence is lost. Despite the potential underestimation of the deformation, ISBAS still successfully detects spatially anomalous patterns over the slump area (Chapter 3). Therefore, the spatial distribution of anomalous deformation are better captured in ISBAS compared to PS-InSAR despite the phase ambiguities. Several InSAR processing approaches such as SqueeSAR combine the benefits of both PS-InSAR and SBAS, leveraging the best of both methodologies. However, in this research, maintaining control over the two processing methods and analysing the results separately allows for a thorough exploration of their respective advantages and limitations. In summary, it is clear that, PS-InSAR and ISBAS should be treated as complementary techniques for TSF monitoring, as they offer distinct insights into the state of the TSF. In contrast to PS-InSAR, ISBAS may be good enough on its own, but the aforementioned limitations suggest that a more reliable system should also include PS-InSAR and FE modelling.

Both InSAR and geotechnical modelling are subject to inherent uncertainties; however, when combined, they offer tools to probe and reduce the uncertainties present within each method. The phase ambiguity corrected S1 PS-InSAR data shows strong agreement with both high resolution RS2 InSAR and FE predictions in terms of deformation magnitude and trend for TSF stages 4 and 5. This suggests that the limitations of S1-ISBAS are not inherent to the InSAR method nor the characteristics of the S1 satellite. By re-processing S1 with PS-InSAR and correcting for its phase ambiguities with FE predictions, it is possible to capture the rapid deformation behaviour resulting from the construction of buttresses.

Interestingly, for TSF stage 7, there is strong agreement between the S1 PS-InSAR ambiguity-corrected data and RS2-InSAR measurements, but not with the FE model. The fact that two independent InSAR methods and SAR data agree is significant, but it is challenging to resolve these discrepancies without an external ground truth data. The prisms cannot be employed for this, because they were removed during this time period to accommodate construction activities. If the FE model is correct, then the discrepancy may be attributed to limitations of InSAR. However, the low sensitivity of InSAR to the North - South direction can be ruled out, since the horizontal components

of RS2-InSAR and FE predictions align well. Therefore, it is likely due to known SAR signal distortions, such as layover and foreshadow, resulting from the steep geometry of the higher TSF stages and the small spatial footprint of stage 7.

On the other hand, if the InSAR datasets represent the truth, then it highlights the limitations of the FE model in accurately capturing the deformation of higher dam stages. This is potentially due to simplifications and uncertainties in the model parameters, such as the tailings properties. As discussed in Chapter 3, the deformation signals of higher dam stages such as stage 7 are dominated by the deformation of the tailings. And within the context of a remote early warning system, such discrepancies between measurements and models should trigger an alert for further detailed in-situ analysis to resolve it.

7.2 Early Warning of TSF Failure

The feasibility of early warning for TSF failure using remote sensing data was explored through a novel deep learning approach in Chapter 4. The use of embedded entities within a deep learning (EE-DL) framework was shown to detect precursors to failure, i.e. anomalous deformation behaviour before TSF failure. The comparison revealed that both novel and traditional machine learning approaches can geolocate anomalous areas of the TSF that were subject to failure. The EE-DL approach outperformed both probabilistic Gaussian Process Regression and Random Forest in predicting ground deformation from S1-ISBAS data.

The performance of the early warning improved with S1 PS-InSAR compared to S1-ISBAS data. This is likely due to the sensitivity of PS-InSAR to changing deformation dynamics, which leads to phase ambiguities that amplify the deformation signal, potentially simplifying the EE-DL task. While phase ambiguities are generally considered a nuisance in most applications, it may actually provide valuable insights into the evolving deformation dynamics for TSFs and assist in early warning.

One of the advantages of EE-DL is its flexibility and ease with which other types of data can be integrated into the workflow. To demonstrate this, a variety of InSAR data types with different resolutions and measurement types were incorporated into the EE-DL workflow in Chapter 6. The transition from S1 to RS2 data represents an

order of magnitude increase in data volume. To accommodate this scaling, several adaptations were required, including changes to the embedding creation rule and retuning of hyper-parameters. Additionally, both line-of-sight and decomposed motion components of RS2 InSAR measurements were successfully incorporated into EE-DL.

The early warning capabilities performed best with the horizontal motion component of the RS2 InSAR data. As expected, the EE-DL predictions based on RS2 InSAR data provided more detailed insights into the development of anomalous deformation patterns than S1, likely owing to its higher spatial resolution. As expected, RS2 horizontal deformation data led the best early warning capabilities. It is the only data in which the failure area can be observed as early as 2018-01-22, with distinct clusters sticking out of the mass of deformation parallel to the TSF. Although, a similar outline can be visually identified in the vertical results, it is not visually clear until 2018-02-27. This clarity of the failure signature in the horizontal data makes sense, as horizontal motion (i.e. strain) is more directly related to failure than vertical motion.

Both ascending and descending datasets are suitable for early warning of failure at Cadia TSF. Both descending and ascending data detect visually clear anomalies at their last temporal acquisitions, which correspond to 2018-02-27 and 2018-02-15, respectively. Due to the differing temporal resolutions and the fact that they are acquired at different dates, it is challenging to compare them fairly and determine which dataset performs best. Although this may indicate that both orbital geometries are suitable for detecting the slump at Cadia TSF, it does not rule out the possibility that one geometry may end up being more suitable than the other, especially if the slump occurred elsewhere on the TSF. As expected, the development of the anomalies are best observed from the decomposed motions, rather than either the ascending or the descending datasets. This improvement is likely due to the higher temporal resolution of the decomposed datasets, which represent the combined insights of both acquisition geometries.

Overall, the EE-DL with S1 InSAR data is potentially good enough for remote monitoring and early warning of TSFs. As anticipated, a significant improvement in the early warning is offered from the higher resolution RS2-InSAR. Therefore, these results support the vision for a global early warning based on S1 InSAR and commercial high resolution data reserved for high risk TSFs. This would justify the cost of the

commercial data, especially because these costs are insignificant compared to the risk and cost of TSF failure.

There is value in EE-DL beyond early warning, particularly in data discovery and twin systems. Interpreting the spatial distribution of InSAR deformations over TSFs is challenging, especially because a lot of different magnitudes of deformation signals are present due to ongoing consolidation. Therefore, EE-DL is demonstrated as a potential tool to help focus on areas of unexpected deformations, aiding in making sense of the large collection of measurements. For example, RS2-InSAR descending data within EE-DL revealed the development of unexpected deformation patterns that appear to correspond to buttress construction. The EE-DL results can then be further validated using other types of satellite data, including SAR back-scatter and multi-spectral optical data. Figure 7.1 outlines the spatial extent of the buttress construction visible in optical data and shows how activities on the ground can be classified, tracked and labelled across the TSF. The large differences in the stress states between areas with and without buttress cover can then be evaluated with the FE model developed in Chapter 3. This is a critical aspect of the digital twin vision, as it allows the capturing of the dynamic state of the TSF by calculating metrics such as the degree of completion of buttresses construction. By integrating insights from satellite remote sensing, geotechnical modelling and deep learning, this thesis has addressed some of the most fundamental research components that are currently missing, before satellite enabled digital twin systems may be achieved for the monitoring of TSFs.

7.3 Future Work

The research highlighted several avenues for future work, particularly at the intersection of the disciplines explored in this thesis, which are outlined in this section. The methodologies developed here, along with the effectiveness of the early warning framework should be assessed for other types of TSFs. Additionally, the flexibility of the EE-DL approach may offer significant advantages for large-scale InSAR projects such as the European Ground Motion Service, and its adaptability to other infrastructures, such as bridges (Cusson et al. (2021)), should also be evaluated.

FIGURE 7.1: A mock up of EO data based verification and labelling of construction activities on the ground. Static FE model is not representative of the dynamic state of a TSF. Therefore, the satellite data can help inform the completion status, therefore, the various stress states at different parts of the TSF through time. Imagery © MAXAR and modified from Thomas et al. (2019).

The suitability of InSAR for the monitoring and early warning for TSF failures depends on its ability to obtain high quality measurements. If there are too many changes occurring on the ground, such as those caused by construction activities, it can lead to significant loss of coherence. Regardless of how advanced the early warning algorithm may be, it becomes redundant with a lack of reliable measurements. Within the context of TSFs, InSAR is likely most suitable for upstream and downstream types compared to centreline construction. This is because, in the upstream method, the construction of the following stages do not completely cover the previous ones. And in the case of the downstream, the whole of the dam is constructed before any tailings deposition commences. In contrast, the centreline method is characterised by continuous construction that covers the entire TSF face of the previous stages as the dam is raised.

Such constant construction activity and changes over the dam surface makes active centreline TSFs particularly challenging for InSAR monitoring, as it may not provide sufficient intervals for obtaining measurements. To demonstrate such a scenario, PS-InSAR has been processed for different years over a centreline TSF as shown in Figures 7.2 (a) 2018-2019, (b) 2019-2020 and (c) 2020-2021. They show that the least amount of construction activity occurred during 2018-2019, compared to the other two years.

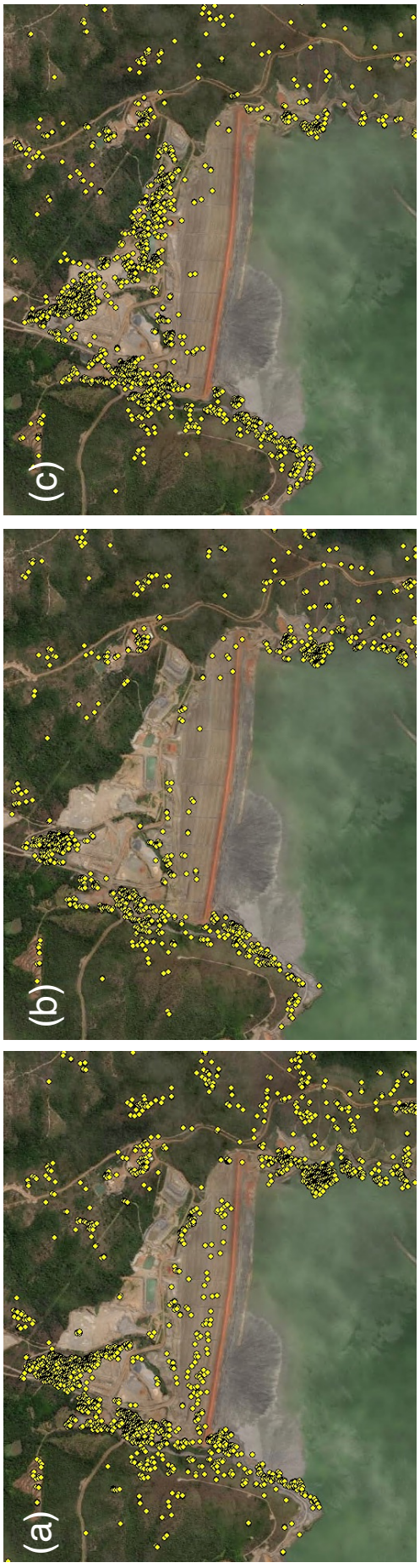

FIGURE 7.2: Impact of SAR acquisition dates on PS-InSAR measurement distribution for (a) 2018-2019; (b) 2019-2020 and (c) 2020-2021. InSAR data © Satellite Applications Catapult. Basemap image copyright © 2023 ESA Sentinel-2.

These figures illustrate how InSAR measurement density may be optimised based on the choice of acquisition dates versus level of changes on the ground. However, they also highlight the potential challenges for automated InSAR processing over some TSFs.

While PS-InSAR is most sensitive to changes on the ground, significant changes occurring throughout the monitoring period is also likely to impact ISBAS. This is evidenced by the fact that neither PS-InSAR nor ISBAS are able to obtain measurements over the tailings slurry (Chapters 3 and 5). In very challenging scenarios, other experimental InSAR processing methods such as 'temporary scatterers' (e.g. Hu et al. (2019)) may be considered as options. Moreover, although at its infancy, data-driven approaches for InSAR processing holds significant potential for overcoming these challenges and obtaining reliable measurements from e.g. a shorter SAR data stack. However, the reliability of temporary scatterers and other novel InSAR processing approaches for TSFs still needs to be evaluated.

Further research is required to explore potential blind-spots to InSAR monitoring for different TSFs. It should take account of known SAR distortions, such as foreshortening or layover effects, as well as the low sensitivity to the North-South directions. The impact of these distortions on the resulting InSAR measurements should be explored.

Moreover, the uncertainties in the FE predictions should be investigated by employing more detailed tailings geometries and advanced soil models, such as NorSand (Jefferies and Shuttle (2005)). In this case, the numerical investigation should be expanded to explore the range of realistic variation in the soil properties, alongside the influence of other parameters, such as the tailings pond size, phreatic water level, tailings spigot schedule and construction timing. This should include evaluating FE parameter sensitivities and its relationship with InSAR measurements. For instance, Chapter 3 demonstrated the sensitivity of the InSAR measurements to the properties of the TSF foundation. It demonstrated that InSAR measurements over the downstream parts of the TSFs are most sensitive to changing foundation properties. Upstream parts also exhibited deformation changes, but were less sensitive, because of the deformation being dominated by the consolidation of the tailings. This future research could strengthen the dual-use of the technologies in the cross-calibration of

InSAR and FE models.

Given the high stakes involved in the potential collapse of TSFs, understanding the reasoning and confidence behind the predictions of the early warning is crucial. There is a growing body of research in making deep learning more explainable. For instance, features that trigger decisions in convolutional networks are typically visualised through class activation maps. A similar approach for EE-DL may be through techniques that use dimension reduction and visualisation to better understand the relationships of what the embeddings capture (e.g. Van der Maaten and Hinton (2008)). Additionally, creative combinations of embeddings have been recently demonstrated for fusing different modalities of data such as in e.g. Girdhar et al. (2023). Moreover, typical model regularisation techniques, such as dropout that are applied within the EE-DL workflow, can serve as a sampling mechanism for quantifying the uncertainties of the model decisions (Gal and Ghahramani (2016)). Given the sensitivity of this task, it is also important to test likely false positives and negatives within an operational early warning system.

Moreover, the performance of the early warning may improve by ingesting other types of data. This may include both data from different ground-based sensors such as piezometers and accelerometers, and other EO data such as precipitation and soil moisture data. Another key variable to consider in future research is the time taken for the whole of the early warning workflow, from data pre-processing to alerts for decision making. When new SAR data is acquired, re-processing the entire SAR stack can be expensive and slow. Therefore, the research exploring this challenge within the remote sensing community, such as RapidSAR (Spaans and Hooper (2016)), should be investigated within the context of infrastructure monitoring. Its ability to reduce the delay in the time taken from satellite data acquisition to early warning alerts sent to TSF engineers should be evaluated.

Finally, the monitoring and modelling technologies are like pieces of a puzzle that can be assembled in different combinations, depending on the stakeholder or user needs. Government bodies, civil society and investors typically lack access to geotechnical ground-based data and may only seek high-level information on the state of the TSF. For them, knowing that no dangerous signals have been detected over the TSF may suffice. On the other hand, mine operators have access to geotechnical data and

require much deeper insights. Therefore, the monitoring and early warning framework proposed in this thesis should be further developed and customised to the particular needs of the envisioned end user. The proposed framework in this thesis focused on the prevention aspect of TSF related disasters; there is also an important role for these technologies in the clean-up and restoration of the surrounding natural environment.

Bibliography

Amazon Web Services. (2024). Amazon web services (AWS) Elastic Compute Cloud (ec2) gpu instances [AWS EC2 G4 Instances for GPU-powered computing]. https://aws.amazon.com/ec2/instance-types/g4/

Anaconda, Inc. (2024). Anaconda distribution for Python 3 [Anaconda Distribution, Version 3.x]. https://www.anaconda.com/products/distribution

Anantrasirichai, N., Biggs, J., Albino, F., Hill, P., & Bull, D. (2018). Application of machine learning to classification of volcanic deformation in routinely generated InSAR data. *Journal of Geophysical Research: Solid Earth*, *123*(8), 6592–6606.

Anantrasirichai, N., Biggs, J., Albino, F., & Bull, D. (2019). A deep learning approach to detecting volcano deformation from satellite imagery using synthetic datasets. *Remote Sensing of Environment*, *230*, 111–179.

Anantrasirichai, N., Biggs, J., Kelevitz, K., Sadeghi, Z., Wright, T., Thompson, J., Achim, A. M., & Bull, D. (2020). Detecting Ground Deformation in the Built Environment using Sparse Satellite InSAR data with a Convolutional Neural Network. *IEEE Transactions on Geoscience and Remote Sensing*, *59*(4), 2940–2950.

Arroyo, M., & Gens, A. (2021). Computational analyses of dam I failure at the Corrego de Feijao mine in Brumadinho. *Methods in engineering*, *561*.

Bamler, R. (2000). Principles of synthetic aperture radar. *Surveys in Geophysics*, *21*(2), 147–157.

Bamler, R., & Hartl, P. (1998). Synthetic aperture radar interferometry. *Inverse problems*, *14*(4), 1–54.

Bateson, L., Novali, F., & Cooksley, G. (2010). Terrafirma user guide. *A guide to the use and understanding of Persistent Scatterer Interferometry in the detection and monitoring of terrainmotion. ESA GNES*.

Bayaraa, M., Rossi, C., Kalaitzis, F., & Sheil, B. (2023). Entity Embeddings in Remote Sensing: Application to Deformation Monitoring for Infrastructure. *Remote Sensing*, *15*(20), 4910.

Bayaraa, M., Sheil, B., & Rossi, C. (2024). InSAR and numerical modelling for tailings dam monitoring–the Cadia failure case study. *Geotechnique*, *74*(10), 985–1003.

Bayaraa, M., Spittle, S., Williams, C., Stoijkovic, V., Lumbroso, D., & Goff, C. (2018). Tailings Dams Monitoring using Satellite-enabled Technologies. https://www.gecaminpublications.com/tailings2018/

BBC. (2020). Brazil's Dam Disaster. https://www.bbc.co.uk/news/topics/cl12wv2w275t

Bentley Systems International Ltd. (2019). *PLAXIS 2D Reference Manual*. https://bentleysystems.service-now.com/community?id=kb_article_view&sysparm_article=KB0107989

Berardino, P., Fornaro, G., Lanari, R., & Sansosti, E. (2002). A new algorithm for surface deformation monitoring based on small baseline differential SAR interferograms. *IEEE Transactions on geoscience and remote sensing*, *40*(11), 2375–2383.

Bhanbhro, R., Auchar Zardari, M., Ahmed Memon, B., Ali Soomro, M., Edeskär, T., & Knutsson, S. (2021). Mechanical properties and particle breakage of uniform-sized tailings material. *Journal of Materials in Civil Engineering*, *33*(3), 1–15.

Biggs, J., & Pritchard, M. E. (2017). Global volcano monitoring: What does it mean when volcanoes deform? *Elements*, *13*(1), 17–22.

Blight, G., Troncoso, J., Fourie, A., & Wolski, W. (2000). Issues in the geotechnics of mining wastes and tailings. *ISRM International Symposium*.

Blog, G. D. (2017). Introducing TensorFlow Feature Columns. https://developers.googleblog.com/2017/11/introducing-tensorflow-feature-columns.html

Boni, R., Herrera, G., Meisina, C., Notti, D., Béjar-Pizarro, M., Zucca, F., González, P. J., Palano, M., Tomás, R., Fernández, J., et al. (2015). Application of multi-sensor advanced DInSAR analysis to severe land subsidence recognition: Alto guadalentín basin (spain). *Proceedings of the International Association of Hydrological Sciences*, *372*(372), 45–48.

Brengman, C. M., & Barnhart, W. D. (2021). Identification of Surface Deformation in InSAR Using Machine Learning. *Geochemistry, Geophysics, Geosystems*, *22*(3), 1–13.

Carlà, T., Intrieri, E., Raspini, F., Bardi, F., Farina, P., Ferretti, A., Colombo, D., Novali, F., & Casagli, N. (2019). Perspectives on the prediction of catastrophic slope failures from satellite InSAR. *Scientific reports*, *9*(1), 1–9.

Chen, Y., Bruzzone, L., Jiang, L., & Sun, Q. (2021). ARU-Net: Reduction of Atmospheric Phase Screen in SAR Interferometry Using Attention-Based Deep Residual U-Net. *IEEE Transactions on Geoscience and Remote Sensing*, *59*(7), 5780–5793.

Chicco, D., Warrens, M. J., & Jurman, G. (2021). The coefficient of determination R-squared is more informative than SMAPE, MAE, MAPE, MSE and RMSE in regression analysis evaluation. *Peerj computer science*, *7*, 1–24.

Cigna, F., Bianchini, S., & Casagli, N. (2013). How to assess landslide activity and intensity with Persistent Scatterer Interferometry (PSI): the PSI-based matrix approach. *Landslides*, *10*(3), 267–283.

Cigna, F., Osmanoğlu, B., Cabral-Cano, E., Dixon, T. H., Ávila-Olivera, J. A., Garduño-Monroy, V. H., DeMets, C., & Wdowinski, S. (2012). Monitoring land subsidence and its induced geological hazard with Synthetic Aperture Radar Interferometry: A case study in Morelia, Mexico. *Remote Sensing of Environment*, *117*, 146–161.

Cigna, F., & Tapete, D. (2021). Satellite InSAR survey of structurally-controlled land subsidence due to groundwater exploitation in the Aguascalientes Valley, Mexico. *Remote Sensing of Environment*, *254*(11), 865–881.

Clarkson, L., Williams, D., & Seppala, J. (2021). Real-time monitoring of tailings dams. *Georisk: Assessment and Management of Risk for Engineered Systems and Geohazards*, *15*(2), 113–127.

Cloude, S. (2009). *Polarisation: Applications in remote sensing*. OUP Oxford.

Colesanti, C., Ferretti, A., Novali, F., Prati, C., & Rocca, F. (2003). SAR monitoring of progressive and seasonal ground deformation using the permanent scatterers technique. *IEEE Transactions on Geoscience and Remote Sensing*, *41*(7), 1685–1701.

Corsetti, M., Fossati, F., Manunta, M., & Marsella, M. (2018). Advanced SBAS-DInSAR technique for controlling large civil infrastructures: An application to the genzano di lucania dam. *Sensors*, *18*(7), 2371.

Crosetto, M., Monserrat, O., Cuevas-González, M., Devanthéry, N., & Crippa, B. (2016). Persistent Scatterer Interferometry: A review. *ISPRS Journal of Photogrammetry and Remote Sensing*, *115*, 78–89.

Crosetto, M., Solari, L., Mróz, M., Balasis-Levinsen, J., Casagli, N., Frei, M., Oyen, A., Moldestad, D. A., Bateson, L., Guerrieri, L., et al. (2020). The evolution of wide-area DInSAR: From regional and national services to the European Ground Motion Service. *Remote Sensing*, *12*(12), 2043.

Cuervo, V., Burge, L., Beaugrand, H., Hendershot, M., & Evans, S. G. (2017). Downstream geomorphic response of the 2014 Mount Polley tailings dam failure, British columbia. *Workshop on World Landslide Forum*, 281–289.

Curnick, D. J., Davies, A. J., Duncan, C., Freeman, R., Jacoby, D. M., Shelley, H. T., Rossi, C., Wearn, O. R., Williamson, M. J., & Pettorelli, N. (2022). SmallSats: a new technological frontier in ecology and conservation? *Remote Sensing in Ecology and Conservation*, *8*(2), 139–150.

Cusson, D., Rossi, C., & Ozkan, I. F. (2021). Early warning system for the detection of unexpected bridge displacements from radar satellite data. *Journal of Civil Structural Health Monitoring*, *11*(1), 189–204.

De Brébisson, A., Simon, É., Auvolat, A., Vincent, P., & Bengio, Y. (2015). Artificial neural networks applied to taxi destination prediction. *arXiv preprint arXiv:1508.00021*, 1–15.

Devanthéry, N., Crosetto, M., Monserrat, O., Cuevas-González, M., & Crippa, B. (2014). An approach to persistent scatterer interferometry. *Remote sensing*, *6*(7), 6662–6679.

Do, T. M., Laue, J., Mattsson, H., & Jia, Q. (2021). Numerical Analysis of an Upstream Tailings Dam Subjected to Pond Filling Rates. *Applied Sciences*, *11*(13), 6044.

Esri. (2024). ArcGIS Geographic Information System. https://www.esri.com/en-us/arcgis/

European Space Agency. (2024). Sentinel-1 User Guide [Copernicus Open Access Hub]. https://sentinels.copernicus.eu/web/sentinel/missions/sentinel-1

Even, M., & Schulz, K. (2018). InSAR deformation analysis with distributed scatterers: A review complemented by new advances. *Remote Sensing*, *10*(5), 744.

Fern, J., Rohe, A., Soga, K., & Alonso, E. (2019). *The material point method for geotechnical engineering: A practical guide*. CRC Press.

Ferretti, A., Fumagalli, A., Novali, F., Prati, C., Rocca, F., & Rucci, A. (2011). A new algorithm for processing interferometric data-stacks: SqueeSAR. *IEEE transactions on geoscience and remote sensing*, *49*(9), 3460–3470.

Ferretti, A., Prati, C., & Rocca, F. (2001). Permanent scatterers in SAR interferometry. *IEEE Transactions on geoscience and remote sensing*, *39*(1), 8–20.

Flores-Anderson, A. I., Herndon, K. E., Thapa, R. B., & Cherrington, E. (2019). *The SAR handbook: Comprehensive methodologies for forest monitoring and biomass estimation*. NASA.

Franks, D. M., Stringer, M., Torres-Cruz, L. A., Baker, E., Valenta, R., Thygesen, K., Matthews, A., Howchin, J., & Barrie, S. (2021). Tailings facility disclosures reveal stability risks. *Scientific reports*, *11*, 5353.

Frattini, P., Crosta, G. B., Rossini, M., & Allievi, J. (2018). Activity and kinematic behaviour of deep-seated landslides from PS-InSAR displacement rate measurements. *Landslides*, *15*(6), 1053–1070.

Gal, Y., & Ghahramani, Z. (2016). Dropout as a bayesian approximation: Representing model uncertainty in deep learning. *international conference on machine learning*, 1050–1059.

Gardner, J., Pleiss, G., Weinberger, K. Q., Bindel, D., & Wilson, A. G. (2018). Gpytorch: Blackbox matrix-matrix gaussian process inference with gpu acceleration. *Advances in neural information processing systems*, *31*, 1–12.

Gardner, J. R., Pleiss, G., Bindel, D., Weinberger, K. Q., & Wilson, A. G. (2018). GPyTorch: Blackbox Matrix-Matrix Gaussian Process Inference with GPU Acceleration. *Advances in Neural Information Processing Systems*, *31*, 7576–7586.

Garino Libardi, L. M., Oldecop, L. A., Romero Morales, E. E., & Rodriguez Pacheco, R. L. (2021). Tailings desiccation process studied in environmental chamber experiment. *Proceedings of the Institution of Civil Engineers-Geotechnical Engineering*, *175*(2), 261–271.

Gens, A., & Alonso, E. E. (2006). Aznalcóllar dam failure. part 2: Stability conditions and failure mechanism. *Géotechnique*, *56*(3), 185–201.

Gernhardt, S., Adam, N., Eineder, M., & Bamler, R. (2010). Potential of very high resolution SAR for persistent scatterer interferometry in urban areas. *Annals of GIS*, *16*(2), 103–111.

Gillies, S., & contributors to Rasterio. (2024). Rasterio: Geospatial Raster Data Access for Python. https://rasterio.readthedocs.io/en/stable/

Girdhar, R., El-Nouby, A., Liu, Z., Singh, M., Alwala, K. V., Joulin, A., & Misra, I. (2023). Imagebind: One embedding space to bind them all. *Proceedings of the IEEE/CVF Conference on Computer Vision and Pattern Recognition*, 15180–15190.

Goodfellow, I., Pouget-Abadie, J., Mirza, M., Xu, B., Warde-Farley, D., Ozair, S., Courville, A., & Bengio, Y. (2014). Generative adversarial nets. *Advances in neural information processing systems*, *27*, 1–9.

Google Cloud. (2024). Google Cloud GPU Instances [Google Cloud Platform GPU Instances for high-performance computing]. https://cloud.google.com/gpu

Grebby, S., Sowter, A., Gluyas, J., Toll, D., Gee, D., Athab, A., & Girindran, R. (2021). Advanced analysis of satellite data reveals ground deformation precursors to the Brumadinho tailings dam collapse. *Communications Earth & Environment*, *2*(1), 1–9.

Guo, C., & Berkhahn, F. (2016). Entity embeddings of categorical variables. *arXiv preprint arXiv:1604.06737*.

Harris, C. R., Millman, K. J., Van Der Walt, S. J., Gommers, R., Virtanen, P., Cournapeau, D., Wieser, E., Taylor, J., Berg, S., Smith, N. J., et al. (2020). Array programming with NumPy. *Nature*, *585*(7825), 357–362.

He, T., Zhang, Z., Zhang, H., Zhang, Z., Xie, J., & Li, M. (2019). Bag of tricks for image classification with convolutional neural networks. *Proceedings of the IEEE/CVF Conference on Computer Vision and Pattern Recognition*, 558–567.

Holden, D., Donegan, S., & Pon, A. (2020). Brumadinho Dam InSAR study: analysis of TerraSAR-X, COSMO-SkyMed and Sentinel-1 images preceding the collapse. *Proceedings of the 2020 International Symposium on Slope Stability in Open Pit Mining and Civil Engineering*, 293–306.

Hooper, A. (2008). A multi-temporal inSAR method incorporating both persistent scatterer and small baseline approaches. *Geophysical Research Letters*, *35*(16), 1–8.

Hooper, A. (2016). UNAVCO InSAR lecture. www.unavco.org/education/professional-development/short-courses/course-materials/InSAR/2016-InSAR-isce-giant-course-materials/Hooper%20%5Ctextunderscore%20Lecture%20%5Ctextunderscore%20PS.pdf

Hooper, A., Zebker, H., Segall, P., & Kampes, B. (2004). A new method for measuring deformation on volcanoes and other natural terrains using inSAR persistent scatterers. *Geophysical research letters*, *31*(23), 1–5.

Howard, J., & Gugger, S. (2020a). *Deep Learning for Coders with fastAI and PyTorch*. O'Reilly Media.

Howard, J., & Gugger, S. (2020b). FastAI: a layered API for deep learning. *Information*, *11*(2), 108.

Hu, F., Wu, J., Chang, L., & Hanssen, R. F. (2019). Incorporating Temporary Coherent Scatterers in Multi-Temporal InSAR Using Adaptive Temporal Subsets. *IEEE Transactions on Geoscience and Remote Sensing*, *57*(10), 7658–7670.

Hudson, R., Sato, S., Morin, R., & McParland, M. A. (2021). Comparison of Sentinel-1 and RADARSAT-2 Data for Monitoring of Tailings Storage Facilities. *EUSAR 2021; 13th European Conference on Synthetic Aperture Radar*, 1–6.

Hudson-Edwards, K. A., Kemp, D., Torres-Cruz, L. A., Macklin, M. G., Brewer, P. A., Owen, J. R., Franks, D. M., Marquis, E., & Thomas, C. J. (2024). Tailings storage facilities, failures and disaster risk. *Nature Reviews Earth and Environment*, *5*, 612–630.

Hund, K., La Porta, D., Fabregas, T., Laing, T., & Dexhage, J. (2020). Minerals for climate action: The mineral intensity of the clean energy transition. climate-smart mining facility.

Hunter, J. D. (2007). Matplotlib: A 2D graphics environment. *Computing in Science & Engineering*, *9*(3), 90–95.

ICME, T. I. C. o. M., & UNEP, U. N. E. P. (1998). Case studies on tailings management.

Ioffe, S., & Szegedy, C. (2015). Batch normalization: Accelerating deep network training by reducing internal covariate shift. *International conference on machine learning*, 448–456.

Itoh, K. (1982). Analysis of the phase unwrapping algorithm. *Applied optics*, *21*(14), 2470–2470.

Jefferies, M., Morgenstern, N. R., Van Zyl, D., & Wates, J. (2019). Report on NTSF Embankment Failure. Cadia Valley Operations for Ashurst Australia. www.newcrest.com/sustainability/dams-and-tailings-management

Jefferies, M., & Shuttle, D. (2005). NorSand: features, calibration and use. In *Soil constitutive models: Evaluation, selection, and calibration* (pp. 204–236).

Jordahl, K., & contributors to GeoPandas. (2024). GeoPandas: Python tools for geographic data. https://geopandas.org/

Kampes, B. M. (2006). *Radar interferometry* (Vol. 12). Springer.

Kluyver, T., Ragan-Kelley, B., Perez, F., Granger, B., Bussonnier, M., Frederic, J., Kelley, K., Hamrick, J., Grout, J., Corlay, S., et al. (2016). Jupyter notebooks - a publishing format for reproducible computational workflows. *Positioning and Power in Academic Publishing: Players, Agents and Agendas*, 87–90.

Lanari, R., Casu, F., Manzo, M., Zeni, G., Berardino, P., Manunta, M., & Pepe, A. (2007). An overview of the small baseline subset algorithm: A DInSAR technique for surface deformation analysis. *Deformation and Gravity Change: Indicators of Isostasy, Tectonics, Volcanism, and Climate Change*, *164*, 637–661.

Lanari, R., Reale, D., Bonano, M., Verde, S., Muhammad, Y., Fornaro, G., Casu, F., & Manunta, M. (2020). Comment on "Pre-Collapse Space Geodetic Observations of Critical Infrastructure: The Morandi Bridge, Genoa, Italy" by Milillo et al.(2019). *Remote Sensing*, *12*(24), 4011.

Lenail, A. (2019). NN-SVG: Publication-Ready Neural Network Architecture Schematics. *Journal of Open Source Software*, 1–16.

Leps, T. M. (1970). Review of shearing strength of rockfill. *Journal of the Soil Mechanics and Foundations Division*, *96*(4), 1159–1170.

Llano-Serna, M., Williams, D., & Ruest, M. (2017). Analysis of tailings dam-break and run-out. *4th International Seminar on Tailings Management, Tailings*, 1–8.

Lumbroso, D., McElroy, C., Goff, C., Collell, M. R., Petkovsek, G., & Wetton, M. (2019). The potential to reduce the risks posed by tailings dams using satellite-based information. *International journal of disaster risk reduction*, *38*, 1–22.

Lumbroso, D., Roca, M., Petkovsek, G., Davison, M., Liu, Y., Goff, C., & Wetton, M. (2021). DAMSAT: An eye in the sky for monitoring tailings dams. *Mine Water and the Environment*, *40*, 113–127.

Ma, P., Zhang, F., & Lin, H. (2020). Prediction of InSAR time-series deformation using deep convolutional neural networks. *Remote Sensing Letters*, *11*(2), 137–145.

Macchiarulo, V., Milillo, P., DeJong, M. J., Gonzalez Marti, J., Sanchez, J., & Giardina, G. (2021). Integrated InSAR monitoring and structural assessment of tunnelling-induced building deformations. *Structural Control and Health Monitoring*, 1–26.

Mánica, M., Arroyo, M., Gens, A., & Monforte, L. (2021). Application of a critical state model to the Merriespruit tailings dam failure. *Geotechnical Engineering*, *175*, 151–165.

Marsh, D. (2018). For What It's Worth: Copper. https://www.dillonmarsh.com/for-what-its-worth

Massonnet, D., & Feigl, K. L. (1998). Radar interferometry and its application to changes in the Earth's surface. *Reviews of geophysics*, *36*(4), 441–500.

McHutchon, A., & Rasmussen, C. (2011). Gaussian process training with input noise. *Advances in neural information processing systems*, *24*, 1–9.

McKinney, W. (2010). Data structures for statistical computing in Python. *445*, 51–56.

MDA Space Missions. (2024). RADARSAT-2: Advanced Radar Imaging Satellite [MDA Space Missions, Version 2]. https://www.mdacorporation.com/space/radarsat-2/

Meyer, F. J. (2023). University of Alaska GEOS 657 Microwave Remote Sensing course. www.radar.community.uaf.edu/wp-content/uploads/sites/667/2023/04/2023-Lectures16-InSARTimeSeriesAnalysis-II.pdf

Milillo, P., Bürgmann, R., Lundgren, P., Salzer, J., Perissin, D., Fielding, E., Biondi, F., & Milillo, G. (2016). Space geodetic monitoring of engineered structures: The ongoing destabilization of the Mosul dam, Iraq. *Scientific reports*, *6*(1), 1–7.

Milillo, P., Giardina, G., Perissin, D., Milillo, G., Coletta, A., & Terranova, C. (2019). Pre-collapse space geodetic observations of critical infrastructure: the Morandi Bridge, Genoa, Italy. *Remote Sensing*, *11*(12), 1403.

Milillo, P., Giardina, G., Perissin, D., Milillo, G., Coletta, A., & Terranova, C. (2020). Reply to Lanari, R., et al. comment on "pre-collapse space geodetic observations of critical infrastructure: The morandi bridge, Genoa, Italy" by Milillo et al.(2019). *Remote Sensing*, *12*(24), 4016.

Milillo, P., Perissin, D., Salzer, J. T., Lundgren, P., Lacava, G., Milillo, G., & Serio, C. (2016). Monitoring dam structural health from space: Insights from novel InSAR techniques and multi-parametric modeling applied to the Pertusillo dam Basilicata, Italy. *International Journal of Applied Earth Observation and Geoinformation*, *52*, 221–229.

Morgenstern, N. R., Vick, S. G., Viotti, C. B., & Watts, B. D. (2015). Fundão Tailings Dam Review Panel: Report on the immediate causes of the failure of Fundao dam. Published online at http://fundaoinvestigation.com/.

NASA. (2024). The National Aeronautics and Space Administration. www.landsat.gsfc.nasa.gov/satellites/landsat-1/

Navarro, L., Aravena, G., Engels, J., & Turner, J. (2019). Satellite bathymetry for the monitoring of supernatant water volumes within tailings storage facilities. *Paste 2019: Proceedings of the 22nd International Conference on Paste, Thickened and Filtered Tailings*, 205–217.

O'Donovan, C., Adam, E., & Torres-Cruz, L. (2022). Remote sensing of the decant pond of tailings dams: Insights from a South African case study. *Journal of the Southern African Institute of Mining and Metallurgy*, *122*(4), 167–172.

Ormann, L., Zardari, M. A., Mattsson, H., Bjelkevik, A., & Knutsson, S. (2013). Numerical analysis of strengthening by rockfill embankments on an upstream tailings dam. *Canadian Geotechnical Journal*, *50*(4), 391–399.

Paszke, A., Gross, S., Massa, F., Lerer, A., Bradbury, J., Chanan, G., Killeen, T., Lin, Z., Gimelshein, N., Antiga, L., et al. (2019). Pytorch: An imperative style, high-performance deep learning library. *Advances in neural information processing systems*, *32*, 1–9.

Pedregosa, F., Varoquaux, G., Gramfort, A., Michel, V., Thirion, B., Grisel, O., Blondel, M., Prettenhofer, P., Weiss, R., Dubourg, V., et al. (2011). Scikit-learn: Machine Learning in Python. *Journal of Machine Learning Research*, *12*(85), 2825–2830.

Peduto, D., Elia, F., & Montuori, R. (2018). Probabilistic analysis of settlement-induced damage to bridges in the city of Amsterdam (The Netherlands). *Transportation Geotechnics*, *14*, 169–182.

Peduto, D., Giangreco, C., & Venmans, A. A. (2020). Differential settlements affecting transition zones between bridges and road embankments on soft soils: Numerical analysis of maintenance scenarios by multi-source monitoring data assimilation. *Transportation Geotechnics*, *24*, 100369.

Peduto, D., Huber, M., Speranza, G., van Ruijven, J., & Cascini, L. (2017). DInSAR data assimilation for settlement prediction: case study of a railway embankment in the Netherlands. *Canadian Geotechnical Journal*, *54*(4), 502–517.

Peduto, D., Santoro, M., Aceto, L., Borrelli, L., & Gullà, G. (2021). Full integration of geomorphological, geotechnical, A-DInSAR and damage data for detailed geometric-kinematic features of a slow-moving landslide in urban area. *Landslides*, *18*(3), 807–825.

Pierce, I. (2021). *Applying the Material Point Method to identify key factors controlling runout of the Cadia tailings dam failure of 2018* [Doctoral dissertation, Virginia Tech].

PRI. (2020). Principles for Responsible Investment: Investor Mining and Tailings Safety Initiative. https://www.unpri.org/showcasing-leadership/investor-mining-and-tailings-safety-initiative/8943.article

Priscu, C., Mitri, H., & Keira, H. (1999). *Behavior of mine tailings dams under high tailings deposition rates* [Doctoral dissertation, Citeseer].

Psarropoulos, P. N., & Tsompanakis, Y. (2008). Stability of tailings dams under static and seismic loading. *Canadian Geotechnical Journal*, *45*(5), 663–675.

QGIS Development Team. (2024). QGIS [Open Source Geospatial Foundation]. https://qgis.org/

Reid, D., Fanni, R., & Fourie, A. (2022). Effect of tamping conditions on the shear strength of tailings. *International Journal of Geomechanics*, *22*(3), 04021288.

Reinders, K. J., Hanssen, R. F., van Leijen, F. J., & Korff, M. (2021). Augmented satellite InSAR for assessing short-term and long-term surface deformation due to shield tunnelling. *Tunnelling and Underground Space Technology*, *110*, 103745.

Robertson, P., de Melo, L., Williams, D. J., & Wilson, G. W. (2020). Expert panel report on the causes of failure of Feijão Dam I. www.b1technicalinvestigation.com

Rosen, P. A., Hensley, S., Joughin, I. R., Li, F. K., Madsen, S. N., Rodriguez, E., & Goldstein, R. M. (2000). Synthetic aperture radar interferometry. *Proceedings of the IEEE*, *88*(3), 333–382.

Rossi, C., Bateson, L., Bayaraa, M., Butcher, A., Ford, J., & Hughes, A. (2022). Framework for remote sensing and modelling of lithium-brine deposit formation. *Remote Sensing*, *14*(6), 1383.

Rouet-Leduc, B., Jolivet, R., Dalaison, M., Johnson, P. A., & Hulbert, C. (2021). Autonomous extraction of millimeter-scale deformation in InSAR time series using deep learning. *Nature communications*, *12*(1), 1–11.

Sacks, R., Brilakis, I., Pikas, E., Xie, H. S., & Girolami, M. (2020). Construction with digital twin information systems. *Data-Centric Engineering*, *1*, 1–12.

Sadeghi, Z., Wright, T. J., Hooper, A., Jordan, C., Novellino, A., Bateson, L., & Biggs, J. (2021). Benchmarking and inter-comparison of Sentinel-1 InSAR velocities and time series. *Remote Sensing of Environment*, *256*, 112306.

Santurkar, S., Tsipras, D., Ilyas, A., & Madry, A. (2018). How does batch normalization help optimization? *Advances in neural information processing systems*, *31*, 1–10.

SARmap, S. (2025). ENVI SARscape. https://www.nv5geospatialsoftware.com/

Selvakumaran, S., Plank, S., Geiß, C., Rossi, C., & Middleton, C. (2018). Remote monitoring to predict bridge scour failure using Interferometric Synthetic Aperture Radar (InSAR) stacking techniques. *International journal of applied earth observation and geoinformation*, *73*, 463–470.

Selvakumaran, S., Rossi, C., Marinoni, A., Webb, G., Bennetts, J., Barton, E., Plank, S., & Middleton, C. (2020). Combined InSAR and Terrestrial Structural Monitoring of Bridges. *IEEE Transactions on Geoscience and Remote Sensing*, *58*(10), 7141–7153.

Shamshiri, R., Motagh, M., Baes, M., & Sharifi, M. A. (2014). Deformation analysis of the Lake Urmia causeway (LUC) embankments in Northwest Iran: insights from multi-sensor interferometry synthetic aperture radar (InSAR) data and finite element modeling (FEM). *Journal of Geodesy*, *88*(12), 1171–1185.

Siegmund, R., Brcic, R., Kotzerke, P., & Eineder, M. (2022). The European Ground Motion Service EGMS - Processing Central Europe with First Results on Quality

and Point Densities. *IGARSS 2022 - 2022 IEEE International Geoscience and Remote Sensing Symposium*, 5105–5108.

Simons, M., Fialko, Y., & Rivera, L. (2002). Coseismic deformation from the 1999 M w 7.1 Hector Mine, California, earthquake as inferred from InSAR and GPS observations. *Bulletin of the Seismological Society of America*, *92*(4), 1390–1402.

Smith, L. N. (2017). Cyclical learning rates for training neural networks. *2017 IEEE winter conference on applications of computer vision (WACV)*, 464–472.

Soderberg, R. L., & Busch, R. A. (1977). Design Guide for Metal and Nonmetal Tailings Disposal IC 8755.

Soga, K., Alonso, E., Yerro, A., Kumar, K., & Bandara, S. (2016). Trends in large-deformation analysis of landslide mass movements with particular emphasis on the material point method. *Géotechnique*, *66*(3), 248–273.

Sorabatake. (2020). *Structural Classifications Using SAR Polarimetry (Polarimetric Decomposition)*. https://sorabatake.jp/en/15097/#:~:text=Polarimetric%20decomposition%20is%20useful%20for,help%20with%20handling%20SAR%20images.

Sowter, A., Bateson, L., Strange, P., Ambrose, K., & Syafiudin, M. F. (2013). DInSAR estimation of land motion using intermittent coherence with application to the South Derbyshire and Leicestershire coalfields. *Remote Sensing Letters*, *4*(10), 979–987.

Spaans, K., & Hooper, A. (2016). InSAR processing for volcano monitoring and other near-real time applications. *Journal of Geophysical Research, Solid Earth*, *121*(4), 2947–2960.

Thomas, A., Edwards, S., Engels, J., McCormack, H., Hopkins, V., & Holley, R. (2019). Earth observation data and satellite InSAR for the remote monitoring of tailings storage facilities: a case study of Cadia Mine, Australia. *Proceedings of the 22nd International Conference on Paste, Thickened and Filtered Tailings*, 183–195.

Torres, R., Snoeij, P., Geudtner, D., Bibby, D., Davidson, M., Attema, E., Potin, P., Rommen, B., Floury, N., Brown, M., et al. (2012). Gmes sentinel-1 mission. *Remote Sensing of Environment*, *120*, 9–24.

Torres-Cruz, L. A., & O'Donovan, C. (2023). Public remotely sensed data raise concerns about history of failed Jagersfontein dam. *Scientific Reports*, *13*(1), 4953.

UKSA. (2018). United Kingdom Space Agency, International Partnership Programme. www.gov.uk/government/collections/international-partnership-programme

USGS. (2022). The United States Geological Survey. https://keyhole.engelsjk.com/

Van der Maaten, L., & Hinton, G. (2008). Visualizing data using t-SNE. *Journal of machine learning research*, *9*(86), 2579–2605.

Vick, S. G. (1990). Planning, design, and analysis of tailings dams.

Virtanen, P., Gommers, R., Oliphant, T. E., Haberland, M., Reddy, T., Cournapeau, D., Burovski, E., Peterson, P., Weckesser, W., Bright, J., et al. (2020). SciPy 1.0: Fundamental algorithms for scientific computing in Python. *Nature Methods*, *17*, 261–272.

Whittle, A. J., El-Naggar, H. M., Akl, S. A., & Galaa, A. M. (2022). Stability Analysis of Upstream Tailings Dam Using Numerical Limit Analyses. *Journal of Geotechnical and Geoenvironmental Engineering*, *148*(6), 1–14.

Williams, C. K., & Rasmussen, C. E. (2006). *Gaussian processes for machine learning* (Vol. 2). MIT press Cambridge, MA.

Witt, K., Schönhardt, M., Saarela, J., Frilander, C., Csicsak, J., Csovari, M., Várhegyi, A., Georgescu, D., Radulescu, D., & Zlagnean, D. (2004). Tailings management facilities–risks and reliability, Report of the European RTD project.

WMTF. (2020). World Mine Tailings Failures Initiative. www.worldminetailingsfailures.org/estimate-of-world-tailings-portfolio-2020/

Yu, H., Lan, Y., Yuan, Z., Xu, J., & Lee, H. (2019). Phase Unwrapping in InSAR : A Review. *IEEE Geoscience and Remote Sensing Magazine*, *7*(1), 40–58.

Zabala, F., & Alonso, E. (2011). Progressive failure of Aznalcollar dam using the material point method. *Géotechnique*, *61*(9), 795–808.

Zhao, Z., Wu, Z., Zheng, Y., & Ma, P. (2021). Recurrent neural networks for atmospheric noise removal from InSAR time series with missing values. *ISPRS Journal of Photogrammetry and Remote Sensing*, *180*, 227–237.

Zhou, W., Li, S., Zhou, Z., & Chang, X. (2016). InSAR observation and numerical modeling of the earth-dam displacement of shuibuya dam (China). *Remote sensing*, *8*(10), 877.

Appendix A

Published Work

A.1 InSAR and numerical modelling for tailings dam monitoring – the Cadia failure case study

Bayaraa, Maral, Brian Sheil, and Cristian Rossi. 2024. "InSAR and numerical modelling for tailings dam monitoring–the Cadia failure case study." Géotechnique, 74, no.10: 985-1003.

A.2 Entity Embeddings in Remote Sensing: Application to Deformation Monitoring for Infrastructure

Bayaraa, Maral, Cristian Rossi, Freddie Kalaitzis, and Brian Sheil. 2023. "Entity Embeddings in Remote Sensing: Application to Deformation Monitoring for Infrastructure" Remote Sensing, 15, no. 20: 4910.